

**DEVELOPMENT OF NOVEL ELECTRICALLY
CONDUCTIVE SCAFFOLDS BASED ON SILK FIBROIN
WITH ELECTRICAL STIMULATION FOR PERIPHERAL
NERVE REGENERATION**

A thesis submitted to the University of Manchester for the degree of
Doctor of Philosophy in the Faculty of Science and Engineering

2022

Chinnawich Phamornnak

School of Natural Sciences

Department of Materials

CONTENTS

LIST OF FIGURES.....	8
LIST OF TABLES.....	20
LIST OF ABBREVIATIONS.....	21
ABSTRACT	24
DECLARATION.....	25
COPYRIGHT STATEMENT	26
ACKNOWLEDGEMENT.....	27
THE AUTHOR.....	28
CHAPTER 1 Introduction	29
1.1. Statement of Problems	29
1.2. Objectives.....	31
1.3. Hypothesis.....	32
1.4. Scope of the Study	32
CHAPTER 2 Literature Review.....	34
2.1. Anatomy and Physiology of Peripheral Nervous System.....	34
2.1.1. Histology of nerves	34
2.1.2. Structure of spinal nerves	37
2.1.3. Electrical signals of neurons	38
2.1.4. Synaptic transmission	42
2.2. Peripheral Nerve Injury.....	44
2.2.1. Seddon classification	44
2.2.2. Sunderland classification	46
2.3. Peripheral Nerve Regeneration.....	47
2.3.1. Neurobiology of peripheral nerve injury	48
2.3.2. Factors and molecules associated with neuron growth.....	49

2.4.	Clinical Peripheral Nerve Therapy and Tissue Engineered Peripheral Nerve Approaches	51
2.4.1.	Autologous nerve grafts	52
2.4.2.	Artificial nerve conduits and tissue engineered nerve scaffolds	52
2.4.3.	Electrical stimulation	54
2.4.4.	Other external stimuli for non-surgical peripheral nerve treatment	56
2.5.	Materials for Tissue Engineered Peripheral Nerve Scaffolds	56
2.5.1.	Silk fibroin (SF)	65
2.5.2.	Poly(3,4-ethylenedioxythiophene) polystyrene sulfonate (PEDOT: PSS).....	69
2.6.	Electrospinning	71
2.6.1.	Electrospinning apparatus	71
2.6.2.	Jet generation	72
2.6.3.	States of materials for electrospinning.....	75
2.6.4.	Electrospinning parameters	76
2.7.	Interpenetrating Polymer Networks (IPNs).....	77
2.7.1.	The chemistry of preparation	77
2.7.2.	The structure of IPN	77
2.8.	Electrical Stimulation Methods	78
2.8.1.	Direct stimulation	78
2.8.2.	Capacitive stimulation	84
2.8.3.	Inductive stimulation	85
2.9.	Peripheral Nerve Cell Lines.....	86
2.9.1.	Rat adrenal pheochromocytoma cell line (PC-12)	87
2.9.2.	Mouse neuroblastoma x rat glioma hybrid cell line (NG108-15)....	87
2.10.	<i>In Vitro</i> Effects of Electrical Stimulation on Peripheral Nerve	88
	CHAPTER 3 Optimisation of double layer electrospun silk fibroin	90
3.1.	Materials and Methods	91

3.1.1.	Extraction of silk fibroin	91
3.1.2.	Electrospinning solution preparation.....	91
3.1.3.	Optimisation of electrospinning parameters	92
3.1.4.	Post-treatment of electrospun mats and FTIR analysis.....	94
3.1.5.	Scanning electron microscopy (SEM) analysis.....	95
3.1.6.	Fibre alignment with 2D FFT analysis	96
3.2.	Results.....	96
3.2.1.	Qualitative analysis of degummed silk fibroin	96
3.2.2.	Optimal conditions for preparation of electrospinning solution	97
3.2.3.	Effects of different electrospinning parameters on electrospun SF mats	100
3.2.4.	Diameter of fibre and degree of alignment	105
3.2.5.	β -sheet formation in electrospun SF mats.....	108
3.3.	Discussion	111
3.3.1.	Optimal parameters for preparing electrospinning SF solution ...	111
3.3.2.	Effects of electrospinning solution on electrospun SF mats	114
3.3.3.	Effects of humidity and temperature on electrospun SF mats.....	115
3.3.4.	Effects of apparatus orientation on electrospun SF mats.....	117
3.3.5.	Effects of rotating speed of collector on electrospun SF mats	119
3.3.6.	Effects of post-treatment on electrospun SF mats	120
3.3.7.	General discussion of double layer electrospun mats	122
3.4.	Conclusion.....	124
CHAPTER 4 Electrical Modification of Electrospun Silk Fibroin		126
4.1.	Materials and Methods	127
4.1.1.	Interpenetrating polymer network (IPN).....	127
4.1.2.	Dip coating	128
4.1.3.	ATR-FTIR analysis.....	129
4.1.4.	Scanning electron microscopy (SEM).....	129

4.1.5.	Tensile testing	129
4.1.6.	X-ray and Hard X-ray photoelectron spectroscopy (XPS and HAXPES)	130
4.1.7.	Electrochemical characterisation	131
4.1.8.	Statistical analysis.....	133
4.2.	Results.....	133
4.2.1.	The presence of PEDOT:PSS on electrospun SF	133
4.2.2.	Tensile profiles of electrospun SF and IPN mats.....	135
4.2.3.	Surface and bulk chemical species of electrospun SF and IPN mats	138
4.2.4.	Electrochemical characters of electrospun SF and IPN mats	144
4.3.	Discussion	147
4.3.1.	Physical properties of IPN mats.....	147
4.3.2.	Mechanical properties of IPN mats.....	149
4.3.3.	Electrochemical properties of IPN mat	153
4.4.	Conclusion.....	155
CHAPTER 5 <i>In Vitro</i> , Neuron Growth and Neurite Extension on Electrically Conductive		
	Electrospun Mats	157
5.1.	Materials and Methods	158
5.1.1.	Sample preparation for cell culture	158
5.1.2.	NG108-15 cell culture	160
5.1.3.	Indirect test (conditioned medium).....	162
5.1.4.	Direct contact test	163
5.1.5.	Cell metabolic activity <i>via</i> resazurin assay	165
5.1.6.	DNA concentration <i>via</i> PicoGreen® assay	165
5.1.7.	Live/dead staining	166
5.1.8.	Scanning electron microscopy (SEM) of cell samples.....	166
5.1.9.	Immunofluorescence (IF)	166

5.1.10.	Measurement of neurite extension length.....	167
5.1.11.	Statistical analysis.....	168
5.2.	Results.....	169
5.2.1.	NG108-15 grown on TCP substrates.....	169
5.2.2.	NG108-15 grown on TCP substrates with conditioned media from electrospun SF and IPN mats	175
5.2.3.	NG108-15 grown on electrospun SF and IPN mats without differentiation factors.....	178
5.2.4.	NG108-15 grown on electrospun SF and IPN mats with differentiation factors.....	183
5.3.	Discussion	187
5.3.1.	Activation of cell differentiation	187
5.3.2.	Toxicity of PEDOT:PSS and other chemical residues	188
5.3.3.	Neuron growth and neurite extension on electrospun SF based materials.....	190
5.4.	Conclusion	194
CHAPTER 6 Effects of Electrical Regimes on Neuronal Cells		195
6.1.	Materials and Methods	197
6.1.1.	Electrical stimulation apparatus	197
6.1.2.	Sample preparation for electrical stimulation.....	197
6.1.3.	Finite element analysis by COMSOL Multiphysics®	198
6.1.4.	NG108-15 Cell culture	200
6.1.5.	Electrical stimulation of NG108-15 on electrospun SF and IPN mats	201
6.2.	Results.....	202
6.2.1.	Computational modelling	202
6.2.2.	Optimisation of electrical parameters	213

6.2.3.	Effect of electrical stimulation on neurite outgrowth for NG108-15 grown on electrospun SF and IPN ($\alpha = 2.3$) mats	219
6.3.	Discussion	229
6.3.1.	Effect of different types of electrode on electrical stimulation.....	229
6.3.2.	Distribution of EF and current density in cell culture system	230
6.3.3.	Electrochemical reaction of cell culture medium during electrical stimulation	232
6.3.4.	Effect of electrical stimulation on neurite outgrowth	233
6.3.5.	Suggestions for the further analysis	237
6.4.	Conclusion	240
CHAPTER 7 Overall Conclusion.....		242
7.1.	Summary	242
7.1.1.	Fabrication of non-woven mats (Chapter 3)	242
7.1.2.	Modification of electrical conductive property of the fibre mat (Chapter 4)	243
7.1.3.	<i>In vitro</i> biocompatibility (Chapter 5)	243
7.1.4.	Electrical stimulation (Chapter 6)	244
7.2.	General Discussion	244
7.3.	Limitations of Study	245
7.3.1.	Electrospinning tools	245
7.3.2.	Cell culture	246
7.4.	Future Work	246
7.4.1.	Electrically conductive material fabrication	246
7.4.2.	Electrical stimulation <i>via</i> electrically conductive material	246
7.4.3.	Potential applications	247
REFERENCES		249

Final word count: 55,955 words

LIST OF FIGURES

Figure 2.1 Diagram of the major components of the central and peripheral nervous systems and their functions, this figure has been adapted and redrawn from [25].	35
Figure 2.2 Structure of the peripheral nerve extending from the spinal cord (spinal nerve) classified by functions [29].	36
Figure 2.3 Microstructure of peripheral nerve: (a) a typical peripheral nerve and its connective tissue wrappings, which associated to spinal nerve and (b) a pseudo coloured scanning electron micrograph showing peripheral nerve fibres (SEM x 340), this figure is adapted from [37].	38
Figure 2.4 Schematic of the resting membrane potential and typical action potential (AP) of peripheral nerves: (1) resting membrane potential, (2) depolarisation, (3) repolarisation, and (4) hyperpolarisation, this figure is based on information from [25, 38].	39
Figure 2.5 Schematic of action potential (AP) and the activation of ion channels (Na^+ and K^+ channels) in the different states, this figure is based on information from [25, 38].	40
Figure 2.6 Schematic diagram of action potential conduction in axons, this figure is adapted and redrawn from [38].	42
Figure 2.7 Schematic model of the synaptic transmission: (a) a chemical synapse and synaptic cleft between pre- and post-synaptic membranes and (b) an electrical synapse touching with very closed intercellular junctions (gap junctions) and the arrows represent the transfer of electrical signals, ions, metabolites, and small molecules of secondary messengers, this figure is based on information and adapted from [26, 27].	43
Figure 2.8 Schematic of nerve injury, Wallerian degeneration, and regeneration process, this figure is adapted from [7].	49
Figure 2.9 Schematic of different structures of nerve guidance conduits (NGCs) and the modification of scaffolds with either physical or biological cues [64].	54
Figure 2.10 Schematic of regenerated silk fibroin molecular chain including hydrogen bonding, secondary protein structures, and amino acid sequences [124].	66

Figure 2.11 Chemical structure of poly(3,4-ethylenedioxythiophene) (PEDOT), polystyrene sulfonate (PSS), and the complex form of PEDOT:PSS.	71
Figure 2.12 Schematic of electrospinning jet from needle to collector, this figure is based on information from [166].	74
Figure 2.13 Transition of droplet due to the increase of voltage, this figure is based on information from [168, 169].	74
Figure 2.14 Schematic of simultaneous IPN and sequential IPN, this figure is based on information from [177, 178].	78
Figure 2.15 The direct ES model: the electrodes and electrochemical cell in (a) horizontal axis and (b) vertical axis, this figure is adapted and redrawn from [179].	79
Figure 2.16 Schematic representation of the electrical double layer (EDL): (a) the charge injection at the surface of electrode and (b) the relative electrical potential in each layer, this figure is adapted and redrawn from [179].	80
Figure 2.17 Alternative direct ES model: (a) double salt bridges model without direct contact of electrodes to cell culture medium and faradic by-products and (b) single salt bridge model with the separation of faradic by-product from each electrode, this figure is adapted and redrawn from [179].	82
Figure 2.18 Direct ES through an electrically conductive scaffold with cells on top, this figure is adapted and redrawn from [179].	84
Figure 2.19 Capacitive ES model and the generation of electric field by two parallel electrodes at the outer surface of TCP: (a) horizontal direction of electrodes and (b) vertical direction of electrodes, this figure is adapted and redrawn from [179].	85
Figure 2.20 Inductive ES model with the generation of electromagnetic field (EMF) by solenoid coils at the outer surface of TCP: (a) horizontal direction of solenoid coils and (b) the combination of horizontal solenoid coils and static magnetic field from magnets, this figure is adapted and redrawn from [179].	86

Figure 3.1 Schematic of horizontal electrospinning setup composing of a syringe pump, silk solution in a syringe with 19 G needle, a rotating mandrel collector, and a high voltage supply between needle and collector.	93
Figure 3.2 Schematic of vertical electrospinning setup in an environmental control system composing of a syringe pump, silk solution in a syringe connecting to PTFE tube, luer, and needle, a rotating mandrel collector, and outside DC power supplies charging to needle (+) and collector (-).	94
Figure 3.3 Morphologies of silk worm cocoons and degummed silk fibroin: (a) 5 g of <i>B. mori</i> silk cocoons cut into pieces $\sim 2 \times 2 \text{ cm}^2$ before degumming, (b) degummed silk fibroin (cotton-like fluffy fibres prepared from 5 g of silk cocoons) of size $\sim 10 \times 10 \text{ cm}^2$ after spreading, (c) SEM image of silk cocoons composing of fibroin and sericin, and (d) SEM image of degummed silk fibroin with the scale bar of $10 \mu\text{m}$	97
Figure 3.4 Electrospun SF mats (white colour) on aluminium foils collector (silver colour), prepared from electrospinning solutions of 6% wt/v SF in various ratios of FA/CaCl ₂ (ml:g): (a) 98:2, (b) 95:5, and (c) 90:10, and those mats after leaving at room temperature for one day: (d) 95:5 and (e) 90:10, and (f) the electrospinning solution of 6% wt/v SF in FA/CaCl ₂ (left) 98:2 and (right) 95:5 after leaving at room temperature for 7 days, the undissolved SF is shown in the circles, and the figures (a – e), the size of aluminium foils are $\sim 5 \times 5 \text{ cm}^2$	99
Figure 3.5 Image of the electrospinning solution of 10% wt/v SF in FA/CaCl ₂ with the ratio 98:2 at different time points: (a) after stirring at room temperature for 5 min and (b) after incubating at 45° C overnight (approximately 10 – 12 h).	99
Figure 3.6 Horizontal electrospinning of 10% wt/v SF in FA/CaCl ₂ (98:2) operated with 0.4 ml/h feed rate, 12 cm distance, and 15 kV voltage supply for 4 h: (a) electrospun SF mats on greaseproof paper cut in to pieces $\sim 2 \times 3 \text{ cm}^2$, (b) post-treatment process with 80% EtOH, and representative SEM images from three independent experiments of electrospun SF fibres collected with the rotating speed of (c) 1,000 rpm and (d) 1,500 rpm, the scale bar represented is $10 \mu\text{m}$	101

- Figure 3.7 Electrospun SF mats (white colour) on aluminium foil (silver colour) fabricated by vertical electrospinning of 10% SF in FA/CaCl₂ (98:2) in the different feed rates (ml/h) and voltage supply (kV) with the constant distance of 12 cm at room temperature: (a) 0.3 ml/h, 15 kV, (b) 0.3 ml/h, 18 kV, (c) 0.3 ml/h, 20 kV, (d) 0.05 ml/h, 15 kV, (e) 0.05 ml/h, 18 kV, (f) 0.4 ml/h, 25 kV, (g) 0.4 ml/h, 30 kV, and (h) 0.4 ml/h, 35 kV, sizes of aluminium foils are ~5 x 5 cm²..... 104
- Figure 3.8 Representative SEM images from three independent experiments of vertical electrospinning of 10% SF in FA/CaCl₂ (98:2) in the different voltage supplies and % R.H. with the constant feed rate of 0.4 ml/h and distance of 12 cm: (a) 25 kV, 35% R.H., (b) 30 kV, 35% R.H., (c) 35 kV, 35% R.H., (d) 25 kV, 50% R.H., (e) 30 kV, 50% R.H., and (f) 35 kV, 50% R.H., the scale bars represent 10 µm..... 105
- Figure 3.9 Distribution of fibre diameters of electrospun SF mats: (a) horizontal electrospinning with parameters of 0.4 ml/h feed rate, 12 cm distance, 15 kV voltage supply, 1000 rpm (n = 100) and 1500 rpm (n = 100) collector speeds and (b) vertical electrospinning with parameters of 0.3 ml/h (n = 123) and 0.4 ml/h (n = 115) feed rate, 12 cm distance, 35 kV voltage supply, 35% R.H., ~800 rpm collector speed, where n is the number of fibres, representing three samples fabricated from three independent electrospinning experiments. 106
- Figure 3.10 Example of 2D FFT alignment analysis: 8-bit SEM images of electrospun SF (a) aligned fibres and (d) random fibres, FFT images of (b) aligned fibres and (e) random fibres, and oval profiles analysis with radial sums mode and 360 number of points of FFT images of (c) aligned fibres and (f) random fibres. 107
- Figure 3.11 Schematic of double layer electrospun SF mat and the electrospinning parameters of each layer. 107
- Figure 3.12 Fibre diameter and alignment of electrospun SF mat: (a) distribution of fibre diameters: the bottom layer (n = 405) and the top layer (n = 200), where n is the number of fibres and (b) average 2D FFT alignment value in each angle (0° – 180°) in both layers, bottom

is random fibres and top is aligned fibres ($n = 3$), where n is the number of electrospun samples fabricated from independent experiments with independent solutions.	108
Figure 3.13 ATR-FITR spectra of electrospun SF mats after post-treatment with: (a) untreated, (b) water (c) various % EtOH in water, and (d) various % MeOH in water.	109
Figure 3.14 Relative percentage of secondary protein structures composing of β -sheet, random coil, and turns and bend after post-treatment in different solutions: (a) untreated, water, and MeOH, and (b) EtOH.	110
Figure 3.15 Representative SEM images of electrospun SF mats from three independent experiments fabricated using 10% w/v SF in FA/CaCl ₂ (98:2) after post-treatment with different solutions: (a) untreated, (b) 80% EtOH treated, and (c) water treated fibres.	110
Figure 3.16 Example of electrospun SF removal from the greaseproof paper: (a) one layer of aligned fibres with the thickness of $\sim 70 \mu\text{m}$ (~ 8 h electrospinning), the arrow shows the direction of fibre alignment, the circle shows the fibre breakage following the alignment of fibres, (b) the schematic of aligned fibre breakage following the fibre alignment, and (c) one layer of random fibre with the thickness of $\sim 70 \mu\text{m}$ (~ 8 h electrospinning), the size of the mat is $2 \times 3 \text{ cm}^2$	123
Figure 4.1 Schematic process of electrospun fibre modification <i>via</i> IPN of PEDOT:PSS.	128
Figure 4.2 Schematic of Randles RC model: R_e is electrolyte resistance, R_c is charge transfer resistance, C_{dl} is double layer capacitance and W is Warburg element.	133
Figure 4.3 Examples of electrospun SF and IPN ($\alpha = 2.3$) mats with the size of $3 \times 1 \text{ cm}^2$: (a) electrospun SF mats (opaque white, in the left) and IPN of PEDOT:PSS on electrospun SF mats (dark blue or black, in the right) after washing 2 – 3 times with DI water and (b) the box-whisker plot of fibre diameters of eletrospun SF, 80% EtOH-treated electrospun SF, and IPN mats of PEDOT:PSS in the various ratios ($\alpha = 1.3 - 3.3$), the middle line is median, the mark (+) is mean, and n is the number of fibres representing a sample.	134
Figure 4.4 ATR-FTIR spectra of 80% EtOH treated electrospun SF and a representative of IPN mats in the wavenumber of $600 - 1900 \text{ cm}^{-1}$	135

Figure 4.5 Examples of the stress (MPa) and strain profile of electrospun SF: (a) dry-state electrospun SF mats (n = 3 samples) and (b-d) 80% EtOH treated electrospun SF mats in (b) dry-state (n = 3 samples), (c) wet-state, immersing in water for a few days (n = 3 samples), and (d) wet-state, immersing in water over a week (n = 4 samples).	136
Figure 4.6 Mechanical properties of electrospun SF and IPN mats: (a) ultimate tensile strength, (b) % strain at break, (c) Young's modulus, and (d) toughness, * represents statistically different (p -value < 0.01) <i>via</i> the nonparametric test (Kruskal-Wallis test), all wet state groups were compared with the control (SF-EtOH (w)), the error bar represents SD, and n is the number of samples from three independent electrospinning experiments....	138
Figure 4.7 Relative atomic percentage of S in/on electrospun SF and IPN mats: (a) bulk – sensitive HAXPES comparing between 80% EtOH treated electrospun SF mat, dip coating mat with the custom-made PEDOT:PSS (α = 1.3), and IPN (α = 1.3) mat and (b) surface – sensitive (~11nm) XPS and bulk – sensitive (~54 nm) HAXPES comparing between 80% EtOH treated electrospun SF mat, IPN (α = 2.3) mat, and IPN (α = 3.3) mat.	139
Figure 4.8 XPS and HAXPES results representing surface and bulk chemicals in the different depths of samples: (a) the relative atomic percentage of S in the different depths of IPN (α = 2.3) and IPN (α = 3.3) mats and (b) percentage of PEDOT and PSS compounds polymerised through the depths of material, calculated from spectra of XPS s2p and HAXPES S 1s.	140
Figure 4.9 The spectra of XPS and HAXPES fitted with S 2p and S 1s respectively: (left) IPN (α = 2.3) mat and (right) IPN (α = 3.3) mat.	141
Figure 4.10 The spectra of XPS and angle – resolved HAXPES of C, O, N and S in/on the IPN sample.	143
Figure 4.11 CV and EIS of electrospun SF and IPN samples measured with three – electrodes system of potentiostat: (a) CV plot between the sweeping potential of -1 and +1 V, (b) Nyquist plot derived from EIS measurement.	145
Figure 4.12 Examples of Bode and Nyquist plots derived from EIS measurement fitted with Randles model: (a – c) bode plots of electrospun SF, IPN (α = 2.3), and IPN (α = 3.3)	

respectively, and (d – f) Nyquist plots of electrospun SF, IPN ($\alpha = 2.3$), and IPN ($\alpha = 3.3$).	146
Figure 5.1 Schematic of the mounting protocol of electrospun SF mat on glass coverslip before IPN of PEDOT:PSS on samples.....	160
Figure 5.2 Examples of neurite orientation analysis, black dots-line and blue arrow represent the distance and displacement of neurite extension in coordinate x-y axis respectively: (a) showing θ in case of $X_2 > X_1$ and (b) showing θ in case of $X_2 < X_1$	168
Figure 5.3 Cell morphology of NG108-15 culturing in growth medium on: (a – c) TPC and (d – f) laminin-coated TCP, the cell confluence of (a and d) ~50%, (b and e) ~80 – 90%, and (c and f) over-confluence. The scale bar represents 250 μm	171
Figure 5.4 Cell morphology of NG108-15 culturing in (left) cAMP differentiation medium and (right) DMSO differentiation medium on different substrates and times: (a and e) TCP for 2 days, (b and f) TCP for 4 days, (c and g) laminin-coated TCP for 2 days, and (d and h) laminin-coated TCP for 4 days. Neurites are shown in magenta lines and the scale bar represents 250 μm	172
Figure 5.5 Cellular activities of NG108-15 cultured in different media: (a) cell metabolic activity and (b) DNA concentration of subconfluent NG108-15 in different cell culture media on TCP and laminin-coated TCP (n = 2 wells of cells).	173
Figure 5.6 Neurite extension lengths of subconfluent NG108-15 in different cell culture media on TCP and laminin-coated TCP, box – whisker plots from min – max with the median at the middle line: (a) incubating time of 1 day and 2 days and (b) incubating time of 3 days and 4 days, n represents the number of neurites measured from 2 – 3 images (10x, bright field microscope) of 2 wells of cells.	174
Figure 5.7 NG108-15 cultured in different conditioned media on TCP for 72 h: (a – d) live/dead staining and (e – h) bright field microscopy, (a and e) control growth medium, (b and f) conditioned SF medium, (c and g) conditioned IPN ($\alpha = 1.3$) medium, and (d and h) conditioned IPN ($\alpha = 1.8$) medium and the scale bar represented 250 μm	176

- Figure 5.8 NG108-15 cultured in different conditioned media on TCP for 72 h: (a – c) live/dead staining and (d – f) bright field microscopy, (a and d) conditioned IPN ($\alpha = 2.3$) medium, (b and e) conditioned IPN ($\alpha = 2.8$) medium, and (c and f) conditioned IPN ($\alpha = 3.3$) medium and the scale bar represented 250 μm 177
- Figure 5.9 Characterisation of cell growth and proliferation of subconfluent NG108-15 in different conditioned media: (a) metabolic activity and (b) DNA concentration (n = 6 wells of cells in parallel experiments), the error bar represents SD, the statistical analysis with nonparametric (Kruskal-Wallis test), control is the growth medium, * represents $p < 0.05$, ** $p < 0.01$, *** $p < 0.001$, and **** $p < 0.0001$ 178
- Figure 5.10 Characterisation of cell growth and proliferation of NG108-15 on electrospun SF and IPN mats: (a and b) metabolic activity and (c and d) DNA concentration (n = 3 samples of fibre mats in parallel experiments), the error bar represents SD, the statistical analysis with nonparametric (Kruskal-Wallis test), control is the growth medium, * represents $p < 0.05$ 179
- Figure 5.11 Neurite extension lengths of NG108-15 cultured in growth medium on different substrates, box – whisker plots from min – max with the median at the middle line, the mark (+) is mean, and n is the number of neurites on a fibre mat. 180
- Figure 5.12 SEM images of NG108-15 cultured in growth medium on different electrospun mats for 7 days: (a) SF, (b) IPN ($\alpha = 2.3$), (c) IPN ($\alpha = 3.3$), (d) laminin-coated SF, (e) laminin-coated IPN ($\alpha = 2.3$), and (f) laminin-coated IPN ($\alpha = 3.3$), the scale bar of 50 μm ... 180
- Figure 5.13 Example of neurite length and orientation of NG108-15 in growth phase cultured for 7 days on uncoated substrates: (a – c) polar scatter with the radian of 110 μm and (d – f) polar histogram with the radian of 30%, the position of 90° is the parallel direction to the fibre alignment, n is the number of neurites on a fibre mat. These graphs are replotted from the same data presented in Figure 5.11. 181
- Figure 5.14 Example of neurite length and orientation of NG108-15 in growth phase cultured for 7 days on laminin-coated substrates: (a – c) polar scatter with the radian of 110 μm and (d – f) polar histogram with the radian of 30%, the position of 90° is the parallel direction

to the fibre alignment, n is the number of neurites on a fibre mat. These graphs are replotted from the same data presented in Figure 5.11.	182
Figure 5.15 Neurite extension lengths of NG108-15 cultured in cAMP differentiation medium on different substrates, box – whisker plots from min – max with the median at the middle line, the mark (+) is mean, and n is the number of neurites on a fibre mat.	184
Figure 5.16 Differentiation phase of NG108-15 cultured in cAMP medium on laminin-coated substrates for 5 days: (a – c) SEM images of SF, IPN ($\alpha = 2.3$), and IPN ($\alpha = 3.3$) with the scale bar of 50 μm and (d – f) IF images of SF, IPN ($\alpha = 2.3$), and IPN ($\alpha = 3.3$) with the scale bar of 250 μm , β -III tubulin in neurites showed in green and nucleus showed in blue, the double-head arrow indicates the direction of aligned fibres.	184
Figure 5.17 Example of neurite length and orientation of NG108-15 in differentiation phase cultured for 7 days on uncoated substrates: (a – c) polar scatter with the radian of 350 μm and (d – f) polar histogram with the radian of 50%, the position of 90° is the parallel direction to the fibre alignment, n is the number of neurites on a fibre mat. These graphs are replotted from the same data presented in Figure 5.15.	185
Figure 5.18 Example of neurite length and orientation of NG108-15 in differentiation phase cultured for 7 days on laminin-coated substrates: (a – c) polar scatter with the radian of 350 μm and (d – f) polar histogram with the radian of 50%, the position of 90° is the parallel direction to the fibre alignment, n is the number of neurites on a fibre mat. These graphs are replotted from the same data presented in Figure 5.15.	186
Figure 6.1 Schematic of fibre mat positions in the C-dish™ electrical stimulation system.	198
Figure 6.2 3D model of an electrical stimulation system with C-dish™ electrodes, the component of fibre mat is not shown in this figure.	199
Figure 6.3 Distribution of current density in a cell culture chamber system with the applying voltage of 3 V: (a and c) distribution in the whole system, in (a) H-fibre, (c) F-fibre and (b and c) distribution in PEDOT:PSS mat, in (b) H-fibre, and (c) F-fibre.	205

Figure 6.4 Electric field (EF) in the middle position of cell culture chamber system generated by the input of pulse stimulation: (a) medium of H-fibre, (b) PEDOT:PSS mat of H-fibre, (c) medium of F-fibre, and (d) PEDOT:PSS mat of F-fibre.....	206
Figure 6.5 Current density in the middle position of cell culture chamber system generated by the input of pulse stimulation: (a) medium of H-fibre, (b) PEDOT:PSS mat of H-fibre, (c) medium of F-fibre, and (d) PEDOT:PSS mat of F-fibre.....	206
Figure 6.6 EF in H-fibre condition during a pulse stimulation with the input amplitude of 3 V: (a – c) ON period, $t = 0.2, 0.3$, and 0.4 s and (d – i) OFF period, $t = 0.5, 0.6, 0.7, 0.8, 0.9$, and 1.0 s respectively, the left scale is for arrow surface EF (V/m) and the right scale is for contour EF (v/m).	207
Figure 6.7 EF in F-fibre condition during a pulse stimulation with the input amplitude of 3 V: (a – c) ON period, $t = 0.2, 0.3$, and 0.4 s and (d – i) OFF period, $t = 0.5, 0.6, 0.7, 0.8, 0.9$, and 1.0 s respectively, the left scale is for arrow surface EF (V/m) and the right scale is for contour EF (v/m).	208
Figure 6.8 Current density in H-fibre condition during a pulse stimulation with the input amplitude of 3 V: (a – c) ON period, $t = 0.2, 0.3$, and 0.4 s and (d – i) OFF period, $t = 0.5, 0.6, 0.7, 0.8, 0.9$, and 1.0 s respectively, the left scale is for arrow surface current density (A/m^2) and the right scale is for contour current density (A/m^2).	209
Figure 6.9 Current density in F-fibre condition during a pulse stimulation with the input amplitude of 3 V: (a – c) ON period, $t = 0.2, 0.3$, and 0.4 s and (d – i) OFF period, $t = 0.5, 0.6, 0.7, 0.8, 0.9$, and 1.0 s respectively, the left scale is for arrow surface current density (A/m^2) and the right scale is for contour current density (A/m^2).	210
Figure 6.10 Space charge and current density at the microenvironment of fibres: (a – c) the input EF direction parallel to fibres and (d – e) the input EF direction perpendicular to the fibre alignment, the left scale is for arrow lines current density (A/m^2) and the right is for contour space charge density (C/m^3).	212
Figure 6.11 Schematic of the input and output signals of different types of electrodes measured in cell culture medium.....	213

- Figure 6.12 NG108-15 after electrical stimulation with DC of 3 V (~100 V/m) for 2 h: (a) before stimulation, (b) after stimulation, and (c) after stimulation and incubated for 24 h, the scale bar of 250 μ m. 215
- Figure 6.13 Neurite extension length after electrical stimulation with 1 V amplitude, 2 ms pulse cycle, 24 h/day, and various periods of pulse cycle (10, 100, and 1000 ms) on TCP, presented in a box – whisker plot from min – max with the median at the middle line and the mean at the mark (+): (a) uncoated TCP and (b) laminin-coated TCP, n represents the number of neurites measured from 2 wells of cells in parallel experiments of cell culture. 217
- Figure 6.14 NG108-15 after electrical stimulation with 1 V pulse amplitude, 2 ms pulse width, and 24 h/day for 3 days, (left) uncoated TCP and (right) laminin-coated TCP, the stimulation with the variation of pulse cycle periods: (a and e) control without stimulation, (b and f) 10 ms, (c and g) 100 ms, and (d and f) 1000 ms, the scale bar of 250 μ m. The arrow shows the direction of the EF. 218
- Figure 6.15 Neurite extension length on control materials (without ES) presented in a box – whisker plot from min – max with the median at the middle line and the mean at the mark (+): (a) uncoated mats and (b) laminin-coated mats (n = 120 neurites representing 2 samples of fibre mats in parallel experiments of cell culture) except the uncoated SF (F-fibre) at day 1 (n = 36). 220
- Figure 6.16 Example of neurite length and orientation of NG108-15 control (without the Op-ES) for 3 days on various materials of H-fibre condition: (left) uncoated mats, (right) laminin-coated mats, (a – d) polar scatter with the radian of 700 μ m, and (e – h) polar histogram with the radian of 50%, the position of 90° is the parallel direction to the fibre alignment, (n = 120 neurites representing 2 samples of fibres in parallel experiments of cell culture). These graphs are replotted from the same data presented in Figure 6.15. 221
- Figure 6.17 Example of neurite length and orientation of NG108-15 control (without the Op-ES) for 3 days on various materials of F-fibre condition: (left) uncoated mats, (right) laminin-coated mats, (a – d) polar scatter with the radian of 700 μ m, and (e – h) polar histogram

with the radian of 50%, the position of 90° is the parallel direction to the fibre alignment, (n = 120 neurites representing 2 samples of fibres in parallel experiments of cell culture). These graphs are replotted from the same data presented in Figure 6.15.	222
Figure 6.18 Immunofluorescence staining of NG108-15 after electrical stimulation with Op-ES for 3 days on various materials, (left) uncoated mats and (right) laminin-coated mats: (a, b, g, and h) control, (c, d, i, and j) stimulation on H-fibre, and (e, f, k, and l) stimulation on F-fibre, the double head arrow indicates the direction of aligned fibres.	225
Figure 6.19 Neurite extension length on materials with the Op-ES presented in a box – whisker plot from min – max with the median at the middle line and the mean at the mark (+): (a) uncoated H-fibre, (b) laminin-coated H-fibre, (c) laminin-coated F-fibre, and (d) laminin-coated F-fibre, all of Op-ES groups (n = 240 neurites representing 2 samples of fibre mats in parallel experiments of electrical stimulation) and all of the control groups (n = 120) except some conditions n were shown in the figure.....	226
Figure 6.20 Example of neurite length and orientation of NG108-15 with the Op-ES for 3 days on various materials of H-fibre condition: (left) uncoated mats, (right) laminin-coated mats, (a – d) polar scatter with the radian of 700 µm, and (e – h) polar histogram with the radian of 50%, the position of 90° is the parallel direction to the fibre alignment, (n = 240 neurites representing 2 samples of fibres in parallel experiments of cell culture). These graphs are replotted from the same data presented in Figure 6.19.	227
Figure 6.21 Example of neurite length and orientation of NG108-15 with the Op-ES for 3 days on various materials of F-fibre condition: (left) uncoated mats, (right) laminin-coated mats, (a – d) polar scatter with the radian of 700 µm, and (e – h) polar histogram with the radian of 50%, the position of 90° is the parallel direction to the fibre alignment, (n = 240 neurites representing 2 samples of fibres in parallel experiments of cell culture). These graphs are replotted from the same data presented in Figure 6.19.	228
Figure 6.22 The interaction of nerves and H ₂ O ₂ during the regeneration and development stages, blue areas and red lines represent the H ₂ O ₂ gradients and axons, respectively [226].	239

LIST OF TABLES

Table 2.1 Signs of nerve injuries in sensory and motor functions [43]	45
Table 2.2 Electrically conductive scaffolds for peripheral nerve regeneration.....	58
Table 2.3 Electrical conductive SF for tissue engineering and biomedical applications	61
Table 3.1 Optimisation of electrospinning solution preparation (electrospinning operation with the parameters of 1 ml/h feed rate, 12 cm distance, 15 kV voltage for 2 h on a static collector).	98
Table 3.2 Optimisation of electrospinning parameters of the horizontal system (electrospinning operation with parameters of 12 cm distance and 15 kV voltage).	101
Table 3.3 Optimisation of electrospinning parameters of the vertical system (electrospinning operation with parameters of 12 cm distance and 15 kV voltage).	103
Table 4.1 Mechanical properties of electrospun SF and IPN mats: (d) represents dry state testing, (w) represents wet state testing, and n is the number of samples from three independent electrospinning experiments.	137
Table 4.2 RC components associated with EIS fitting with Randles model, n is the number of samples.....	147
Table 5.1 Compositions of each cell culture medium.	162
Table 5.2 Cell culture activities for 7 days in the indirect test (conditioned medium).	163
Table 5.3 Cell culture activities for 7 days in the direct contact test.	164
Table 6.1 Materials properties used in electrical stimulation.	199
Table 6.2 the electrical parameters for optimisation.	202
Table 6.3 Computational results of electric field (EF) in cell culture chamber.	203
Table 6.4 Computational results of current density in cell culture chamber.	203
Table 6.5 Variation of electrical potential between C-dish™ electrodes in cell culture medium system.....	214

LIST OF ABBREVIATIONS

2D – Two dimensions	CV – Cyclic voltammetry
3D – Three dimensions	DC – Direct current
AC – Alternating current	DCM – Dichloromethane
Ag/AgCl – Silver/silver chloride	DI – Deionised
Ang II – Angiotensin 2	DLK-1 – Dual leucine zipper kinase-1
AP – Action potential	DMEM – Dulbecco's modified eagle medium
AT – Angiotensin receptor	DMSO – Dimethylsulfoxide
ATP – Adenosine triphosphate	DNA – Deoxyribonucleic acid
ATR – Attenuated total reflectance	DPBS – Dulbecco's phosphate buffer saline
Au – Gold	DRG – Dorsal root ganglion
B-50 – Neural phosphoprotein B-50	ECM – Extracellular matrix
BE – Binding energy	EDL – Electrical double layer
bFGF – Basic fibroblast growth factor	EEG – Electroencephalogram
C – Carbon	EF – Electric field
Ca²⁺ – Calcium ion	EIS – Electrochemical impedance spectroscopy
CaCl₂ – Calcium chloride	EMA – European Medicine Agency
CaM – Calmodulin	EMF – Electromagnetic field
CAM – Cell adhesion molecule	ER – Endoplasmic reticulum
cAMP – Cyclic adenosine monophosphate	ES – Electrical stimulation
CE – Counter electrode	EtOH – Ethanol
CNS – Central nervous system	F1 – Protein F1
CNT – Carbon nanotube	FA – Formic acid
CNTF – Ciliary neuronotrophic factor	FBS – Fetal bovine serum
col12a1a/b – Collagen type 12 alpha 1 chain	FDA – the United State, Food and Drug Administration

Fe₂SO₄·7H₂O – Iron (II) sulphate heptahydrate	MAP – Microtubule associated protein
FFT – Fast Fourier transformation	MAP2 – Microtubule associated protein 2
FTIR – Fourier transform infrared	MeOH – Methanol
GABA – Gamma (γ) aminobutyric acid	mRNA – Messenger ribonucleic acid
GAP43 – Growth associated protein 43	Na⁺ – Sodium ion
GCE – Glassy-carbon electrode	Na₂S₂O₈ – Sodium persulfate
GdNPF – Glial derived neurite promoting factor	NG108-15 – Mouse neuroblastoma x rat glioma hybrid cell line
GGF – Glial growth factor	NGC – Nerve guidance conduit
GO – Graphene oxide	NGF – Neural growth factor or nerve growth factor
H₂O – Water	NGNF – Non-functional graphene nano-film
H₂O₂ – Hydrogen peroxide	NRCM – Neonatal rat cardiomyocyte
HA – Hydroxyapatite	Op-ES – Optimal electrical stimulation
HAXPES – Hard X-ray photoelectron spectroscopy	p75 – p75 neurotrophin receptor
HCA – High-content analysis	PANi – Polyaniline
HFIP – hexafluoroisopropanol	PBS – Phosphate buffer saline
hiPSC-CM – human-induced pluripotent stem cell-derived cardiomyocyte	PC-12 – Rat adrenal pheochromocytoma cell line
HL-1 – Mouse cardiomyocyte cell line	PCL – Polycaprolactone
hMSC – Human mesenchymal stem cell	PCLF – Polycaprolactone fumarate
IPN – Interpenetrating polymer network	Pd – Palladium
iPSC – Induced pluripotent stem cell	PDMA – Japan, Pharmaceuticals and Medical Devices Agency
K⁺ – Potassium ion	PEDOT – Poly(3,4-ethylenedioxythiophene)
L929 – Mouse fibroblast cell line	PEDOT:PSS – Poly(3,4-ethylenedioxythiophene) polystyrene sulfonate
LiBr – Lithium bromide	PEG – Polyethylene glycol

PEGDE – Poly(ethylene glycol) diglycidyl ether	SNAP-25 – Synaptosomal-associated protein 25
PGA – Poly(glycolide)	SS – Stainless steel
PIP2 – Phosphatidylinositol 4,5-biophosphate	PLLA – Poly-L-lactide
PKC – Protein kinase C	PMEF – Pulse electromagnetic field
PLA – Poly(lactide)	PMMA – Poly(methyl methacrylate)
PLCL – poly(DL-lactide-co-ε-caprolactone)	SWCNT – Single-walled carbon nanotube
PNI – Peripheral nerve injury	SYP – Synaptophysin
PNS – Peripheral nervous system	TCP – Tissue culture plastic
PPy – Polypyrrole (PPy)	TE – Tris-ethylenediaminetetraacetic acid
Pt – Platinum	TENS – Transcutaneous electrical nerve stimulation
PTFE – Polytetrafluoroethylene	TFA – Trifluoroacetic acid
PVA – polyvinyl alcohol	Ti – Titanium
R.H. – Relative humidity	TIPS – Thermal-induced phase separation
RE – Reference electrode	TrkA – Tropomyosin receptor kinase A
rGO – Reduce graphene oxide	USSC – Human unrestricted somatic stem cell
ROS – Reactive oxygen species	UTS – Ultimate tensile strength
SAM – Substrate adhesion molecule	UV – Ultraviolet
SC – Schwann cell	VGCC – Voltage gated calcium channel
SECM – Scanning electrochemical microscopy	VIPS – Vapour-induced phase separation
SEM – Scanning electron microscopy	WE – Working electrode
SF – Silk fibroin	Wnt/β-catenin – Wingless and Int-1/beta-catenin
SH-SY5Y – Thrice cloned subline of human neuroblastoma cell line SK-N-SH	XPS – X-ray photoelectron spectroscopy
SICM – Scanning ion conductance microscopy	

ABSTRACT

Electrically conductive materials represent a new generation of biomedical materials for tissue engineering and regenerative medicine, particularly for peripheral nerve regeneration. The use of an electrically conductive scaffold with electrical stimulation (ES) has the potential to facilitate regeneration of the fully functional nerve. Herein, non-woven mats of silk fibroin (SF) with fibre diameters of ~200 nm are fabricated by electrospinning for use as an acellular peripheral nerve scaffold. The electrospinning SF solution is prepared *via* a dialysis free protocol, which is far less time-consuming in comparison to conventional methods. The double layer electrospun SF mat consisting of random fibres as the base and aligned fibres as the top surface is designed to improve processability and handling of the scaffold and support the unidirectional alignment of neurites on the mat, respectively. Electrical properties are then imparted to the electrospun SF mat by post-modification using an interpenetrating polymer network (IPN) of poly(3,4-ethylenedioxythiophene) polystyrene sulfonate (PEDOT:PSS) with various molar ratios (α) of PSS and EDOT monomers. *In vitro*, the IPN ($\alpha = 2.3$) mat is non-toxic and evidences many promising results to promote neurite outgrowth following the alignment of fibres and has potential for ES application. In addition, the neurite outgrowth on fibre mats under the influence of electrical regime is considered here in a preliminary study. Direct ES with the monophasic pulse of 1 V amplitude, 2 ms pulse width, 100 ms pulse cycle, and 24 h/day was applied to differentiated cells in culture for 3 days. Although the neuronal cells can grow as expected on the IPN ($\alpha = 2.3$) mat with ES, the lengths of neurites have no significant difference from the control without ES. However, further investigation of electrical parameters optimisation may give more favourable results on neurite outgrowth. Without ES, the IPN ($\alpha = 2.3$) mat can promote longer neurite extension length compared to the pristine electrospun SF mat, especially for those without laminin coating. This study provides a platform for the use of electrically conductive material based on SF as scaffolds for peripheral nerve regeneration, which has potential for integration with ES therapy towards realising fully functional tissue recovery.

DECLARATION

The author of this thesis declares that no portion of the work referred to in the thesis has been submitted in support of an application for another degree or qualification of this or any other university or other institute of learning.

COPYRIGHT STATEMENT

1. The author of this thesis (including any appendices and/or schedules to this thesis) owns certain copyright or related rights in it (the “Copyright”) and s/he has given the University of Manchester certain rights to use such Copyright, including for administrative purposes.
2. Copies of this thesis, either in full or in extracts and whether in hard or electronic copy, may be made only in accordance with the Copyright, Designs and Patents Act 1988 (as amended) and regulations issued under it or, where appropriate, in accordance with licensing agreements which the University has from time to time. This page must form part of any such copies made.
3. The ownership of certain Copyright, patents, designs, trademarks and other intellectual property (the “Intellectual Property”) and any reproductions of copyright works in the thesis, for example graphs and tables (“Reproductions”), which may be described in this thesis, may not be owned by the author and may be owned by third parties. Such Intellectual Property and Reproductions cannot and must not be made available for use without the prior written permission of the owner(s) of the relevant Intellectual Property and/or Reproductions.
4. Further information on the conditions under which disclosure, publication and commercialisation of this thesis, the Copyright and any Intellectual Property and/or Reproductions described in it may take place is available in the University IP Policy (see <http://documents.manchester.ac.uk/DocuInfo.aspx?DocID=24420>), in any relevant Thesis restriction declarations deposited in the University Library, the University Library's regulations (see <http://www.library.manchester.ac.uk/about/regulations/>) and in the University's policy on Presentation of Theses.

ACKNOWLEDGEMENT

Firstly, I would like to appreciate my supervisor, Prof. Sarah Cartmell, who gave me a chance and welcomed me into the research group at The University of Manchester, and Dr. Jonny Blaker, my co-supervisor. I am very pleased to work with them, their kind support throughout the years of my PhD studies have helped me to gain more confidence and develop myself to be more professional in my research area.

Moreover, in studying here, I have learnt a lot about many aspects, with many experiences not only academic but also in life. I gratefully appreciate support from the Royal Thai Government scholarship for their financial support of both tuition fees and living costs in the United Kingdom.

For my research, the advanced tools and equipment are supported by the Henry Royce Institute for Advanced Materials, funded through EPSRC grants EP/R00661X/1, EP/P025021/1 and EP/P025498/1. I am appreciative for all the support from my external collaborator, Dr. John Hardy at Lancaster University and his team for guiding me regarding the silk preparation and modification, and also supporting me with our manuscript revisions. I also thank the following people for their support: Dr. Christopher Blanford for electrochemical measurement, Dr. Ben Spencer for surface analysis, Dr. Adrian Magaz for advice on working with silk, Dr. Zara Smith for advice on electrospinning and immunofluorescence, Dr. Kasama Srirussami for advice on electrical stimulation, Ms. Miruna Verdes for the computational model, Dr. Louise Carney, Mr. Nathan Murray, and other staff for laboratory support.

I also express my appreciation for the support from colleagues in the biomaterial group especially the workgroups of Sarah Cartmell and Jonny Blaker. Furthermore, I would like to thank all my Thai friends here in Manchester for supporting each other during our studies.

Most importantly, none of this could have happened without the support from my parents. I would like to express my gratitude to my mother and my father for their unceasing encouragement throughout the years of my PhD study abroad.

THE AUTHOR

Education

2017 – Present	PhD student in Biomedical Materials The University of Manchester, United Kingdom
2012 – 2015	M.Eng Biomedical Engineering (GPA 3.94) Mahidol University, Thailand
2008 – 2011	B.Eng Biomedical Engineering (GPA 3.54) Mahidol University, Thailand

Honour and awards

2020	Prize winner for abstract competition and oral presentation SACC (Samaggi Academic Conference and Careers Fairs, Thai student association in the United Kingdom)
2017	Full scholarship from the Royal Thai Government
2014	SAKURA and JASSO scholarships for student exchange (Kyushu University, Japan)

Publications

Phamornnak C., Spencer B.F., Ashton M.D., Blanford C.F., Hardy J.G., Blaker J.J., Cartmell S.H., "Instructive electroactive electrospun silk fibroin-based biomaterials for peripheral nerve tissue engineering", manuscript submitted to Materials Sciences and Engineering: C

Presentations at international and national conferences

2020	Generation of electrically conductive scaffolds composed of silk fibroin and PEDOT:PSS for peripheral nerve regeneration SACC, London, United Kingdom (Oral presentation)
2019	Non-woven mats of electroactive composites of silk-PEDOT:PSS for peripheral nerve regeneration TCES, Nottingham, United Kingdom (Oral presentation)
2019	Engineering nerve tissue with silk: graphene oxide fibres TERMIS, Rhodes, Greece (Oral presentation)
2014	The low frequency ultrasonic wave caused cell lysis and modulated dielectrophoresis property in breast cancer cell line BMEiCON, Fukuoka, Japan (Oral presentation)

CHAPTER 1

Introduction

The peripheral nervous system (PNS) consists of neural branches from the brain and spinal cord toward every muscle and gland in our bodies. It controls the movement of the muscular system in both voluntary and involuntary activities. A severe problem of peripheral nerve injuries (PNIs) is paralysis, which affects the quality of life. Although peripheral nerves have some regenerative capacity after injury, their functionalities (e.g. skeletal muscle movement control) are typically unsatisfactory in comparison to healthy nerves. This is maybe due to limitations in neural sizes, distances, and regenerating periods [1].

1.1. Statement of Problems

PNI commonly occurs in traumatic patients, with up to 300,000 cases in Europe and 200,000 cases in the United States every year [2]. In addition, the United States spends circa \$150 billion on PNIs annually [3, 4]. The PNI of upper extremities (e.g. shoulders, arms, hands, wrists, and fingers) is a concerning issue because it relates to the working disability of people and links to high socio-economic costs [5]. Typically, mechanical injuries (e.g. home accidents, car accidents, sports injuries, and complicated surgeries) are the major causes of PNIs [6, 7]. Previously, statistical studies revealed that approximately 70 – 80% of patients with upper extremities traumas and PNIs are male working adults and 50% of them have a nerve transection, which urgently requires surgical operation [8-11].

The surgical treatment with tensionless epineurial sutures is a common strategy for small injuries. However, it may not be suitable to operate in the case of wide and entire nerve transection [7]. Provided the nerve gap is larger than 5 mm, autologous nerve grafts or artificial nerve conduits are desired to bridge the nerve gap [12] since the primary repair (end-to-end suturing) places ischemic stress on the nerve and is associated with worse functional outcomes [13]. Due to the frequency of complications resulting from autologous nerve graft [14], the use of artificial nerve conduits is preferable. Several types of artificial nerve conduits from biomaterials such as collagen

type I, poly(glycolide) (PGA), poly(DL-lactide-co-ε-caprolactone) (PLCL), and polyvinyl alcohol (PVA) have been approved for clinical by the United States, Food and Drug Administration (FDA) and European Conformity (CE) marking [15, 16]. However, other countries also have their own regulatory agencies for approving medicines and medical products, such as the European Medicine Agency (EMA) in Europe [17] and the Pharmaceuticals and Medical Devices Agency (PDMA) in Japan, amongst others [18]. Although these nerve conduits can support peripheral nerve regrowth quite well, fully functional nerve regeneration is still challenging. Thus, traumatic patients with PNIs experience poor nerve functionality due to the limitation of nerve regeneration (*i.e.* the uncontrolled direction of neurite outgrowth, neurite extension length, and recovery time). Moreover, the formation of scar and fibrosis during the wound healing process interferes with peripheral nerve regrowth.

Recently, many studies have been focusing on the development of novel materials for facilitating improved recovery, and to rapidly extend neurite length as far as possible. One of the interesting materials is silk fibroin (SF), which has been used in biomedical applications for a long time. Another important class of materials are electrically conductive polymers, a relatively new generation of biomedical materials.

SF, extracted from silkworm cocoons, is a fascinating biopolymer for nerve regeneration due to its reported biocompatibility, mechanical strength, and optimal permeability of body fluids such as water, as well as oxygen [19]. It is able to be fabricated into many forms, which can effectively support recovering nerves, including forms such as sponges, tubes, gels, microspheres, films, and aligned fibres [20]. Moreover, it can be integrated with Schwann cells (SCs), neural growth factors (NGFs), as well as conductive polymers, to create a more active and stimulatory environment for rapid regeneration.

Electrically conductive polymers have emerged as a new generation of materials for fabricating scaffolds for use in tissue engineering and regenerative medicine. Many of them such as graphene oxide (GO), reduced graphene oxide (rGO), polyaniline (PANI), polypyrrole (PPy), poly(3,4-ethylenedioxythiophene) (PEDOT), and poly(3,4-ethylenedioxythiophene) polystyrene sulfonate (PEDOT:PSS) are widely used to provide additional functionality in peripheral nerve

scaffolds. These electrically conductive scaffolds can mimic, to some degree, native electrical conductivities in the body and also transfer exogenous electricity to nerve cells directly [21, 22]. More details concerning SF and the conductive polymer (PEDOT:PSS) are given in the Literature review of this thesis, Chapter 2, section 2.5.

The electrical regimes can affect the neurite outgrowth, expression of neurotrophic factors, and SC migration [23]. It has been reported to increase the protein adsorption rate to scaffolds, resulting in a more active environment for cell adhesion and proliferation [24]. Indeed, the use of electrical regimes *via* conductive scaffolds is an alternative way to accelerate and promote functional recovery of peripheral nerves.

In summary, the opportunity of effective peripheral nerve regeneration *via* artificial nerve conduits could be furthered by the development of a new generation of materials, which have two important properties. First, the scaffold should align neurites and SCs unidirectionally towards their targets. Second, it should provide an electroactive environment for faster regeneration when applying electrical stimulation.

1.2. Objectives

Overall, this study aims to develop a novel electroactive scaffold based on SF and PEDOT:PSS for peripheral nerve regeneration. The scaffold should have not only biocompatibility but also the ability to support neuron growth and control the direction of neurite outgrowth. To achieve this, an electrospun aligned fibre scaffold is produced *via* electrospinning to provide morphological guidance cues to cells and enable electrical stimulation.

Moreover, the neuron growth and neurite outgrowth on the developed fibre mat under the influence of an external electrical regime are studied to evaluate the potential of using electrically conductive fibre mats with electrical stimulation to facilitate fully functional nerve regeneration. It is anticipated that the combination of electrical stimulation and electrically conductive SF-base material developed in this study will go towards a new therapeutic strategy for peripheral nerve regeneration, with potential for future clinical application.

1.3. Hypothesis

This study has three hypotheses:

- (1) Aligned fibres in the range of submicron to nanometre are able to guide neurite extension prominent to fibre alignment.
- (2) Electrically conductive fibre mats promote longer neurites than non-conductive mats.
- (3) Electrically conductive fibre mats with electrical stimulation (ES) promote the longer neurite extension length in comparison to those without ES.

1.4. Scope of the Study

To fabricate the novel electrically conductive material and evaluate its potential for use as a peripheral nerve scaffold under the influence of different electrical regimes. This study is divided into four experimental chapters (chapters 3 – 6).

1. Fabrication of non-woven fibre mats (chapter 3)

SF extracted from silk cocoons is the raw material used in this study and is fabricated into aligned fibre mats by electrospinning. The secondary protein structure of electrospun SF mats after post-treatment is assessed as well as its morphology (*i.e.* fibre diameter and degree of alignment).

2. Modification of electrical conductive properties of the fibre mats (chapter 4)

Various ratios of PEDOT:PSS are integrated in/on electrospun SF mats using a modification approach exploiting interpenetrating polymer networks (IPNs). Optimal conditions are evaluated by the physical, mechanical, and electrical properties of fibre mats after modification.

3. *In vitro* biocompatibility (chapter 5)

Electrospun SF and selected IPN modified mats are chosen for testing with two major assays. First, the effects of chemical residues from electrospun and IPN modified mats is assessed using medium extraction (conditioned medium). Second, a direct contact assay is used to evaluate the neuron growth and neurite extension on the fibre mats. The optimal IPN mat is then determined based on these *in vitro* results.

4. Electrical stimulation (chapter 6)

All electrical parameters are optimised and the optimal electrical stimulation (Op-ES) condition is decided according to the result of neurite extension length of cells on tissue culture plastic (TCP). The Op-ES is then applied to the developed fibre mats (*i.e.* electrospun SF and most promising IPN mats). The effects on neurite extension length and orientation are considered here in a preliminary study.

CHAPTER 2

Literature Review

2.1. Anatomy and Physiology of Peripheral Nervous System

The nervous system is a vital life system for our bodies that responds to the five human senses (*i.e.* vision, audition, gustation, olfaction, and somatosensation) and controls the muscle movement in both voluntary and involuntary behaviours, simultaneously with the hormone system. It is commonly divided by structures and functions into two systems: the central nervous system (CNS) and the peripheral nervous system (PNS). The CNS is the processing centre of the body and consists of the brain and spinal cord. The PNS is the signal-transferring part that connects receptor cells to the CNS and the CNS to target organs, which also known as the sensory and motor units respectively [25].

Peripheral nerves can be categorised into two parts by their origins: cranial and spinal nerves [25]. Cranial nerves branch from the brain and control the electrical signals around the face and head including eyes, nose, mouth, and ears. Spinal nerves originate from the spinal cord and control the skeletal muscles of the whole body from the neck down and the smooth muscles of the inner organs in the thoracic, abdominal, and pelvic cavities.

In addition, the motor units of PNS are further categorised into two divisions: somatic and autonomic nervous systems. The somatic system controls skeletal muscles, while the autonomic system controls smooth muscles, cardiac muscles, and glands. The relation of neural signal pathways between CNS and PNS is shown in Figure 2.1 [25].

2.1.1. Histology of nerves

In the nineteenth century, there were many histological studies of the nervous system. Ramón y Cajal, a neuroanatomist, explained that nerves contain thousands of discrete cells, which communicate together by using chemical neurotransmitters through the gaps between them called

synapses [25-27]. Moreover, the nerve tissue is made up of two types of cells: nerve cells (neurons) and supporting cells [25].

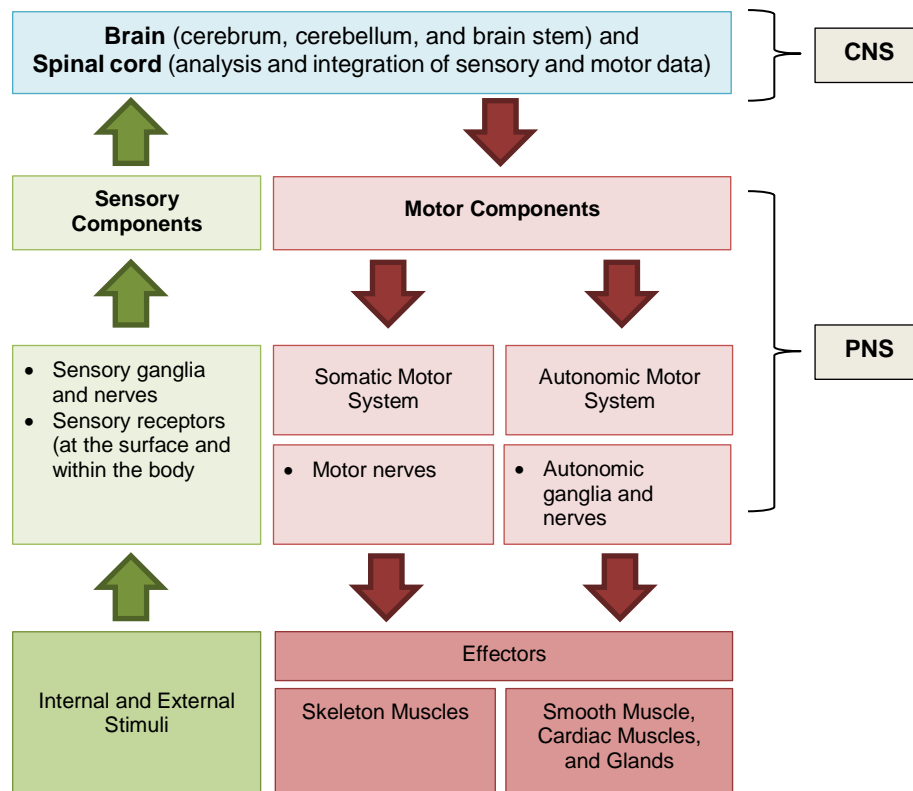


Figure 2.1 Diagram of the major components of the central and peripheral nervous systems and their functions, this figure has been adapted and redrawn from [25].

2.1.1.1. Nerve cells (neurons)

Neurons are electrically conductive cells, which have several shapes. Some neurons are thin and long; others look like the branches of a mature tree [25, 28]. However, every neuron has two components: a cell body and neurites. In PNS, cell bodies of the sensory neurons are often in the dorsal root ganglia close to the spinal cord, while those of the motor neurons are usually in the ventral horn of the spinal cord, as shown in Figure 2.2 [29]. The cell body contains many organelles such as a nucleus, endoplasmic reticulum (ER), ribosomes, mitochondria, *etc.* Its major function is to control neurons' activities, especially the self-generation of the electrical signal, also known

as the action potential (AP). The neurites are the extended processes of the cell body; most of these are dendrites except for an outstanding large ones known as axons.

Dendrites or dendritic processes are usually short and have many branches [28, 30]. Their entities have the neurotransmitter receptors for receiving neuronal signals from neighbour cells. The number of dendrites per neuron indicates the quantity of input information that a neuron can transfer.

On the other hand, axons have different functions and they are always longer than dendrites [25, 28]. After dendrites are triggered, the cell body generates AP at the axon hillock area. The AP is then transferred towards the target cells, tissues, and organs *via* the axon. The lengths of axons vary from a hundred micrometres to a metre depending on their locations. For example, femoral nerves and saphenous nerves, which connect from the spinal cord to the legs and feet, respectively, have very long axons of circa one metre. The axon synaptic endings have many synaptic vesicles containing chemical neurotransmitters that can release towards the dendrites of other neurons or specific tissues.

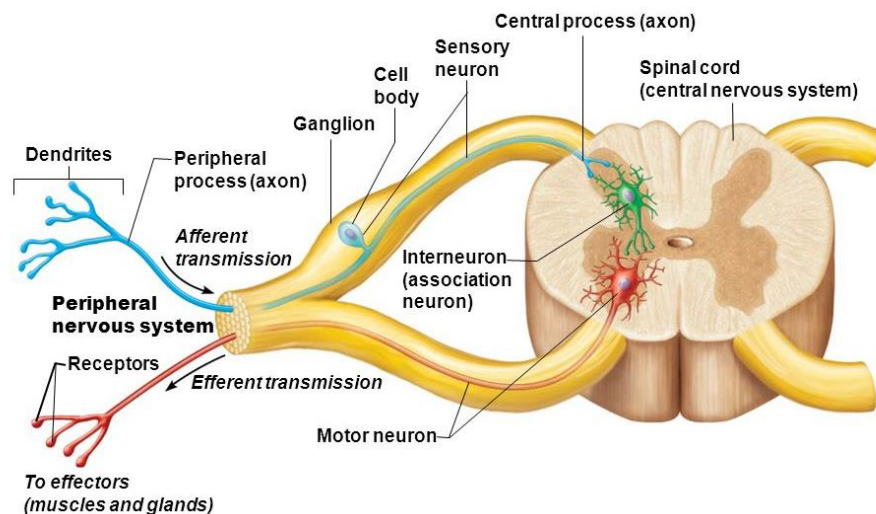


Figure 2.2 Structure of the peripheral nerve extending from the spinal cord (spinal nerve)
classified by functions [29].

2.1.1.2. Supporting cells

Supporting cells are a crucial part of nerves. They are electrical insulators and smaller than neurons [25]. In CNS, they are called neuroglial or glial cells, which can be divided into three sub-types: astrocytes, oligodendrocytes, and microglia. Schwann cells (SCs) are a type of supporting cell in PNS. Generally, SCs are in the myelinated phenotype that can produce myelin sheaths wrapping around the axon to maintain the electrical functionality of neurons. However, some SCs are non-myelinated (*e.g.* Remak bundles), which can support the slower conducting nerve fibres [31]. In addition, some axons have no myelin sheath; these are termed unmyelinated axons. The diameter of unmyelinated axons is small (typically 0.2 – 1.2 μm , and even up to 3 μm) [32].

In nerve regeneration, both types of SCs (*i.e.* myelinated and non-myelinated SCs) can convert to repair-promoting phenotype (Büngner) cells immediately after the nerve is damaged [7, 33, 34]. The repair-promoting phenotype SCs produce the essential nerve growth factors (NGFs) for axonal regeneration. In contrast, the unmyelinated axon has lesser regenerative potential, even with intact SC tubes [32]. The role of SCs in nerve regeneration is described further below in section 2.3.1.

2.1.2. Structure of spinal nerves

There are thirty-one pairs of spinal nerves in our bodies, extending from the spinal cord through intervertebral foramina. Sunderland S., 1990, defined that a spinal nerve has an epineurium membrane covering along its length [35, 36]. It contains many bundles of axons (nerve fascicles), blood vessels, and other supportive tissues such as areolar connective tissue, fat, collagen, and elastin. The nerve fascicle transfers electrical signals toward target organs, while the supportive tissues protect these axons from external forces, for example pressing or compression. The numbers of nerve fascicles in each spinal nerve typically vary from 1 – 100 fascicles, which are approximately 30 – 70% of the nerve cross-section area [35, 36].

Typically, cell bodies of all peripheral neurons are in the dorsal root ganglia and the spinal cord [37]. Only nerve fascicles and SCs align along spinal nerves. Every nerve fascicle is wrapped by the perineurium membrane individually. It usually contains various units of axons such

as sensory, motor, and autonomic axons, which can be both myelinated and non-myelinated structures. Furthermore, every axon is individually surrounded by the endoneurium as its membrane. All nerve membranes: epineurium, perineurium, and endoneurium, promote elasticity and tensile strength of peripheral nerves due to the collagen fibres in their structures, as shown in Figure 2.3 [37]. They can balance the intrafascicular pressure and be the natural cell matrix for peripheral nerve regeneration.

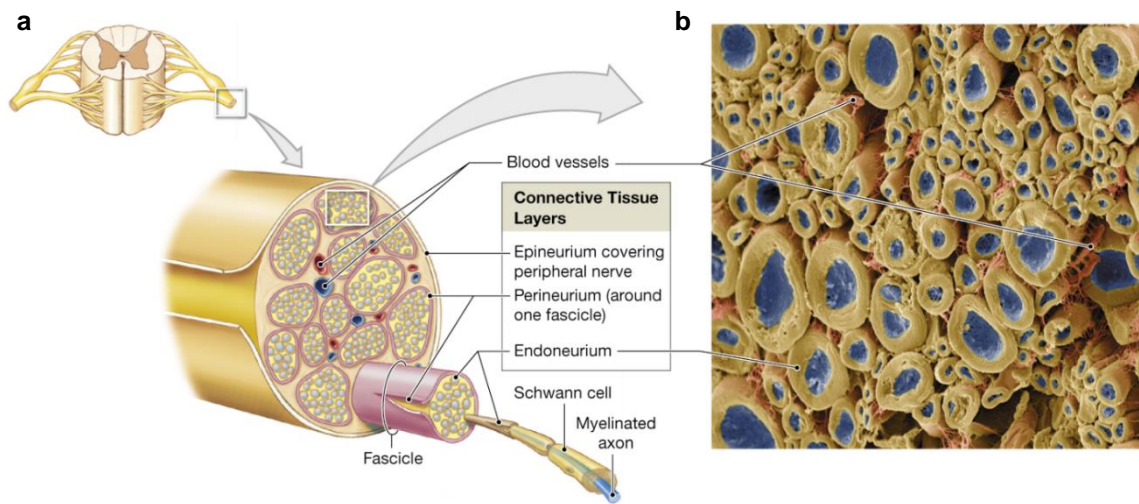


Figure 2.3 Microstructure of peripheral nerve: (a) a typical peripheral nerve and its connective tissue wrappings, which associated to spinal nerve and (b) a pseudo coloured scanning electron micrograph showing peripheral nerve fibres (SEM x 340), this figure is adapted from [37].

2.1.3. Electrical signals of neurons

There are many types of ions in both the intracellular and extracellular fluids of neurons. The overall ionic concentrations and ionic charges in each matrix differ, resulting in the transmembrane potential of neurons. In the resting state, the intracellular potential is lower than the extracellular potential leading to the negative membrane potential (-40 to -90 mV), which is typically -70 mV.

If a neuron is triggered by either internal or external stimuli, the ion fluxes (*i.e.* influx and efflux) are then generated across its cell membrane. Thus, the membrane potential at the stimulated spot of the neuron rapidly spikes up to a positive potential (+40 mV) and reverses back to the resting potential within a few milliseconds, as shown in Figure 2.4. The AP generated by

these ion fluxes will propagate along the axon to the synaptic ends. Interestingly, the amplitude of AP does not relate to the stimulation force, but it depends on the functions of ionic pumps and channels around the cell membrane [25].

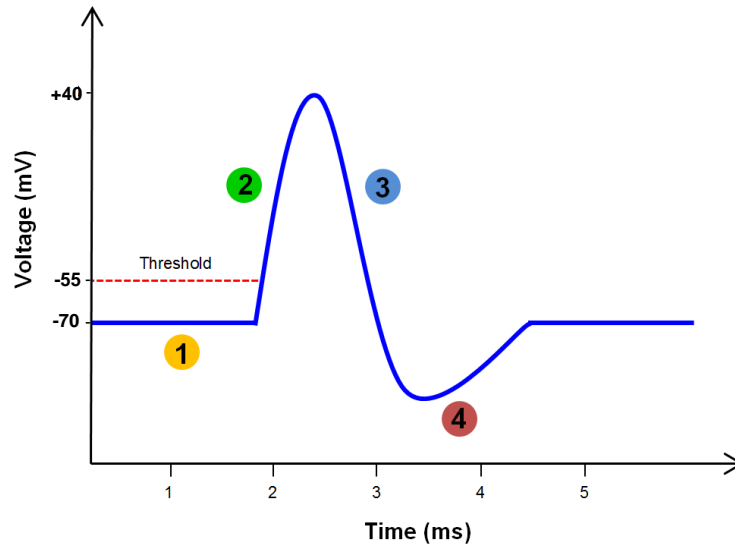


Figure 2.4 Schematic of the resting membrane potential and typical action potential (AP) of peripheral nerves: (1) resting membrane potential, (2) depolarisation, (3) repolarisation, and (4) hyperpolarisation, this figure is based on information from [25, 38].

2.1.3.1. The relationship between ion movement and action potential

In general, the AP can be classified into three states: depolarisation, repolarisation, and hyperpolarisation. These states are determined by the influx and efflux of potassium (K^+) and sodium (Na^+) ions across the cell membrane *via* their specific ion channels and pumps, as shown in Figure 2.5. The ion channel allows the diffusion of a specific ion following its concentration gradient, which is also known as passive transportation. On the other hand, the ion pump transfers ions against their concentration gradients also called active transportation [25].

The intracellular fluid of neurons contains a high concentration of K^+ , while its extracellular fluid has a great deal of Na^+ . In the resting state, the K^+ channels are always opened, and K^+ can then move across the cell membrane all the time. Thus, the extracellular potential is

approximately 70 mV higher than the intracellular potential resulting in a resting membrane potential -70 mV.

After stimulation, the AP immediately goes into the depolarisation phase. The neuron closes K^+ channels and opens Na^+ channels leading to Na^+ influx. The intracellular Na^+ is then dramatically increased. Therefore, the membrane potential is rapidly increased and becomes positive, with a peak potential of approximately +40 mV.

The Na^+ channels are opened for a few milliseconds and then rapidly closed; this is the beginning of repolarisation. The exceeded intracellular Na^+ triggers the K^+ channels to open. Then, the intracellular K^+ leaks out again in order to re-balance the ionic concentration. Thus, the membrane potential is reduced back to the resting state (-70 mV).

Compared to Na^+ , the K^+ channels are slowly closed. This results in an undershoot potential, also termed hyperpolarisation. The undershoot potential will be reset into the resting potential by the Na^+/K^+ pump exchanging $3Na^+$ efflux with $2K^+$ influx.

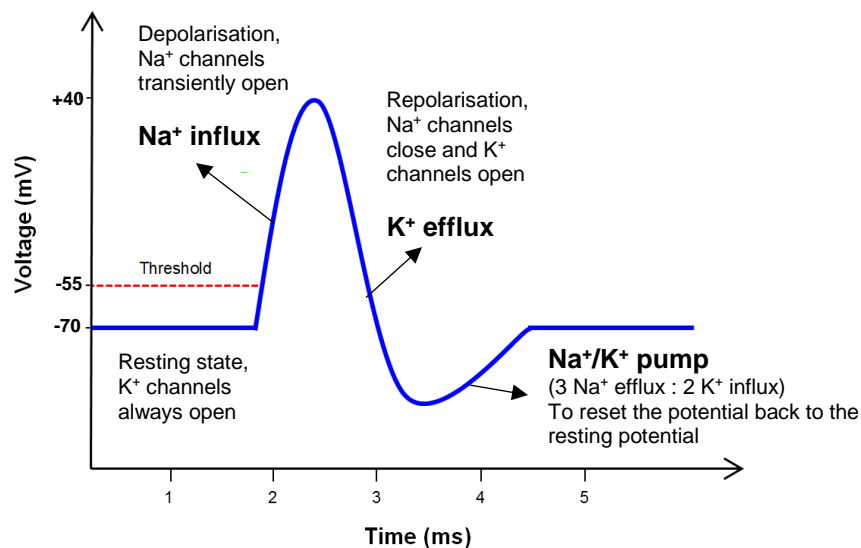


Figure 2.5 Schematic of action potential (AP) and the activation of ion channels (Na^+ and K^+ channels) in the different states, this figure is based on information from [25, 38].

2.1.3.2. The propagation of action potential along the nerve

The nerve axon acts as a conductive tube containing aqueous electrolytes. The propagation of AP along the axon can be divided into five steps, as shown in Figure 2.6 [38].

The intracellular Na^+ and its concentration gradient is of key importance for AP propagation along the axon toward synapses. According to the depolarisation process, the Na^+ channels are activated only at the stimulation area. The Na^+ influx occurs locally at that area and then generates a high concentration of intracellular Na^+ compared to the neighbouring areas. The Na^+ influx can spontaneously diffuse to the neighbouring areas following its concentration gradient (Figure 2.6 (ii)). At the neighbour area, the membrane potential is gradually increased depending on the diffusion rate of Na^+ . Once the accumulated Na^+ in the neighbour area is high enough such that the membrane potential reaches a threshold of -50 mV, the Na^+ channels at that area are activated and opened immediately (Figure 2.6 (iii)). Thus, the Na^+ influx at the neighbour area is significantly enhanced, eventually leading to depolarisation (Figure 2.6 (iv)).

In summary, the AP of the axon does not occur all along its length at the same time. It happens at only the stimulated part and propagates to other parts *via* the diffusion of intracellular Na^+ . Interestingly, the movement direction of an action potential is one way. As seen in Figure 2.6, the AP moves from left to right, even though the intracellular Na^+ can diffuse both ways (*i.e.* left to right and right to left) following the concentration gradient. The propagation signal is unable to go back because the initial area has a refractory period (hyperpolarisation and Na^+/K^+ pump). Although Na^+ ions move backwards, they are incapable of reaching the threshold and re-open Na^+ channels.

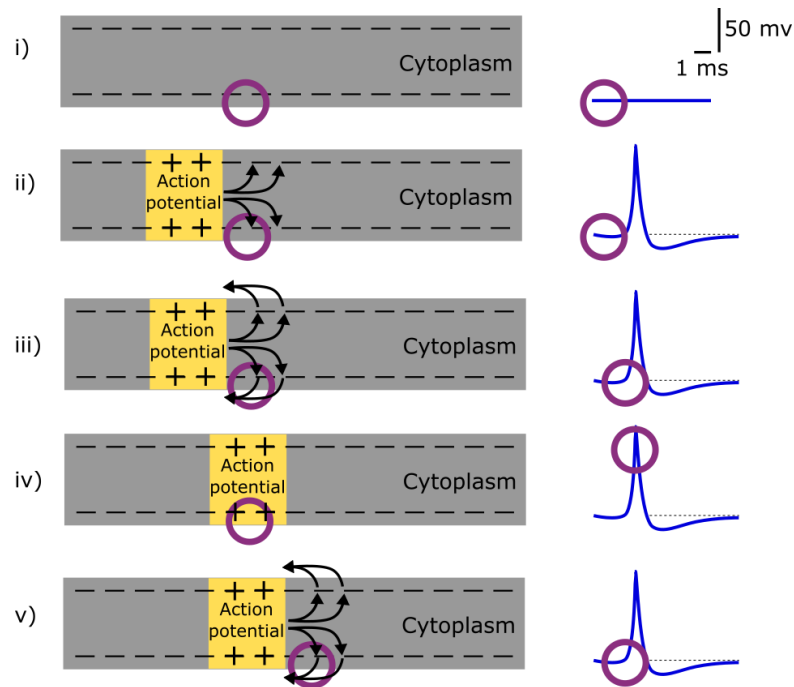


Figure 2.6 Schematic diagram of action potential conduction in axons, this figure is adapted and redrawn from [38].

2.1.4. Synaptic transmission

A synapse is the connection point, space, and gap for transferring information either *via* electrical currents or chemical agents between neurons. It is of key importance for peripheral nerve communication. At the synapse area, two particular compartments: pre-synaptic and post-synaptic cells, are connected by either synaptic clefts or intercellular junctions. The synapse can be categorised into two classes: chemical and electrical synapses, as shown in Figure 2.7 [25-27].

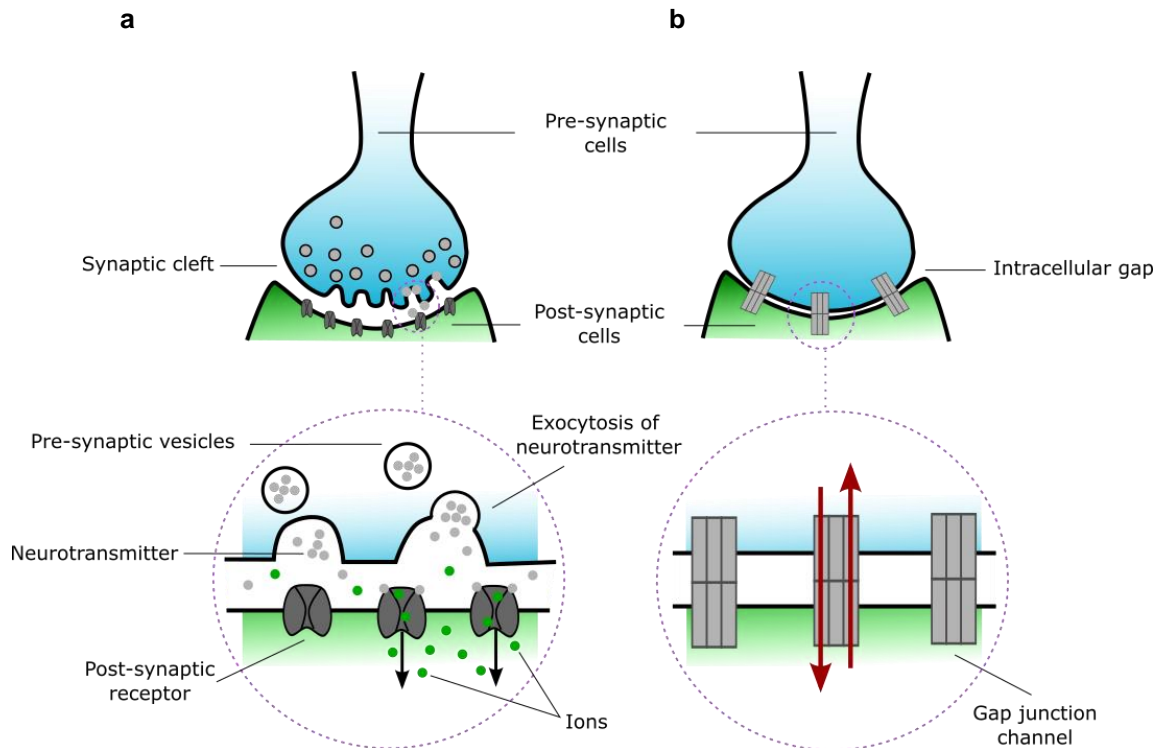


Figure 2.7 Schematic model of the synaptic transmission: (a) a chemical synapse and synaptic cleft between pre- and post-synaptic membranes and (b) an electrical synapse touching with very closed intercellular junctions (gap junctions) and the arrows represent the transfer of electrical signals, ions, metabolites, and small molecules of secondary messengers, this figure is based on information and adapted from [26, 27].

2.1.4.1. Chemical synapses

The chemical synapse transfers chemical signals (neurotransmitters) from the pre-synaptic cell to the synaptic cleft. In the pre-synaptic cell, neurotransmitters are packed in the form of tiny vesicles (pre-synaptic vesicles). Once the pre-synaptic cell is activated, vesicles will release neurotransmitters into the synaptic cleft. Typically, there are many types of neurotransmitters such as acetylcholine, dopamine, serotonin, epinephrine, norepinephrine, *etc.* [39, 40]. One of the most well-known neurotransmitters is acetylcholine, which is usually found in the synaptic clefts between nerves/nerves and nerves/muscles (neuromuscular synapse) [25].

The release of neurotransmitters begins when the AP is propagated to the pre-synapse. The depolarisation of axons is literally induced by the Na^+ channels. In contrast, the pre-synaptic

depolarisation is generated by calcium (Ca^{2+}) channels [41]. This Ca^{2+} signal plays a critical role in fusing synaptic vesicles and the pre-synaptic membrane. After that, the neurotransmitters are secreted by exocytosis into the synaptic cleft. The released neurotransmitters can bind with the receptors at the post-synaptic membranes and then initiate the AP of the post-synaptic cell.

2.1.4.2. Electrical synapses

The electrical synapse transfers electrical signals, ions, metabolites, and small molecules of secondary messengers through specific intercellular junctions, which also known as gap junctions [26]. The gap junction connects pre-synaptic and post-synaptic membranes very closely resulting in the smaller space than the chemical synapses. The gap between lipid parts of adjacent membranes are only 2 nm and the channels are positioned by membrane protein connexions [42]. Moreover, the pore size of the gap junction is relatively large, thus it can transfer ions and small molecules (approximately ≤ 1 kDa) [26].

Although the current flow through gap junctions is bi-directional (*i.e.* upstream and downstream), it is the fastest way to communicate between neurons [26]. Therefore, the electrical synapse is usually found in the CNS because it requires rapid processing and complex synchronization between large amounts of neurons.

2.2. Peripheral Nerve Injury

The nerve injury is defined into three or five levels depending on the classification methods. Seddon H.J., 1942, classified three types of nerve injuries based on the level of the lesion and the loss of function [43]. After that, Sunderland S., 1951, expanded Seddon classification into five levels based on the changes induced in the normal structure of the nerve [44].

2.2.1. Seddon classification

Sudden determined two significant signs of nerve injuries: loss of functions and perversion of functions. The details of sensory and motor functions of nerve injuries from both signs are explained in Table 2.1 [43]. Neurologists agreed that these irregularities are signs of nerve problems such as transient block, lesion continuity, and anatomical transection. Therefore,

Sudden classified these injuries into three specific syndromes: neurapraxia, axonotmesis, and neurotmesis in order of increasing harshness.

Table 2.1 Signs of nerve injuries in sensory and motor functions [43]

Signs	Sensory functions	Motor functions
Loss of functions	Loss of tactile sensibility	Paralysis of muscle
	Loss of pain sensibility	Sudomotor paralysis
	Loss of thermal sensibility	Pilomotor paralysis
	Loss of joint and postural sensibility	Vasomotor paralysis
	Loss of deep sensibility	
Perversion of functions	Paraesthesia	Muscle twitching
	Possibly spontaneous pain	Muscle spasm
	More pain than the regular situation	Abnormal sweating
	Abnormal thermal response (heat and cold)	Vasomotor disturbances

2.2.1.1. Neurapraxia

Neurapraxia is a type of electrically conductive block of the peripheral nerve. It occurs when the endoneurium is compressed but the axon remains intact. Therefore, neurapraxia is a minor injury with low damage and it can spontaneously and rapidly recover. There are several types of neurapraxia such as tourniquet, crutch, and the most common type, which is Saturday night paralysis or palsy [43]. Saturday night palsy is the radial nerve compression in the upper arm and it usually occurs in the night-time when people fall asleep. In general, this neurapraxia can be resolved simply with physical therapy.

2.2.1.2. Axonotmesis

Axonotmesis is a type of partial nerve transection, in which nerve fibres are cut but one of these connective tissues: epineurium, perineurium, and endoneurium, remain [43]. Although the distal stump of the injured nerve degenerates, the neurites from the proximal end can spontaneously regenerate. The regeneration direction is guided by the remaining connective tissues either epineurium, perineurium, or endoneurium. Commonly, axonotmesis is a side effect of bone

fracture. For example, the complicating fragments of humerus bone can press on the radial nerve resulting in radial paralysis, in which patients lose the ability to move their hands and fingers.

2.2.1.3. Neurotmesis

Neurotmesis is a total nerve transection, in which nerve fibres and connective tissues are completely cut into two divisions [43]. On the other hand, neurotmesis may cause neuroma due to failure of the regenerating nerve growth cone to reach peripheral targets. This can be also be termed neuroma-in-continuity [45].

Neurotmesis is very difficult to repair without surgical intervention. However, the surgical results are still imperfect due to the reversible degenerative muscles, the formation of scar and fibrosis, and the interference of suture lines [46, 47]. Several alternative treatments such as autograft nerve transplant and artificial nerve conduits may give better performance than the operations reliant on suturing.

2.2.2. Sunderland classification

Sunderland explained the details of the microstructure of nerve trunks including fascicular plexus, epineurium, and vascular bundles and then defined five levels of nerve injuries by expanding two intermediated degrees between axonotmesis and neurotmesis [36, 48, 49].

2.2.2.1. The first degree (conductive block)

This degree is a non-permanent conductive block, which electrical signals are stuck. It is also the same level as neurapraxia defined by Seddon [36, 48, 49].

2.2.2.2. The second degree (axon discontinuity)

This degree occurs when axons are separated into two parts: proximal and distal stumps but the other three outside membranes (*i.e.* epineurium, perineurium, and endoneurium) are undamaged [36, 48, 49]. After injury, the distal part is degenerated as known as Wallerian degradation, while the proximal part can easily regenerate since the surrounding endoneurium can function as the axonal conduit.

2.2.2.3. The third degree (axon and endoneurium discontinuity)

The inner structures of fascicular consisting of axons, myelin sheaths, and endoneurium are damaged [36, 48, 49]. The nerve fibres can regenerate themselves, but they are disorganised because of fibrosis and continuity of nerve fibres. The intrafascicular fibrosis disturbs and delays axonal growth. Fibrosis is usually occurred in between nerve gaps resulting in disorderly axon outgrowth and eventually loss of continuity of nerve fibres.

Another concern of the third degree is the cross-shunting of axons from different endoneurium. However, this is often overlooked in current clinical treatment, which probably leads to deficiently functional nerves.

2.2.2.4. The fourth degree (fasciculi and perineurium discontinuity)

This level is a severe case because all nerve fascicles are destroyed remaining disorganised connective tissues of the nerve trunk (*i.e.* epineurium) [36, 48, 49]. Fibrosis is a concerning issue for this degree, as it is with the third degree. The regenerated axons are able to grow freely in random directions. The cross-connection of axons from the different fascicles probably leads to imperfect functional regeneration. This injury requires surgery for cutting the damaged nerve segment out and replacing the nerve gap with either nerve grafts or artificial nerve conduits.

2.2.2.5. The fifth degree (transection of entire nerve trunk)

This highest degree is the same as that for neurotmesis classified by Seddon [36, 48, 49]. It represents the whole nerve trunk transection. It usually occurs in the trauma case when the nerve is completely separated into two sections.

2.3. Peripheral Nerve Regeneration

The PNS has better potential to recover than the CNS due to the versatile supporting cells, which are Schwann cells (SCs). Provided the peripheral nerve is injured, the SCs will convert themselves into a regenerating phenotype to support axonal outgrowth. Moreover, the peripheral neurons will produce the factors and molecules associated with neural growth for promoting cell adhesion at the site of injured nerve and target tissues [7].

2.3.1. Neurobiology of peripheral nerve injury

As studied by Sunderland S, 1987, many organelles in a neuronal cell body decrease their levels such as the endoplasmic reticulum (ER) associated with ribosomes and the cytoskeleton elements (*e.g.* actins, neurotubules, neurofilaments) after the early period of injury (6 h) [49]. The neuronal cell body perhaps receives the first signal from the antidromic electrical activity in the form of a high frequency burst of APs; however, the removal of target-derived neurotrophic support is likely to be a prominent clue to neuronal survival [7]. The balance of gene and protein expressions of the injured nerve may determine whether neurons attempt regeneration or induce apoptosis [7, 50].

Prior to regenerating axons, a series of molecular and cellular degradation occurs at the distal end of the damaged nerve, this process is called Wallerian degeneration, as shown in Figure 2.8. On the first day (24 h), the myelinated SCs detach from axons and turn their forms into non-myelinated phenotypes. The non-myelinated SCs play a critical role in both degenerating and regenerating axons. They down-regulate structural proteins and cooperate with macrophages to destroy axonal debris. On the other hand, they up-regulate neural growth factors (NGFs) and cell adhesion molecules (CAMs), form axonal guided columns called Bands of Büngner, and support environmental trophic factors for axonal regeneration from the proximal toward distal part [7]. The details of NGFs, CAMs, and other molecules will be described in the following section (section 2.3.2).

Unfortunately, the formation of scar and fibrosis, misdirection of atrophied muscle fibres, and apoptotic satellite cells occur during the same period of axonal regeneration [46]. Sometimes, it grows faster than the neurite extension resulting in non-functional regenerated nerves.

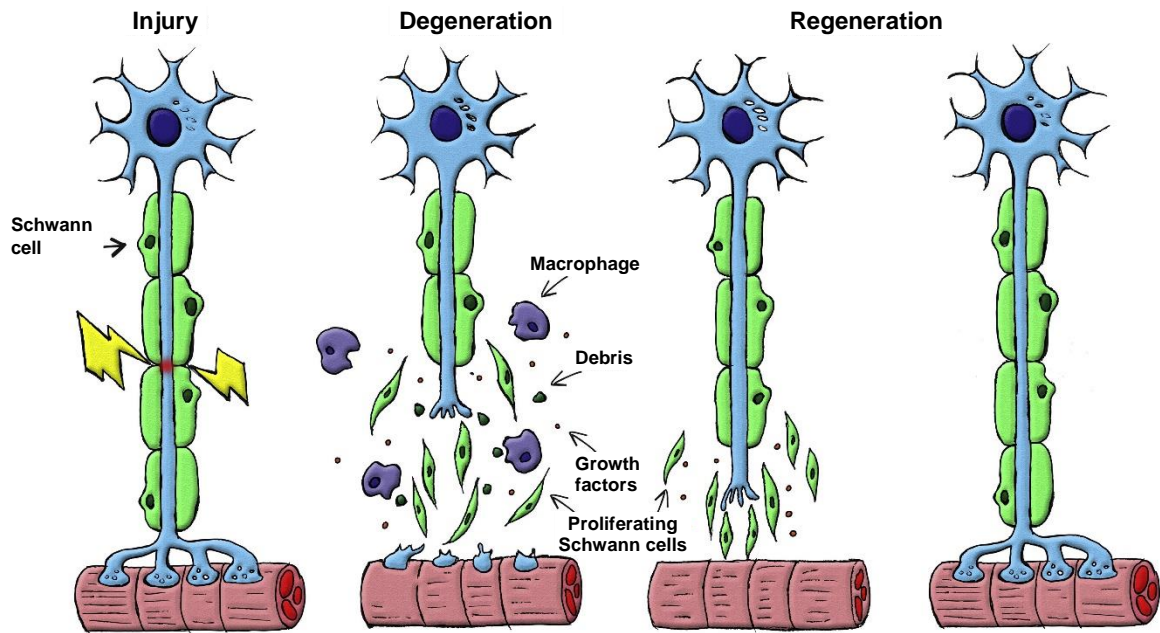


Figure 2.8 Schematic of nerve injury, Wallerian degeneration, and regeneration process, this figure is adapted from [7].

2.3.2. Factors and molecules associated with neuron growth

Ramón y Cajal explained that the direction of axon regrowth is induced by chemotropism and neurotropism. These neuronal factors composed of tropic and trophic factors can attract nerve fibres especially on the distal stump, promote cell survival, and stimulate neuron differentiation [51]. Moreover, several glycoprotein molecules on the cell membrane are significantly increased and play a critical role in the regeneration process as well [49]. Therefore, all of these factors can be categorised into four groups: tropic factors, trophic factors, cell adhesion molecules (CAMs) and substrate adherence molecules (SAMs) that will be described in the following sub-section.

2.3.2.1. Tropic factors

Many studies confirm that the distal stump of the injured nerve attracts neurite outgrowth from the proximal stump toward itself by the chemical and neuronal tropic factors. Actually, the neurite extension should be in random directions, but almost all neurites spontaneously grow toward the distal stump. The tropic factor is secreted by the target and establishes a concentration gradient in the surrounding environment before or during the normal period of axon extension, which is

necessary for axonal guidance to the target *in vivo* [51]. Thus, the tropic factor is the basic guide for axonal direction particularly in a small nerve gap; however, the effect of tropic factors can be reduced for larger nerve gaps [49].

2.3.2.2. Trophic factors

The trophic factors are external molecules for accomplishing peripheral nerve regeneration. Apart from neural growth factor (NGF), many types of trophic factors are in the neurotrophins family, such as glial growth factor (GGF), glia-derived neurite promoting factor (GdNPF), basic fibroblast growth factor (bFGF), and ciliary neurotrophic factor (CNTF) [49, 52, 53].

NGF is a type of neurotrophin found in the central and peripheral nervous systems of vertebrate. It can bind with specific neurotrophin receptors on the neuron membrane in both low and high affinity. Receptors p75 and TrkA are well-known receptors for low and high affinity, respectively [52]. The effect of NGF on neural growth have been well studied. *In vitro*, the NGF promotes differentiation and neurite outgrowth in the rat pheochromocytoma (PC-12) cell *via* induced synthesis of growth associated protein (GAP-43) [54, 55].

In vivo, the GAP-43, also known as F1, B-50, or neuromodulin is a substrate for the formation of new synapses and neurite extension after injury [56]. In addition, the NGF receptors are commonly found in autonomic and sensory ganglion neurons [49]. Therefore, it is important for the survival of sympathetic and sensory neurons. Loss of NGF may result in neuron apoptosis [57].

2.3.2.3. Cell adhesion molecules (CAMs)

CAMs are proteins on the cell surface, which can bind to other specific molecules and influence cell aggregation and tissue formation. They play a critical role in the neurite outgrowth of the PNS. There are six general types of CAMs distributed by molecular weights and identified by epitopes or lymphocyte markers [49]. The expression of CAMs is always found within a few months (50 – 150 days) after the nerve transection in both myelinated and non-myelinated nerves. *In vitro*, the SCs with NGF can enhance the expression of CAMs.

2.3.2.4. Substrate adhesion molecules (SAMs)

SAMs are the protein molecules in the extracellular matrix (ECM), which can interact with CAMs for cell adhesion purposes. Laminin, fibronectin, and type IV collagen are well-known types of SAMs, which are extensively found in nerves in particular during the process of neurite outgrowth. The strength of neurite attachment is dependent on SAMs. Some studies assert that neurite outgrowth on laminin absorbed in type IV collagen is better than pure laminin and fibronectin matrices [49].

A study of axonal regeneration in zebrafish demonstrates that the Wnt/ β -catenin signalling from non-neural cells invading the injured site can induce col12a1a/b expression and collagen XII deposition [58]. Collagen XII is an axonal regeneration promoter. It is necessary for navigating axons toward the non-neural injured site.

Recently, melanin has become an alternative molecule for supporting neuron and SC attachment. Melanin is the natural skin pigment in the human body. Some studies have confirmed that melanin is an electrically conductive molecule and that it can support neural growth. Bettinger C.J., *et al.*, 2009 determined that melanin films in the hydrated state have a conductivity of 7.00 ± 1.10 S/cm and the neurite extension and SC growth on melanin films are better in comparison to collagen films [59].

2.4. Clinical Peripheral Nerve Therapy and Tissue Engineered Peripheral Nerve Approaches

Peripheral nerves have some ability to regenerate themselves towards their target tissues. In the clinic, the microsurgical technique is a successful strategy for small injuries, which can rapidly promote axonal regrowth. However, nerve grafting and artificial nerve conduits are standards for large nerve transection (over 5 mm) [15]. Although these techniques are helpful, full functional recovery remains challenging. To accelerate the axonal outgrowth and improve the quality of functional regeneration, the combination of these conventional techniques and external electrical stimulation is an alternative [23]. Contemporary peripheral nerve therapy is categorised into three approaches: 1) autologous nerve grafts, 2) artificial nerve conduit, and 3) electrical stimulation.

2.4.1. Autologous nerve grafts

Autologous nerve graft or autograft is a nerve transplant technique to replace the damaged section with another tissue from other parts of the patient's own body (the donor site) such as small nerves, muscles, vessels, and fat. This method is the current gold standard for peripheral nerve treatment. It is relatively safe due to no rejection from the immunological system of the patient body. Autografts provide appropriate levels of neurotrophic factors and viable SCs associated with axon regeneration [60]. However, autografts still have their disadvantages, in particular the loss of function of the donor site. In addition, the limitation of donor site morbidity, number of grafts, and amount of tissues should be considered [61].

Donor tissues from other people, termed nerve allografts, can be used instead of autograft. Unfortunately, the use of allografts require systemic immunosuppression to reduce antigenicity prior to transplantation, which may affect the health of the recipient. In addition, there remain limitations on immunological matching, including the ABO blood types between the host and donor [60].

2.4.2. Artificial nerve conduits and tissue engineered nerve scaffolds

Artificial nerve conduits or nerve guidance conduits (NGCs) are useful in clinical work. They obviate the need for a donor site and associated problems (e.g. morbidity, amount of tissues, and nerve site mismatch). Many commercial NGCs have already been approved by the FDA for clinical use. The materials of commercial NGCs are based on both synthetic and natural polymers. For example, Neurotube® is made from PGA, Neurolac™ from PLCL, and Salutunnel™ from PVA, while NeuraGen®, NeuroFlex™, NeuroMatrix™, NeuraWrap™, and NeuroMend™ have collagen type I as their base materials [15, 62, 63].

Most NGCs are acellular scaffolds with designs using hollow tube structures for wrapping around the damaged nerves or bridging the nerve gap, as shown in Figure 2.9 [64]. The inner wall of hollow NGCs is key success in facilitating peripheral nerve regeneration. Apart from smooth surfaces, several inner wall structures have been developed to mimic the native ECM, such as porous, grooved, and fibrous surfaces [12, 64-66]. On the other hand, the hollow space

of the NGCs can be filled or loaded with aligned filaments, multichannel microtubes, sponge structures, hydrogels, *etc.* [64, 66].

Furthermore, not only the physical structure of scaffold but also the active intraluminal environments of cell-based scaffold and electrically conductive or electroactive scaffolds can improve the efficiency of NGCs. The incorporation of cells (*e.g.* primary cells, stem cells, and genetically modified stem cells) in NGCs have been studied in axonal regeneration because these cells can release the imperative molecules for axon regeneration [66].

The cell-loading techniques applied can be divided into two main methods: incorporation and post-fabrication cell seeding. 3D bioprinting is a well-known technique to fabricate scaffolds according to a pre-set structure. It is an example of cell-loading during fabrication because the bioink of 3D printers is usually made from a hydrogel-cell mixture. On the other hand, the post-fabrication cell seeding techniques (*e.g.* static seeding, vacuum cell seeding, and perfusion bioreactor) are widely used because they can reduce the risk of fabrication conditions. Alternatively, growth factors can be loaded in NGCs instead of cells [66].

Cell-based scaffolds represent future generation NGCs, which have the potential to improve axonal outgrowth. Cell-based NGCs may be difficult to use in clinical work due to the complication of cell seeding protocols and cells antigenicity. Therefore, most commercial NGCs are still based on acellular scaffolds. In acellular scaffolds, not only intraluminal guidance structure but also the optimisation of material properties for the induction of external stimuli such as ultrasound [12, 67], electromagnetic field [68, 69], and especially electrical stimulation [68, 70] have been developed to enhance peripheral nerve repair. The development of electrical conductive NGCs is described later (in section 2.5).

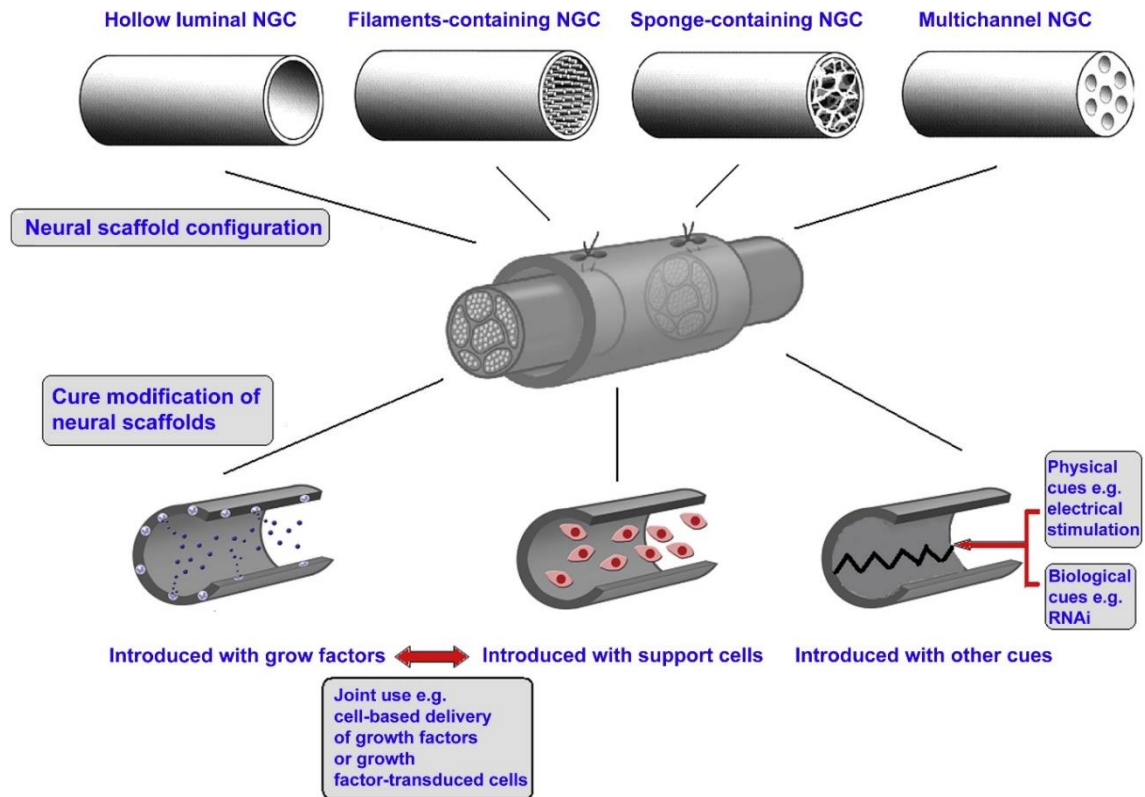


Figure 2.9 Schematic of different structures of nerve guidance conduits (NGCs) and the modification of scaffolds with either physical or biological cues [64].

2.4.3. Electrical stimulation

Electrical stimulation is a known method for non-surgical peripheral nerve treatment and is an alternative therapeutic strategy usually applied after surgery across injury sites. There are four different ways to stimulate the peripheral nerve: transcutaneous electrical nerve stimulation (TENS), direct stimulation, stimulation through synthetic nerve graft, and combination with other methods [23].

TENS is a method of pain relief by exposing electrical impulses (around 2 – 150 Hz) through the skin to reduce pain signals, which are transferring from sensory nerves to the brain [23]. TENS can not only interrupt pain signals, but also enhances the release of neurotransmitters such as serotonin and γ -aminobutyric acid (GABA) [71]. For these reasons, many researchers have focused their attention on applying TENS in peripheral nerve regeneration.

TENS with the condition of 0.8 – 1 mA, low frequency of 2 Hz for 15 minutes per day after a week of surgery with silicone tubes have been reported to significantly reduce the gap of 10 mm transected nerves [72, 73]. In addition, some studies have attempted to compare the effect of continuously direct and pulse electrical currents on nerve regeneration. For example, Cheng W.L., *et al.*, 2004, reported that a direct current of 10 μ A can increase the area of nerve bundles but the same number of myelinated fibres, resulting in the decrease of nerve density. In contrast, all conditions of pulse stimulation of 10 and 20 μ A with various frequencies and pulse widths (*e.g.* 50 Hz – 0.3 ms, 100 Hz – 1.5 ms, and 200 Hz – 0.75 ms) increased nerve density [74].

In animal work, direct electrical stimulation with a low frequency to the proximal nerve ending is a fascinating approach for peripheral nerve recovery [70, 75, 76]. It can be applied together with surgical treatments (*e.g.* suture surgery and autologous nerve graft) [75, 77]. The combination of electrical stimulation and surgery can accelerate axonal outgrowth, especially for small nerve gaps [77]. *In vivo*, the direct electrical stimulation with a low frequency also reached the gold standard of nerve regeneration in case of the nerve gap of 10 – 15 mm in rat sciatic nerves (Sprague-Dawley rats) [70, 75, 76].

Induced electric field is another method for stimulating nerves covered by the synthetic nerve graft. Piezoelectric materials or microelectrode systems need to be deposited into the nerve tube to generate electric fields at the injured nerve [78, 79]. Currently, the development of this method focuses on stimulation *via* electrically conductive materials. The electrical property of scaffolds and the optimal electrical stimulation parameters still warrant further investigation for fully functional regeneration [23].

Electrical stimulation can also be combined with cell-based scaffolds (*e.g.* active SCs) and gene therapy [23]. The injury site of the nerve directly receives the growth factors secreted from the SCs. Scaffolds with these active factors and electrical stimulation have been reported to exhibit the highest rate of regeneration and functional reconnection to target muscle compared to scaffolds without electrical stimulation [76].

2.4.4. Other external stimuli for non-surgical peripheral nerve treatment

Although electrical stimulation is a popular method for non-surgical peripheral nerve treatment, the range of frequency has to be decided carefully since the high frequency is likely to damage the tissue rather than heal [65]. Magnetic stimulation and laser phototherapy are alternative methods for non-surgical treatment.

There have been few studies into magnetic stimulation. Once such study showed magnetic stimulation enhanced the functional recovery of peripheral nerves with a similar number of motor neurons between the treatment side and the normal side *in vivo* [80]. Laser phototherapy is another promising method for maintaining the functional activities of the injured nerve and decreasing the formation of scars at the injury site [81]. Most studies found that low-power laser irradiation (at wavelengths 780, 808, 904, 905 nm) has a positive effect on peripheral nerve regeneration [82-85]. However, laser irradiation may have side effects on healthy tissues [65].

2.5. Materials for Tissue Engineered Peripheral Nerve Scaffolds

As mentioned in artificial nerve conduits for clinical applications, several types of synthetic polymers and natural materials, especially those based on collagen, have been developed as peripheral nerve scaffolds. Many synthetic polymers are accessible and relatively easy to fabricate into patterned scaffolds, while their biocompatibilities are in general lower compared to some natural polymers.

Although conventional nerve conduits (e.g. hollow luminal NGC) provide appropriate environments for neurite outgrowth, fully functional regeneration remains challenging. Scaffold that promote unidirectional axon regrowth are key for functional nerve regeneration. Unidirectional growth from the proximal to distal ends increases the possibility of effective recovery compared to random direction growth [86-89]. Moreover, it also reduces the chance of scar and fibrosis formation between nerve gaps, which obstructs neurite outgrowth during the wound healing process.

Recent research trends in materials for peripheral nerve regeneration have been focusing on scaffold with active environment, which can provide essential factors to accelerate

neurite outgrowth. Scaffolds with active environments include those for example, with stem cells, SCs, trophic factors, CAMs, SAMs, and electrically conductive scaffolds as alternative strategies for effective regeneration of peripheral nerve [89, 90].

In the case of synthetic polymers, many of them have been developed or used as matrices in electrically conductive scaffolds for peripheral nerve regeneration, as shown in Table 2.2. These studies indicate that composite materials with electrical stimulation can promote neurite extension.

SF, a natural polymer is the focus of this study because it can be fabricated into many forms such as films, sponges, hydrogel, and fibres (*i.e.* random and aligned fibres) [20]. It can be easily modified to form electrical conductive scaffolds with various types of conductive polymers PPy, PANi, PEDOT, PEDOT:PSS, and even by incorporation of graphene family materials (*i.e.* GO and rGO), as shown in Table 2.3. Electrically conductive SF can be used as an electrode to stimulate neurovascular activity [91], manipulating cell-laden nanopellets [92], and biosensors [93, 94].

Electrical conductive scaffolds have been studied for a long time to mimic the electrophysiology of peripheral nerves, which can transfer action potential toward target tissues and organs. After the first enhancement of electrical conductivity of polyacetylene in 1978 [95, 96], other polymers were developed and attended by the scientific community, especially for the nerve regeneration study. Thus, conductive polymers become favourable compositions associated with electrical stimulation for the modern evolution of neural tissue engineering [97].

For peripheral nerve regeneration, PPy, graphene family (*i.e.* GO and rGO), and CNTs have attained traction as composite scaffolds. However, PEDOT:PSS is also interesting for this application due to its low cost and high conductivity. It was used as a model polymer to investigate the relationship between electrical stimulation and neural differentiation [97]. SF and PEDOT:PSS, which are the main materials in this study, are discussed further in detail in the following section.

Table 2.2 Electrically conductive scaffolds for peripheral nerve regeneration

Year	Base polymers	Conductive polymers	Fabrication	Electrical stimulation	Cell type (<i>in vitro</i>)	Key results	Ref.
2009	PLGA	PPy	Electrospinning and coating	10 mV/cm, 2 h	PC-12 E18	Conductive material with electrical stimulation exhibited 40 – 50% longer neurites and 40 – 90% more neurite formation compared to unstimulated conditions. Aligned fibres supported the neurite extension and neurite-bearing cells better than random fibres.	[98]
2011	PLLA	PANi	Electrospinning and blending	100 mV/mm, 1 h	Rat neuron stem cells	The fibre material with a diameter of 195 nm greatly supported cell proliferation. Conductive material with electrical stimulation enhanced neurite extension.	[99]
2011	PCLF	PPy	Mould casting and coating	10 μ A, 24 h (DC) 10 μ A, 20 Hz, 24 h (pulse)	PC-12	Electrical stimulation enhanced the percentage of neurite-bearing cells, the number of neurites, and neurite length on composite material. The neurites extended following the direction of applied current.	[100]
2013	PLGA and PCL	PPy	Spray coating	100 mV/cm, 2 h (DC) \pm 100 mV peak-peak, 60 Hz (sine wave)	Rat DRGs PC-12	The DC stimulation increased axonal outgrowth 13% in the parallel direction of electrical current, while the AC increased 21%.	[101]

Year	Base polymers	Conductive polymers	Fabrication	Electrical stimulation	Cell type (<i>in vitro</i>)	Key results	Ref.
2014	PU (membrane)	NGNF	Spray coating	50, 100, and 200 mV/mm for 4, 6, 24, and 48 h (DC) 100 mV/mm, 1 and 10 Hz for 4, 6, 24, and 48 h (pulse)	PC-12	The DC of 100 mV/mm for 6 h greatly enhanced the plasticity of PC-12. The pulse stimulation of 100 mV/mm, 1 and 10 Hz promoted more neurites and increased neurite length.	[102]
2016	PLLA and HA	PEDOT	Film casting	0.5 mA, 2 h	PC-12	The conductive material with electrical stimulation increased mRNA expression levels of GAP-43 and SYP indicating neurite extension. The longest neurite outgrowth was $122 \pm 5 \mu\text{m}$.	[55]
2016	PLCL	PPy	Electrospinning and coating	100 mV/cm, 4 h/day	PC-12 Rat DRGs Rat sciatic nerves (<i>in vivo</i>)	The neurites of PC-12 on the conductive material had a similar length to those on TCP. The conductive material with electrical stimulation significantly promoted neurite length. It also increased the levels of NGFs (e.g. GDNF and BDNF) from DRGs. Furthermore, it could assess in the rat sciatic nerve model.	[103]
2016	Collagen type I	SWCNT	Film casting and coating	50 mV/mm, 1 mA, 8 h	Rat DRGs	The SWCNT-loaded material with electrical stimulation increased neurite outgrowth 7 folds to non-loaded materials without stimulation.	[104]

Year	Base polymers	Conductive polymers	Fabrication	Electrical stimulation	Cell type (<i>in vitro</i>)	Key results	Ref.
2017	PLLA	PPy	Film casting	100 mV/cm, 2 h/day for 14 days	PC-12 L929	ECM coating supported cell adhesion, neurite-bearing cell, neurite alignment, and neurite length on the conductive material. The ECM coated conductive material with electrical stimulation promoted early state neurite extension of PC-12 within the first 3 days.	[105]
2018	PCLF	CNT	Mould casting and UV-induced crosslinking	100 mV/mm, 20 Hz, 2 h/day for 5 days	PC-12	The PCLF-CNT scaffold with electrical stimulation enhanced PC-12 cell proliferation, cell migration, and the formation of intracellular connections.	[106]
2021	PLA	rGO and PPy	Electrospinning of composite solution (PLA/rGO) and plasma treatment (<i>In situ</i> PPy)	100, 400, and 700 mV/cm, 50 Hz, 0.5 h/day for 3 days	PC-12	The PLA/rGO/PPy composite nanofibres with electrical stimulation could effectively promote cell proliferation, differentiation and neurite outgrowth. The suitable content of rGO was 3.5 wt% relative to PLA. The electric density of 400 mV/cm promoted DMEM protein adsorption on composite scaffold better than other electrical conditions.	[107]

Table 2.3 Electrical conductive SF for tissue engineering and biomedical applications

Year	Base polymers	Conductive polymers	Fabrication	Electrical stimulation	Cell type (<i>in vitro</i>)	Key results	Ref.
2012	SF	PPy	Electrospinning and chemical polymerisation	N/a	hMSCs and fibroblast	The PPy coated electrospun SF supported hMSC and fibroblast adhesion and growth.	[108]
2015	SF	PPy-co-2-hydroxy-5-sulfonic aniline	Freeze-dry and IPN	100 mV/mm, 4 h/day for 6 days	hMSCs	hMSC differentiated toward the cell with osteogenic potential under the condition of electrical stimulation through a 4 mm thick scaffold.	[109]
2016	SF	GO and rGO	Electrospinning and dip coating	N/a	L929	GO and rGO coated electrospun SF supported cell proliferation as well as uncoated electrospun SF.	[110]
2016	SF and PLCL	PPy	Electrospinning and coating	100 mV/cm, 1 h/day	PC-12	The electrical stimulation on PPy coated material without NGF treatment promoted the neural differentiation factors (<i>i.e.</i> β -III tubulin, GAP43, and synapsin I) and axonal extension.	[111]
2017	SF	PANi	Electrospinning and blending	N/a	SCTM41 and rat sciatic nerves (<i>in vivo</i>)	<p>The 10 mm sciatic nerve gap, which was covered by the PANi/SF electrospun fibre seeded with SCs for 12 months, grew healthily with thick myelinated axons.</p> <p>The recovered nerve had excellent neurophysiological properties (<i>e.g.</i> 50 m/s nerve conduction velocity, 12.8 mV compound muscle potential, and 124 μV motor unit potential).</p>	[19]

Year	Base polymers	Conductive polymers	Fabrication	Electrical stimulation	Cell type (<i>in vitro</i>)	Key results	Ref.
2017	SF	rGO	Electrospinning and dip coating	100 mV, 2 h/day for 2 days	PC-12	<p>Cell viability on the rGO coated material was over 95%.</p> <p>The rGO coated material induced the differentiation of PC-12 to the neural-like phenotype.</p> <p>The electrical stimulation enhanced the production of neurite outgrowth on the rGO coated material.</p>	[112]
2017	SF and chitosan	PEDOT	Double layer electrospinning	200 μ A, 10 min on and 20 min off for various time conditions (1, 3, 5, and 7 days)	USSCs	<p>The stem cell growth and proliferation on PEDOT/SF fibres were higher than those on TCP.</p> <p>Electrical stimulation on PEDOT/SF fibres increased the gene expression associated with ligament formation.</p>	[113]
2018	SF	Graphene	Film casting	N/a	iPSCs	Graphene content of 4% in SF film increased the neural differentiation process of iPSCs.	[114]
2018	SF	rGO	Electrospinning and coating	5 V/cm, 1 Hz for 4 days	Cardiomyocyte isolated from neonatal rats	<p>The rGO/SF supported cell spreading, cardiac-specific protein expression, the formation of sarcomeric structure, and cell-cell gap junctions.</p> <p>The parallel electrical stimulation to rGO/SF fibre enhanced the functionalities of cardiac tissue.</p>	[115]

Year	Base polymers	Conductive polymers	Fabrication	Electrical stimulation	Cell type (<i>in vitro</i>)	Key results	Ref.
2018	SF	PPy	3D printing and polymerisation Electrospinning	N/a	L929 SCs	The PPy/SF scaffold was biocompatible and it supported SC adhesion.	[116]
2019	SF	Melanin	Electrospinning of composite solution	N/a	SH-SY5Y	SF/melanin composite fibres showed high free radical scavenging activity and they supported the neuronal cell adhesion and viability.	[117]
2020	SF	PPy	Film casting 3D printing and coating Electrospinning	100 mV/mm (<i>in vitro</i>) 3 V, 20 Hz, 0.1 ms pulse width, 1 h/day, every 2 days for 7 times (<i>in vivo</i>)	SCs isolated from the sciatic nerve of Sprague-Dawley rats Sciatic nerves of Sprague-Dawley rats (<i>in vivo</i>)	The PPy/SF with electrical stimulation promoted SCs growth and proliferation, accelerated wound healing of SCs, and increased gene expression of neurotrophic factors. <i>In vivo</i> , the defected sciatic nerve extensively extended neurites in the PPy/SF nerve conduit with electrical stimulation	[118]
2021	SF	PPy	Electrospinning of composite solution	5 V, 1 Hz, 2 ms pulse width	HL-1 NRCMs hiPSC-CMs	The electrospun fibre with a PPy to SF ratio of 15:85 showed sufficient electrical conductivity for cardiomyocytes. With electrical stimulation, the hiPSC-CMs on the fibre with a PPy to SF ratio of 30:70 exhibited strong contraction	[119]
2021	SF	PEDOT:PSS	Electrospinning and dip coating/ DMSO treatment	N/a	NG108-15	The DMSO treated PEDOT:PSS/SF enhanced cell proliferation compared to untreated fibres.	[120]

Year	Base polymers	Conductive polymers	Fabrication	Electrical stimulation	Cell type (<i>in vitro</i>)	Key results	Ref.
2021	SF	GO and rGO	Electrospinning of composite solution	N/a	NG108-15	<p>The SF/GO and SF/rGO greatly supported cell adhesion.</p> <p>Graphene content in materials in particular SF/rGO enhanced the metabolic activity and cell proliferation.</p>	[121]

2.5.1. Silk fibroin (SF)

Silk fibroin (SF) is a protein extracted from silk cocoons of silkworms, *Bombyx mori* (*B. mori*), also known as mulberry silks [20, 122, 123]. Silk cocoons contain two proteins: fibroin and sericin as the core fibres and glue-like proteins for attaching all core fibres respectively. The majority (~75%) of silk cocoon weight is fibroin protein, while the other is sericin approximately 25 – 30% [20]. Only the fibroin protein is known to be biocompatible for the application topic of this study, so the sericin must be degummed before further use. Silk fibroin has been used in medical sutures and developed for biomedical materials, especially scaffolds for tissue engineering of bone, tendon, ligament, cartilage, neural, skin, etc.

2.5.1.1. Structure and mechanical properties of silk fibroin

The fibroin protein is a block copolymer containing light and heavy chains, which have molecular weights of 25 – 26 and 325 – 390 kDa respectively, linked by disulphide bonds [20, 122, 123]. The light and heavy chains represent hydrophilic and hydrophobic domains of fibroin respectively. Almost all molecules in a natural silk fibroin are formed in the β -sheet structure that is the hydrophobic part and provides the mechanical strength of fibres. However, these hydrophobic segments are connected together by small hydrophilic linkers and non-covalent bonds of light chain molecules for maintaining the elasticity.

A hydrophobic molecule is formed as a hexapeptide sequence consisting of repeated amino acids: glycine – alanine – glycine – alanine – glycine – x, where x is serine or tyrosine as shown in Figure 2.10 [124]. The secondary protein structures of these hydrophobic molecules are typically organised to be nano-crystalline or semi-crystalline regions, which are termed β -sheets. The presence of β -sheets in fibroin fibres enhances the mechanical property of natural *B. mori* silk fibres resulting in the ultimate tensile strength (UTS) of 740 MPa [125-127], which is higher than that of other fibres such as 0.9 – 7.4 MPa reported for collagen [127-129], 28 – 50 MPa for PLA [123, 130], and 50 MPa for synthetic rubber [123, 131]. Silk fibre has high elasticity with strain at break of circa 20% [123, 125].

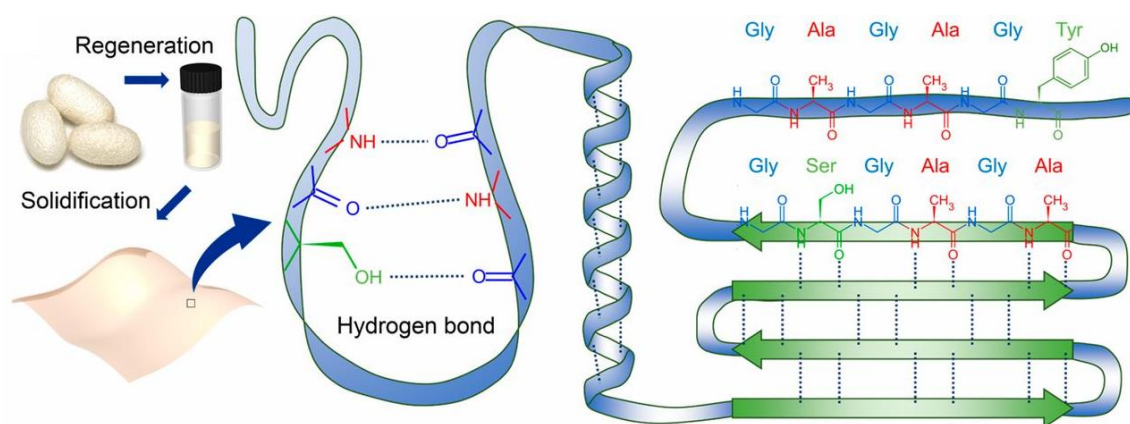


Figure 2.10 Schematic of regenerated silk fibroin molecular chain including hydrogen bonding, secondary protein structures, and amino acid sequences [124].

β -sheet formation can be divided into two subtypes: parallel and anti-parallel β -sheet, depending on the hydrogen bonds between two polypeptide strands and the direction of N-terminal and C-terminal of protein backbone [132, 133]. The major structure of many native proteins (e.g. silk from silkworms and spiders) is the antiparallel β -sheet [134]. Apart from the β -sheet crystalline structure, SF also contains other secondary protein structures (e.g. α -helix and random coil). These are non-crystalline or amorphous structures and are related to the elasticity of SF fibres [135]. On the other hand, the amorphous and crystalline structures of silk are called Silk I and Silk II, respectively. Silk I is referred to as α -helix, random coil, or metastable structure, while Silk II is dominated by anti-parallel β -sheets [135, 136].

Attenuated total reflectance Fourier transform infrared (ATR-FTIR) spectroscopy is the most common method for observing the secondary protein structure of SF. Three regions of absorbance peaks represent the chemical bonding of amide, which are labelled as amide I, amide II, and amide III. The amide I peak ($1600 - 1700 \text{ cm}^{-1}$) is associated with C=O stretch, amide II peak ($1520 - 1550 \text{ cm}^{-1}$) with N-H deformation, and amide III peak ($1200 - 1300 \text{ cm}^{-1}$) with C-N stretch and N-H bends [137]. Analysis of the amide I region is commonly used for identifying all secondary structures of SF since it refers to the small variation of geometry molecules and hydrogen bonds [138].

However, the mechanical property of regenerated SF material is significantly lower than natural SF due to the loss of β -sheet formation during the fabrication process (e.g. heating and dissolving in solvents). For example, the dry silk film has been reported to have UTS ~20 MPa and the elastic range is less than 2% resulting in brittle material [122].

The diversity of amino acids in the side chain is another noticeable property of SF. Both amine and acid groups can be easily modified by various chemicals for surface decoration. Adhesive molecule genes such as fibronectin, elastin, and collagen can be genetically inserted into silkworms in order to produce recombinant SF [139, 140].

2.5.1.2. Biocompatibility and degradation

Silk fibroin has a special combination between strength and elasticity that is very attractive to be the matrix of mammalian cell adhesion. Many studies have confirmed that silk fibroin is a biocompatible material even though it is an endogenous material and hence could be rejected by the immunological system. There is only minimal inflammation and no extra specific signs of the immune response expressed when testing silk materials *in vitro* and *in vivo* [141]. Currently, the degummed silk fibroin without sericin is widely accepted to use in biomedical applications, similar to those where PLA and collagen are used [122]. However, another concerning problem is the degradation products and debris. Although most products are non-toxic, their long-term effects in the body still need to be properly investigated.

Silk fibroin can be retained in our bodies for a long duration of more than 60 days without losing any mechanical strength but it can be slightly degraded [123]. The degradation period of silk fibroin is dependent on both the silk structure and implantation regions. For example, a report into *in vitro* degradation showed that the SF scaffold with a larger pore size collapses faster and exhibits a faster rate of weight loss; therefore, the pore size of the SF scaffold is inversely proportional to the degradation rate [142]. The highly crystallized structure (β -sheet) degraded gradually [20].

In general, protein structures are usually digested *via* enzymatic degradation by protease enzymes resulting in the surface erosion of silk material. Protease XIV is a common

enzyme for studying silk degradation *in vitro* and it can be incubated with *B. mori* for up to 12 weeks [143]. Porous SF sheet has been reported to be broken down by protease XIV into free amino acids, indicating that the SF sheet would be susceptible to human metabolic processes [144]. Moreover, the degradation time of SF material can be controlled by the exposure to gamma radiation [145]. Gamma irradiation alters the secondary structure of β -sheets into random coils resulting in the fragile structure and increase of hydrolysis rate.

2.5.1.3. Electrospun silk fibroin

Electrospinning is a fibre fabrication method using electrical gradients to induce the moving of polymer solution from a syringe and turn them into fibres with a small diameter at a collector. The diameters of these fibres are usually in a few hundred nanometres and the alignment of fibres are can be controlled to some degree by collector type and rotation speed/linear velocity. Static collectors typically result in random fibres, while the rotating mandrel collector can give aligned fibres that are very useful in peripheral nerve application.

Recently, SF extracted from silk cocoons has gained traction for electrospinning, using two different solvents: aqueous and other organic solvents. SF electrospun fibres from aqueous solvents (water-based solution) are non-toxic and compatible with cells; however, the solution preparation takes a long time, particularly the dialysis and concentrating processes. In contrast, the organic solvents are maybe toxic to cells even if they can dissolve SF rapidly.

The water-based electrospinning solution is initially prepared by dissolution of degummed SF fibres either in lithium bromide (LiBr) or the solution of calcium chloride, ethanol, and water ($\text{CaCl}_2/\text{EtOH}/\text{H}_2\text{O}$), dialysis in water, and then increasing concentration of SF by dialysis against polyethylene glycol (PEG) [20, 146-148]. After electrospinning, the fibre mats should be immersed in ethanol or methanol to induce β -sheet formation. However, by using organic solvents the dialysis processes can be obviated. For example, Zhang K.H., *et al.*, 2011 reported that 12% wt/v of degummed SF can be readily dissolved in a mixture of hexafluoroisopropanol and trifluoroacetic acid (HFIP:TFA) at a volume ratio of 9:1 [149]. Formic acid (FA) is another suitable solvent for silk fibroin. SF dissolution in 6% wt/v of FA with addition of CaCl_2 can be electrospun

into fibres, as confirmed by Liu Z., *et al.*, 2015 [150]. FA is usually used for dissolving 12 – 20% wt/v lyophilized silks and dried films to prepare electrospinning solution [151-154].

Electrospun SF fibres are reportedly biocompatibility, and enable scaffolds with suitable mechanical strength, tuneable structure, and optimal permeability of oxygen and moisture, all intrinsic properties for supporting cell survival [113, 155]. Electrically conductive polymers are usually added into electrospun SF mat either during the preparation of electrospinning solution or after electrospinning (post-processing) to improve the electrical conductivity of fibres. The electrically conductive fibres are applicable in electrical stimulation, in which the external electrical current can transfer to the cell directly, as shown in Table 2.3. Moreover, many conductive polymers are biocompatible and some have high protein adsorption properties that may promote cell growth. For instance, Kotwal A. and Schmidt C.E., 2001 and Forcinito L, *et al.*, 2014 reported that PPy can greatly adsorb fibronectin, laminin, and NGF [24, 156]. Das S., *et al.*, 2017 reported that the high percentage of swelling of electrospun PANi/SF that improve the recovery rate of rat sciatic nerve [19].

2.5.2. Poly(3,4-ethylenedioxythiophene) polystyrene sulfonate (PEDOT: PSS)

PEDOT:PSS is a flexible, transparent, and conductive polymer. In addition, it has high thermal stability and water solubility [157]. Its structure comprises of two differently charged polymers (ionomers) in both positive and negative charges, which are found in PEDOT and PSS respectively [158], as shown in Figure 2.11. Therefore, an electrical double layer (EDL) is spontaneously formed in the bulk of PEDOT:PSS, and is suitable to be a part of organic electronic devices such as capacitors, conductors, and transistors [159].

Many research reports into PEDOT-incorporated peripheral nerve scaffolds have shown good results in terms of neurogenic differentiation *in vitro*, and similar morphology of recovered nerves *in vivo* to use autologous nerve grafts [97]. For example, the PC-12 cell line expressed high levels of neurogenic factors such as MAP2 and β -III tubulin when cultured on the PEDOT-infused collagen hydrogel even without electrical stimulation [160]. Unfortunately, the PEDOT scaffold is nondegradable and a high quantity of PEDOTs might reduce the porous size of the

scaffold and then inhibit the exchange of nutrients and metabolic wastes. An appropriate neural scaffold should be a degradable in a period that is matched to the recovery time. As a consequence, cross-linked PEDOT:PSS scaffolds are an alternative choice because not only does the EDL property support extraneously electrical stimulation but also surface erosion can be controlled by PSS concentration [22, 97].

PEDOT:PSS scaffolds can provide high cell proliferation and cell viability. Hardy J.G., *et al.*, 2015 reported DC stimulation with 10 mV/mm for 4 h across PEDOT:PSS films to result in fibroblast alignment on the material [161]. For peripheral nerve regeneration, neurite outgrowth is significantly greater when exposed with the electrical pulse stimulation on PEDOT:PSS scaffolds [97].

PEDOT:PSS has electrochemical stability and it is suitable for modification of the electrical conductivity of scaffolds for peripheral nerve applications. Although PEDOT:PSS incorporated scaffolds has been previously developed, few studies have been focused on incorporation with in silk fibres. PEDOT:PSS on or as a penetrating network in electrospun silk fibroin fibres is an interesting material that might improve the neurite extension of neurons and SCs proliferation especially when combined with the active electrical stimulation.

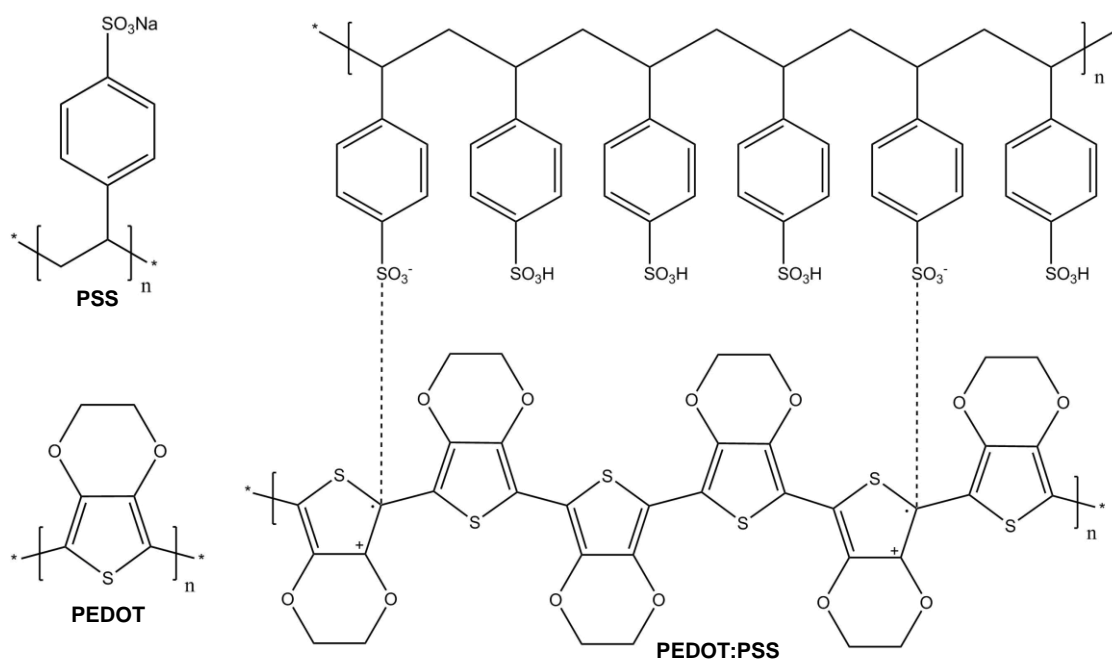


Figure 2.11 Chemical structure of poly(3,4-ethylenedioxythiophene) (PEDOT), polystyrene sulfonate (PSS), and the complex form of PEDOT:PSS.

2.6. Electrospinning

Electrospinning is a well-known fibre fabrication technology, which has become popular across several research fields in the last two decades [162, 163]. Electrospinning uses high electrostatic force to transform the solution into fibres in the range of submicron to nanometres. Polymers, metals, ceramics, and composites can be utilised as the raw materials for electrospinning. Wide ranges of polymers from both synthetic and natural polymers including SF can be electrospun into scaffolds for biomedical applications and tissue engineering. The basic principle of electrospinning is described in the following section.

2.6.1. Electrospinning apparatus

In general, electrospinning consists of three main components: a spinneret or nozzle, a collector, and a high voltage DC power supply.

The conventional spinneret is a needle-based system comprising of an electrospinning solution in a syringe connecting with a metallic needle and a syringe infusion pump. The ejected solution from a needle is then spun into fibres, solvent evaporation typically occurs in flight and the dry fibres are eventually collected. Another type of spinneret is a needle-less system. Metallic spinnerets are designed in various geometric shapes instead of needles and the fibres are directly spun from an open liquid surface [164].

The collector is always made from an electrically conductive material, and depending on set-up can manipulate the alignment of electrospun fibres. The static flat plate is commonly used for collecting random fibres, while parallel plates, rotating drums, rotating dishes, and conveyors can be used to collect unidirectionally aligned fibres [162].

Common voltage ranges are 10 – 30 kV and 30 – 80 kV for needle-based and needle-less electrospinning, respectively [165]. The electrostatic force between the spinneret and collector is generated by the high voltage DC power supply. The high voltage source applied to the spinneret is commonly positive, while it is a grounded or negative charge is typically applied to the collector. In this case the electrospinning solution at the spinneret is charged by positive ions and is able to move following the electric field towards the collector. The movement of the charged solution under the influence of an electric field is also termed an electrospinning jet.

2.6.2. Jet generation

The electrospinning jet from the spinneret to the collector can be divided into three phases: The Taylor cone, straight jet, and bending/whipping region [166]. These phases are sequentially created following the distance from the spinneret to the collector (*i.e.* Taylor cone at the tip of needle, straight jet at the middle, and bending/whipping at the area close to collector), as shown in Figure 2.12.

The Taylor cone is a conical shape of solution, formed due to the strong electric field, and first described by Taylor G.I., 1964 [167]. In electrospinning, the Taylor cone is created by the effects of pressure, voltage, and heating [168]. Herein, the pressure refers to the mechanical feed of the syringe pump and the gravity force (if ejected downwards) resulting in the extrusion of

solution at the tip of the spinneret. The surface tension due to the cohesive force of liquid molecules leads to the spherical droplet of ejected solution at the tip. Therefore, the different properties of electrospinning liquid or solution (e.g. viscosity and concentration) and temperature affect the surface tension of the ejected solution at the tip of the spinneret.

Increase in voltage can transition the spherical droplet to paraboloid and hyperbolic surface [168, 169], as shown in Figure 2.13. At a threshold voltage, the electric field is strong enough to charge the solution and the charged droplet is induced to be a fine fluid jet from the apex of the meniscus eventually. Therefore, the balance between the surface tension due to pressure and the voltage is imperative for generating the perfect Taylor cone and electrospinning jet.

The length of the straight jet is defined by sufficient distance driven by the current due to the charged surface of the solution. The straight jet thins rapidly and it enters the bending/whipping region when all forces except initial and electrostatic forces stop to dominate the jet [169]. Therefore, the surface charge density or the current passing through the jet is an important parameter for the stability of the jet, as well as the fluid parameters of the jet, such as viscosity and conductivity [170].

The bending/whipping region occurs when the jet becomes convectively unstable. It begins with a short sequence of unstable bending back and forth followed by a winding and looping path in 3D. Many loops are produced during the travel of the whipping jet to the collector. The first jet loop is very tiny with a small circumference. The following loops slowly grow up and their circumferences are gradually increased; meanwhile, the diameters of jet solution are gradually decreased [171]. The whipping instability is largely responsible for fibre solidification [169].

The solidification of fibres from the electrospinning jet is commonly due to the heat transfer or solvent evaporation, depending on the states of the electrospinning material. In the case of a liquid state prepared from melt material, the heat of the jet is transferred to the environment during travel to the collector, termed electrohydrodynamic quenching [168]. Additionally, the air current enhances the thermal quenching of the jet, which increases the solidification rate.

In solution-based electrospinning, solvent evaporation is required for solidification. Before evaporating, the solvent needs to be separated from polymers or other composites, which is called phase separation. Two common mechanisms of phase separation in electrospinning are thermal-induced phase separation (TIPS) and vapour-induced phase separation (VIPS) [166]. The TIPS occurs when the electrospinning jet is rapidly cooled down leading to the evaporation of the solvent. On the other hand, the vapour can act as a nonsolvent during VIPS. It causes the precipitation of the polymer out of the solvent.

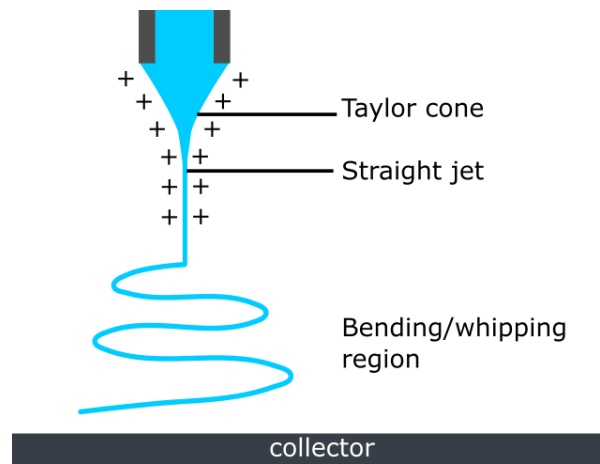


Figure 2.12 Schematic of electrospinning jet from needle to collector, this figure is based on information from [166].

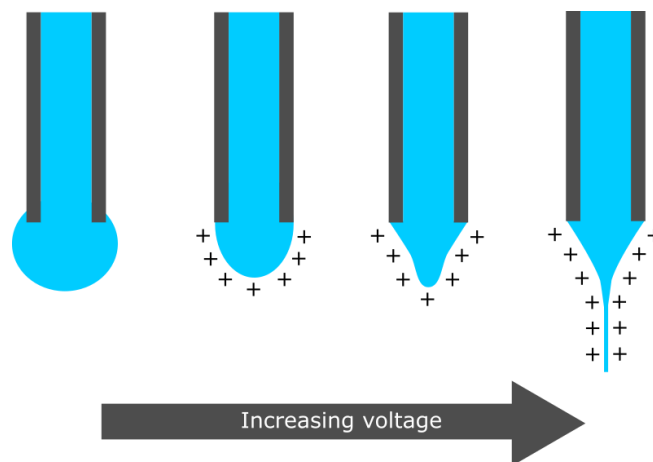


Figure 2.13 Transition of droplet due to the increase of voltage, this figure is based on information from [168, 169].

2.6.3. States of materials for electrospinning

Electrospinning can transform either the solution or the liquid state into solid fibres. The states of materials for electrospinning can be classified into three states: solution spinning, melt spinning, and emulsion spinning. These states have their unique advantages. The melt spinning offers a high throughput rate, the solution spinning is applicable to a large variety of materials, and emulsion spinning is suitable for polymers with high melting points [162].

2.6.3.1. Melt spinning

Electrospinning materials are prepared as flowing or molten polymers. The take-up speed, drawing temperature, and drawing ratio (*i.e.* the amount of stretching undergone by the material) are important factors to control the structural properties of fibres [162]. The flowing or molten polymer must be heated all the time during electrospinning to maintain homogenous distribution of heat over the substrate [168]. Several types of synthetic polymers can use the melt electrospinning for fabricating nonwoven mats such as PCL [172-174], PLA [174], PMMA [175], amongst others.

2.6.3.2. Solution spinning

As mentioned above, solution spinning is the most reported method for polymer electrospinning, since many types of polymers can easily be prepared as solutions. Solution electrospinning can be divided into two subtypes according to the solvent removal process: dry and wet electrospinning.

In dry electrospinning, solvent evaporation and fibre solidification are achieved in dry air with either a normal atmosphere or blowing gas or hot air. In wet spinning, the polymer solution is spun in a coagulation bath comprising of a nonsolvent and miscible liquid with respect to the electrospinning solvent [162]. Generally, dry electrospinning is the simplest method for electrospinning and it is accessible for a variety of polymers including SF.

2.6.3.3. Emulsion spinning

Emulsion spinning is a technique for compounds, which are insoluble and non-melting such as certain fluorocarbons and ceramics [162]. Catalysts and emulsifier agents are often prerequisites for this technique. Emulsions can be spun in both dry and wet electrospinning, similar to solution electrospinning.

2.6.4. Electrospinning parameters

The electrospinning process and the quality of fibres are mainly influenced by six factors: polymer concentration, solution viscosity, flow rate, electric field, working distance, and air humidity [163]. These factors can be arranged into three groups following the electrospinning steps: the solution preparation, the setup of the electrospinning apparatus, and environmental control during electrospinning.

In solution preparation, the concentration and viscosity of the solution need to be optimised. High viscosity may result in difficulties in delivery from the syringe needle and blockages, whereas low viscosity may result in beading/droplet formation, defect in continuity of fibres, and damage to any formed fibre mat by excess solvent landing.

In terms of electrospinning apparatus, there are three sequential setup steps: the spinneret, collector, and applied voltage. The flow rate of the droplet solution at the tip of the spinneret can be controlled by the diameter of the needle and the feed rate of the syringe pump. The working distance is commonly measured from the tip of the needle to the surface of the collector. The electrospinning axis (e.g. horizontal/vertical) is necessary to consider since there may be influenced by gravity [176]. The high voltage supply must be adjusted carefully. The threshold voltage, which can generate a suitable Taylor cone and straight jet, is most ideal for electrospinning. Thus, the voltage and solution flow rate both need to be in equilibrium to maintain the fibre production and quality. Humidity and temperature during electrospinning should also be controlled since they may affect the solvent evaporation, phase separation and fibre solidification processes [166].

2.7. Interpenetrating Polymer Networks (IPNs)

Fibres of SF and conductive polymers can be prepared by either pre-electrospinning (electrospinning solution preparation) or post-electrospinning (post-processing of electrospun SF mats). For pre-electrospinning, the conductive polymers are mixed with SF solution as a blended electrospinning solution. This technique is rarely used; however, a few articles have explored this method for electrospinning electrically conductive SF solutions, such as PANi/SF [19], PPy/SF [119], and GO/SF or rGO/SF [121].

For post-electrospinning, the electrospun SF mat is functionalised with conductive polymers in/on the network of SF. The most renowned functionalisation for electrospun SF is the coating method, especially dip coating. Unfortunately, dip coating only partially attaches the complex molecules of PEDOT:PSS in/on the surface of electrospun SF mat *via* electrostatic interaction [87]. The growing of PEDOT:PSS polymer chains in/on the network of SF using an interpenetrating polymer network (IPN) approach is an alternative method to produce electrically conductive PEDOT:PSS/SF material effectively.

IPNs are a combination of two or more polymers in networks, in which the molecules between polymer chains are partially interlaced or cross-linked in the matrix [177]. The types of IPN are categorised by the chemistry of preparation or the structure of IPN composition [178].

2.7.1. The chemistry of preparation

There are two types of IPN: simultaneous and sequential IPN. In the case of simultaneous IPN, two polymer networks are prepared from their precursors independently. The interlacing between networks occurs simultaneously. For sequential IPNs, the precursors of one polymer network are grown and polymerised on another existing polymer network. For example, a single network of polymer, which is in the form of hydrogel or fibre, is swollen in a solution of monomers, initiators, and activators for another type of polymer, as shown in Figure 2.14 [177, 178].

2.7.2. The structure of IPN

According to the interaction between the networks, there are two main structures of IPN: full IPN and semi-IPN (also termed pseudo-IPN). Two networks are ideally connected side by side with

many entanglements in full IPNs, while a polymer is cross-linked in the presence of another in semi-IPN. The semi-IPN is able to produce a mixture of fine morphology.

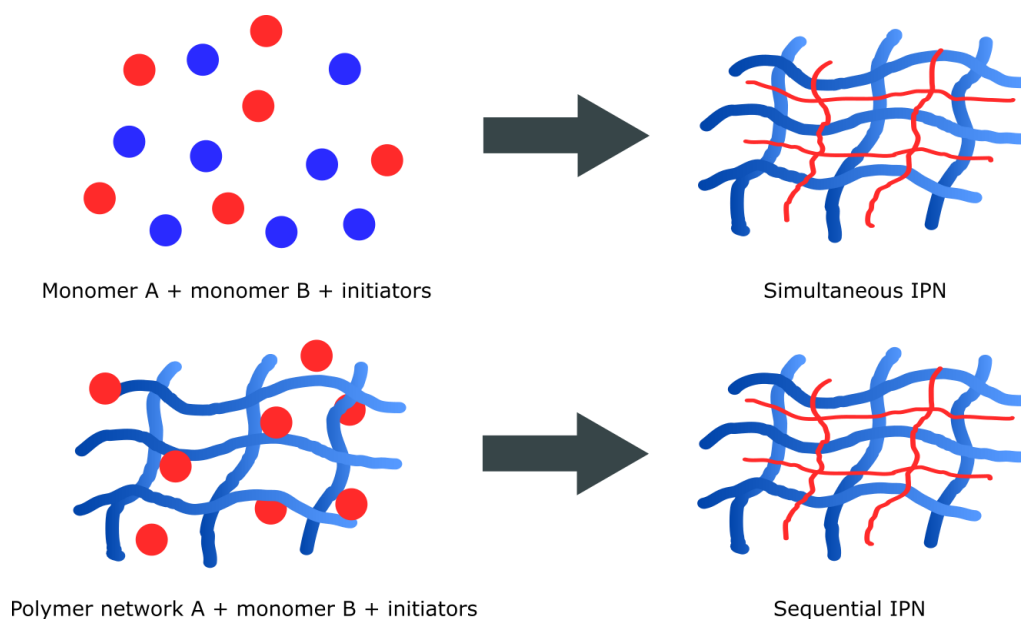


Figure 2.14 Schematic of simultaneous IPN and sequential IPN, this figure is based on information from [177, 178].

2.8. Electrical Stimulation Methods

Electrical stimulation (ES) is an effective technique for manipulating cellular behaviours both *in vitro* and *in vivo*. In regenerative medicine and tissue engineering, ES aims to promote cell growth, differentiation, and tissue functionality by triggering the expression of associated genes or proteins. Typically, ES can be categorised into three methods: direct stimulation, capacitive stimulation, and inductive stimulation [179].

2.8.1. Direct stimulation

Direct stimulation is a method by which electrodes touch the target system [180, 181]. The electrodes are directly placed or implanted at the injured tissue or nearby tissue *in vivo*, while the positions and number of electrodes can be designed in various patterns. *In vitro*, the simplest model of direct ES in the cell culture chamber is in the form of an electrochemical cell with either horizontal or vertical axes [180, 181], as shown in Figure 2.15.

The electrical potential is applied to a pair of electrodes by using an external DC power supply or function generator. The outcomes of electrical signals (e.g. current flow and electric field) are mostly generated across the cell culture medium due to its electrolytic property. Consequently, ions in the cell culture medium are attracted to the electrodes, resulting in the formation of an electrical double layer (EDL) at the medium-electrode interface [182-184]. Electrochemical reaction (*i.e.* oxidation and reduction) generates electron transmission between electrodes and charged ions in the medium resulting in faradic current and by-products [182, 183, 185].

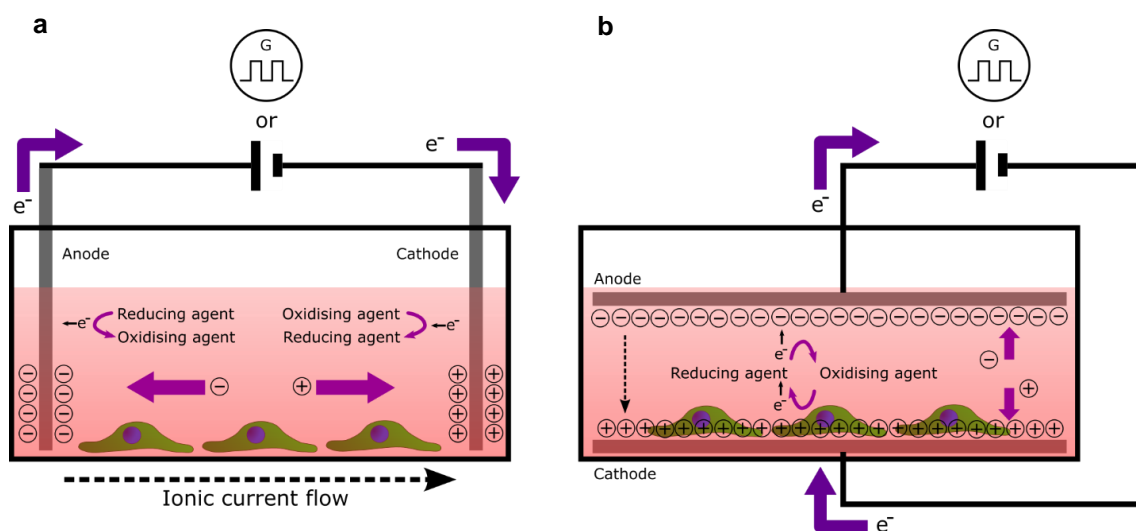


Figure 2.15 The direct ES model: the electrodes and electrochemical cell in (a) horizontal axis and (b) vertical axis, this figure is adapted and redrawn from [179].

2.8.1.1. Electrical double layer (EDL)

Once the voltage is applied to the electrodes, it induces the opposite charges of ions in the medium to form a layer (e.g. a layer of positive ions at the cathode and a layer of negative ions at the anode), which is defined as the Stern layer, at the medium-electrode interface [184, 186], as shown in the Figure 2.16. Since the Stern layer has a high ionic concentration of the opposite charge to the electrode, the potential across this layer is rapidly and linearly decreased [184]. Due to the electrostatic force and ionic gradient, the region next to the Stern layer has a lower ionic concentration. Although the majority type of ions in this region remains the same as in the Stern layer, it contains both charges (*i.e.* positive and negative). This region is called a diffuse layer and

the potential across this region is decreased exponentially [184, 186]. Therefore, the Stern layer and diffuse layer generated at the medium-electrode interface are collectively referred to as the EDL.

The thickness of the EDL is also known as Debye length [184, 186]. The region further away from the Debye length is less influenced by electrode potential and referred to as bulk electrolyte [186]. Furthermore, the electrical currents through the EDL and bulk electrolyte are induced by two mechanisms of charge transfer: non-faradic and faradic [182]. Faradic charge transfer is between electrode and electrolyte due to redox reaction, whereas non-faradic is the movement of ions driven by the adsorption and re-distribution of ions at the surface of the electrode [182]. Therefore, the surface of the electrode is another factor that may affect the current flow through the electrolyte.

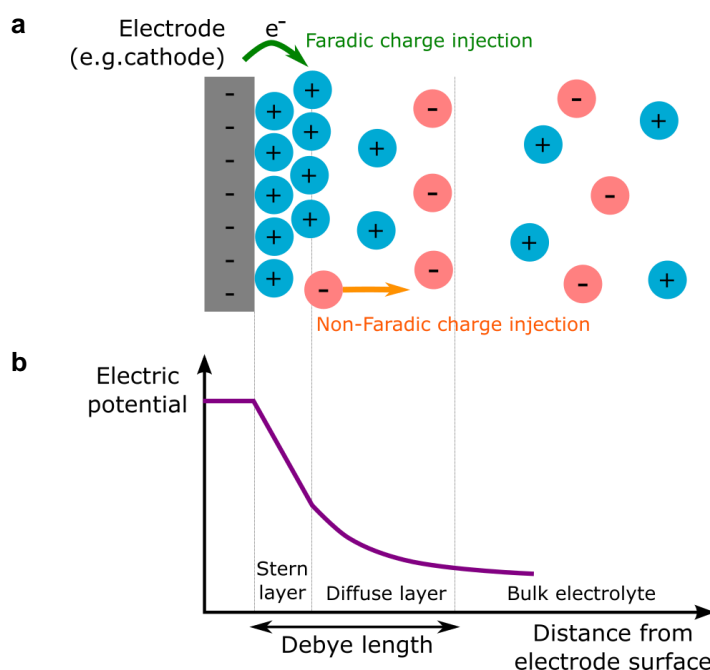


Figure 2.16 Schematic representation of the electrical double layer (EDL): (a) the charge injection at the surface of electrode and (b) the relative electrical potential in each layer, this figure is adapted and redrawn from [179].

2.8.1.2. Electrode materials

Several materials are used as electrodes for ES, which can be categorised into three major groups: metallic electrodes, carbon-base (graphite) electrodes, and conductive polymers.

Metallic electrodes such as platinum (Pt), gold (Au), stainless steel (SS), and titanium (Ti) are commonly used for ES [181, 184, 185]. The Pt-electrode is preferable for *in vitro* ES over other metallic electrodes because it has high biocompatibility, conductivity, and corrosion resistance [181, 184]. However, Pt-electrodes can be difficult to use *in vivo* due to its relatively poor mechanical properties [181, 187]; thus, Ti-electrodes and SS-electrodes are commonly preferred as alternatives [181, 187-189]. Metallic electrodes also have high polarisation resistance, which is the resistance of the electrode to oxidation during ES [190]. The polarisation resistance can indicate the corrosion material since it is inversely proportional to the corrosion current and thus to the corrosion rate [191]. Unfortunately, it may reduce the charge transfer efficiency [181, 182, 184, 189].

Carbon electrodes (C-electrodes) are promising electrodes for *in vitro* ES due to their excellent conductivity, corrosion resistance, and charge transfer efficiency [181, 187, 189]. However, it may have high protein adsorption on the surface, which could affect the homogeneity and stability of electrical signals [181, 187, 189]. Although common graphite plate may be the most brittle electrode, other conductive C-base family materials (e.g. graphene and CNT) can be fabricated into flexible electrodes [192].

On the other hand, conductive polymers can functionalise many types of substrates and used as electrodes for ES. Their mechanical and electrical properties are modifiable depending on the fabrication.

2.8.1.3. Alternative patterns of direct stimulation

Besides the simplest ES model with two electrodes, a salt bridge or a reference electrode of silver/silver chloride (Ag/AgCl) can be added into the system to avoid faradic by-products during ES [181, 184, 185]. Ag/AgCl electrodes are commonly in glass or plastic tubes that are filled with a salt solution (e.g. KCl) with the ion-exchange layer at the tip of the electrode [184, 185]. The salt

solution from Ag/AgCl reference electrode may leak and penetrate the cell culture medium causing long-term toxicity to cells. Hence, the salt bridge system can be used as an alternative. During ES, the salt bridge functions as the quasi-cathode or quasi-anode to the system without generating faradic by-products, as shown in Figure 2.17 [179].

In the case of electrically conductive scaffolds, the ES may be directly applied to materials from the outside of the cell culture chamber. Then, the electric current mainly passes through the material instead of generating ion currents across the cell culture medium. The electrochemical reaction may be produced at the surface of conductive material.

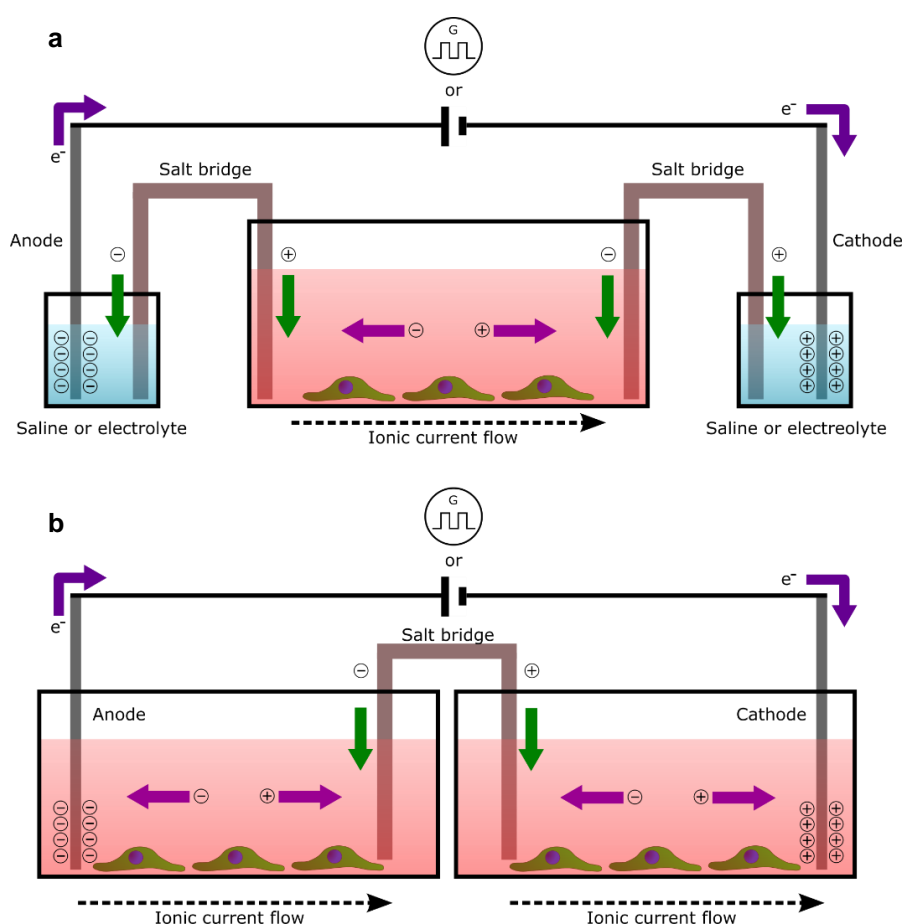


Figure 2.17 Alternative direct ES model: (a) double salt bridges model without direct contact of electrodes to cell culture medium and faradic by-products and (b) single salt bridge model with the separation of faradic by-product from each electrode, this figure is adapted and redrawn from [179].

2.8.1.4. The role of material impedance in electrical stimulation

In general, electrically conductive materials or conductors are materials that allow for the flow of electrons or electrical current passing through such as metals, electrolytes, and conductive polymers. The resistance and conductance are the basic properties of the conductive material, which indicate the ability to transfer electrical current. The resistance in the unit of Ohm (Ω) is inversely proportional to conductance in the unit of Ω^{-1} or Siemens (S).

In ES of cells on a conductive scaffold, the electrical current passing through the scaffold is dependent on the resistance of the material and the voltage supply to material according to Ohm's law ($V = IR$, where V is voltage supply, I is current passing through the material, and R is the resistance of material). Thus, when the voltage supply is fixed constantly, a scaffold with lower resistance or higher conductance can transfer higher current that may considerably influence the cells on the scaffold as shown in Figure 2.18. However, common scaffolds for tissue engineering are composite materials and/or proteins-based materials that can have a complex system of resistances, capacitances, and others (e.g. inductances and Warburg elements), which is termed impedance.

Notably, proteins are polarised because they contain neutral polar, polar, and charged side chains and their structures are comprised of the repeat of polar units of amino acids [193]. Due to the polarisability, proteins are sensitive to applied electric fields, resulting in dielectric character material (*i.e.* dielectric permittivity and dielectric loss) [193].

Moreover, the passive electrical properties of the material located between two parallel electrodes can be characterised by two measurements: capacitance (C) and conductance (G) following the equations below [194]:

$$C = \frac{A\epsilon\epsilon_0}{d} \text{ and } G = \frac{A\sigma}{d}$$

where, A is the area of the electrode, d is the distance between electrodes, ϵ is the permittivity of the material, and ϵ_0 is the dielectric permittivity of free space. The units of capacitance and conductance are Farads (F) and Siemens (S), respectively.

Electrochemical impedance spectroscopy (EIS) is a well-known technique to assess the capacitance and conductance of materials [195-198]. The result from EIS is typically shown in Nyquist plot of impedance, which can be fitted to the electrical equivalent circuit in order to interpret the fundamental components of capacitances and resistances in the measuring system, including material and electrolyte [199, 200].

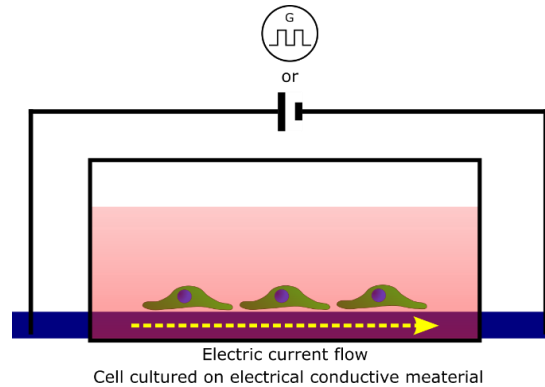


Figure 2.18 Direct ES through an electrically conductive scaffold with cells on top, this figure is adapted and redrawn from [179].

2.8.2. Capacitive stimulation

Capacitive ES is an indirect stimulation, typically using a couple of parallel plate electrodes without touching the electrolyte or cell culture medium. The electrodes are placed outside of the cell culture chamber; this means that the target cells are insulated from the electrical current due to the air gaps and non-conductive chambers, as shown in Figure 2.19. Capacitive ES generates only the electric field (EF) to the system without electrochemical reactions. The generated EF can induce intracellular and extracellular diffusion [181, 185]. However, capacitive ES requires a much higher applied voltage than direct ES due to the dielectric property, which drastically reduces the EF strength to cells [185, 201-203].

Capacitive ES is an interesting technique for use *in vivo*, since it can be set up as non-invasive electrodes. The electrodes can be attached to the skin and deliver the EF to the injured tissues [204].

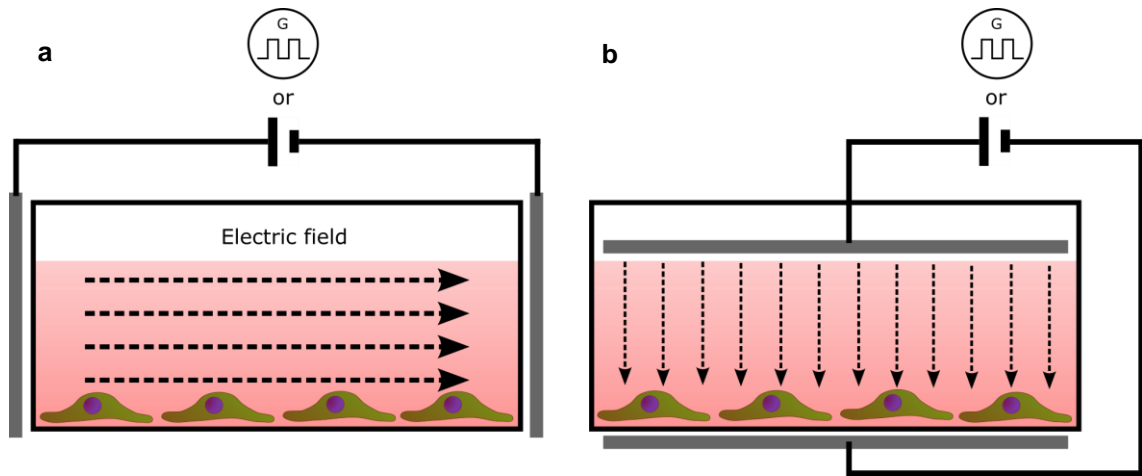


Figure 2.19 Capacitive ES model and the generation of electric field by two parallel electrodes at the outer surface of TCP: (a) horizontal direction of electrodes and (b) vertical direction of electrodes, this figure is adapted and redrawn from [179].

2.8.3. Inductive stimulation

Inductive ES is an indirect stimulation approach, without the contact between the electrode system and cell culture medium, similar to capacitive ES. However, a solenoid coil or Helmholtz coil is used instead of a common plate electrode, as shown in Figure 2.20. The application of alternating current (AC) to the coil generates the electromagnetic field (EMF); thus, the inductive ES delivers the EMF to the target cells [181, 205].

The changing of EMF may induce the electrical current, which is also known as Eddy current, and heat in the cell culture system [206]. Additionally, the inductive ES can combine with the static magnetic field generated by magnets [180, 204].

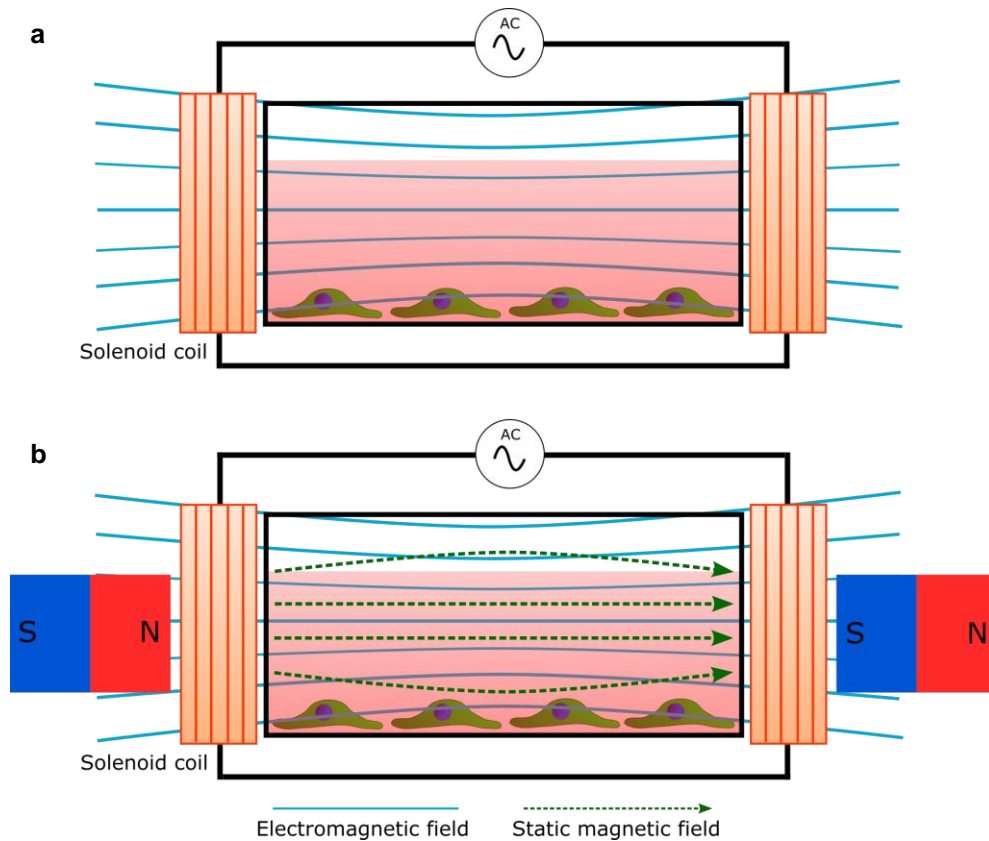


Figure 2.20 Inductive ES model with the generation of electromagnetic field (EMF) by solenoid coils at the outer surface of TCP: (a) horizontal direction of solenoid coils and (b) the combination of horizontal solenoid coils and static magnetic field from magnets, this figure is adapted and redrawn from [179].

2.9. Peripheral Nerve Cell Lines

Neuron alignment and neurite outgrowth behaviour on materials are crucial to understand, in addition to the physical material properties. Most studies use cell lines instead of primary cells such as dorsal root ganglions (DRGs) in these tests. Although the function of neuronal cell lines is not exactly the same as the peripheral nerves, at least their phenotypes and growth rate can be referred and related to them. Moreover, neuronal cell lines are inexpensive compared to DRGs. They can be subcultured, expanded, and stored for long periods of time. Therefore, *in vitro* testing with a neuronal cell line is the first simple step to evaluate the best material for fully functional regeneration.

2.9.1. Rat adrenal pheochromocytoma cell line (PC-12)

The PC12 cell line, derived from the adrenal gland of rats (rat, pheochromocytoma), is the most commonly used cell type in the field of peripheral nerve regeneration, as explained in Table 2.2 and Table 2.3. This cell line is differentiated into the neuron phenotype when cultured with NGFs. Neurite extension is clearly observed by light microscopy and the levels of neurogenic factors such as synapsin I, GAP43, and β -III tubulin can be easily investigated after differentiation [55, 111]. However, their electrophysiological properties, which is a factor for confirming the fully functional nerve, is not measurable with this cell line.

2.9.2. Mouse neuroblastoma x rat glioma hybrid cell line (NG108-15)

Recently, another type of cell line, NG108-15, has been used in this research field [120, 121, 207-209]. It is a hybrid cell of mouse neuroblastoma and rat glioma, which can differentiate into the neuron phenotype and present the necessary electrophysiology (action potential) after stimulation. Thus, NG108-15 is quite commonly used as a model of action potential study including neuromuscular signalling [210-212]. Since NG108-15 can produce action potential, it is applicable for nerve regeneration studies. This cell line can also extend neurite outgrowth and possibly respond to stimuli (e.g. electrical regime) and then generate action potential, suggesting the function of neurons to transfer electrical signals. Furthermore, NG108-15 can be co-cultured with SCs that might be very useful in future applications [213, 214].

Although PC-12 is commonly used in the research field of neural regeneration, NG108-15 is chosen in this study. Since the effect of external electrical regimes on neuronal cells is under study in this work. It is known that NG108-15 cell lines are able to produce action potential after stimulation, which can be recorded *via* the patch-clamp [215, 216]. For example, Pawar K., *et al.*, 2019 reported the electrophysiology of NG108-15 grown on spider silk fibres to study the functionality of differentiated neuronal cells [217]. However, the electrophysiology of NG108-15 after stimulation is out of this thesis scope (section 1.4); it is to be hoped that using NG108-15 in the nerve regeneration study will provide useful results regarding nerve function in future studies.

2.10. *In Vitro* Effects of Electrical Stimulation on Peripheral Nerve

As mentioned in section 2.1.3, neurons in the peripheral nervous system are commonly known as electrically conductive and excitable cells. They always function to connect and transfer the action potential between CNS and target organs. Therefore, some researchers have expected that the external electrical stimulation should enhance the neurite extension of damaged nerves and induce the direction of axons following electrical currents both *in vitro* and *in vivo* [70, 75, 218-220].

In previous studies, many conditions of electrical regimes with various parameters (*e.g.* voltages, currents, waveforms, frequencies, durations, and the directions of electric fields) were exposed to neurons, as detailed in Table 2.2 and Table 2.3. An interesting idea is the use of pulse stimulation to mimic action potentials. For example, the exposure of a short pulse of 2.5 V/cm and frequency of 5 Hz, which imitates the theta potential of electroencephalogram (EEG), on PC-12 cells promoted the neurite outgrowth as similar quality as using NGFs [218]. The pulse stimulation with the frequency of 20 Hz showed the opportunity to restore the DRGs within 21 days [219]. Additionally, a conductive scaffold under a pulse ES of 20 Hz frequency also been reported to accelerate nerve growth leading to a better functional regeneration in a 15 mm sciatic nerve defect in rats (Sprague-Dawley rats) [220]. Unfortunately, the best condition of electrical stimulation is difficult to define since it is maybe depended on any bioreactor or electrical stimulation system in each study.

A previous study (Zhu R., *et al.*, 2019) revealed that ES triggers the calcium ion (Ca^{2+}) influx on cell surfaces mediating subsequent cell behaviours [221]. In the cell signalling pathway, the Ca^{2+} influx is an initial factor to promote neurite extension and is also associated with cyclic adenosine monophosphate (cAMP) [222, 223]. The extracellular Ca^{2+} penetrates through the cell *via* voltage-gated calcium channels (VGCCs) on the cell membrane [224], and the penetration rate is faster when applying an electrical regime [225]. However, the neuron growth on electrically conductive scaffolds without electrical stimulation also showed positive result in terms of increased neurite length; this may be because the electrically conductive polymer can adsorb proteins in the medium that can also aid neurite outgrowth [24]. Therefore, the combination of conductive

scaffolds and electrical stimulation should be an alternative way to improve fully functional regeneration.

On the other hand, the effect of hydrogen peroxide (H_2O_2) has been a focus for nerve regeneration for circa a decade. Most researchers report that H_2O_2 is toxic to cells and can induce neurodegenerative diseases [226]. However, it can promote peripheral axonal growth if it is used at the optimal level. The H_2O_2 level is concerned with the electrical stimulation because it probably occurs when applying electricity into the water.

CHAPTER 3

Optimisation of double layer electrospun silk fibroin

Uniformly aligned fibres are appropriate structures for non-woven mats for orientating neurites of neurons. However, they are easily torn and have poor handling and processability, compared to random fibres mats. Herein, a double layer electrospinning method has been chosen to fabricate a peripheral nerve scaffold. The base layer is formed of random fibres, while the top layer is of uniformly aligned fibres with fibre diameters in the sub-micron range. The optimal condition and method for fabricating a double layer silk fibroin (SF) scaffold with a total thickness of 100 μm are described in this chapter.

The main purpose of the experiments in this chapter is to find the optimal electrospinning process for fabricating double layer fibre mats from silk fibroin. The double layer mat is easier to handle for post-processing than the mat with a single layer of aligned fibres [227]. A layer of aligned fibres is weak and easy to break when the tearing direction is parallel to fibres (transverse direction), resulting in difficult processability (e.g. folding and bending). Thus, the layer of random fibres is designed to act as a support layer without contacting cells. Aligned fibres can effectively guide cell invasion, while random fibres maybe hamper the migration of cells [228]; hence, the double layer mat is co-incidence with the function of endoneurium and perineurium that is to support the growth of nerve tissue and to be a barrier between nerve tissue and other connective tissues [37].

Moreover, the optimal electrospinning protocol should be short, simple, and reproducible. The reproducibility of electrospun mats is evaluated by the diameter of fibres and the degree of alignment. The fibre diameter was analysed by using scanning electron microscopy (SEM) images, and the degree of alignment is determined using ImageJ software with a two-dimensional fast Fourier transform (2D FFT) protocol [229]. There is no expectation of the fibre diameter range, but it should be similar every time, independent of experiments.

As mentioned in section 2.5.1, electrospinning is a common technique for fabricating SF into nanoscale or microscale fibres. However, there are many recommendations for

electrospinning protocols. There were two custom-made electrospinning systems used in this study: the horizontal axis without the environmental control chamber and the vertical axis with the environmental control chamber; therefore, the electrospinning protocol was then optimised again since these systems are different from other studies. The scope of the optimisation is divided into three topics: the preparation of electrospinning solution (e.g. degumming process, silk concentration, and solvent), the electrospinning parameters (e.g. feed rate, voltage, and working distance), and the post-treatment process (e.g. ethanol, methanol, and water treatment), which are explained in the following sections of this chapter.

3.1. Materials and Methods

3.1.1. Extraction of silk fibroin

Bombyx mori silk cocoons (Wild Colours natural dyes, Birmingham, UK) were cut into small pieces and then degummed in order to purify silk fibroin. According to the traditional protocol, 5 g of cut silk cocoons were boiled in a 2 L solution of 0.02 M sodium carbonate (Na_2CO_3) (Merck) for exactly 30 min [20]. During the boiling process, the temperature was constantly controlled at $\sim 75^\circ$ to 80° C and the solution was occasionally stirred to disperse the silk fibres. The boiled silk fibroin was then rinsed and stirred in distilled or ultrapure water for a total of 1 h, changing the water every 20 min. The purified silk fibroin was squeezed, stretched on a tray, and left to evaporate overnight at room temperature in the fume cupboard. The dry weight of degummed silk fibroin was measured and the percentage of weight loss was calculated following the equation below:

$$\% \text{ wt.} = \frac{wt._c - wt._d}{wt._c} \times 100$$

where, % wt. is the percentage of weight loss, $wt._c$ is the total weight of silk cocoons pieces before degumming, and $wt._d$ is the total weight of dried silk fibroin after degumming.

3.1.2. Electrospinning solution preparation

The degummed silk fibroin (SF) was prepared in a compound solution of formic acid (FA) (Fisher) and calcium chloride (CaCl_2) (Fisher) in various ratios of 98:2, 95:5, and 90:10 (ml:g). The weight

percentages of SF in FA/CaCl₂ were varied from 6% to 10% w/v. The SF in FA/CaCl₂ solution was transferred to the glass vial with a tightly closed lid and mixed well using a vortex for a few minutes until a homogenously light-yellow solution was observed. After that, the electrospinning solution was incubated overnight; a water bath was recommended for controlling temperature constantly at 45° C. The incubated solution, dark pink in appearance, was filtered to get rid of tiny silkworm residues by using a vacuum pump and a borosilicate glass crucible with porosity grade 1 (pore size of 100 – 160 µm) prior to electrospinning.

3.1.3. Optimisation of electrospinning parameters

The electrospinning solution (SF in FA/CaCl₂) was transferred to a 10 ml plastic syringe (Becton Dickinson, BD) connecting to a straight dispensing tip, 19G needle, with an inner diameter of 0.69 mm (Becton Dickinson, BD) and was then set up in the electrospinning kit. Uni-sharp needle tips were rendered flat using sandpaper before use.

Herein, electrospinning parameters: feed rates of the solution, electrical voltages, and speeds of the rotating collector were optimised in both horizontal axis and vertical axis electrospinning systems. The horizontal system was for fabricating uniformly aligned fibres, while the vertical one was for random fibres. After electrospinning, the thickness of electrospun mats was measured by a digital thickness gauge (DML3032, Digital Micrometers Ltd).

3.1.3.1. Horizontal axis electrospinning

The horizontal electrospinning was a custom-made lab-scale system. All electrospinning components were set up in a fume cupboard in the common atmosphere without humidity and temperature-controlled system. The syringe was placed on a dual-syringe infusion pump (Cole-Parmer®) and operated with the various feed rates from 0.3 – 1.0 ml/h. A metal rotating mandrel with a width of 5 cm and a diameter of 12 cm was used as a collector. A greaseproof paper or aluminium foil of size 5 x 38 cm² were tightly wrapped around the circular surface of the mandrel before use. The distance between the tip of the needle and the edge of the collector was 12 cm. The speeds of the rotating mandrel were varied from 1,000 – 1,500 rpm (linear velocity of 6.28 – 9.42 m/s). The electrical voltage of 12 – 20 kV generated by a high voltage direct current (DC)

power supply was charged between the needle and collector as the positive and ground (0 kV) respectively. The setup of the horizontal electrospinning apparatus is shown in Figure 3.1.

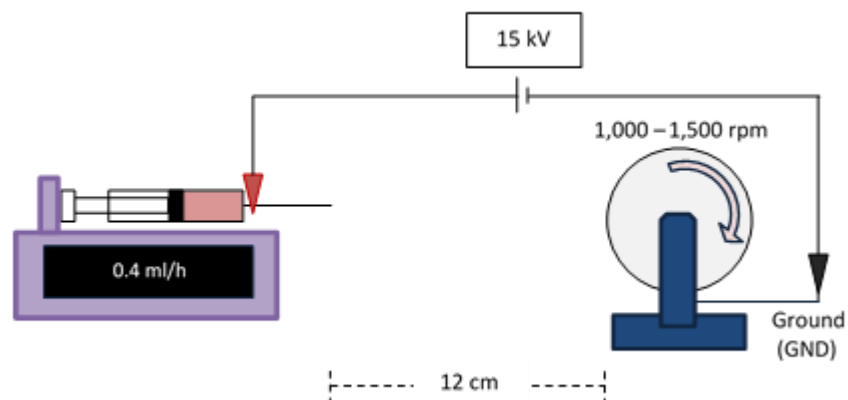


Figure 3.1 Schematic of horizontal electrospinning setup composing of a syringe pump, silk solution in a syringe with 19 G needle, a rotating mandrel collector, and a high voltage supply between needle and collector.

3.1.3.2. Vertical axis electrospinning

The vertical electrospinning was a custom-made lab-scale system with an environmental control chamber (humidity and temperature). The syringe was placed on a dual-syringe infusion pump (Cole-Parmer®) operating with similar feed rates as the horizontal axis system (0.3 – 1.0 ml/h). In particular, the syringe and needle were spanned by a polytetrafluoroethylene (PTFE) tube with an inner diameter of 0.8 mm (Sigma) and syringe luers. The tip needle was also placed 12 cm upward from the edge of the collector. The rotating mandrel must be wrapped by a piece of greaseproof paper or aluminium foil (5 x 38 cm²) akin to that used in horizontal electrospinning. The maximum speed of the rotating mandrel in this system was ~800 rpm (~5.03 m/s linear velocity). The setup of the vertical electrospinning apparatus is shown in Figure 3.2.

High voltage between 15 – 35 kV was applied to the system by using two DC power supplies: positive and negative voltage supplies. A positive voltage was applied to the emitter needle, while a negative voltage was applied to the collector. Here, the voltage of 35 kV was

operated by applying +30 and -5 kV. Other voltages were used by varying positive potentials and the constant negative potential of -3 kV (e.g. +27 and -3 kV for the voltage of 30 kV).

Moreover, almost all electrospinning apparatus except high voltage power supplies were placed in the environmental control chamber (Source BioScience®). A temperature of 25° C was controlled constantly throughout the electrospinning period with relative humidity (R.H.) of either 35% or 50% maintained.

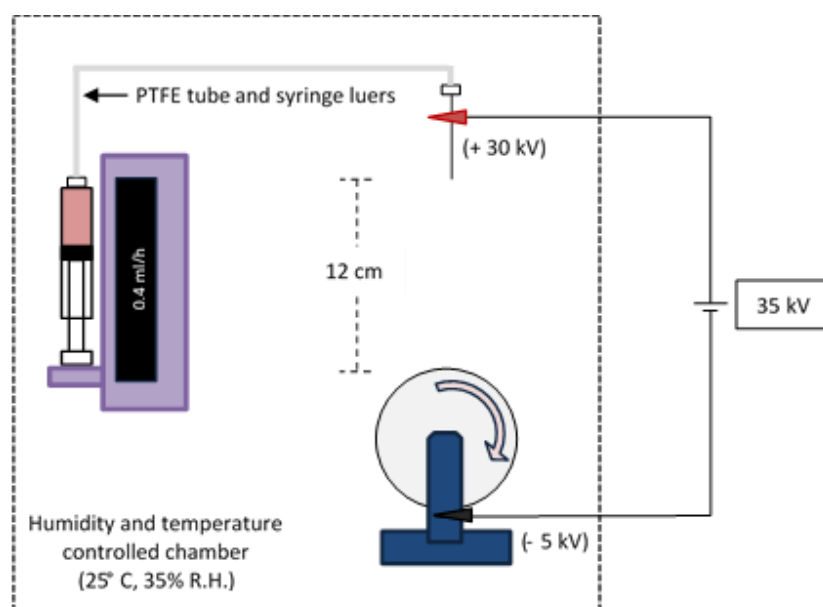


Figure 3.2 Schematic of vertical electrospinning setup in an environmental control system composing of a syringe pump, silk solution in a syringe connecting to PTFE tube, luers, and needle, a rotating mandrel collector, and outside DC power supplies charging to needle (+) and collector (-).

3.1.4. Post-treatment of electrospun mats and FTIR analysis

Electrospun mats were immersed in various concentrations (70 – 100% v/v) of ethanol (EtOH) and methanol (MeOH) in water for 20 min. These mats were then washed with distilled water and dried overnight in a fume cupboard. The secondary protein structure of electrospun SF mats was analysed by using an attenuated total reflectance Fourier transform infrared (ATR-FTIR) spectroscopy equipment (Nicolet 5700 FTIR spectrometer, Thermo Fisher Scientific). The FTIR

spectra were acquired over the wavenumber range $4000 - 400 \text{ cm}^{-1}$ with 32 scans in absorbance mode. Spectra were collected using OMNIC software (OMNIC™, Thermo Fisher Scientific). The amide I band of $1700 - 1600 \text{ cm}^{-1}$, representing the C=O stretching vibration and minor contributions from the out-of-phase CN stretching vibration, was mainly assessed to determine the patterns of hydrogen bonding of the protein backbone [230, 231]. These spectra were then deconvoluted using Origin software (OriginLab, USA) to analyse the components of secondary protein structure [232, 233].

According to a previous study of conformational transitions of silk peptides [234], β -sheet was examined in the wavenumber of $1629 - 1621 \text{ cm}^{-1}$ and $1679 - 1671 \text{ cm}^{-1}$. The random coil was considered in the range of $1649 - 1641 \text{ cm}^{-1}$, while turns and bends were explored in the spectra of $1671 - 1658 \text{ cm}^{-1}$ and $1696 - 1681 \text{ cm}^{-1}$. Afterwards, the relative area of each deconvoluted FTIR spectra was converted to the percentage of each secondary protein structure.

3.1.5. Scanning electron microscopy (SEM) analysis

Electrospun silk fibroin mats were attached on SEM specimen stubs using conductive double-sided adhesive carbon taps. They were then coated with a thickness of $\sim 5 \text{ nm}$ gold/palladium (Au/Pd) using an automatic gold sputter coater (Quorum Q150TES). The surface morphology of the electrospun mats was observed using Zeiss and TESCAN microscopes (Zeiss Evo 50, TESCAN Mira 3 and TESCAN Vega 3), operating in secondary electron (SE) imaging mode, depth or resolution modes, and magnifications of 1, 5, 10, and 20 kX. Additionally, the samples of aligned fibres were rotated to the 90° position following the Cartesian coordinate system prior to imaging. The images were saved in the format of .tiff files for measuring the diameter of fibres and degree of alignment in ImageJ software (ImageJ 1.52a, USA) subsequently.

Average fibre diameters and standard deviations were calculated, where the number of isolated fibres (n), number of electrospun mats, and number of independent electrospinning experiments will be described in the figure caption.

3.1.6. Fibre alignment with 2D FFT analysis

The alignment of fibres was determined using a two-dimensional fast Fourier transform (2D FFT) approach following the protocol of Ayres C.E., *et al.*, 2008 [229]. The oval profile plugin is required for this ImageJ analysis. The alignment data were counted in all angles (0 – 359°) of a unit circle with the conventional position (0° at 3 o'clock, 90° at 12 o'clock, 180° at 9 o'clock, and 270° at 6 o'clock). Alignment results were later converted and reported in the range 0° – 180°.

The following procedure was applied – first, the SEM image is opened in ImageJ, converted to 8-bit, and rotated such that the fibre alignment is parallel to the ground. The FFT process is then applied to convert the raw image to an FFT image and enhance the contrast of the FFT image, with a normalise mode of saturated pixels at 0.3%. Next, the oval tool is used to draw a circle in the middle of the FFT image. The circle covers all the brightest spots of the FFT image. The analysis of the FFT image is then made using the oval profile plugin with the radial sums mode (360 number of points), resulting in the greyscale value of different angles (0° – 359°).

The greyscale values of all angles were normalised by dividing with their minimum value and then subtracted by 1. The normalised data (the 2D FFT values) are presented in the results of this chapter. In this study, the 2D FFT value are counted and shown in the direction of a half-circle (0° – 180°). Then, the value of 181° – 359° was added to 1° – 179° sequentially (e.g. add the value of 181° to 1°, 182° to 2°, 183° to 3°, etc.) prior to finalising.

3.2. Results

3.2.1. Qualitative analysis of degummed silk fibroin

The length of natural silk cocoons was ~4 cm. The cocoons were cut into small pieces of ~2 cm², and the total weight of 5 g cut silk cocoons were degummed each time. The average percentage of weight loss (% wt.) was $27 \pm 2\%$ ($n = 12$), where n is the number of independent experiments. Sericin removal was confirmed by SEM imaging, as shown in Figure 3.3. The diameter of degummed silk fibroin fibres was larger than 10 μm .

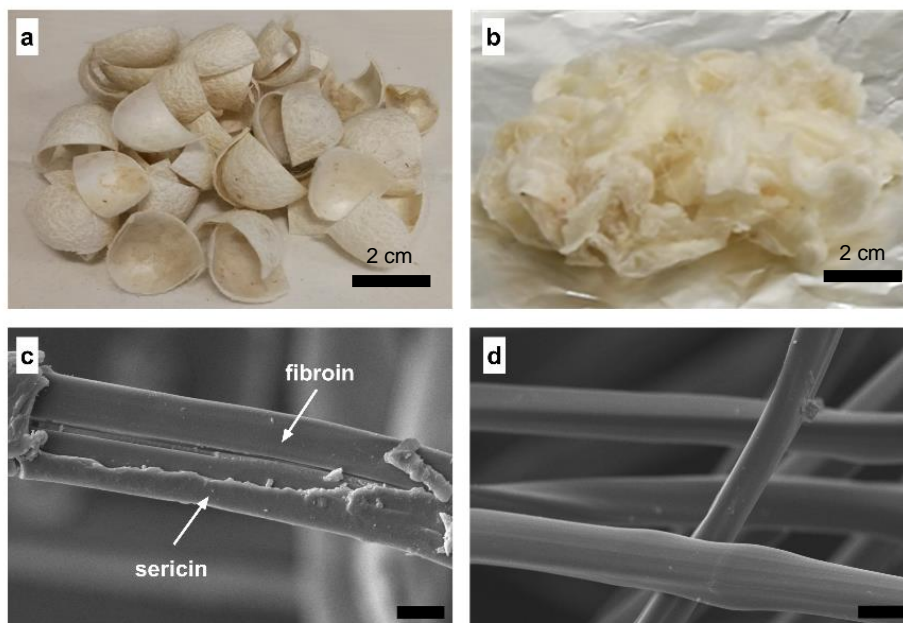


Figure 3.3 Morphologies of silk worm cocoons and degummed silk fibroin: (a) 5 g of *B. mori* silk cocoons cut into pieces $\sim 2 \times 2 \text{ cm}^2$ before degumming, (b) degummed silk fibroin (cotton-like fluffy fibres prepared from 5 g of silk cocoons) of size $\sim 10 \times 10 \text{ cm}^2$ after spreading, (c) SEM image of silk cocoons composing of fibroin and sericin, and (d) SEM image of degummed silk fibroin with the scale bar of $10 \mu\text{m}$.

3.2.2. Optimal conditions for preparation of electrospinning solution

In this experiment, the concentrations of SF was 6% wt/v, and the ratios of FA/CaCl₂ were varied at 98:2, 95:5, and 90:10, as shown in Table 3.1. The effective electrospinning solution was briefly observed by the homogeneity of the solution. Additionally, these prepared solutions were then electrospun using the horizontal electrospinning system on the static collector of aluminium foil. The droplets of solution on electrospun mats were then observed as well.

Firstly, 6% wt/v SF in FA/CaCl₂ was partly dissolved at room temperature, as shown in Figure 3.4. Pellets of undissolved SF were seen easily unless the solutions were prepared for 7 days, particularly in the condition of FA/CaCl₂ with the ratio of 98:2. Thus, solutions were filtered before electrospinning.

After filtration, 6% wt/v SF in FA/CaCl₂ with the ratio of 98:2, 95:5, and 90:10 were initially electrospun in the horizontal system on a static collector plate. By varying voltage supplies (from 12 – 20 kV), the tiny electrospinning jet at the tip of the needle was observed when operating with 15 kV. Examples of electrospun SF mats from these solutions, operated with the feed rate of 1 ml/h, the distance of 12 cm, the voltage of 15 kV, and the electrospinning period of 2 h, are shown in Figure 3.4 (a-d). A few tiny spots were seen in the condition of 98:2, while many droplets were observed in the condition of 98:5. Unfortunately, the electrospun SF mats for the 98:5 and 98:10 ratio conditions disappeared (lost their fibrous morphology/re-dissolved) after a day preserving at room temperature without humidity control.

However, the degummed SF dissolved well in FA/CaCl₂ when incubated at 45° C overnight. It took a shorter time to dissolve at 45° C compared to room temperature. This incubating method was also able to fully dissolve a high percentage of SF up to 10% wt/v SF in FA/CaCl₂ with the low ratio of CaCl₂ (98:2), as shown in Figure 3.5. In addition, SF must be well stirred in FA/CaCl₂, until the solution turned light yellow or amber. The eventual electrospinning SF solution was pink in appearance after incubation. Thus, 10% wt/v SF in FA/CaCl₂ (98:2) was carried forward for the next experiments due to its high viscosity compared, more suited to effective electrospinning in comparison to the 6% wt/v SF solution [154].

Table 3.1 Optimisation of electrospinning solution preparation (electrospinning operation with the parameters of 1 ml/h feed rate, 12 cm distance, 15 kV voltage for 2 h on a static collector).

SF concentrations	FA:CaCl ₂ ratios	Incubation periods	Homogeneity of solutions	Electrospun fibre mats
6% wt/v	98:2	7 days (room temperature)	Partly dissolve (~60%)	Success
6% wt/v	95:5	7 days (room temperature)	Mostly dissolve (~90%)	Failure (re-dissolved)
6% wt/v	90:10	7 days (room temperature)	Mostly dissolve (~90%)	Failure (re-dissolved)
6% wt/v	98:2	Overnight (45° C)	Fully dissolve (100%)	Success
10% wt/v	98:2	Overnight (45° C)	Fully dissolve (100%)	Success

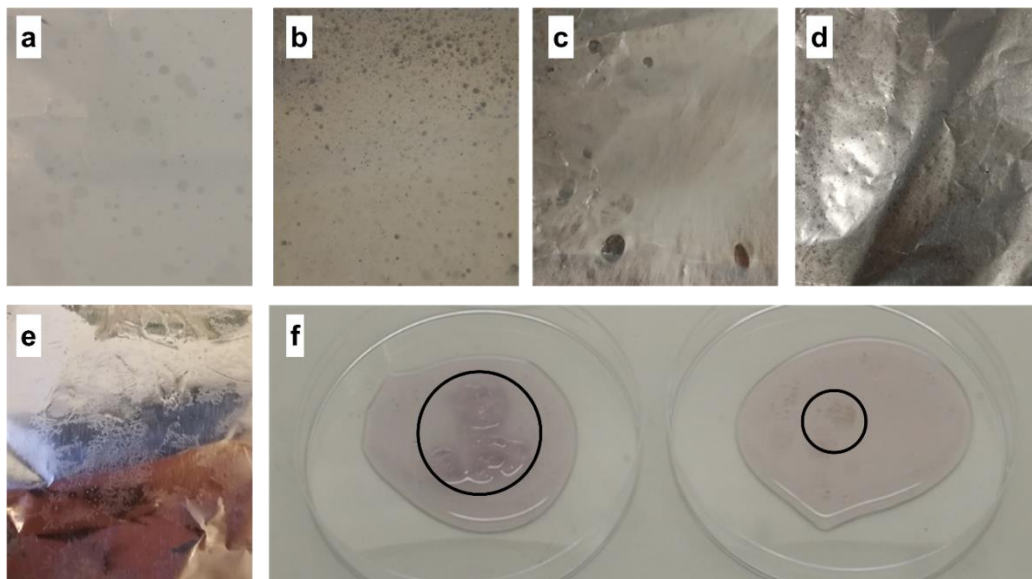


Figure 3.4 Electrospun SF mats (white colour) on aluminium foils collector (silver colour), prepared from electrospinning solutions of 6% wt/v SF in various ratios of FA/CaCl₂ (ml:g): (a) 98:2, (b) 95:5, and (c) 90:10, and those mats after leaving at room temperature for one day: (d) 95:5 and (e) 90:10, and (f) the electrospinning solution of 6% wt/v SF in FA/CaCl₂ (left) 98:2 and (right) 95:5 after leaving at room temperature for 7 days, the undissolved SF is shown in the circles, and the figures (a – e), the size of aluminium foils are ~5 x 5 cm².

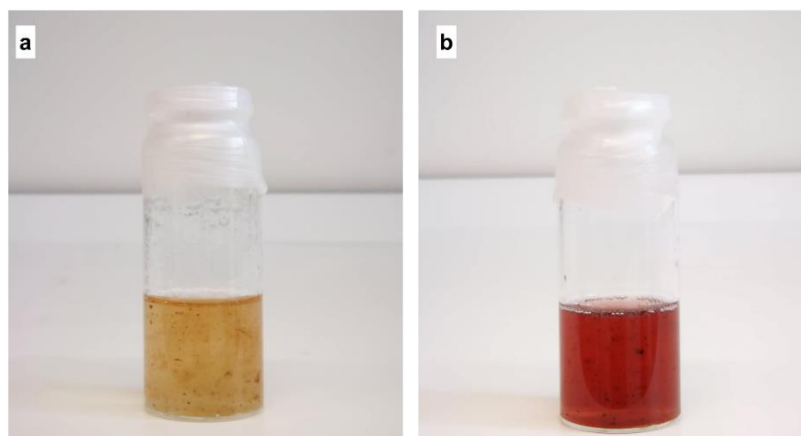


Figure 3.5 Image of the electrospinning solution of 10% wt/v SF in FA/CaCl₂ with the ratio 98:2 at different time points: (a) after stirring at room temperature for 5 min and (b) after incubating at 45° C overnight (approximately 10 – 12 h).

3.2.3. Effects of different electrospinning parameters on electrospun SF mats

According to the initial result of the dissolution of SF in FA/CaCl₂, 10% wt/v SF in FA/CaCl₂ with the ratio of 98:2 was chosen for electrospinning with different parameters such as feed rate of solution, rotating speed of collector, *etc.* The optimal electrospinning parameters were decided on the quality of electrospun mats and morphology of electrospinning fibres.

3.2.3.1. Horizontal axis electrospinning

According to the results from 3.2.2 above, the electrospinning condition of 12 cm distance and 15 kV voltage suitable for effective electrospinning. The feed rate of the solution was then varied at 0.4, 0.5, and 1 ml/h, as shown in Table 3.2, in order to improve the yield and enable faster spinning of the structures for downstream physical characterisation and *in vitro* testing.

The effective electrospinning was operated with the feed rate of 0.4 ml/h, the distance of 12 cm, and the voltage of 15 kV. Other feed rates were possible to electrospin, but there were many solution droplets on the floor of the hood and on the electrospun samples. Although formation of a Taylor cone at the needle could not be seen clearly, the solution was evidently pulled and moved following the electric field towards the rotating mandrel collector. Examples of electrospun SF mats and their fibre morphologies are shown in Figure 3.6. Sometimes, there were droplets of solution on the floor of the hood and collector during electrospinning, but these droplets did not significantly interfere with the morphology of electrospun mats. SEM images evidenced that SF fibres were smoothly and continuously electrospun without beads or other defects. The high-speed rotating mandrel between 1,000 and 1,500 rpm had a similar effect on fibre morphology. Unfortunately, the electrospun SF mats were prone to tightly stick to the aluminium foils and were difficult to remove. Therefore, a method was developed whereby greaseproof paper was used instead of aluminium foil. SF mats could then be peeled off easily after soaking in 80% EtOH for 20 min (Figure 3.6 (b)).

Table 3.2 Optimisation of electrospinning parameters of the horizontal system (electrospinning operation with parameters of 12 cm distance and 15 kV voltage).

Feed rate (ml/h)	Collectors	Electrospun fibre mats
0.4	Statics	Success (few solution droplets on the mat)
0.5	Statics	Failure (many solution droplets on the mat)
1	Statics	Failure (many solution droplets on the mat)
0.4	Rotating mandrel (~1,000 rpm)	Success (few solution droplets on the mat) with the aligned fibre morphology
0.4	Rotating mandrel (~1,500 rpm)	Success (few solution droplets on the mat) with the aligned fibre morphology

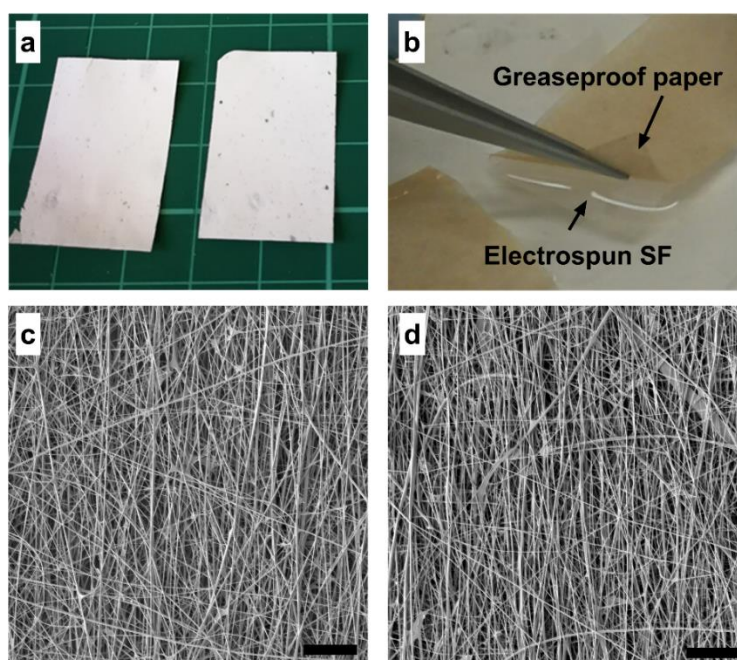


Figure 3.6 Horizontal electrospinning of 10% wt/v SF in FA/CaCl₂ (98:2) operated with 0.4 ml/h feed rate, 12 cm distance, and 15 kV voltage supply for 4 h: (a) electrospun SF mats on greaseproof paper cut in to pieces ~2 x 3 cm², (b) post-treatment process with 80% EtOH, and representative SEM images from three independent experiments of electrospun SF fibres collected with the rotating speed of (c) 1,000 rpm and (d) 1,500 rpm, the scale bar represented is 10 µm

3.2.3.2. Vertical axis electrospinning

Parameters mentioned in horizontal electrospinning (0.4 ml/h feed rate, 12 cm distance, and 15 kV voltage) were not suitable to electrospin in the vertical axis due to the influence of gravity, resulting in the presence of solution spots on the electrospun mats. In fact, either reducing feed rate or increasing voltage should be varied again in order to obtain more homogeneous electrospun mats. It would certainly take a longer period to electrospin using a reduced feed rate, thus the voltage supply was prioritised in this experimental study. The optimisation of electrospinning parameters of the vertical system is shown in Table 3.3.

There were many spots of solution on aluminium foil collectors when electrospinning with 0.3 ml/h feed rate and 15, 18, and 20 kV voltage supplies, as shown in Figure 3.7 (a – c). However, electrospun mats were very smooth without solution spots when electrospinning with 0.05 ml/h feed rate and 15 and 18 kV voltage supplies, as shown in Figure 3.7 (d – e). At the feed rate of 0.4 ml/h, the electrospun mats had small numbers of solution spots when electrospinning with a 25 kV voltage supply, as shown in Figure 3.7 (f). On the other hand, it was smooth when operated with 30 and 35 kV voltage supplies, as shown in Figure 3.7 (g – h).

The effects of different % R.H. and temperature during electrospinning on the quality of fibres were observed by SEM, as shown in Figure 3.8. There was no significant difference in the fibre diameter without defects when electrospinning with different voltage supplies of 25, 30, and 35 kV in both 35% and 50% R.H.

Table 3.3 Optimisation of electrospinning parameters of the vertical system (electrospinning operation with parameters of 12 cm distance and 15 kV voltage).

Feed rate (ml/h)	Voltage (kV)	Humidity (% R.H)	Collectors	Electrospun fibre mats
0.05	15	n/a	Statics	Success (few solution droplets on the mat)
0.05	18	n/a	Statics	Success (few solution droplets on the mat)
0.3	15	n/a	Statics	Failure (many solution droplets on the mat)
0.3	18	n/a	Statics	Failure (many solution droplets on the mat)
0.3	20	n/a	Statics	Failure (many solution droplets on the mat)
0.4	25	n/a	Statics	Failure (many solution droplets on the mat)
0.4	30	n/a	Statics	Success (few solution droplets on the mat)
0.4	35	n/a	Statics	Success (few solution droplets on the mat)
0.4	25	35%	Rotating mandrel (~500 rpm)	Failure (many solution droplets on the mat) with the random fibre morphology
0.4	30	35%	Rotating mandrel (~500 rpm)	Success (few solution droplets on the mat) with the random fibre morphology
0.4	35	35%	Rotating mandrel (~500 rpm)	Success (few solution droplets on the mat) with the random fibre morphology
0.4	25	50%	Rotating mandrel (~500 rpm)	Failure (many solution droplets on the mat) with the random fibre morphology
0.4	30	50%	Rotating mandrel (~500 rpm)	Success (few solution droplets on the mat) with the random fibre morphology
0.4	35	50%	Rotating mandrel (~500 rpm)	Success (few solution droplets on the mat) with the random fibre morphology

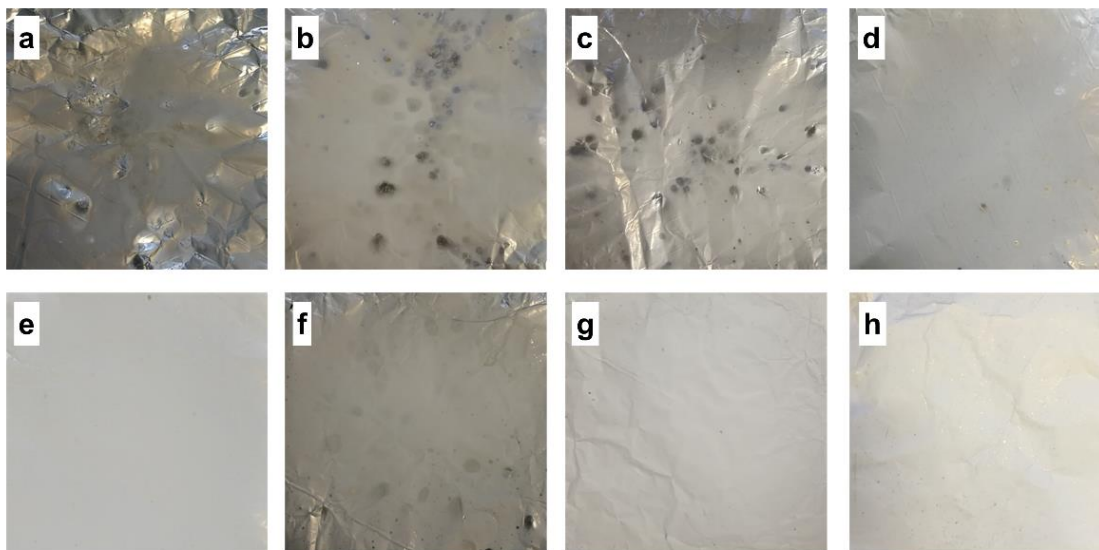


Figure 3.7 Electrospun SF mats (white colour) on aluminium foil (silver colour) fabricated by vertical electrospinning of 10% SF in FA/CaCl₂ (98:2) in the different feed rates (ml/h) and voltage supply (kV) with the constant distance of 12 cm at room temperature: (a) 0.3 ml/h, 15 kV, (b) 0.3 ml/h, 18 kV, (c) 0.3 ml/h, 20 kV, (d) 0.05 ml/h, 15 kV, (e) 0.05 ml/h, 18 kV, (f) 0.4 ml/h, 25 kV, (g) 0.4 ml/h, 30 kV, and (h) 0.4 ml/h, 35 kV, sizes of aluminium foils are ~5 x 5 cm².

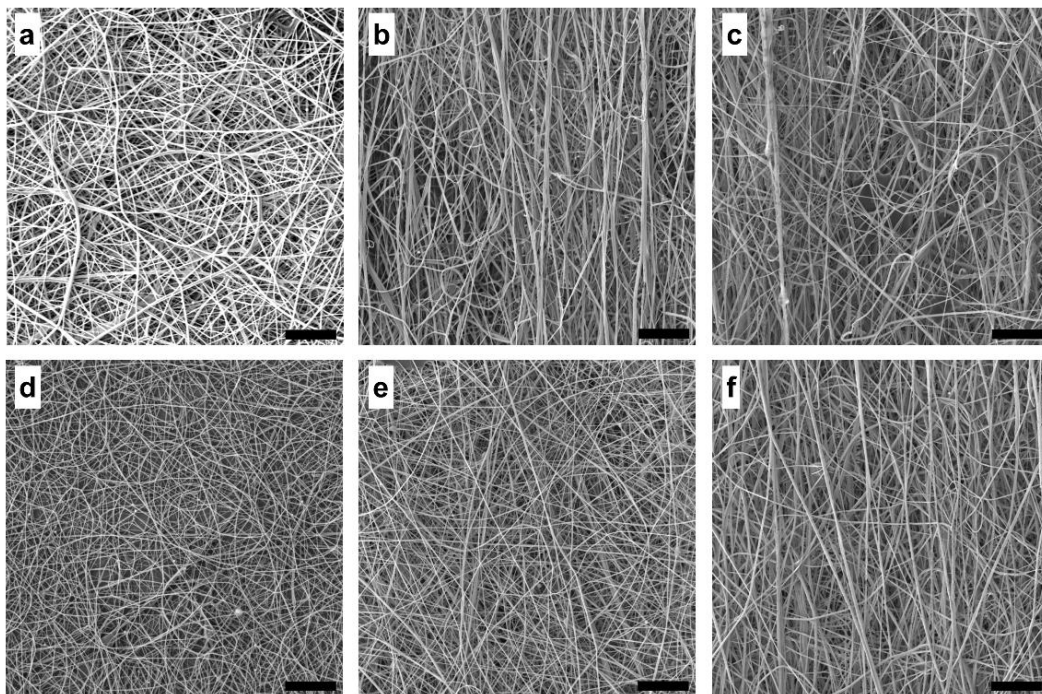


Figure 3.8 Representative SEM images from three independent experiments of vertical electrospinning of 10% SF in FA/CaCl₂ (98:2) in the different voltage supplies and % R.H. with the constant feed rate of 0.4 ml/h and distance of 12 cm: (a) 25 kV, 35% R.H., (b) 30 kV, 35% R.H., (c) 35 kV, 35% R.H., (d) 25 kV, 50% R.H., (e) 30 kV, 50% R.H., and (f) 35 kV, 50% R.H., the scale bars represent 10 µm.

3.2.4. Diameter of fibre and degree of alignment

The average diameter of fibres was 180 ± 50 ($n = 100$) and 190 ± 60 ($n = 100$) nm when using horizontal electrospinning with a high rotating speed of 1,000 and 1,500 rpm respectively, as shown in Figure 3.9 (a). Where n represents the number of isolated fibres collected from three samples (three independent electrospinning experiments). They were similar to vertical electrospinning with low rotating speed (~ 800 rpm); the average diameter of fibres was 160 ± 30 ($n = 123$) and 190 ± 60 nm ($n = 115$) at the feed rates of 0.3 and 0.4 ml/h respectively, as shown in Figure 3.9 (b). These results indicated that electrospinning parameters such as voltage, apparatus orientation, feed rate, humidity, and collector speed have no significant effects on the

diameter of fibres. However, the average fibre diameter was slightly increased to 220 ± 40 ($n = 66$) nm after post-treatment of 80% EtOH for 20 min.

The alignment of fibres was markedly high when using horizontal electrospinning with a high-speed collector (1,000 – 1,500 rpm), as confirmed by SEM and 2D FFT alignment results. As shown in Figure 3.10 (c and f), two highly peaks of greyscale value were observed at 90° and 270° representing the high alignment of fibres in these directions. In contrast, vertical electrospinning with a low-speed collector less than 800 rpm showed a similar greyscale value in all angles representing random alignment.

In this study, the vertical electrospinning (0.4 ml/h, 12 cm, 35 kV, less than 800 rpm, and 35% R.H.) and horizontal electrospinning (0.4 ml/h, 12 cm, 15 kV, and 1,500 rpm) represented the bottom layer of random fibres and the top layer of uniformly aligned fibres respectively as shown in Figure 3.11. The total thickness of electrospun SF mats was approximately 100 μm after electrospinning bottom layer for 8 – 10 h followed by top layer for 4 – 5 h.

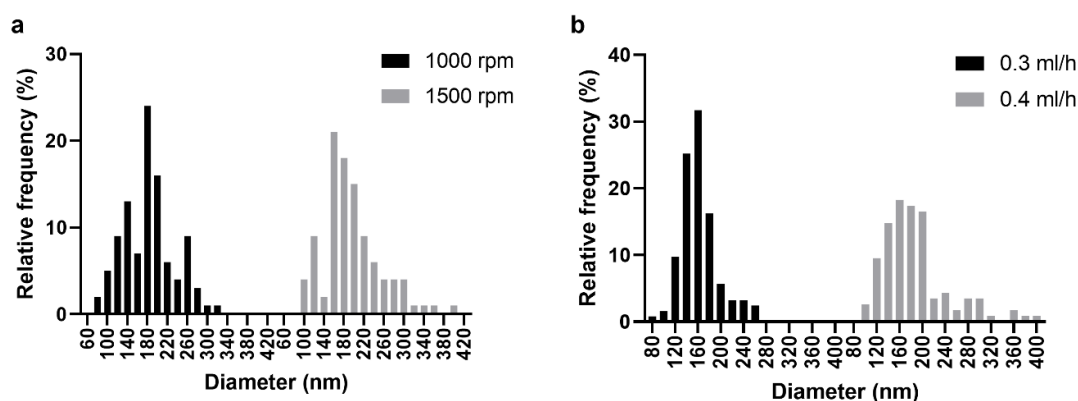


Figure 3.9 Distribution of fibre diameters of electrospun SF mats: (a) horizontal electrospinning with parameters of 0.4 ml/h feed rate, 12 cm distance, 15 kV voltage supply, 1000 rpm ($n = 100$) and 1500 rpm ($n = 100$) collector speeds and (b) vertical electrospinning with parameters of 0.3 ml/h ($n = 123$) and 0.4 ml/h ($n = 115$) feed rate, 12 cm distance, 35 kV voltage supply, 35% R.H., ~800 rpm collector speed, where n is the number of fibres, representing three samples fabricated from three independent electrospinning experiments.

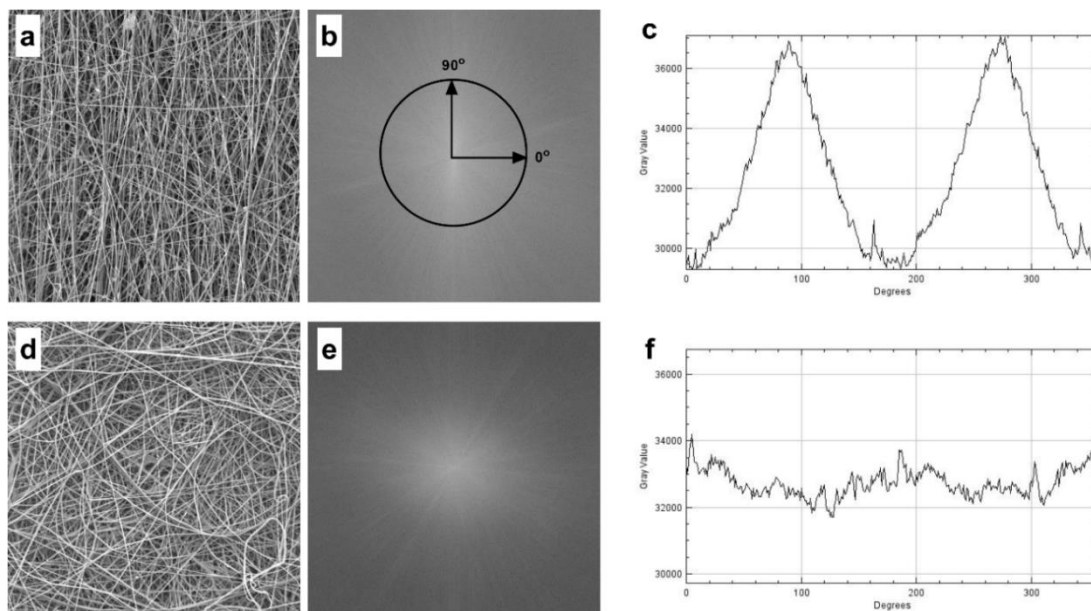


Figure 3.10 Example of 2D FFT alignment analysis: 8-bit SEM images of electrospun SF (a) aligned fibres and (d) random fibres, FFT images of (b) aligned fibres and (e) random fibres, and oval profiles analysis with radial sums mode and 360 number of points of FFT images of (c) aligned fibres and (f) random fibres.

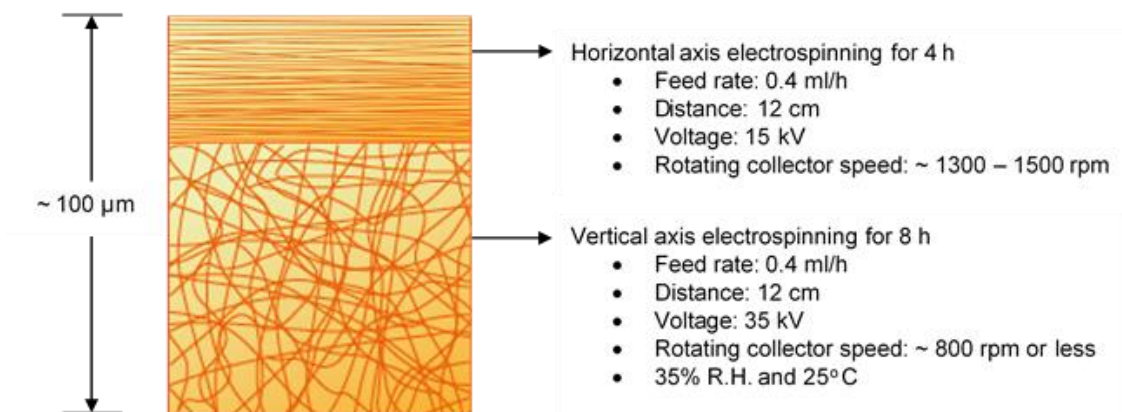


Figure 3.11 Schematic of double layer electrospun SF mat and the electrospinning parameters of each layer.

By using these electrospinning parameters to electrospin double layered fibre mats, verified with three independent experiments from three reproductions of the electrospinning solution, 10% wt/v in FA/CaCl₂ (98:2), similar results of fibre diameter and alignment in each layer

were obtained, as shown in Figure 3.12. The average fibre diameters of the top and bottom layers were 190 ± 50 ($n = 200$) and 180 ± 60 ($n = 405$) nm respectively, where n was the number of isolated fibres (Figure 3.12 (a)). The 2D FFT alignment results, normalised from greyscale values, explained that the top layer contained the uniform alignment of fibres compared to the bottom layer, which could be confirmed by the peak of 90° (Figure 3.12 (b)). The 2D FFT peak of the bottom layer was 0.2 units at the position of 90° and similar to other positions. However, the peak of the top layer was approximately 10 folds higher than that of the bottom layer; it was 2.3 units at the position of 90° and significantly higher than other positions.

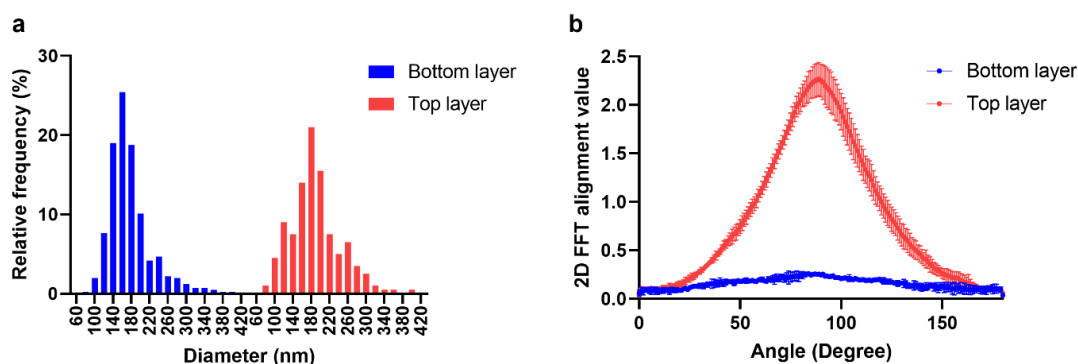


Figure 3.12 Fibre diameter and alignment of electrospun SF mat: (a) distribution of fibre diameters: the bottom layer ($n = 405$) and the top layer ($n = 200$), where n is the number of fibres and (b) average 2D FFT alignment value in each angle ($0^\circ - 180^\circ$) in both layers, bottom is random fibres and top is aligned fibres ($n = 3$), where n is the number of electrospun samples fabricated from independent experiments with independent solutions.

3.2.5. β -sheet formation in electrospun SF mats

ATR-FTIR results for electrospun SF mats with and without post-treatments are shown in Figure 3.13. The amide I peak of the electrospun SF was at 1650 cm^{-1} and shifted to 1625 cm^{-1} or 1621 cm^{-1} after post-treatment either with EtOH or MeOH. The deconvolution results also show that both EtOH and MeOH treatment certainly increased β -sheet formation and decreased random coil structures in electrospun SF mats as shown in Figure 3.14. Compared to the untreated sample, the percentage of β -sheet was increased by 8 – 10% reaching up to 63 – 65%, the random coil

was decreased by 7 – 9% reaching 13 – 15%, and the β turns and bends was quite constant at 23% (around 21 – 24%). However, only treatment with 75% EtOH slightly increased β -sheet up to 59% and also β turns up to 26%.

Although the amide I peak was shifted to 1621 cm^{-1} after soaking electrospun SF mats in water as well as in EtOH and MeOH treatment, the deconvolution showed the opposite result. With water treatment, both β -sheet and random coil were decreased down to 48% and 19% respectively. Meanwhile, β turns and bend was 10% increased up to 33%. Moreover, electrospinning SF fibres were mostly re-dissolved when immersing in water confirmed by SEM, as shown in Figure 3.15 (c). The morphology of electrospinning SF fibres of untreated and 80% EtOH treated samples were quite similar even though their diameters were slightly different. Additionally, the fibres of 80% EtOH treated sample were unable to re-dissolve again in water.

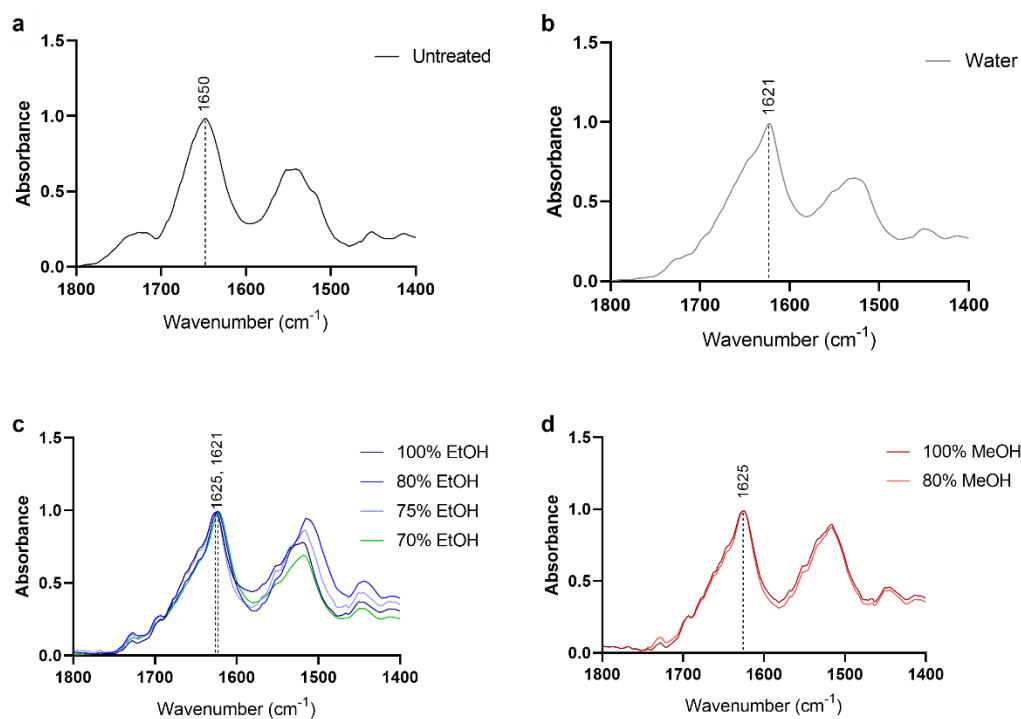


Figure 3.13 ATR-FITR spectra of electrospun SF mats after post-treatment with: (a) untreated, (b) water (c) various % EtOH in water, and (d) various % MeOH in water.

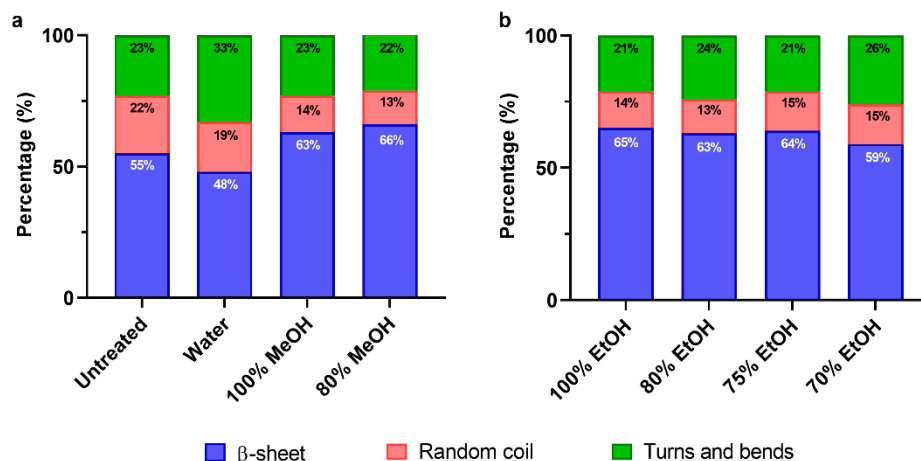


Figure 3.14 Relative percentage of secondary protein structures composing of β -sheet, random coil, and turns and bend after post-treatment in different solutions: (a) untreated, water, and MeOH, and (b) EtOH.

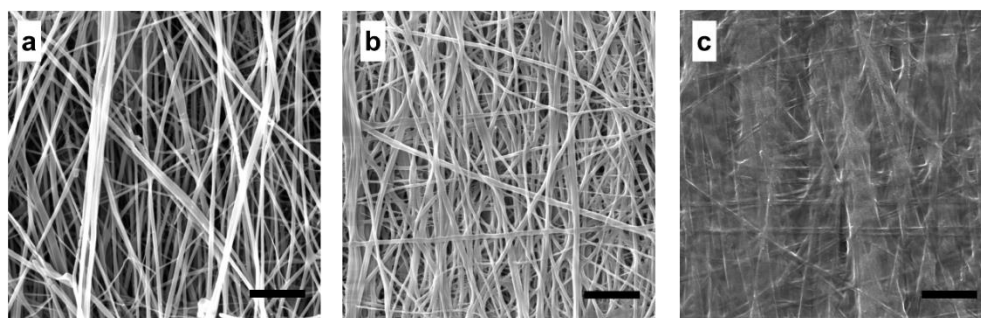


Figure 3.15 Representative SEM images of electrospun SF mats from three independent experiments fabricated using 10% w/v SF in FA/CaCl₂ (98:2) after post-treatment with different solutions: (a) untreated, (b) 80% EtOH treated, and (c) water treated fibres.

According to Figure 3.15, the water treated sample was prone to dissolution and becoming a film-like structure, this is due to a lack of β -sheet structures, discussed further below. This treatment was therefore not taken forward as it is unsuitable for making fibrous double-layered structures. Herein, the thickness of $\sim 100\ \mu\text{m}$ was determined for the double layer mats of untreated and 80% EtOH samples. It also highlights that untreated electrospun mats should not get into contact with water.

3.3. Discussion

3.3.1. Optimal parameters for preparing electrospinning SF solution

3.3.1.1. Degumming and other preparations

Degumming is the first important step for preparing the electrospinning solution of SF. The SF should be fully extracted from silk cocoons without sericin residues. Not only toxicity to cells but also sericin obstructs the dissolution of SF in solvents. According to the well-known protocol (Rockwood D.N., *et al.*, 2011), the boiling process affects to quality and quantity of SF [20]. To increase reproducibility, they mentioned that the boiling time should be restricted to 30 min every time. However, there was no mention of the exact temperature for boiling. The temperature of water was then controlled in this study.

The heating temperature was ideally set at 80° C instead of fully boiled at 100° C. However, it was still unstable for 30 min, it always varied between ~75° – 80° C each time. The percentage of weight loss and SEM results confirm that boiling at ~75° – 80° C for 30 min is acceptable for purifying SF. Generally, 25 – 30% of the total weight of silk cocoons is sericin [20, 136]. Therefore, the weight loss of $27 \pm 2\%$ is suitable to get rid of sericin without damaging SF fibres. If the percentage of weight loss is over 29.4%, the SF will be fragile with extensive fibroin fibrillation, which has a low tensile property [235].

Prior to electrospinning, the degummed SF actually needs to go through the other four sequential steps: dissolution, dialysis, re-concentration, and preparation of regenerated SF by either lyophilisation or film casting [20, 151, 236]. Compared to the degummed SF, the regenerated SF has smaller SF molecules, which is more readily prepared for electrospinning [151]. However, these sequential steps are time-consuming, especially the dialysis step(s).

Two well-established protocols recommend the use of aqueous solvents: lithium bromide (LiBr) solution [20] and the solution of $\text{CaCl}_2/\text{EtOH}/\text{water}$ [237] for dissolving the degummed SF. They are efficient methods to break the large SF molecules into tiny molecules *via* transforming the β -sheet to other conformations within a few hours. The dissolution of degummed SF is then dialysed in DI water.

Dialysis is the longest process to prepare SF. Gelation of the solution may occasionally occur due to protein concentration, temperature, pH, and residues of salt ions in the solution [238, 239]. This unexpected gel formation can occur from time to time even when all factors (e.g. quality of water, the pore size of dialysis sack, temperature, numbers of water changing, total dialysis period, etc.) are controlled. The dialysis process commonly takes at least 48 h (2 days). In order to avoid the complication of gelation and reduce the preparation time, the electrospinning SF solution should be prepared via a dialysis free protocol.

3.3.1.2. Solvent choice for electrospinning SF solution

Commonly, electrospinning SF solution can be prepared in both aqueous solvents [20, 146-148] and non-aqueous solvents [149-154, 236, 240]. In the case of an aqueous-based solution, it still requires preparation by dialysis. Some polymers such as polyethylene glycol [20, 146] may need to be added into the solution before electrospinning, and can be washed out eventually in a subsequent step.

Many studies revealed that either lyophilised or film cast SF could be prepared first in the preparation of electrospinning solutions using organic solvents such as FA [150-154], hexafluoroisopropanol (HFIP) [120, 149], dichloromethane (DCM) [240]. With a dialysis free protocol, FA and FA/CaCl₂ can also partly dissolve the degummed SF within 3 h, which is enough to cast a regenerated SF film. The film can serve as a basis for subsequent further dissolution and electrospinning [151]. However, the electrospinning of SF solution can successfully be prepared without pre-casting regenerated SF film. Providing degummed SF in FA/CaCl₂ is heated up with the appropriate temperature and time, the SF will be completely dissolved and be suitable for electrospinning. According to the results of the present study, incubating at 45° C for overnight (~10 – 12 h) is recommended. Thus, this dialysis free protocol reduces a lot of time in preparing electrospinning solutions. Although the degummed SF takes longer dissolving time than SF film and lyophilised SF prepared by dialysis, the total time consumed is considerably shorter.

The high amount of CaCl₂ in FA (FA/CaCl₂ ratio 95:5 and 90:10) can entirely dissolve degummed SF within a week at room temperature, while the low amount of CaCl₂ in FA (FA/CaCl₂

ratio of 98:2) possibly take longer for dissolving. Therefore, CaCl_2 may function as a catalyst to increase the dissolving rate of SF in FA. Liu Q., *et al.*, 2018, reported that increasing CaCl_2 concentration could reduce β -sheet contents *via* disrupting hydrogen bonds between SF chains [241].

Unfortunately, electrospinning solutions of 6% wt/v SF in FA/ CaCl_2 with both the ratio of 95:5 and 90:10 were unsuccessful in this study. Their electrospun mats were re-dissolved and disappeared when left in the normal atmosphere conditions of the lab. This finding is contrary to the apparent reported successful electrospinning in a report by Liu Z., *et al.*, 2015 [150].

A reason for fibre re-dissolution is the drastically high humidity in the air. If there are CaCl_2 residuals in/on the electrospinning SF network, CaCl_2 , also known as an excellent dehumidifier, can adsorb and retain significant moisture from the air. Then excessive water molecules in the bulk electrospun mats can turn from solid fibres to viscous liquid SF [242, 243]. Furthermore, untreated electrospinning SF contains a low β -sheet content and a high number of random coil amorphous molecules, as shown in the result of this study (Figure 3.14). This suggests that humidity may affect the glass transition temperature of untreated electrospun SF mat; this is recommended for further investigation but falls outside of the scope of the study presented in this thesis.

There are several suggestions to avoid the re-dissolution of electrospinning SF in FA/ CaCl_2 with a high amount of CaCl_2 , such as increasing the percentage of SF in solution, keeping electrospun SF in a desiccator, and post-treatment with EtOH. Thus, SF in FA/ CaCl_2 with a low amount of CaCl_2 (ratio of 98:2) was preferred due to the reproducibility and quality of the electrospun mats.

3.3.1.3. Concentration of SF

This study found that 10% SF is suitable for the preparation of electrospinning solution in FA/ CaCl_2 (ratio of 98:2). The fibre diameter was evidenced to increase following increase in the concentration of SF in FA. Lower concentrations of SF are reportedly challenging to electrospin in to fibres [152].

Tiny spots of solution were apparently dropped on the electrospun mat, indicating that either viscosity of the solution or electrical parameters (e.g. voltage and distance) are inappropriate. Electrospun mats of 10% SF have a lower number of solution spot artefacts compared to those of 6% SF. This may be because 10% SF has a high viscosity, which is more suitable for electrospinning. Min B.M., *et al.*, 2004 confirmed that the viscosity of SF solution depended on the concentration of SF in FA [154].

In general, there are four factors that affect the rate of chemical reactions: the concentration of reactants, temperature, the physical state of reactants and surface area, and catalyst. Apart from adding CaCl_2 as a catalyst, mechanical stirring and heating can possibly increase the rate of dissolution of SF in FA/ CaCl_2 (ratio of 98:2) as well. SF must be stirred until it disperses well in FA/ CaCl_2 , indicated by its appearance as a transparent light yellow solution. This process increases the contact area between SF and the solution of FA/ CaCl_2 . The solution needs to be heated and incubated at 45° C overnight (~10 – 12 h) and turns pink afterwards, which is possible to readily electrospin.

The incubating temperature is adjustable; higher temperatures are likely to increase the rate of reaction, resulting in a shorter incubation period. The temperature of 60° C is an interesting point for further investigation, as it has been reported as an evaporating temperature that affects the interaction between water and protein in *B. mori* SF [244].

Changing in solution colour can be indicative evidence of reaction even though the reason for this colour change remains uncertain. The colour of organic compounds originates from the absorbance of light in chemical structures [245]. Since the SF molecule is dissolved, it affects chemical bonding between protein molecules, resulting in visible colour changing. Additionally, the colour may be altered by the pH of solutions as well.

3.3.2. Effects of electrospinning solution on electrospun SF mats

Viscosity, solution charge, and electrospinning parameters such as solution flow rate and voltage supply affect the quality of electrospun mats. The solution properties, especially the size of dissolved SF fibres, mainly affect the diameter of electrospinning fibre [151]. Here, the average fibre

diameter of electrospun SF mats was in the sub-micron scale of ~200 nm when dissolving degummed SF in FA/CaCl₂ with the ratio of 98:2.

Several previous studies indicated that SF in different solvents could generate different ranges of electrospun fibre diameters. For example, Magaz A.M., *et al.*, 2020, found that the diameter of electrospun SF can be varied from ~500 nm up to 1 µm when preparing electrospinning solution by using regenerated SF in HFIP [120]. Others showed that dissolution of SF in FA could provide the fibre diameter in the range of nano-scale and sub-micron scale [152-154]. The increase of CaCl₂ in FA can reduce the diameter of electrospinning SF [150].

Additionally, the size of SF molecules before dissolving and concentration of SF affects the morphology of the electrospun fibres. For example, lyophilised SF could be electrospun into nanofibres with an average diameter less than 100 nm [153, 154]. Zhang F., *et al.*, 2012, found an interesting relationship between the size of SF molecules of electrospinning solution and the fibre diameter of electrospun mat. The regenerated SF film containing SF nanospheres was able to be electrospun into a mat with nanofibres of diameter ~50 nm. In contrast, regenerated SF film containing SF nanofilaments generated the thicker electrospinning fibres in the diameter range ~200 nm [151].

In this work, the size of degummed SF before preparing electrospinning solution is in the range of microfilament (larger than 10 µm), as shown in Figure 3.3 (d). The SF molecules after dissolving in FA/CaCl₂ (98:2) at 45° C overnight may be nanofilaments due to the fact that the fibre diameter of electrospun mats is ~180 – 200 nm [151].

3.3.3. Effects of humidity and temperature on electrospun SF mats

Humidity is a key factor affecting the morphology of electrospinning fibres. It plays an intrinsic role in solvent evaporation and fibre solidification [166]. Bead-on-string fibres, beads, internal pore fibres, and pores at the surface of fibres may occur as a consequence of inappropriate humidity to polymer and solvent systems. Several studies have confirmed that SF and SF blended with other polymers are possible to electrospin under a wide range of relative humidities, from 20 – 60% [146, 246, 247]. However, fibres are more prone to defects at high humidity.

Mailley D., *et al.*, 2021 explained that solvent evaporation occurs in all regions of electrospinning: the Taylor cone, straight jet, and whipping/bending jet. The strong movement of the whipping/bending jet enhances solvent evaporation rate *via* the convection mechanism. At higher humidity, water vapour molecules in the air are increased; thus, the electrospinning jet is discharged (deionised) even more so by water molecules. Therefore, the charge density of the electrospinning jet is decreased at higher humidity. The reduction of the charge density of the electrospinning jet also reduces the movement of the electrospinning jet under an electric field, leading to slower evaporation [166].

Moreover, the electrospinning jet can adsorb water in the air. The higher humidity may induce a higher number of beads forming during solidification in both hydrophobic and hydrophilic polymers *via* different mechanisms. For example, it causes precipitation and fast solidification leading to thicker diameter and bead-on-string fibres. On the other hand, it causes water plasticising in hydrophilic polymers, along with slow solidification and evaporation. The electrospinning jet is thinned until it reaches a capillary instability resulting in beads fibres [166]. In addition, several studies have revealed that bead formation is encountered when electrospinning SF in relatively high humidity atmospheres; this may be because SF contains both hydrophilic chains interspersed among hydrophobic proteins chains [248].

Temperature is perhaps an indirect factor influencing electrospinning fibres. Its effect is reportedly inversely proportional to humidity. Changing temperatures can affect humidity. Therefore, humidity and temperature should be constantly controlled throughout the electrospinning period. Herein, the temperature was 25° C in vertical electrospinning.

In this study, the horizontal electrospinning set-up with a high-speed rotating mandrel was not amenable to control humidity and temperature due limitations of the machine. Humidity and temperature should be recorded at least prior to electrospinning. If the humidity is not extremely high, the morphology of electrospun SF is still acceptable without defects, as confirmed by SEM of uniformly aligned layers.

Finally, there was no significant difference in fibre morphology and diameter between 35% R.H. and 50% R.H. To avoid bead-on-string fibres or other defects, the lower R.H. of 35% was preferred.

3.3.4. Effects of apparatus orientation on electrospun SF mats

The movement of the electrospinning jet was chiefly driven by electric force (F_E) between the needle and collector. The direction of F_E is always generated from the needle and moved toward the collector in every orientation of the apparatus. However, gravity (F_G) and dynamic airflow also affect the direction of the electrospinning jet [176]. In general, electrospinning was operated under the static atmosphere without additional airflow. Thus, the net electrospinning force (F_N) from F_E and F_G was considered in both horizontal and vertical electrospinning systems.

According to well-known Coulomb's and Newton's laws, the magnitude of F_E depends on charges of particles (q) and electric field (E), while F_G depends on the mass of the object. If the electric field is generated by two plates that are supplied by different voltages, its magnitude is directly proportional to the different voltage between plates (V) but inversely proportional to the distance between those plates (d). The relation between F_E and other related parameters is explained by the equations below.

$$F_E = qE$$

$$V = dE$$

Compared to the electrospinning system in this study, the distance between the needle and collector was fixed. The electrospinning solution was homogenous, and it was prepared using the same protocol each time. Therefore, within reason, it can be assumed that the total charges of the solution are constant as well. Therefore, the magnitude of F_E depends on the voltage supply between the needle and collector. On the other hand, F_G depends on the mass of ejected solution, especially at the tip of the needle, because the solution can accumulate here as a consequence of adhesive and cohesive forces.

In the horizontal axis electrospinning set-up, the direction of F_E and F_G are perpendicular. The low voltage supply resulting in low F_E leads to the projectile movement of solution from the tip

of the needle (Taylor cone region) and electrospinning jet down to the floor of the fume hood instead of electrospinning at the collector. In fact, the volume of solution in the Taylor cone region gradually changes throughout the electrospinning period. The volume of drop solution at the tip of the needle is decreased by inducing the electrospinning jet, while it is increased by the ejection of solution. These decrease and increase rates should be balanced in order to get steady electrospinning and avoid droplets deposition. If the ejection rate is too high compared to the decrease rate, the volume of solution at the Taylor cone region will increase, resulting in a higher mass of solution. The excessive mass, which cannot electrospin, will be strongly pulled down by F_G . Once it was removed from the tip of the needle, it will be slightly pushed away toward the collector by F_E , causing projectile drop deposition.

Several droplets were still found on the floor of the fume hood set-up during electrospinning with the optimised parameters. This suggests that either the flow rate of 0.4 ml/h should be reduced or the voltage of 15 kV should be raised to get more steady-state electrospinning. The lower flow rate leads to a longer electrospinning period, then increasing the voltage would be a suggestion for further study. The voltage supply of 15 kV was high enough and acceptable to electrospin efficiently, as confirmed by the SEM and image analysis.

F_E and F_G are in the same direction towards the collector in vertical axis electrospinning. The solution will certainly drop towards the collector if there is an excessive solution at the Taylor cone region. Unsurprisingly, there were a lot of droplets on the electrospun mat when applying the horizontal electrospinning parameters (0.4 ml/h flow rate and 15 kV voltage) to the vertical electrospinning axis. The results of electrospun products supported that droplets of solution can be avoided by either decreasing flow rate or increasing voltage. With a voltage of 15 kV, the smooth electrospun mats without droplets were successfully fabricated by the flow rate of 0.05 ml/h. In contrast, a flow rate of 0.4 ml/h was appropriate for electrospinning with a voltage of 30 – 35 kV.

3.3.5. Effects of rotating speed of collector on electrospun SF mats

According to the results, the orientation of the electrospinning apparatus, voltage supply, flow rate of solution, and rotating speed of collector had no significant effects on fibre diameter. It seems that the solvent of electrospinning solutions and humidity during electrospinning affected the morphology of electrospinning fibres and their diameters. However, the alignment of electrospinning fibres is directly proportional to the rotating speed of the collector [88, 249]. The bending and whipping electrospinning jet commonly generates random fibres directions with static collection.

Using a rotating mandrel collector is a simple way to improve the alignment of fibres from unstable whipping jets [249]. Several studies revealed that the balance between the linear velocity of the rotating drum and the velocity of the evaporating jet depositions is a critical criterion for the obtaining highest alignment [249, 250]. Too low a speed cannot initiate fibre alignment, while too high a speed may generate turbulent airflow around the surface of the collector leading to the non-uniform alignment [249, 251].

As shown from the 2D FFT alignment results (Figure 3.12 (b)), the electrospinning fibres were highly uniformly aligned at the high rotating speed of the collector (1,000 – 1,500 rpm) compared to using a lower rotating speed (~800 rpm). The difference between aligned and random fibres, which are fabricated by the high and low rotating speed of mandrel, can be observed clearly by SEM (Figure 3.10 (a and d)). Unfortunately, the highest rotating speed in this study was imperfect to produce unidirectionally aligned fibres. Almost all electrospinning fibres were aligned in the same direction (unidirectional). Some fibres were still straight lines but orientated at various angles. This may be due to the effect of turbulent airflow generated by the high speed of the collector. A minor change of speed is recommended for assessment in further study to improve the alignment of fibres. On the other hand, aligned electrospun fibres can be generated by using parallel collectors [252, 253], using wire-drum collectors [254], and even using external magnetic force [255, 256]. Thus, the different designs of collectors are another interesting point to study for electrospinning SF.

3.3.6. Effects of post-treatment on electrospun SF mats

The β -sheet is the most important structure of SF because it supports fibre strength and decreases water solubility due to its hydrophobic property. Electrospun SF mats are typically treated with alcohols (-OH group) such as EtOH [147, 150, 151, 240] and MeOH [20, 146, 148, 152-154, 236] to induce β -sheet formation prior to use as regenerative tissue scaffolds. However, these treatment solutions were always diluted in water before use. Here, the effects of different percentages of EtOH and MeOH treatment on β -sheet conformation and other secondary protein structures were considered, as well as water. The treatment time of 20 min was fixed as a control parameter in this study [120, 257].

3.3.6.1. EtOH and MeOH treatments

ATR-FTIR results showed that the amide I peaks were shifted from 1650 cm^{-1} to 1625 and 1621 cm^{-1} after treatment with all percentages of dilution of EtOH and MeOH, confirming the increase of β -sheet. The total percentage of β -sheet reached around 63 – 66% once treated with 75% EtOH, 80% EtOH, 100% EtOH, 80% MeOH, and 100% MeOH, while it was 59% once treated with 70% EtOH. These results indicate that both EtOH and MeOH have the same ability to induce β -sheet of electrospinning SF. According to the result shown in Figure 3.14, the low amount of water in the alcohol-based solution (<20%) does not interfere with β -sheet induction. The effectiveness of alcohol-based treatment solution may be inhibited, provided that the water in the solution is higher than 30%.

Alcohols can rearrange the secondary protein structures of SF due to their polarities [258, 259]. They turn random coil to β -sheet [138, 234, 258, 260, 261]. Um I.C., *et al.*, 2003 reported that the polarities of alcohols attracted water molecules in SF and this evidently induced more aggregation of hydrophobic amino acids, particularly Ala and Gly [259], which are the main components of β -sheets. Due to its strong polarity, MeOH is deemed a more effective solution than EtOH to induce β -sheet crystallisation, however it does have unwanted toxicity and handling issues in comparison to EtOH.

Apart from β -sheets, the β -turns and bends structures form part of the crystalline structure [261]. The total percentage of the crystalline structure of electrospun SF mats was calculated by the sum of % β -sheet and % β -turns. This was increased up to ~85% after treatment by all EtOH and MeOH conditions from 78% of untreated samples (Figure 3.14). In contrast to SF films, a previous study reported that the degree of crystallisation in MeOH treated SF was higher than both untreated and EtOH treated samples when using X-ray diffraction (XRD) analysis [261]. Puerta M, *et al.*, 2020 also revealed that EtOH treatment provided a similar degree of crystallinity between immersing for 15 min and 1 h. Whilst, MeOH treatment for 1 h showed a higher degree of crystallinity than the treatment for 15 min [261]. Another study also confirmed that the crystalline structure was constant after treatment for 10 min to 24 h. After 24 h, it was slightly fluctuated [262]. Moreover, EtOH has a lower risk than MeOH and is typically used for disinfection and sterilisation. Then 80% EtOH was recommended as a suitable treatment solution.

However, EtOH treated electrospun SF mats always shrank after air-drying at room temperature. EtOH can soak and penetrate through the network of the electrospun mats. Once it is evaporated, the fibre gaps are reduced and are evident from SEM, as shown in Figure 3.15, with fibre shrinkage observed. Electrospun SF mats should be preserved in DI water all the time after post-treatment to avoid fibre shrinkage. If dried samples are needed, the treated electrospun mats should be slowly evaporated by putting them between filter papers akin to a sandwich, and then putting a suitable weight on top to maintain the shape of electrospun mats. Under normal atmosphere and room temperature, the electrospun mats completely dry off within a few hours. On the other hand, thicker electrospun mats possibly resist the shrinkage after solvent evaporation.

3.3.6.2. Water treatment

Soaking untreated electrospun SF mats in water partly turned SF fibre to thin-films confirmed by SEM. This is because water disrupts cohesive forces and hydrogen bonding between protein chains and enhances the mobility of the amorphous domain [242, 243]. Moreover, water can effectively reduce the glass transition temperature (T_g), which is ~180° C for dried pure silk [243,

260, 263]. Hu X., *et al.*, 2011 revealed that higher humidity (> 90%) brought down the T_g to around room temperature [243]. On the contrary EtOH and MeOH treated electrospun SF mats using the conditions explored here were stable and not morphologically affected in water; this might be due to the effect of a high number of β -sheet crystallisation after treatment.

Interestingly, the water treated electrospun SF mat still exhibited the amide I peak at 1621 cm^{-1} indicating β -sheet formation because it was observed after dehydration. Water annealing at room temperature was reported as a protocol to increase otherwise low β -sheet content [264]. Possibly, the β -sheet formation was slightly elevated during water evaporation, resulting in the presence of the ATR-FTIR peak at $\sim 1621\text{ cm}^{-1}$. However, the percentage of β -sheet formation of water annealing electrospun SF (48%) was still lower than that of electrospun SF (55%).

Finally, electrospun SF mats treated with 80% EtOH is stable in water. It can be presumed that the β -sheet and crystalline structure of the treated fibres are very high and strong, which can resist plasticisation by water. Therefore, the 80% EtOH treatment for 20 min is a suitable and practical protocol to maintain the fibres as electrospun mats.

3.3.7. General discussion of double layer electrospun mats

The aligned fibre is an important key to guide the neurite extension unidirectionally [86-88, 208, 227, 228, 265]. However, only a single layer of aligned fibres may not be strong enough since it can break at low strain, particularly when applying the force in the transverse direction to fibre alignment [266, 267]. It suggests that the aligned fibre is weak and difficult to handle (post-processing), such as bending and folding. According to Figure 3.16, the electrospun SF mat with a single layer of aligned fibres was removed from the greaseproof paper difficultly. This always broke into many strips following the direction of fibre alignment (Figure 3.16 (a)), while the electrospun SF mat with a single layer of random fibres can be peeled away easily (Figure 3.16 (c)). The results here also suggest that the aligned fibre mat should be thicker than $\sim 70\text{ }\mu\text{m}$ to enable handling. However, the thickness of the fibre mat depends on the electrospinning duration. It may take a very long period to electrospin the aligned fibre mat with sufficient thickness.

Therefore, the double layer electrospun scaffolds were formed with the base layer of random fibres ($\sim 70\ \mu\text{m}$) and the top layer of aligned fibre ($\sim 30\ \mu\text{m}$), providing fibre mats that can be handled and further processed. Moreover, the double layer mat is reproducible, confirmed by the similar results of the fibre diameter and fibre alignment from three independent electrospinning experiments with three independent electrospinning solutions, as shown in Figure 3.12.

Recently, literature reports have developed some double layer electrospun mats for tissue-engineered scaffolds [227, 268, 269]. A layer of the double layer electrospun mat is always designed to support cell growth, while the other is for different purposes depending on the applications, such as a reinforcement layer [227], a layer for encapsulating and releasing growth factors [268], or indeed, a protective barrier against external contamination [269]. In peripheral nerve regeneration, double layer electrospun mats with random and aligned nanofibres in the outer and inner layers are more robust and tear-resistant during surgical procedures compared to a single layer of aligned nanofibres [227]. Additionally, the aligned fibres promote cell invasion, while the random fibres hamper unwanted cell migration [228]; thus, the double layer mat is coincident with the function of nerve membranes that the inner layer should support nerve growth, and the outer layer should be a barrier for other connective tissues [37].

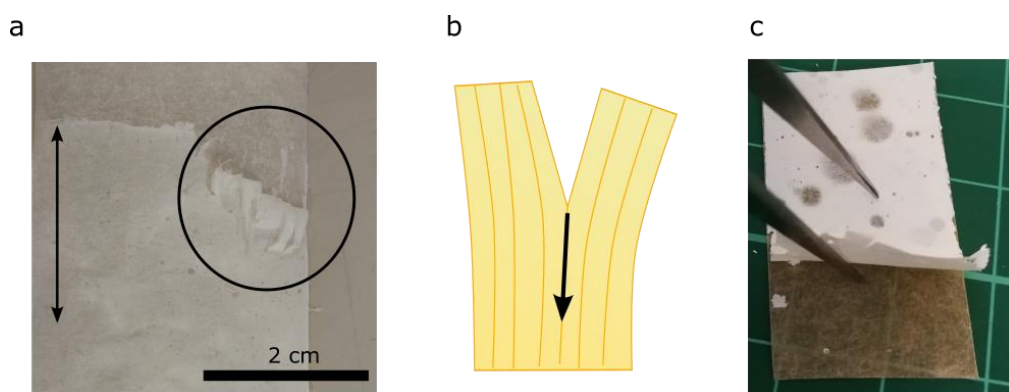


Figure 3.16 Example of electrospun SF removal from the greaseproof paper: (a) one layer of aligned fibres with the thickness of $\sim 70\ \mu\text{m}$ ($\sim 8\ \text{h}$ electrospinning), the arrow shows the direction of fibre alignment, the circle shows the fibre breakage following the alignment of fibres, (b) the schematic of aligned fibre breakage following the fibre alignment, and (c) one layer of random fibre with the thickness of $\sim 70\ \mu\text{m}$ ($\sim 8\ \text{h}$ electrospinning), the size of the mat is $2 \times 3\ \text{cm}^2$.

3.4. Conclusion

A novel method for preparing SF solution and the optimisation of electrospinning parameters are successfully defined. The quality of double layer electrospun SF mats is acceptable and promising to use as a peripheral nerve conduit.

In this chapter, electrospinning SF solution can be prepared *via* a dialysis free protocol. This protocol reduces a lot of time-consuming steps and is also reproducible. With incubation at 45° C overnight (~10 – 12 h), the 10% wt/v degummed SF can directly dissolve in a mixed solution of FA and CaCl₂ with the ratio of 98:2 ml/g. The diameter of electrospinning fibres is consistent with the sub-micron range of ~200 nm. Fibre alignment depends on the rotational speed of the mandrel collector. Higher speed provides a more uniform alignment without effects on fibre diameter.

According to the purpose of this chapter, the double layer electrospun SF mat is required due to improved post-processing ability (e.g. easy to handle, bend, and fold) and is coincident with some aspects of natural nerve membrane. Herein, the double layer electrospun SF mats are composed of a bottom layer of random fibres and a top layer of uniformly aligned fibres. The solution feed rate of 0.4 ml/h and distance of 12 cm are parameters that can be constantly fixed in both horizontal and vertical electrospinning systems, while other parameters are different in each layer. The bottom layer was fabricated by vertical axis electrospinning with the voltage of 35 kV and collector speed of ~800 rpm (linear velocity of ~5.03 m/s) for 8 – 10 h. On the other hand, the top layer was fabricated by horizontal electrospinning with the voltage of 15 kV and collector speed of ~1,200 – 1,500 rpm (linear velocity of ~7.54 – 9.42 m/s) for 4 – 5 h. If possible, the humidity and temperature should be controlled at 35% R.H. and 25° C. The total thickness of electrospun mats of ~100 µm (~70 – 80 µm of the bottom layer and ~20 – 30 µm of the top layer) is sufficient for easy handling.

Finally, the post-treatment of 80% EtOH for 20 min is recommended in order to induce β -sheet crystalline structure in SF fibres promoting fibre strength and insoluble properties. The EtOH treated mats should be preserved in DI water to avoid shrinkage. These developed non-

woven SF mats will be modified to electrically conductive mats and their properties such as mechanical, electrical, and *in vitro* biocompatibility, that are explored in the next chapters.

CHAPTER 4

Electrical Modification of Electrospun Silk Fibroin

Electrically conductive materials are a new generation of peripheral nerve scaffolds to facilitate fully functional regeneration. The electrical conductivity of non-woven SF mats, fabricated using the final protocol from chapter 3, was modified by poly(3,4-ethylenedioxythiophene) polystyrene sulfonate (PEDOT:PSS) with various conditions. The physical, mechanical, and electrical properties of these composite materials will be described in this chapter.

The main purpose of this chapter is to modify the pristine electrospun SF into the composite material of PEDOT:PSS incorporated electrospun SF. To blend the PEDOT:PSS in/on the electrospun sample, an interpenetrating polymer network (IPN) technique is preferred due to its simplicity [91]. By using IPN, the molecules of two polymer chains are partially interlaced [177], so that the molecules of PEDOT:PSS can tightly form the network in/on SF fibres. This composite material is hoped to be used as a peripheral nerve scaffold, therefore, it should be stable in water without the detachment of PEDOT:PSS. Furthermore, this composite material is planned to be applied with electrical stimulation for promoting neurite outgrowth, such as, the electrical conductivity of the composite mat should be at least higher than that of the pristine electrospun SF mat.

The molar ratio of PSS to EDOT monomers (α) affects the elasticity and electrical conductivity of the composite mat [270]. The α ratios were varied at 1.3, 1.8, 2.3, 2.8, and 3.3 in this study. In order to confirm the presence of PEDOT:PSS in/on the electrospun SF mat, the FTIR spectra were assessed in the wavenumber range of 1300 – 600 cm^{-1} , which is associated with PEDOT and PSS [271-273].

After IPN, the diameter of fibres and the mechanical property of the electrospun SF and IPN mats were investigated *via* tensile testing, in the wet state (underwater). The wet state tensile properties can be considered to represent the elasticity of the composite mat in the body and cell culture system. There was no expectation of the tensile results; however, the results of IPN mats

were compared to those of electrospun SF mats to understand how PEDOT:PSS interacts with SF fibres resulting in changing mechanical properties.

The surface and chemical properties of the IPN mats were then analysed *via* X-ray and Hard X-ray photoelectron spectroscopy (XPS and HAXPES). This experiment was performed to understand how deep PEDOT:PSS can penetrate in/on electrospun fibres. Moreover, it was performed to confirm that EDOT monomers and PSS are functionalised and grown as PEDOT:PSS networks.

Finally, the electrical conductivities of IPN mats were measured by cyclic voltammetry (CV) and electrochemical impedance spectroscopy (EIS) techniques. It was expected that the IPN mats should at least have higher electrical conductivity than the electrospun SF mats.

4.1. Materials and Methods

4.1.1. Interpenetrating polymer network (IPN)

The IPN protocol was adapted from the protocol of Horii T., *et al.*, 2018 [270]. The IPN working solution was composed of 3,4-ethylenedioxythiophene monomers (EDOT, Sigma-Aldrich), polystyrene sulfonate (PSS, Sigma-Aldrich), and initiators. Firstly, 0.98% wt/v sodium persulfate ($\text{Na}_2\text{S}_2\text{O}_8$, Sigma-Aldrich) and 0.2% wt/v iron (II) sulfate heptahydrate ($\text{Fe}_2\text{SO}_4 \cdot 7\text{H}_2\text{O}$, Sigma-Aldrich) were dissolved in distilled water. Then 0.5% wt/v EDOT monomer was then added to the prepared solution. After that, the various concentrations of PSS were added to the solution and stirred well. The molar ratios of PSS to EDOT monomer (α) were varied from 1.3 to 3.3, so the PSS concentration was estimated to be 0.84 – 2.13% wt/v. The relation between PSS weight and EDOT volume is explained in the equations below:

$$[\text{PSS}] = \alpha [\text{EDOT}]$$

$$\frac{Y \text{ (mol)}}{(dm^3)} = \alpha \frac{X \text{ (mol)}}{(dm^3)}$$

$$\frac{m_Y \text{ (g)}}{MW_Y} = \alpha \frac{m_X \text{ (g)}}{MW_X}$$

$$\frac{m_Y (g)}{MW_Y} = \alpha \frac{d_X \left(\frac{g}{ml} \right) V_X (ml)}{MW_X}$$

$$\frac{m_Y (g)}{183} = \alpha \frac{1.331 \left(\frac{g}{ml} \right) V_X (ml)}{142.17}$$

$$m_Y (g) = 1.71 \alpha V_X (ml)$$

where, m_Y is the weight of PSS (g), V_X is the volume of EDOT monomer (ml), and α is the ratio of PSS to EDOT (varied from 1.3 – 3.3). The schematic of the IPN process of PEDOT:PSS in/on electrospun SF mats is shown in Figure 4.1.

The 80% EtOH-treated electrospun SF mats were immersed in the IPN working solution as fast as possible when the solution was still yellow. The solution slowly turned dark blue during the functionalisation process between EDOT monomer and PSS as PEDOT:PSS complex. SF mats were then left in the solution for 72 h at room temperature, where they then turned completely dark blue, similar to the original solution. The IPN mats were then washed overnight with distilled water, until no PEDOT:PSS residues leaked from materials. Finally, IPN mats were stored in distilled water to avoid shrinkage.

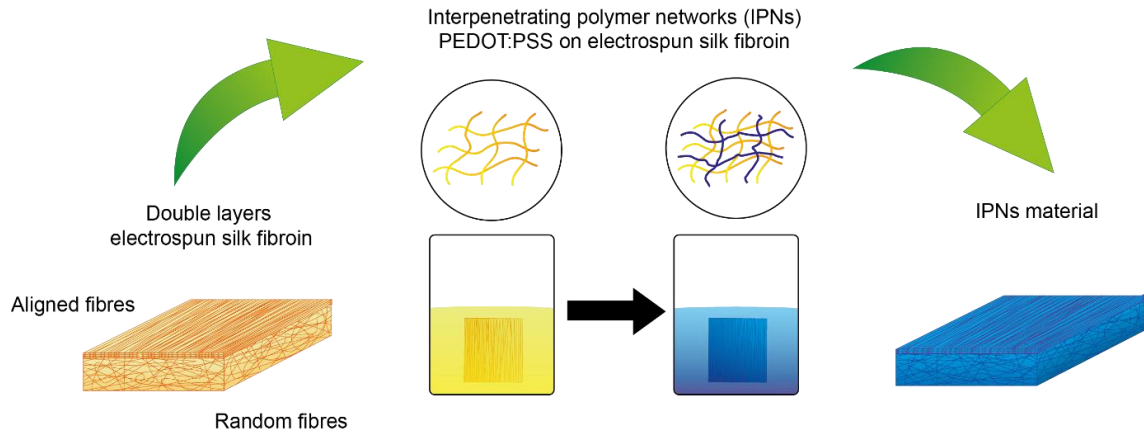


Figure 4.1 Schematic process of electrospun fibre modification *via* IPN of PEDOT:PSS.

4.1.2. Dip coating

The custom-made PEDOT:PSS solution ($\alpha = 1.3$) was prepared by the same process of IPN solution preparation as mentioned in section 4.1.1. However, the custom-made solution was left

at room temperature for a week until the solution turned completely dark blue before, its use as a dip coating solution. The 80% EtOH-treated electrospun SF mats were then immersed in the custom-made PEDOT:PSS solution or commercial PEDOT:PSS solution with 1.3% wt dispersion in water (Sigma-Aldrich) and left for 72 h at room temperature.

4.1.3. ATR-FTIR analysis

The IPN materials of PEDOT:PSS on electrospun SF were characterised using an ATR-FTIR with the same system as mentioned in chapter 3 (section 3.1.4) (Nicolet 5700 FTIR spectrometer, Thermo Fisher Scientific). FTIR spectra were collected from the wavenumber range of 4000 – 400 cm^{-1} with 32 scans in the absorbance mode. The wavenumber range from 1300 – 600 cm^{-1} of SF and IPN samples were assessed. They are associated with PEDOT (*i.e.* C-O-C at 1187, 1138, 1083, and 1048 cm^{-1} [271] and C-S at 831 cm^{-1} [272]) and PSS (*i.e.* SO_3^- at 1058 and SO_2^- at 1010 cm^{-1} [273]). The experiment and the collection of ATR-FTIR data were performed by Jie Ma and independently analysed by the author of this thesis.

4.1.4. Scanning electron microscopy (SEM)

Electrospun and IPN mats were prepared and observed by SEM using the same protocol as described in chapter 3 (section 3.1.5).

4.1.5. Tensile testing

The mechanical properties of electrospun SF and IPN mats were obtained by wet-state horizontal tensile test (ElectroForce, Planar Biaxial, TA instrument). Samples were cut into rectangular pieces of 5 x 35 mm^2 , where the length was parallel to the fibre alignment. The depth of samples (d) was measured by a thickness gauge micrometre (DML3032, Digital Micrometers Ltd). The sample was placed on tensile grips under tap water at room temperature. 5 mm of both ends were hooked by grips, and the initial length (L) of samples was 25 mm. A tensile grip, connected to a load cell of 22 N, was a dynamic end, while another grip without load cell was a stationary end. The moving speed was constantly controlled at 10 $\mu\text{m/s}$. Load force (F) and displacement (ΔL) were collected by WinTest Software (WinTest® for ElectroForce Test System, TA instrument),

and the sampling rate is 20 points/s. The ultimate tensile strength (σ_u) and strain at break (ε) were calculated following these equations below:

$$\sigma_u = \frac{F_{(\max)} (N)}{d \cdot w (mm^2)} \text{ or } (MPa)$$

$$\varepsilon = \frac{\Delta L (mm)}{L (mm)}$$

where, w is the width of sample (5 mm) and L is the length of sample (25 mm).

The data of stress-strain profiles were plotted by GraphPad software (GraphPad Prism 9, version 9.2.0, USA). Then, the Young's modulus (E) and tensile toughness (U_T) were calculated by determining the slope and area under the curve of the stress-strain profile, respectively.

4.1.6. X-ray and Hard X-ray photoelectron spectroscopy (XPS and HAXPES)

The presence of PEDOT:PSS on electrospun SF was determined by hard X-ray photoelectron spectroscopy (HAXPES, Scienta Omicron GmbH). This measurement was kindly performed by Dr. Ben F. Spencer¹.

A Ga K α (9.25 keV) was the X-ray source of HAXPES, this high kinetic energy leads to an increase of sampling depth observation compared to using the surface-sensitive XPS with the energy of 1 – 2 keV [274, 275]. The bulk-like composition was then measured without the influence of surface contamination. The samples were attached to Omicron sample plates using the adhesive copper tape and were then placed in the ultra-high vacuum chamber with a pressure of 6×10^{-10} mbar. After photoexcitation, the electron supply was replenished by a charge neutralising low energy electron gun (FS40A, PREVAC). The survey spectra and core-level spectra of the interesting elements were measured by the EW4000 electron energy analyser with an entrance slit width of 1.5 mm. The binding energy (BE) of C 1s, N 1s, O 1s, and S 1s were at 285, 400, 530, and 2470 eV respectively. A pass energy of 500 eV with an energy resolution of ~2 eV was implemented to the survey spectra, while a pass energy of 200 eV with an energy resolution of ~0.8 eV was applied to the individual elements spectra [276].

¹ Department of Materials and Henry Royce Institute, University of Manchester, Manchester, United Kingdom

Atomic concentrations were calculated using the sensitivity factors for the core levels following the method as described in [277]. The recently published photoionization parameters were up to 10 keV [278, 279]. The sampling depth was defined by the equation below [280]:

$$\text{Sampling depth} = 3\lambda \cos \theta$$

where, λ is the inelastic mean free path of electrons and θ is the electron take-off angle with respect to the surface normal.

The depth of the normal surface was ~54 nm calculated using the TPP-2M formula [281]. The sampling depth can be reduced by tilting the sample. θ was varied up to 70°, which the sampling depth was ~11 nm. Data were analysed using CasaXPS (CasaXPS 2.3.24, Casa Software Ltd.) [282].

4.1.7. Electrochemical characterisation

Electrospun and IPN samples were cut into rectangular pieces of 1 x 3 cm², with the length parallel to the alignment of fibres. These samples were attached to a potentiostat and their electrical properties were measured *via* cyclic voltammetry (CV) and electrochemical impedance spectroscopy (EIS).

4.1.7.1. Cyclic voltammetry (CV)

Electrospun and IPN samples were delivered to Lancaster University for CV measurement with the kind help of Dr. John G. Hardy² and Mark D. Ashton³.

CV measurements were performed using a potentiostat (EmStat3+, PalmSens) connected to a personal computer and operated with the PSTrace 7.4 software. Firstly, an electrospun or IPN sample was attached to a glass slide by using carbon tape. A three-electrode system was connected to the prepared sample as a working electrode (WE). A silver/silver chloride (Ag/AgCl) electrode (CH Instruments, USA) and a platinum wire (Sigma Aldrich, UK) were connected as the reference electrode (RE) and counter electrode (CE) respectively. Herein, the

² Department of Chemistry and Materials Science Institute, Lancaster University, Lancaster, United Kingdom

³ Department of Chemistry, Lancaster University, Lancaster, United Kingdom

electrolytic solution was phosphate buffer saline (PBS) at pH 7.4. Electrodes were degassed with N_2 before dipping in the electrolyte. The potentials of WE vs. RE were back-and-forth swept between -1.0 V to +1.0 V with a scan rate of 0.05 V/s. The changing of currents was measured and plotted compared to potentials.

4.1.7.2. Electrochemical impedance spectroscopy (EIS)

EIS measurements were performed by a potentiostat (CompactStat.h, Ivium) connected to a personal computer and operated with IviumSoft software. A two-electrode system was used in this study. An electrode cell was WE and another cell was the combination of CE, RE, and ground electrode (GE).

An electrospun or IPN sample was connected to the WE cell, while a platinum mesh (Pt-mesh) with a surface area of $\sim 1\text{ cm}^2$ was connected to the CE/RE/GE cell. The electrolytic solution was 0.1 M sodium chloride (NaCl) diluted in DI water. Approximately 1 cm^2 of sample and the Pt-mesh were dipped into the electrolyte and placed with a distance of 1 cm between them.

EIS was measured in the constant voltage (constant E) mode. The input voltages (E) were in the pattern of a single sinusoidal wave with a constant amplitude of 10 mV and 31 different frequencies (f) from 10 – 10,000 Hz (10 frequencies per decade). The output currents (I) were collected within the range below 10 μA .

The results were then fitted with the Randles equivalent circuit consisting of an electrolyte resistance (R_e), a double layer capacitance (C_{dl}), a charge transfer resistance (R_c), and Warburg element (W) [283]. The R_e was in series with a complex unit of C_{dl} , R_c , and W, which consisted of C_{dl} in parallel to the series of R_c and W as shown in Figure 4.2. Finally, the impedance (Z) results were shown in both Nyquist and bode plots. A Nyquist plot is the relation between $-Z$ in imaginary axis and Z in real axis and a bode plot is the relation between either $\log_{10}|Z|$ and $\log_{10} f$ or phase and $\log_{10} f$.

In addition, Dr. John G. Hardy and Mark D. Aston also helped with the EIS measurement using the three-electrode system, as mentioned in section 4.1.7.1. In this case, the electrolyte for EIS was 5 mM ferric ferrocyanide ($[\text{Fe}(\text{CN})_6]^{3-/4-}$) diluted in PBS. The measurement was operated

in an open-circuit potential of 230 mV. An amplitude of applied potential was perturbed ~10 mV, and the frequency range was 0.1 – 105,000 Hz.

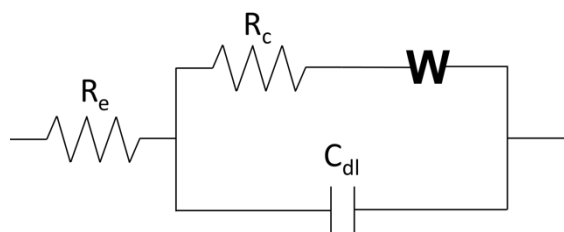


Figure 4.2 Schematic of Randles RC model: R_e is electrolyte resistance, R_c is charge transfer resistance, C_{dl} is double layer capacitance and W is Warburg element.

4.1.8. Statistical analysis

The data were analysed using GraphPad software (GraphPad Prism 9, version 9.2.0, USA). Due to the small sample size, the nonparametric test (Kruskal-Wallis test) was used in this analysis for comparing two or more medians. p -values of less than 0.05 were considered statistically significant. Other definitions (e.g. asterisks, sample sizes, and statistical testing methods) have been indicated in the figure captions.

4.2. Results

4.2.1. The presence of PEDOT:PSS on electrospun SF

Typically, electrospun SF mats were opaque white, while the PEDOT:PSS solution was dark blue as shown in Figure 4.3 (a). After immersing electrospun SF mats in PEDOT:PSS solutions for 3 days, the mats had turned fully dark blue or black in all IPN ratios ($\alpha = 1.3, 1.8, 2.3, 2.8$, and 3.3) and in the dip coating in the custom-made solution. In the case of dip coating in PEDOT:PSS solution with 1.3% wt dispersion in water, electrospun mats were still white in most areas. They were partly turned blue, which easily washed out in the presence of water.

It was clearly seen that the blue colour of IPN mats had bled in the presence of DI water. After 2 – 3 times washing, no further colour bleeding or blue particles were observed leaking out of the mats. However, the colour of IPN mats were still fully dark blue, the same as before washing.

SEM images also showed that the fibre diameters of electrospun SF mats and all IPN mats were in a similar range of ~200 nm as shown in Figure 4.3 (b).

FTIR spectra also showed several specific peaks associated with PEDOT and PSS in all IPN ($\alpha = 1.3, 1.8, 2.3, 2.8,$ and 3.3) mats. As shown in Figure 4.4, IPN mats had outstanding peaks in the range of wavenumber of $600 - 1200 \text{ cm}^{-1}$. The peaks of 831 and 671 cm^{-1} were probably assigned to stretching vibration of the C-S-C bond in thiophene ring, the peak of 1169 and 1124 cm^{-1} to bending of C-O-C bond in the ethylenedioxy group, and the peak of 1033 and 1005 cm^{-1} to symmetric stretching of SO_3^- and SO_2^- . Compared to other studies [271-273, 284], these PEDOT:PSS associated peaks were shifted perhaps due to the incorporation between PEDOT:PSS and SF. On the other hand, the FTIR spectra of the IPN mat were similar to those of EtOH treated the electrospun SF mat in between the wavenumber of $1500 - 1700 \text{ cm}^{-1}$, which is associated with amide structure including β -sheet formation.

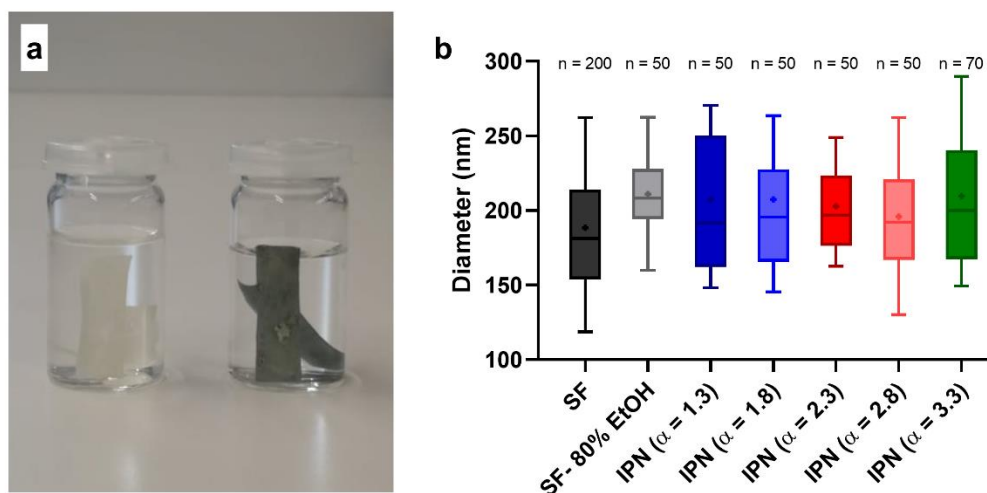


Figure 4.3 Examples of electrospun SF and IPN ($\alpha = 2.3$) mats with the size of $3 \times 1 \text{ cm}^2$: (a) electrospun SF mats (opaque white, in the left) and IPN of PEDOT:PSS on electrospun SF mats (dark blue or black, in the right) after washing 2 – 3 times with DI water and (b) the box-whisker plot of fibre diameters of electrospun SF, 80% EtOH-treated electrospun SF, and IPN mats of PEDOT:PSS in the various ratios ($\alpha = 1.3 - 3.3$), the middle line is median, the mark (+) is mean, and n is the number of fibres representing a sample.

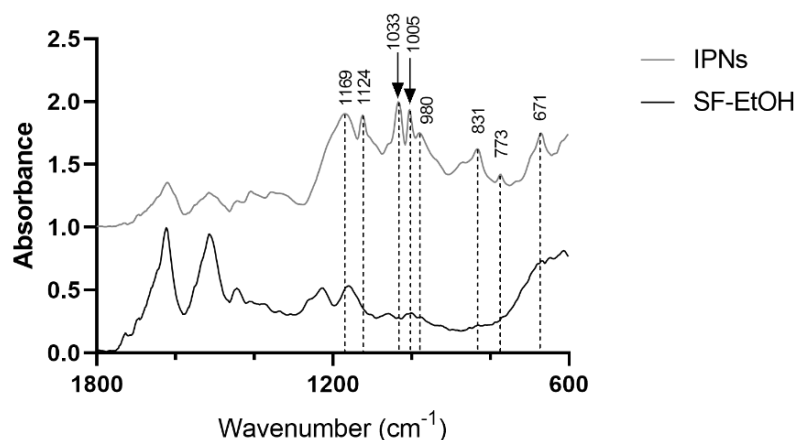


Figure 4.4 ATR-FTIR spectra of 80% EtOH treated electrospun SF and a representative of IPN mats in the wavenumber of 600 – 1900 cm^{-1} .

4.2.2. Tensile profiles of electrospun SF and IPN mats

At the dry state, the relationship between stress and strain showed that untreated electrospun SF mat could stretch longer than 80% EtOH treated sample when applying a low force, as shown in Figure 4.5 (a and b). The untreated sample has lower stress and higher strain than the 80% EtOH treated sample. Thus, stress and Young's modulus of electrospun SF mat were significantly increased after 80% EtOH treatment. However, strain and toughness were still similar. Unfortunately, all IPN samples were unable to be tested because they were very brittle and fragile after dehydration.

In the wet state, all samples were fully immersed in water before the test. They were also tested underwater. The 80% EtOH treated sample was the control sample of this study. Compared to the dry state control, the stress of the wet state control was decreased, while its strain was largely increased, as shown in Figure 4.5 (b – d). Interestingly, the strain of wet state 80% EtOH treated samples were increased over time from 1 – 7 days.

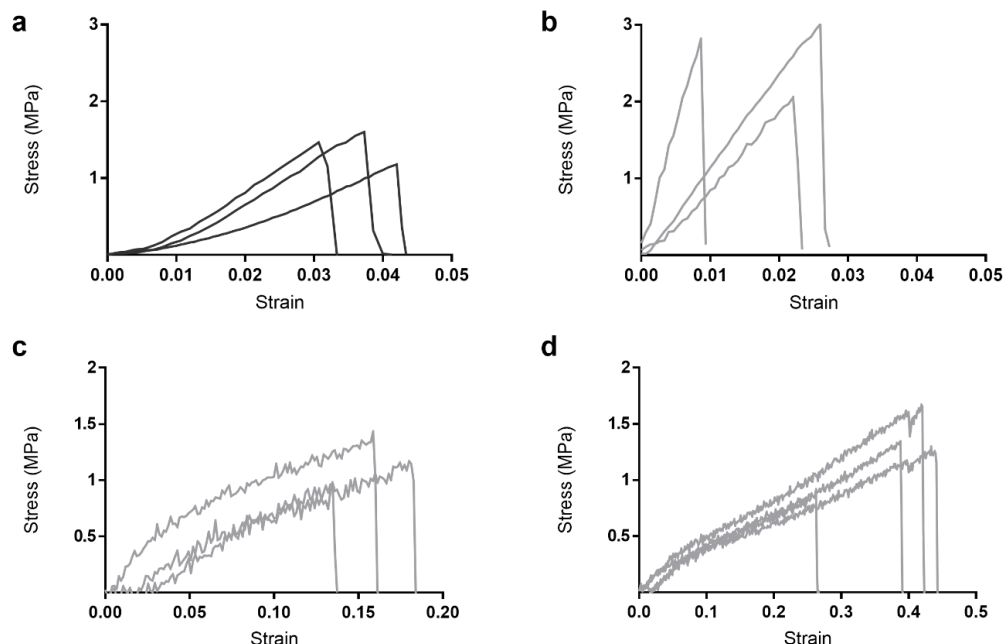


Figure 4.5 Examples of the stress (MPa) and strain profile of electrospun SF: (a) dry-state electrospun SF mats ($n = 3$ samples) and (b-d) 80% EtOH treated electrospun SF mats in (b) dry-state ($n = 3$ samples), (c) wet-state, immersing in water for a few days ($n = 3$ samples), and (d) wet-state, immersing in water over a week ($n = 4$ samples).

In the case of wet state – IPN mats, the force and displacement profiles were slightly different from control. The stress, strain, Young's modulus, and toughness were shown in Table 4.1. The statistical analysis explained that Young's modulus of all IPN mats was similar to control. However, other properties were significantly different, as shown in Figure 4.6. It is to be noted that Figure 4.6 is replotted from the results in Table 4.1.

According to mechanical test results, the IPN ($\alpha = 2.3$) and IPN ($\alpha = 3.3$) mats were collected for further studies such as surface chemistry analysis, electrical property, and *in vitro* biocompatibility. The IPN ($\alpha = 2.3$) represented the condition without effect on mechanical properties, while the IPN ($\alpha = 3.3$) represented the condition that affected mechanical properties.

Table 4.1 Mechanical properties of electrospun SF and IPN mats: (d) represents dry state testing, (w) represents wet state testing, and n is the number of samples from three independent electrospinning experiments.

Materials	Ultimate tensile strength (MPa)	Strain at break	Young's modulus (MPa)	Toughness (kJ/m ³)
SF (d) (n=3)	1.41 ± 0.21	0.03 ± 0.01	43.3 ± 16.8	12.7 ± 1.47
SF-80% EtOH (d) (n=3)	2.62 ± 0.49	0.01 ± 0.01	254 ± 170	14.5 ± 7.85
SF-80% EtOH (w) (n=9)	0.87 ± 0.26	0.12 ± 0.02	7.38 ± 2.35	58.5 ± 23.6
IPN α = 1.3 (w) (n=11)	0.50 ± 0.09	0.09 ± 0.02	6.09 ± 1.52	24.5 ± 7.68
IPN α = 1.8 (w) (n=11)	0.62 ± 0.13	0.11 ± 0.02	6.21 ± 1.27	37.5 ± 15.7
IPN α = 2.3 (w) (n=9)	0.68 ± 0.23	0.09 ± 0.03	8.01 ± 0.87	36.3 ± 21.2
IPN α = 2.8 (w) (n=8)	0.57 ± 0.12	0.07 ± 0.02	8.48 ± 1.97	24.0 ± 10.4
IPN α = 3.3 (w) (n=8)	0.51 ± 0.22	0.07 ± 0.02	7.58 ± 1.43	22.4 ± 16.5

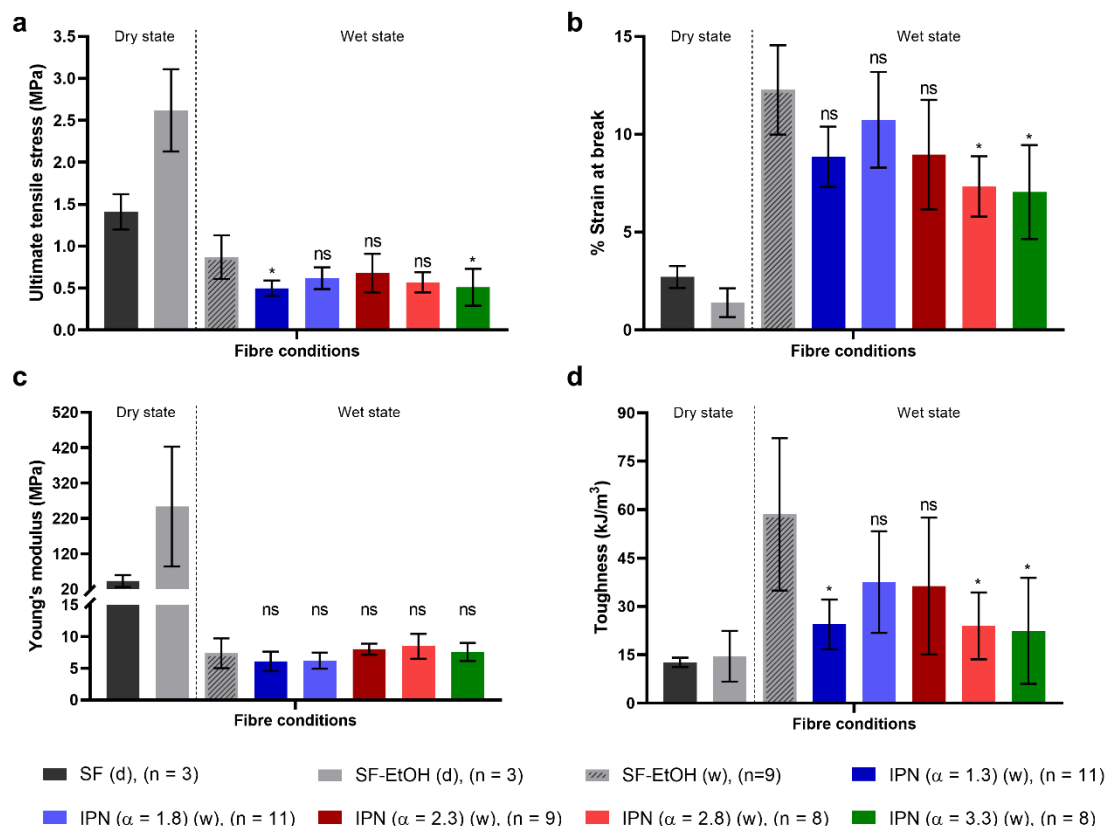


Figure 4.6 Mechanical properties of electrospun SF and IPN mats: (a) ultimate tensile strength, (b) % strain at break, (c) Young's modulus, and (d) toughness, * represents statistically different (p -value < 0.01) via the nonparametric test (Kruskal-Wallis test), all wet state groups were compared with the control (SF-EtOH (w)), the error bar represents SD, and n is the number of samples from three independent electrospinning experiments.

4.2.3. Surface and bulk chemical species of electrospun SF and IPN mats

The surface and bulk chemistry of the electrospun and PEDOT:PSS modified electrospun mats were observed and analysed by XPS and HAXPES. Only the elements of carbon (C), oxygen (O), nitrogen (N), and sulphur (S) were investigated in this study.

The difference between IPN and dip coating protocols was observed by bulk-sensitive HAXPES. The results showed that the IPN ($\alpha = 1.3$) mat had the highest S compared to the dip-coating mat with the custom-made PEDOT:PSS ($\alpha = 1.3$) and electrospun SF mat as shown in the relative atomic percentage of S (%S) in Figure 4.7. The bulk %S of ~0.7% was shown as the

base in electrospun SF mat, and this increased to ~1.5% and ~2.3% after dip coating and IPN respectively.

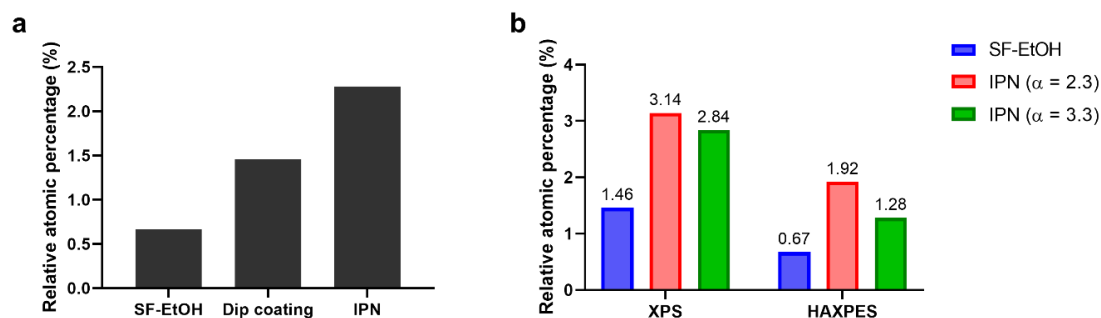


Figure 4.7 Relative atomic percentage of S in/on electrospun SF and IPN mats: (a) bulk – sensitive HAXPES comparing between 80% EtOH treated electrospun SF mat, dip coating mat with the custom-made PEDOT:PSS ($\alpha = 1.3$), and IPN ($\alpha = 1.3$) mat and (b) surface – sensitive (~11nm) XPS and bulk – sensitive (~54 nm) HAXPES comparing between 80% EtOH treated electrospun SF mat, IPN ($\alpha = 2.3$) mat, and IPN ($\alpha = 3.3$) mat.

In addition, the difference between IPN ($\alpha = 2.3$) and IPN ($\alpha = 3.3$) was the further analysed by surface-sensitive XPS and angle-resolved HAXPES to find the confirmation of PEDOT:PSS through the depth of material. As shown in Figure 4.8 (a), the relative %S at the surface (~11 nm) was different compared to the other depths (~19 – 54 nm) in both IPN ratios. However, IPN ($\alpha = 2.3$) had a slightly higher %S than IPN ($\alpha = 3.3$) in all depths. At the surface, the %S reached 3.1% in IPN ($\alpha = 2.3$) and 2.8% in IPN ($\alpha = 3.3$). In other depths, each %S was quite similar, the average %S over bulk material was ~1.6% in IPN ($\alpha = 2.3$) and ~1.3% in IPN ($\alpha = 3.3$).

Furthermore, the peaks of S 2p of XPS and S 1s of HAXPES were fitted to identify the polymerisation of PEDOT:PSS in/on electrospun SF mat. As shown in Figure 4.9, the S 2p peak was fitted with a spin-orbit split doublet resulting in two sub-peaks called S 2p_{1/2} and S 2p_{3/2}. The S 1s was a singlet, which required a single peak fitting in each chemical species. Two spectra associated with PEDOT and PSS were observed in IPN mats. Typically, the S 2p_{3/2} at ~164 eV and S 1s at ~2472 eV binding energy represent PEDOT, whereas the S 2p_{3/2} at ~168 eV and S

1s at ~2477 eV binding energy represent PSS [285-287]. The relative percentages of PEDOT and PSS species in all depths were then calculated from the peak intensity, and the results were shown in Figure 4.8 (b).

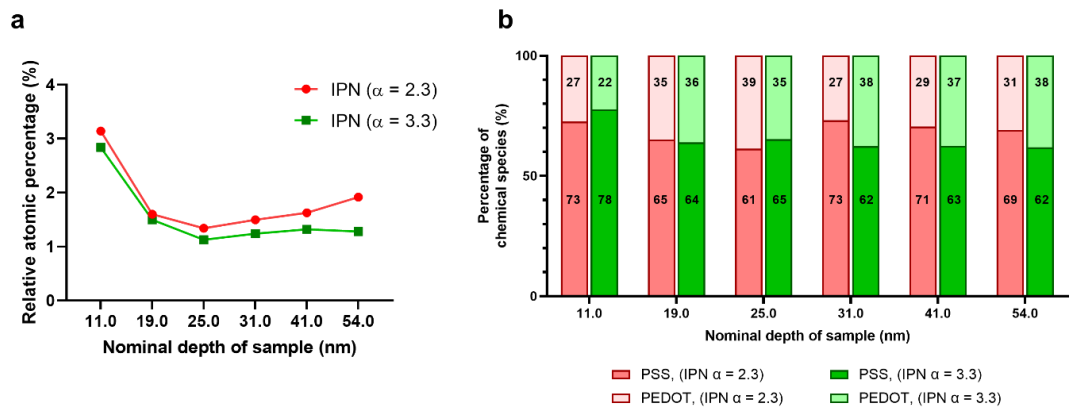


Figure 4.8 XPS and HAXPES results representing surface and bulk chemicals in the different depths of samples: (a) the relative atomic percentage of S in the different depths of IPN ($\alpha = 2.3$) and IPN ($\alpha = 3.3$) mats and (b) percentage of PEDOT and PSS compounds polymerised through the depths of material, calculated from spectra of XPS s2p and HAXPES S 1s.

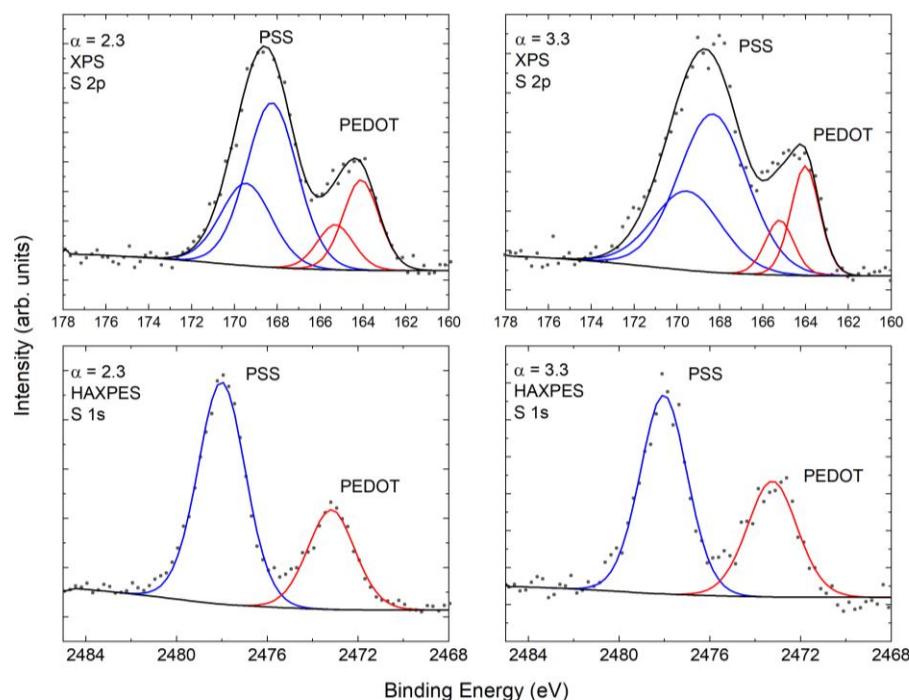


Figure 4.9 The spectra of XPS and HAXPES fitted with S 2p and S 1s respectively: (left) IPN ($\alpha = 2.3$) mat and (right) IPN ($\alpha = 3.3$) mat.

The ratios of PSS to PEDOT of IPN ($\alpha = 2.3$) and IPN ($\alpha = 3.3$) at the surface of ~ 11 nm were $\sim 75:25$. At the sample depth of 19 and 25 nm, their ratios were decreased to $\sim 65:35$. At the depth of 31, 41, and 54 nm, IPN ($\alpha = 2.3$) had higher PSS/PEDOT ratio than IPN ($\alpha = 3.3$). They were $\sim 70:30$ and $\sim 65:35$ in IPN ($\alpha = 2.3$) and IPN ($\alpha = 3.3$) respectively.

The other interesting spectra of C, O, and N were analysed and shown in Figure 4.10. The spectra of C were fitted with four chemical species labelled as C1 (~ 285 eV), C2 (~ 286.5 eV), C3 (~ 288 eV), and C4 (~ 289 eV). C1 represents hydrocarbon chains, C2 with C-N and C-O, C3 with C=O, C=S, and C4 with higher carbon bonding.

The spectra of O were associated with PEDOT and PSS [285-287] as well as spectra of S. They were well fitted with two chemical species. O1 (~ 532 eV) is associated with PSS, while O2 (~ 533.5 eV) with PEDOT. However, the percentages of PSS calculated from O1 intensity would be overestimated compared to S intensity. They were quite consistent at $\sim 75\%$ and only slightly changed from the surface to the bulk.

Additionally, two chemical species of N were identified and labelled as N1 (~400 eV) and N2 (~402 eV). N1 may be associated with C-N bonding and N2 with protonated nitrogen such as NH_2 . The level of N2 gradually decreased following the depth of material from 24% at the surface to 14% at the bulk.

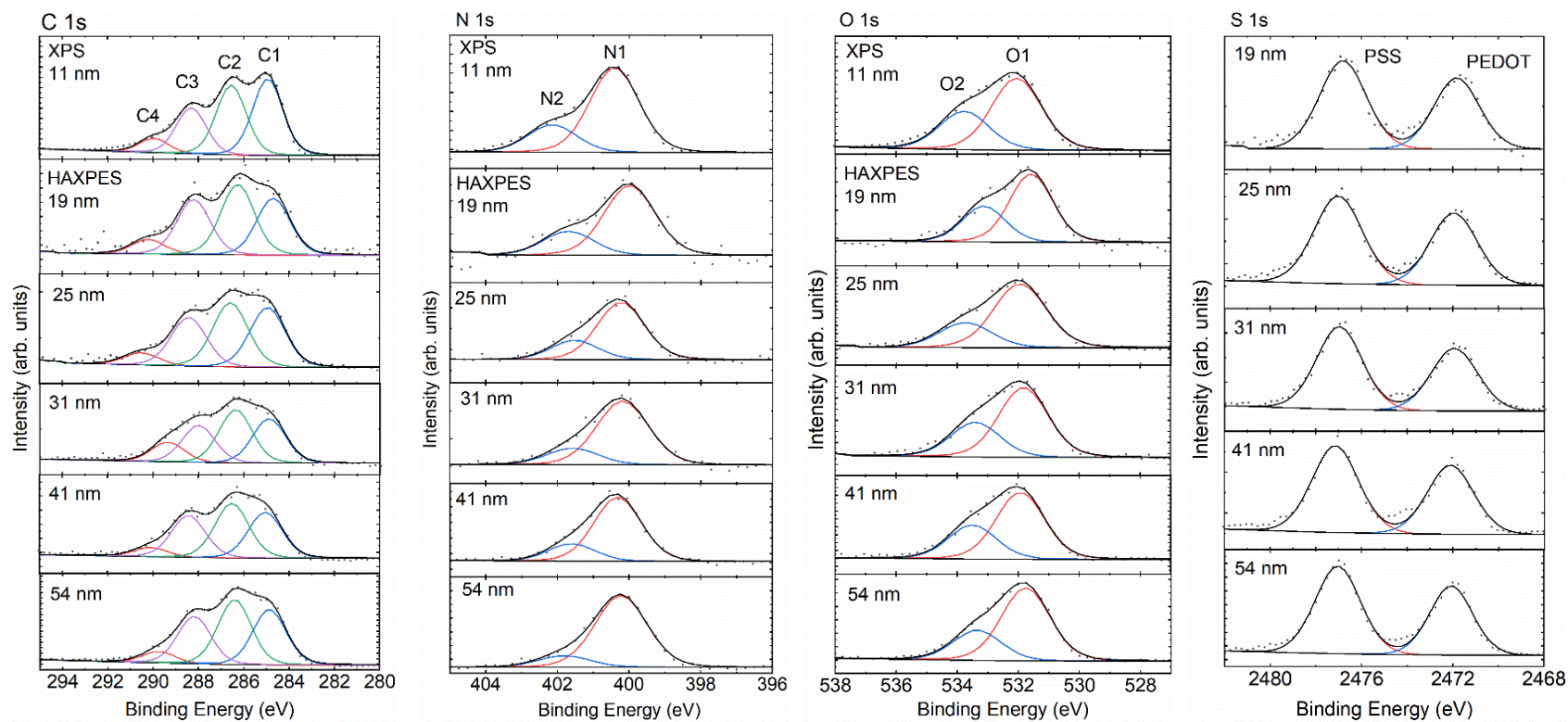


Figure 4.10 The spectra of XPS and angle – resolved HAXPES of C, O, N and S in/on the IPN sample.

4.2.4. Electrochemical characters of electrospun SF and IPN mats

The electrochemical properties of materials were studied in two different systems of potentiostat: three-electrode and two-electrode cells. The results from each system are explained below.

4.2.4.1. Three-electrode system

The results of CV and EIS measurements observed *via* the three-electrode system are shown in Figure 4.11. These measurements were performed by the workgroup of John Hardy, as mentioned previously. The glassy-carbon electrode (GCE) was a representative of inert materials in CV measurement. The electrospun SF showed the same character in CV as the GCE, indicating that the electrospun SF is a non-conductive material. Approximately, an anodic peak at -0.2 V and a cathodic peak at -0.6 V vs. RE (Ag/AgCl) were observed in both IPN ($\alpha = 2.3$) and IPN ($\alpha = 3.3$). The asymmetry between the anodic and cathodic peaks are probably due to differences in background current and kinetic limitations.

The Nyquist plots derived from EIS showed semicircle curves in the high-frequency range. It literally shows the relation of impedances between the real axis and the imaginary axis. The real axis of impedance in the semicircle curve is associated with electron-transfer resistance (R_{et}) [288]. The result showed that R_{et} of IPN ($\alpha = 2.3$) and IPN ($\alpha = 3.3$) were similar at $\sim 350 \Omega$. It also suggested that electrospun SF were homogeneously blended with PEDOT:PSS.

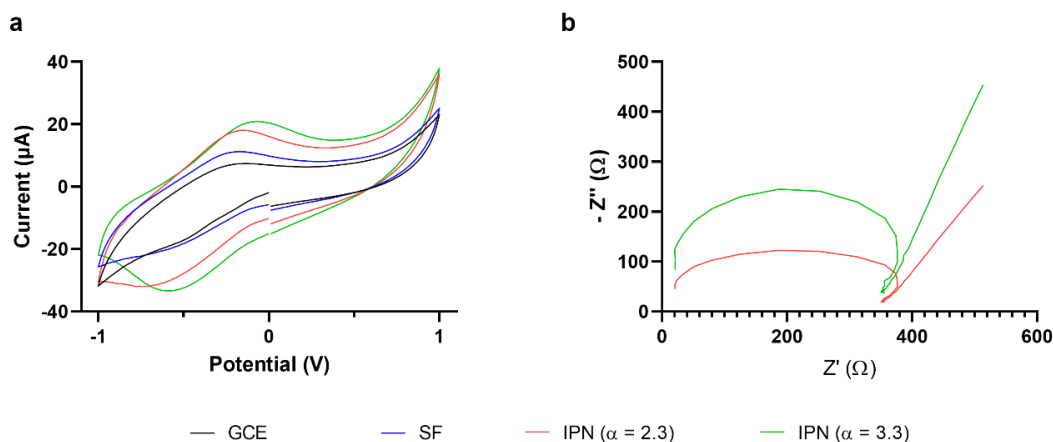


Figure 4.11 CV and EIS of electrospun SF and IPN samples measured with three – electrodes system of potentiostat: (a) CV plot between the sweeping potential of -1 and +1 V, (b) Nyquist plot derived from EIS measurement.

4.2.4.2. Two-electrode system

Only EIS measurements were observed by using the two-electrode system of the potentiostat. The examples of Bode and Nyquist plots, fitted with the Randal circuit model, were shown in Figure 4.12. Compared to the three-electrode system, the semicircle region of the Nyquist plot was low and identified difficulty. After fitting with the Randal circuit model, the results of electrolyte resistance (R_e), a double layer capacitance (C_{dl}), a charge transfer resistance (R_c), and Warburg element (W) were shown in Table 4.2. No significant difference of R_e , R_c , C_{dl} , and W was observed between SF, IPN ($\alpha = 2.3$), and IPN ($\alpha = 3.3$). However, it seems like SF had slightly higher R_e , R_c , and C_{dl} than IPN mats.

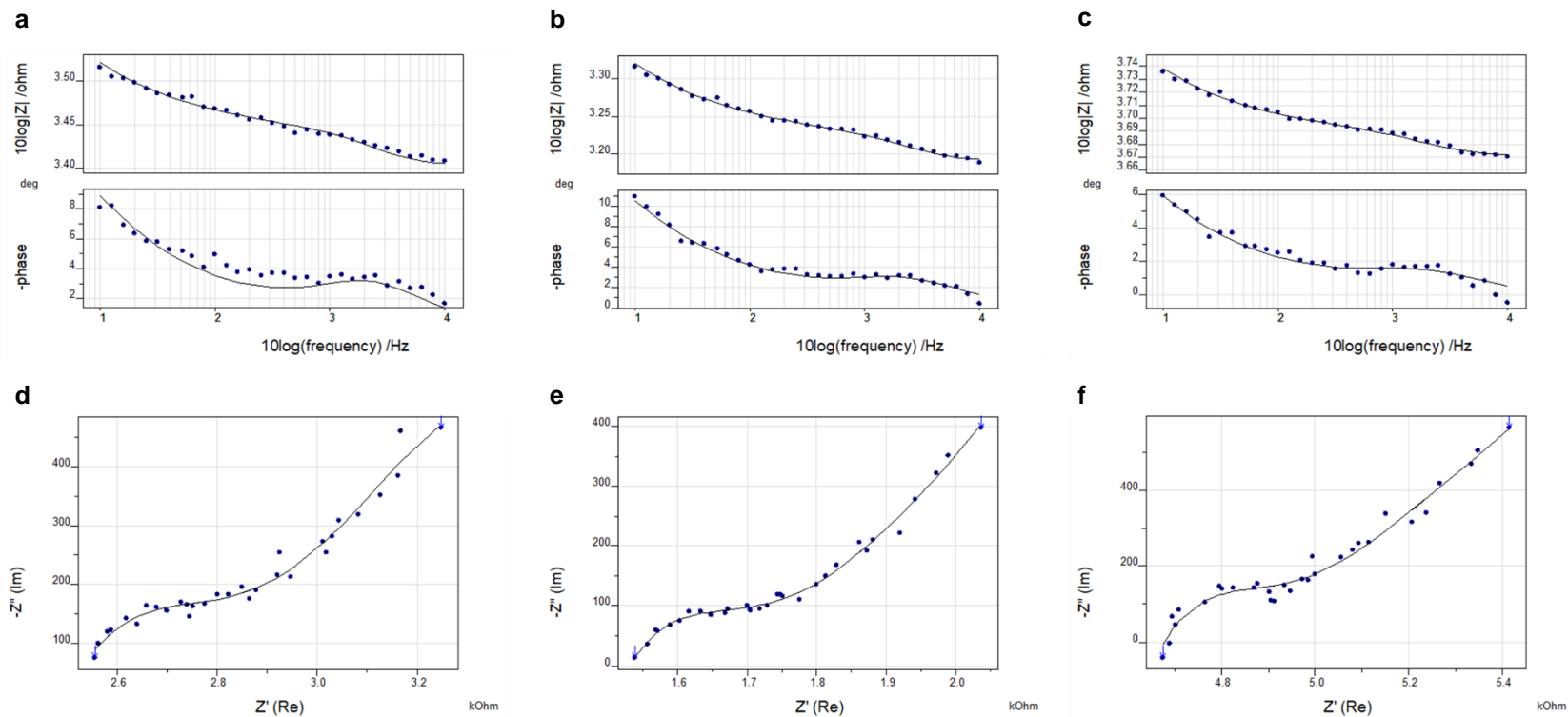


Figure 4.12 Examples of Bode and Nyquist plots derived from EIS measurement fitted with Randles model: (a – c) bode plots of electrospun SF, IPN ($\alpha = 2.3$), and IPN ($\alpha = 3.3$) respectively, and (d – f) Nyquist plots of electrospun SF, IPN ($\alpha = 2.3$), and IPN ($\alpha = 3.3$).

Table 4.2 RC components associated with EIS fitting with Randles model, n is the number of samples.

Materials	Electrolyte resistance (R_e), (Ω)	Charge transfer resistance (R_c), (Ω)	Double layer capacitance (C_{dl}), (μF)	Warburg element (W), ($S^{1/2}/\Omega$)
SF (n=4)	2253 ± 1262	202 ± 68	0.38 ± 0.15	$(2 \pm 0.7) \times 10^{-4}$
IPN ($\alpha = 2.3$) (n=4)	1020 ± 577	149 ± 11	0.28 ± 0.15	$(4 \pm 1) \times 10^{-4}$
IPN ($\alpha = 3.3$) (n=4)	1119 ± 699	192 ± 87	0.25 ± 0.11	$(3 \pm 2) \times 10^{-4}$

4.3. Discussion

4.3.1. Physical properties of IPN mats

Obviously, the dark blue or black colour after IPN for 3 days confirms that PEDOT:PSS can effectively incorporate into electrospun SF mat. PEDOT:PSS particles were bound in/on silk fibres tightly. Small numbers of particles at the surface of the electrospun SF mat were washed out because they could not form the network with silk. Moreover, FTIR results confirm the presence of PEDOT:PSS on IPN mats (dark blue). The absorbance peaks at the wavenumber of 600 – 1300 cm^{-1} representing PEDOT:PSS were noticeable in IPN mats compared to SF mats.

According to the results in this study, PEDOT:PSS incorporated SF exhibits an absorbance peak of 831 cm^{-1} associated with C-S bond in PEDOT [272]. However, other peaks (e.g. 1169, 1124, 1033, 1005, and 671 cm^{-1}) are not in the exact wavenumbers as shown in other studies of PEDOT:PSS [271-273, 284]. Perhaps, it is because the absorbance of PEDOT and PSS are interfered by the presence of SF molecules resulting in peak shifting [284].

Apart from the peak at nearby 831 cm^{-1} , other peaks of the C-S bond should have been presented at 684 cm^{-1} [284] or 674 cm^{-1} [271]. It can be assumed that the peak of the C-S bond was shifted to 671 cm^{-1} in this study. As well as the C-S bond, the peaks of the C-O-C bond at 1187 and 1138 cm^{-1} [271] were shifted to 1169 and 1124 cm^{-1} . Additionally, peaks of SO_3^- and

SO₂⁻ bonds at 1058 and 1010 cm⁻¹ [273] were shifted to 1033 and 1005 cm⁻¹, respectively. Interestingly, all peaks moved toward the positions of lower wavenumber which is known as blue-shift [289]. Since the wavelength is decreased, the frequency is increased because they are in inverse proportions. The energy is then increased too, following this increase in frequency. This blue-shift may be an effect of the interaction between PEDOT:PSS and SF molecules *via* IPN. The FTIR spectra of IPN mats should be investigated and compared with the spectra of purified PEDOT:PSS powder or films to verify this assumption in the future.

Although FTIR results can confirm roughly that the IPN can grow PEDOT:PSS formation in/on the electrospun SF mat, they are unable to quantify how much PEDOT:PSS bind to the SF fibres in the bulk material. In this case, the quantification of surface and bulk chemistry of IPN mats were observed by XPS and angle-resolved HAXPES.

The HAXPES results indicate that the electrospun SF can be modified to conductive material with PEDOT:PSS *via* both dip coating and IPN. However, the IPN is the more successful strategy due to the higher %S in the bulk material also the darker colour after washing. The higher S content of IPN than on dip-coated materials is likely due to the covalent bonds between the EDOT and aromatic amino acids on SF during IPN formation being stronger than the non-covalent adsorption of PEDOT:PSS on SF during dip coating. Both covalent bonds and electrostatic attraction supports tighter bonding between EDOT and SF. Xia Y., *et al.*, 2008 explained that EDOT monomers were oxidised by initiators resulting in the cation radicals, which could be attracted to the negative charges of peptide linkages spontaneously [290].

In the case of IPN material, there were a lot of S at the surface of the material (~11 nm) compared to other depths. It seems like EDOT monomers easily bind to the surface of SF fibre and polymerise to form PEDOT:PSS. However, the spectra of S associated with PEDOT and PSS showed the opposite result. The relative %PSS at the surface was higher (~75%) than at other depths (~65 – 70%). Possibly, EDOT monomers evenly distribute, but PSS is likely to attach at the surface rather than the bulk of materials. On the other hand, surface contamination may affect this measurement as well. As shown in the C1 spectra, it likely indicates the contamination of hydrocarbon at the surface of materials.

Nevertheless, a change in the number of chemical species associating PEDOT and PSS from the surface to the bulk suggests a successful and effective polymerisation. The IPN of PEDOT:PSS in electrospun SF provides a homogeneous material similar to a report of IPN of a copolymer between pyrrole and 3-amino-4-hydroxybenzenesulfonic acid in SF films [291]. On the other hand, this result is in contrast to other reports of IPN of polypyrrole polystyrene sulfonate (PPy:PSS) in SF films [292] and IPN of poly(pyrrole-co-(2-hydroxy-5-sulfonic aniline)) in SF foam [109]. They required two times IPN to achieve homogeneous materials.

Finally, the fibre diameters of SF of IPN mats are similar to SF; this is another piece of supporting evidence that EDOT monomers and PSS can penetrate and polymerise inside SF fibres instead of coating on the surface of SF fibres only.

4.3.2. Mechanical properties of IPN mats

4.3.2.1. Effects of EtOH treatment

Double layer electrospun SF is brittle material due to the ultimate tensile strength (UTS) being similar to the yield stress. This was confirmed by the stress-strain curves seen in Figure 4.5. UTS of dry state – electrospun SF and others mats, as shown in Table 4.1, were extremely low compared to natural *B. mori* SF, which is around 300 – 740 MPa of UTS [127]. Since SF molecules were dissolved in the solvent and reformed as nanoscale or microscale fibres *via* electrospinning, the UTS of electrospun SF was decreased. Similarly to other studies, the UTS of electrospun SF was approximately 1 – 10 MPa [147, 293-296]. After treatment with EtOH or MeOH, their UTSs were increased but their strains were decreased [295-297]. It indicates that β -sheet in SF after treatment mainly affect to tensile property of electrospun SF.

The β -sheet structure is a supporting structure of SF fibre strength and stability. It can block the sliding between molecule chains during tensile loading [258]. Thus, a higher amount of β -sheet tends to exhibit more brittle material. On the other hand, Koh L.-D., *et al.*, 2015 reviewed four interesting aspects regarding the relation of β -sheet and mechanical property of SF: intermolecular and intramolecular β -sheet, arrangement of β -sheet (*i.e.* parallel and anti-parallel), size of β -sheet, and orientation of β -sheet [127]. According to the results in chapter 3, EtOH not

only increased β -sheet formation but also showed relevance to anti-parallel β -sheet, which could also affect the observed stress-strain results as well.

As shown in Figure 3.13, FTIR spectra of electrospun SF mats, the amide I peaks were at 1621 cm^{-1} . This peak commonly determines the characteristics of silk II, anti-parallel β -sheet [234, 298, 299]. In anti-parallel, β -strands arrange in opposite directions of C-terminus to N-terminus, while in parallel, all β -strands are in the same direction of C-terminus to N-terminus. The different arrangement causes the different geometry of hydrogen bonds between strands, which are in-line and zigzag arrangements in anti-parallel and parallel, respectively. However, the hydrogen bond strength in anti-parallel is stronger than in parallel resulting in stiffness of the crystal [300]. Therefore, the higher UTS and lower strain after EtOH treatment are likely to be due to the increase of the anti-parallel β -sheets.

4.3.2.2. Effects of water as plasticiser

After the EtOH treated electrospun SF is re-hydrated, its UTS is drastically reduced to a steady point ($\sim 1\text{ MPa}$) without changing by time. In contrast, its strain at break is extremely increased ($\sim 5 - 10$ times) and likely to be time-dependent, as shown in Figure 4.5. The Young's modulus of the wet state – EtOH treated electrospun SF is lower than the dry state suggesting more flexibility. It can be presumed that the softer and more flexible material is due to the effect of the water plasticiser.

The intermolecular cohesive force between protein chains can be interrupted by water; thus, the chain movement is promoted, especially in the non-crystalline region [242, 301]. Firstly, the protein chains can easily slide away from each other without breaking during tensile loading. Then the displacement of the fibre mat before breaking is longer in the wet state. However, water may not disrupt hydrogen bonds between protein chains in β -sheet [302]; this is likely to be due to the hydrophobic property of the β -sheet folding.

Interestingly, the strain at break is likely to be increased over time when the electrospun mat is immersed in water, as shown in Figure 4.5 (c and d). It is presumed that this is somehow related to water uptake. Water uptake indicates the hydrophilic characterisation of electrospun

material. It is gradually increased until it reaches the saturated point. Andiappan M., *et al.*, 2013 reported that electrospun SF saturated at 96 h [303]. Compared to the results in this study, Figure 4.5 c and d are then representative tensile testing results in the non-saturated and saturated state of water uptake, respectively. Therefore, water molecules in the electrospun mat immersed in water for a week are higher than immersed for a few days resulting in the different strain at break.

In order to confirm this prediction, the water uptake and porosity of the electrospun SF mat should be observed in the future. The water uptake can be measured by weighing the wet sample compared to the dry sample. The percentage of water uptake is then simplified [113, 303, 304]. In addition, porosity determined by the apparent density and the bulk density is recommended [113, 304].

4.3.2.3. Effects of IPN of PEDOT:PSS on electrospun SF mat

PEDOT:PSS has limited stretchability due to its rigid conjugated backbone and strong interchain interaction [305]. The mechanical flexibility of PEDOT:PSS can be enhanced by blending with another polymer. Several studies showed that after blending with a polymer, the stress-strain profile of PEDOT:PSS composite was quite similar to the polymer (*e.g.* waterborne polyurethane (WPU) [306], polyurethane (PU) [307] and SF [308]). However, the higher amount of PEDOT:PSS tends to exhibit a more brittle character of the composite polymer, leading to higher stress and lower strain [306, 307].

In this study, the IPN of PEDOT:PSS on EtOH treated electrospun SF mat was fragile and difficult to handle for tensile loading in the dry state. This suggests that PEDOT:PSS probably promotes more brittleness in comparison to EtOH treated electrospun SF.

In the wet state, IPN mats with the α of 1.3, 2.8, and 3.3 have lower mechanical properties (*i.e.* UTS, % strain at break, and toughness) compared to EtOH treated electrospun SF, as shown in Figure 4.6. Herein, all α ratios contain a similar concentration of PEDOT but a different amount of PSS. This result indicates that the total amount of PEDOT:PSS and also the PSS/EDOT ratio somehow affects the mechanical properties of composite material.

Tsukada S., *et al.*, 2012 revealed a successful modification of SF with PEDOT:PSS *via* electrodeposition coating (E-coating). In the wet state, PEDOT:PSS silk thread, which has similar mechanical properties to pristine SF, was an electrically conductive material, and its conductivity was high enough for use as an electrocardiograph (ECG) electrode [308]. From this aspect, the IPN ($\alpha = 2.3$) and ($\alpha = 3.3$) were then selected as representatives of similar and different mechanical properties to EtOH treated electrospun SF for further studies.

4.3.2.4. Effect of fibre alignment

Typically, the direction of aligned fibres and tensile loading significantly influence the results of mechanical properties. The tensile loading parallel to aligned fibres provides higher UTS and strain at break than tensile loading in the transverse direction. Whilst, UTS and strain of random fibres are in the middle between those two groups [309].

The electrospun mat in this chapter, is fabricated by double-layer electrospinning of random and aligned fibres. The tensile loading direction is parallel to fibre alignment (axial loading). The thickness of the random fibres layer is around 2/3 of bulk material. Possibly, the UTS and strain mainly depend on the mechanical properties of random fibres with a small reinforcement by aligned fibres. In order to prove this hypothesis, the effect of material thickness on the mechanical property is another suggestion for further study. The thickness of each layer should be varied, and the tensile should be loaded in the transverse direction of fibres as well.

4.3.2.5. Possibility to implantation

The double layer electrospun SF mat in the dry state has high processability, which is able to fold or roll without tearing. Both electrospun SF and IPN mats in the hydrated state show more elasticity compared to the dry state; therefore, they maybe able to roll as a hollow tube. However, the current fibre mats developed in this study may not be strong enough for rolling or folding as the nerve conduit, due to two main reasons: the thickness of materials and the softness of fibres in the wet state.

A previous study reported that PEG nerve conduit used in the *in vivo* analyses had a wall thickness of 250 μm [207]. Another study showed that the groove structure nerve conduit

made from PCL/PLA with a wall thickness of 70 μm was able to support peripheral nerve regeneration *in vivo*, and the increase of wall thickness had no positive results on the biological response of the regenerating nerve [310]. The thickness of epineurium is varied depending on the location of nerves, while that of perineurium is typically 7 – 20 μm [311]. For example, the epineurium thickness of a rat sciatic nerve (Sprague-Dawley rats) is $\sim 130 \mu\text{m}$ [312]. In comparison to the results of this chapter, it suggests that the electrospun SF and IPN mats with a thickness of $\sim 100 \mu\text{m}$ may be possible to shape as a nerve conduit as well. However, the shaping process and the stability of the hollow structure should be investigated and considered in the next further steps.

Unfortunately, the ultimate tensile strengths of electrospun SF and IPN mats were seen to be lower than that of peripheral nerve *in situ* (rabbit tibial nerves), which is $\sim 11.7 \text{ MPa}$ [15, 313]. This suggests that the electrospun SF and IPN mats could be preferable to be used as an inner layer for other hollow nerve conduits.

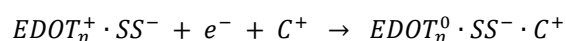
Finally, the mechanical properties of electrospun SF and IPN mats are significantly changed in the wet state due to the water plasticiser effect. This may lead to the collapse of the hollow tube in the wet state. Therefore, it can be presumed that the material thickness of $\sim 100 \mu\text{m}$ is enough for rolling as the hollow tube, but the stability of the tube must be considered in both dry and wet states.

4.3.3. Electrochemical properties of IPN mat

Electrical double layer (EDL) and redox reaction are outstanding electrical properties of PEDOT:PSS. PEDOT containing positive charge works as a backbone of conductive polymer. PSS comprising of a negative charge was doped into the PEDOT which then neutralised the positive charge of the backbone structure.

4.3.3.1. Redox peak current and conductive potential window

In CV measurement, the oxidation and reduction of PEDOT are associated with electrical conductivity and insulation, respectively, as shown in the chemical equation below [157]:



where, EDOT is EDOT monomers of PEDOT, n is the number of EDOT, SS⁻ is styrenesulfonate of PSS, e⁻ is the electron, and C⁺ is cation in the electrolyte.

As shown in Figure 4.11 (a), the higher anodic peak of IPN ($\alpha = 2.3$) and IPN ($\alpha = 3.3$) compared to SF confirms that PEDOT:PSS promotes electron transfer of SF mat [314]. Moreover, the shifting of reduction potential (E^0) to more negative extends the conductive range of PEDOT:PSS [157]. Commonly, E^0 is estimated by the average of anodic (E_a) and cathodic (E_c) peak potentials (*i.e.* $E_0 = (E_a + E_c) / 2$). In comparison to the result in this study, it seems like E^0 of IPN ($\alpha = 2.3$) is more negative shifting than E^0 of IPN ($\alpha = 3.3$). This shifting suggests that IPN ($\alpha = 2.3$) has a wider conductive potential window which might be better to use as EDL electrodes than IPN ($\alpha = 3.3$).

However, the CV measurement in this study is just a qualitative analysis to briefly confirm the character of electrically conductive material of IPN mats. The electrical conductivity should be observed again *via* EIS.

4.3.3.2. Quantification of charge transfer resistance

In EIS measurement, the electron transfer resistance (R_{et}) or charge transfer resistance (R_c), estimated by the real axis of the Nyquist plot, was different between three-electrode and two-electrode systems. Not only the electrodes system but also electrolyte affects the EIS result. The relation between R_c , charge transfer resistivity (ρ), and electrical conductivity (σ) of the IPN mat can be simplified by the equations below:

$$R_c = \rho \frac{L}{A} \text{ and } \sigma = \frac{1}{\rho}$$

where, L is the length (m), and A is the surface area (m²). In this study, L is the thickness of materials ($\sim 100 \mu\text{m} = 10^{-6} \text{ m}$), and A is estimated briefly from the surface area of material, which is immersed in the electrolyte ($\sim 1 \text{ cm}^2 = 10^{-4} \text{ m}^2$). In two-electrode system, the σ are $\sim 4.95 \times 10^{-3}$, $\sim 6.71 \times 10^{-3}$, and $\sim 5.21 \times 10^{-3} \text{ S/m}$ in SF, IPN ($\alpha = 2.3$), and IPN ($\alpha = 3.3$) respectively. These results suggest that lower PSS concentration in the amount of PEDOT:PSS may increase the electrical conductivity of a material as similarly explained in other studies [270, 315].

However, it is still difficult to conclude that IPN ($\alpha = 2.3$) has higher electrical conductivity than IPN ($\alpha = 3.3$) because the measurement in the three-electrode system shows the opposite result. The σ of both IPN ($\alpha = 2.3$) and IPN ($\alpha = 3.3$) are similar as $\sim 2.86 \times 10^{-3}$ S/m. The measurement protocol, including the type of electrolytes and reference electrodes, should be optimised in the future for accurate and precise quantification. Alternatively, scanning electrochemical microscopy (SECM) or scanning ion conductance microscopy (SICM) are recommended for deeply investigating and visualising electrochemical activity in each local area of bulk material [316].

4.4. Conclusion

An interpenetrating polymer network (IPN) is a successful and effective strategy to modify electrospun SF with PEDOT:PSS for the purpose of using it as an electrically conductive material. Basically, IPN mats are dark blue or black in colour, and their chemical species, associated with PEDOT:PSS, can be assessed by FTIR, XPS, and HAXPES. During polymerisation, the network of PEDOT:PSS can grow on the surface of SF fibres and the bulk of material without any effect on SF fibre diameter. The IPN mat is stable in water for a long time and no PEDOT:PSS residual detaching from the mat can be visually observed.

The mechanical properties of IPN mats rely on the properties of electrospun SF mat before modification. Herein electrospun SF is commonly treated with EtOH before IPN, resulting in a brittle material due to the increase of anti-parallel β -sheet crystalline regions in SF. After polymerisation, PEDOT:PSS networks promote the more brittle character of the composite material. Therefore, the IPN mat is fragile and unable to handle easily, especially in the dehydrated state. However, the IPN mat is more soft and flexible similar to EtOH treated SF mat in the hydrated state due to the water plasticiser. All conditions of IPN mats are categorised into two groups depending on their wet state mechanical properties: similar to and different from EtOH treated SF.

IPN ($\alpha = 2.3$) and IPN ($\alpha = 3.3$) are collected as a representative of those two groups respectively (similar to and different from EtOH treated electrospun SF). Their electrochemical properties are observed *via* cyclic voltammetry (CV) and electrochemical impedance spectroscopy

(EIS). The highly negative shifting of anodic and cathodic peaks of IPN mats suggest that both IPN ($\alpha \approx 2.3$) and IPN ($\alpha = 3.3$) are electrically conductive materials. Although their electrical conductivities are still unable to be exactly confirmed in this study, they are possibly higher than the conductivity of pristine SF confirmed by EIS measurement with a two-electrode system.

Finally, both IPN ($\alpha = 2.3$) and IPN ($\alpha = 3.3$) are interesting electrically conductive materials, which are possible to use as a new generation of peripheral nerve tissue scaffolds. Their toxicities, biocompatibilities, and abilities to promote neuron growth and neurite extension will be studied *in vitro*, as shown in the next chapter.

CHAPTER 5

***In Vitro*, Neuron Growth and Neurite Extension on Electrically Conductive Electrospun Mats**

The possibility of using electrospun SF and electrically conductive IPN mats with PEDOT:PSS as a scaffold for peripheral nerve regeneration initially requires *in vitro* biocompatibility testing. The developed materials were tested in both indirect (conditioned or extracted medium) and direct contact protocols. In this study, a hybrid neuroblastoma x glioma cell line (NG108-15) was a representative of peripheral nerve cells. The results of cell proliferation and neurite extension on the various conditions of materials will be described in this chapter.

There are three main purposes of the study in this chapter: (1) to examine the toxicity of chemical residues from IPN mats; (2) to study and compare the cell growth behaviours and the neurite outgrowth on electrospun SF and IPN mats in both with and without laminin coating; and (3) to find the optimal IPN mat, which has the potential for applying electrical stimulation to promote longer neurite extension length.

Although SF and PEDOT:PSS are biocompatible, the solvent in the electrospinning process (e.g. FA) and initiators for functionalising PEDOT:PSS in/on electrospun SF (e.g. FeSO_4 , and $\text{Na}_2\text{S}_2\text{O}_8$) maybe toxic to cells [257, 317, 318]. The IPN ($\alpha = 1.3, 1.8, 2.3, 2.8$, and 3.3) mats were then prepared for indirect testing. They were incubated with cell culture medium for 24 h, and their conditioned media was then collected for separate culturing with NG108-15 cells for 3 days. The results of cell viability *via* live/dead staining, cell metabolic activity, and DNA concentration were investigated to confirm the biocompatibility of IPN mats. Moreover, this experiment highlights the importance of the washing process before using IPN mats in cell culture.

On the other hand, NG108-15 cells were cultured on the electrospun SF and IPN mats for the direct contact test. Electrospun SF, IPN ($\alpha = 2.3$), and IPN ($\alpha = 3.3$) mats were selected for this direct test due to their mechanical and electrical properties, as mentioned in the conclusion of chapter 4. NG108-15 cells can be cultured in two phases: growth and differentiation. They grow

individually with small neurite extension in the growth phase, while they aggregate into clusters and extend longer neurites in the differentiation phase compared to the growth phase. After optimisation, the cAMP medium is preferable to use as the differentiation medium in this chapter. It is to be noted that the optimisation of the differentiation medium will be presented at the first result in this chapter (section 5.2.1).

Apart from the cell metabolic activity and DNA concentration results representing cell viability and proliferation, the image analysis of neurite extension length and orientation of fibre mats were also performed in the direct test. Images of cells in the growth phase on materials were collected by SEM, while the differentiated cells labelled with fluorescent dyes to visualise their nuclei and neurites were collected their images by using a High-Content Analysis (HCA) system. Moreover, the effects of fibre mats with and without laminin coating on cell growth and neurite outgrowth were investigated in this chapter as well, since laminin is a typical molecule for supporting NG108-15 adhesion on substrates [319].

Finally, the best IPN mat was selected, according to cell growth and neurite extension length results. It is to be expected that the IPN mat should extend a longer neurite length than the electrospun SF mat. The IPN mat, which can promote the longest neurite, will be chosen for study with electrical stimulation in the next chapter.

5.1. Materials and Methods

5.1.1. Sample preparation for cell culture

Electrospun SF mats were cut into the specific size (e.g. 3 x 3 cm² for indirect test and 1.5 x 1.5 cm² for direct test). The sample for the direct tests were mounted on glass coverslips before use. The prepared samples were treated with 80% EtOH for 20 min and washed twice with distilled water. They were then functionalised with PEDOT:PSS by using the IPN protocol. The IPN protocol was described in 4.1.1.

5.1.1.1. Sample for indirect test (conditioned medium)

EtOH treated electrospun SF and IPN mats were cut into pieces of 3 x 3 cm² without mounting on glass coverslips. They were washed in DI water overnight, sterilised by immersing in 70% EtOH for 10 min and exposing with UV radiation for 15 min sequentially. The UV source was from the UV lamp of the biosafety cabinet. The distance between the UV source and samples was ~30 – 50 cm. The samples were washed twice with phosphate buffer saline (PBS) before immersing in the growth medium. The total volume of the medium was 6 ml/sample. The samples were then incubated at 37° C for 24 h. Then these conditioned media were then collected for cell culture separately.

5.1.1.2. Sample for direct contact test

Electrospun SF mats of ~1.5 x 1.5 cm² were mounted on square glass coverslips of 1.2 x 1.2 cm² using 80% EtOH, as shown in Figure 5.1. The mounted samples were also treated with 80% EtOH for 20 min, followed by IPN as a later step. The IPN mats were washed overnight and sterilised, as mentioned above. If laminin coating was needed, laminin from Engelbreth-Holm-Swarm murine sarcoma basement membrane (Sigma-Aldrich) was used in the experiment. The laminin was diluted to 5 µg/ml in PBS and was dropped onto a sample with a small volume (~100 – 200 µl), just for covering all surface areas. Finally, laminin-coated samples were incubated at 37° C for 2 h before cell seeding.

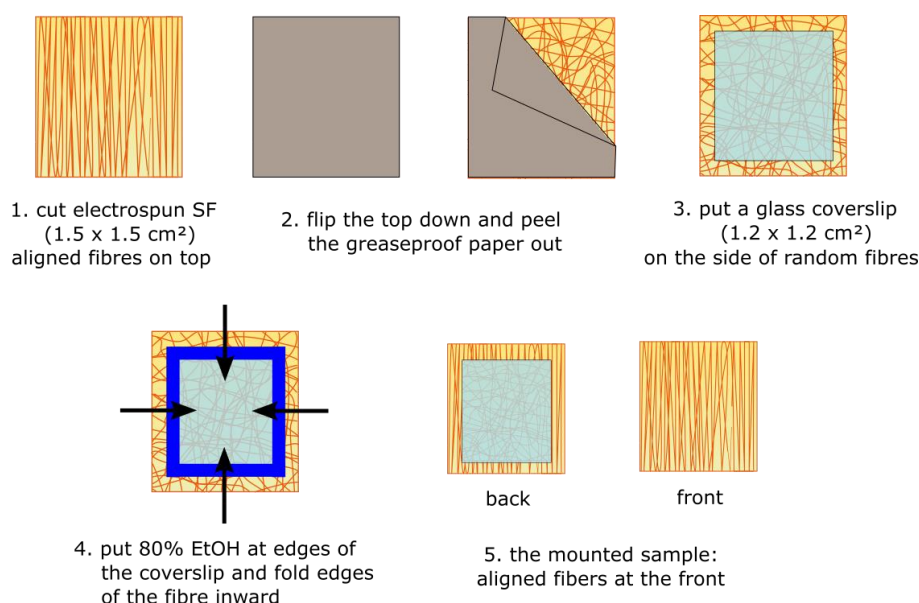


Figure 5.1 Schematic of the mounting protocol of electrospun SF mat on glass coverslip before IPN of PEDOT:PSS on samples.

5.1.2. NG108-15 cell culture

NG108-15 cells were cultured in T-75 flasks with 12 ml of growth medium composed of base medium supplemented with 10% fetal bovine serum (FBS). The base medium was prepared by mixing Dulbecco's modified eagle medium (DMEM, Sigma) high glucose with 1x HAT supplement (Gibco) and 0.01% v/v penicillin/streptomycin (P/S) as the final concentration. The 1x HAT contained 100 μ M sodium hypoxanthine, 0.4 μ M aminopterin, and 16 μ M thymidine. Cells were incubated at 37° C with 5% CO₂, and the growth medium was refreshed every 2 – 3 days to avoid acidic metabolic waste in the medium, which can cause cell detachment. The bright field inverted microscope (EVOS) was used for observing cell morphology during cell culture.

Cells were passaged when the cell confluence reached 80 – 90%. They were gently washed with PBS prior to adding 1 ml of trypsin. Then they were incubated at 37° C for 2 min. After that, the growth medium was added into the cell culture flask up to 12 ml and gently mixed well to disperse single-cell suspension in the medium. Approximately 1/10 (~ 1 ml) or 1/5 (~ 2ml) of the trypsinised cell solution was taken for culture in a new T-75 flask with the final volume of 12 ml growth medium.

5.1.2.1. Cell counting

If a specific cell number or cell seeding density was required for an experiment, the trypsinised cells were transferred to a 15 ml tube and centrifuged at 1400 rpm for 5 min. The supernatant was poured out, and the cell pellet was then re-suspended in 4 ml of fresh growth medium. The cell solution was collected randomly for 10 µl, mixed with 10 µl of trypan blue, and 10 µl of the mixed solution was then seeded in a hemacytometer for cell counting under a bright field inverted microscope (EVOS). Live cells were obviously seen as transparent rounded cells, while dead cells were stained dark blue. Cell number and the percentage of cell viability were calculated following the common protocol as shown in equations below:

$$\text{cell number} = \frac{1}{4} \times \text{dilution factor} \times \text{cell count (live cells)} \times \text{total volume (ml)} \times 10^4$$

$$\% \text{ cell viability} = \frac{\text{cell count (live cells)}}{\text{total cell count (live and dead cells)}} \times 100$$

where, the dilution factor is the ratio between the volume of the cell solution (µl) per the total volume of the cell and trypan blue (µl). By mixing 10 µl of cell with 10 µl of trypan blue, the dilution factor is equal to 2 in this study. Cells were used in the experiment only when the cell viability is more than 90%.

5.1.2.2. Differentiation phase of NG108-15

NG108-15 cells can greatly extend their neurites when they are in the differentiation phase. Cells need to be initially cultured in the growth medium for 2 – 3 days. After cells were tightly attached and expanded on the substrate, the growth medium was changed to a differentiation medium. In this study, there are two types of differentiation media, which will be called cAMP medium and DMSO medium.

The cAMP medium was prepared from the common growth medium (as mentioned above) supplemented with 0.75 mM of dibutyryl cyclic adenosine monophosphate (dibutyryl cAMP, Stratech). The DMSO medium was composed of the basal medium supplemented with 1.5% dimethylsulfoxide (DMSO) and 0.5% FBS.

Finally, there were five types of cell culture media in this study. The compositions of each medium were shown in Table 5.1.

Table 5.1 Compositions of each cell culture medium.

Types of media	Compositions
Basal medium	<ul style="list-style-type: none"> • DMEM high glucose (D5796, Sigma) • 1x HAT supplement (Gibco) <ul style="list-style-type: none"> ○ 100 μM Sodium hypoxanthine ○ 0.4 μM Aminopterin ○ 16 μM Thymidine • 0.01% v/v Penicilin/streptomycin
Growth medium	<ul style="list-style-type: none"> • Basal medium • 10% v/v FBS
Conditioned medium	<ul style="list-style-type: none"> • Basal medium • 10% v/v FBS <p>It is to be noted that the conditioned medium is based on the growth medium incubated with the electrospun SF mat or IPN mats for 24 h. The incubation ratio between the area of the fibre mat and the growth medium is 9 cm² : 6 ml.</p>
Differentiation medium (cAMP medium)	<ul style="list-style-type: none"> • Basal medium • 10% v/v FBS • 0.75 mM cAMP
Differentiation medium (DMSO medium)	<ul style="list-style-type: none"> • Basal medium • 0.5% v/v FBS • 1.5% v/v DMSO

5.1.3. Indirect test (conditioned medium)

NG108-15 cells were cultured in 24-well plates with a cell seeding density of 5,000 cells/cm², approximately 10,000 cells/well, in the total growth medium of 1.5 ml. They were cultured for 7 days in total, as shown in Table 5.2. On day 2, the growth medium was refreshed. On day 4, the growth medium was changed to the conditioned medium, as mentioned in section 5.1.1.1. On

days 5 – 7, cell morphology, metabolic activity, and DNA concentration were examined every day. Therefore, subconfluent cells were cultured in conditioned media for 3 days (72 h) in total. Cell metabolic activity, DNA concentration, and cell viability *via* live/dead staining were assessed to evaluate the toxicity of chemical residues from the electrospun SF mat and IPN mats; the details of these assays will be described in sections 5.1.5, 5.1.6, and 5.1.7, respectively.

Table 5.2 Cell culture activities for 7 days in the indirect test (conditioned medium).

Activities	Incubation period							
	Day 0	Day 1	Day 2	Day 3	Day 4	Day 5	Day 6	Day 7
Study of cell growth, proliferation, and viability	Cell seeding on the TCP with the growth medium at Day 0 and refresh the medium at Day 2				Change the growth medium to the conditioned medium at Day 4 and 6			
					Time in the conditioned medium			
					0 h	24 h	48 h	72 h

5.1.4. Direct contact test

Samples, mounted on glass coverslips (as mentioned in section 5.1.1.2), were plated into 12-well plates with a surface area of ~4 cm²/well. Ideally, the cell seeding density of 5,000 cells/cm² in the total growth medium of 1.5 ml is required in this experiment. Hence, NG108-15 of 20,000 cells in 1.5 ml were seeded into each well of the sample. After seeding, cells were observed under the light microscope immediately to confirm the dispersion of cells in all areas, including the sample surface. If cells were not well dispersed, they were gently mixed again. Therefore, the cell density on a sample was approximately 5,000 cells/cm².

However, it was not possible to assess the cell adhesion of cells cultured on fibre mats with the inverted light microscope due to the opacity of the materials. The cell dispersion on fibre mats was assumed by observing cells on the outer area of the sample (*i.e.* the surface of the cell culture well without being covered by materials). It was assumed that the dispersion of cells on these materials were similar to the control (glass coverslip).

5.1.4.1. Study of cell growth and proliferation

Cells were cultured for 7 days in total; during this period, the growth medium was refreshed every 2 days (at day 2, 4, and 6), as shown in Table 5.3. Cell morphology, metabolic activity, and DNA concentration results were ascertained on days 1, 3, 5, and 7 after seeding. The glass coverslip was a control substrate in this experiment. Prior to testing metabolic activity and DNA concentration, samples were picked and transferred to the new TCP to avoid the overestimated results from cells growing outside the sample. The metabolic activity and DNA concentration protocols are described in sections 5.1.5 and 5.1.6, respectively.

5.1.4.2. Study of cell differentiation and neurite extension

As well as the cell growth and proliferation study, cells were cultured for 7 days in total. First, cells were seeded on materials and cultured in the growth medium for 2 days (48 h). The day of cell seeding was day 0. On day 2, the growth medium was changed to the differentiation medium (cAMP medium), and cells were then cultured in the differentiation medium for 5 days (from day 2 – day 7) with refreshing the medium every 2 days, as shown in Table 5.3. The morphology of differentiation cells grown on samples was observed by SEM and immunofluorescence on days 5 and 7. The sample preparations for imaging *via* SEM and immunofluorescence are described in sections 5.1.8 and 5.1.9, respectively.

Table 5.3 Cell culture activities for 7 days in the direct contact test.

Activities	Incubation period							
	Day 0	Day 1	Day 2	Day 3	Day 4	Day 5	Day 6	Day 7
Study of cell growth and proliferation	Cell seeding on the fibre mat with the growth medium at Day 0 and cultured in the growth medium for 7 days (refresh medium at Day 2, 4, and 6)							
Study of cell differentiation and neurite extension	Cell seeding on the fibre mat with the growth medium at Day 0		At Day 2, change the growth medium to the differentiation medium and cultured for 5 days (refresh differentiation medium at Day 4 and 6)					

5.1.5. Cell metabolic activity *via* resazurin assay

The resazurin solution was prepared by dissolving resazurin sodium salt (Sigma-Aldrich) in PBS with a concentration of 0.125 mg/ml. The prepared solution was filtered for sterilisation with a 0.45 µm filter. By keeping it at 4° C in the opaque container, it can be used for up to a year.

In the metabolic activity experiment, the filtered solution was diluted again in the growth medium with a volume ratio of 1:10, and the working solution was incubated at 37° C for 15 min in a water bath before use. The cell culture medium was discarded the well of the sample and refreshed with 1 ml working solution. Samples with the working solution were incubated at 37° C, 5% CO₂ for 1 h. After that, the supernatant of each sample was collected for 100 µl and transferred to a 96-well plate in triplicate. The fluorescence intensity was assessed by a microplate reader (BMG FLUOstar Optima) with the excitation/emission wavelengths of 544/590 nm.

5.1.6. DNA concentration *via* PicoGreen® assay

Quant-iT™ PicoGreen™ dsDNA assay kit (ThermoFisher) was used for quantification of DNA concentration in this study. Firstly, the 20x Tris-EDTA (TE) buffer was diluted to 1x TE buffer in UltraPure™ DNase/RNase – free distilled water (Invitrogen). PicoGreen® reagent was then diluted in 1x TE buffer with the volume ratio of 1:200, which is called PicoGreen® working solution.

Meanwhile, cells were gently washed with PBS 1 time and lysed using a needle or cell scraper in 500 µl of 1x TE buffer. The whole lysed solution, including fibre mats, was transferred to a sterile microcentrifuge tube. It was lysed again *via* the freeze-thaw process in triplicate. After that, the solution was centrifuged to separate fibres from the solution. The supernatant was collected and mixed with the PicoGreen® working solution with the volume ratio of 1:1 in a 96-well plate. Here, the volume of either 50:50 µl or 100:100 µl was recommended. The well plate was protected from the light and incubated at room temperature for 5 min. The fluorescence intensity was observed by a microplate reader (BMG FLUOstar Optima) with the excitation/emission wavelengths of 485/520 nm.

5.1.7. Live/dead staining

The live/dead assay is used for visualising live and dead cells of non-differentiated cells after culturing with conditioned media (indirect test). It is the qualitative analysis of cell viability. Calcein AM (Invitrogen) and ethidium homodimer (EthD-1, Invitrogen) were diluted in PBS with the final concentration of 2 and 4 μM , respectively. After cell samples were washed with PBS, the diluted live/dead solution was added to the cell samples before incubating at 37° C for 10 min. 100 – 200 μl of the solution was recommended and this was enough to cover all surface areas of the sample. The stained cell samples were observed under a fluorescent microscope (Nikon Eclipse 50i). The excitation/emission wavelength of 495/515 nm is associated with calcein AM and 495/635 nm with EthD-1, resulting in green and red images respectively. Live cells were stained as green regions in the cytoplasm and dead cells as red spots at nuclei.

5.1.8. Scanning electron microscopy (SEM) of cell samples

Cells growing on electrospun samples were gently washed with PBS 1 time, and they were then fixed with 2.5% v/v of glutaraldehyde in PBS at 4° C for 30 min. The fixed samples were washed with PBS twice. After that, they were dehydrated by a series of EtOH gradients: 50%, 70%, 90%, and 100% for 5 min/each. Lastly, samples were immersed in hexamethyldisilazane (HMDS) at room temperature for 5 min and evaporated in the fume cupboard overnight. The morphologies of cells on fibre mats were observed by SEM, using the same protocol mentioned in chapter 3 (in section 3.1.5).

5.1.9. Immunofluorescence (IF)

β -III tubulin, an element of microtubule in neurites, was stained by an antibody labelled with a fluorescent dye and observed by a High-Content Analysis (HCA) system (CQ1, Yokogawa).

Firstly, cells on electrospun samples were gently washed with PBS 1 time and fixed with 10% neutral buffer formalin solution, containing ~4% paraformaldehyde (Sigma – Aldrich) at room temperature for 15 min. The fixed samples were washed with PBS twice and permeabilised by adding 500 μl of Q&P solution and leaving them at room temperature for 5 min. Herein, Q&P

stands for quenching and permeabilising, and the Q&P solution was prepared by diluting 0.5% v/v of Triton X-100 (Sigma) in 0.2 M glycine in PBS. Next, each permeabilised sample was washed with PBS twice and blocked non-specific proteins by adding 300 µl of 2% w/v of gelatin from cold-water fish skin (FSG, Sigma - Aldrich) in PBS solution and leaving at room temperature for 30 min.

After blocking, the FSG solution was removed, and 200 – 250 µl of the primary antibody solution was immediately added to each sample and incubated at 4° C overnight. Rabbit polyclonal to β -III tubulin (Abcam) was diluted in 2% FSG solution with the volume ratio of 1:1000, and it was then used as primary antibody solution. After incubating with the primary antibody overnight, each sample was washed with PBS twice prior to staining with secondary antibody, goat anti-rabbit IgG H&L labelled with Alexa Flour® 488 (Abcam). The secondary antibody was diluted in 2% FSG solution with the volume ratio of 1:1000 before use. A volume of 200 – 250 µl was recommended to be added to each sample. All samples were protected from light and incubated with the secondary antibody solution at room temperature for 2 h.

The antibody-stained samples were washed with PBS twice. If the nuclei of cells were needed to be visualised, a 4',6-diamidino-2-phenylindole (DAPI, Invitrogen) stain was used. DAPI was diluted in PBS with the volume ratio of 1:1000 before staining each sample at room temperature for 5 min. It was then washed with PBS twice. Finally, the stained samples were mounted onto glass slides using a ProLong™ Diamond antifade mountant (Invitrogen).

5.1.10. Measurement of neurite extension length

The length of neurites was measured *via* image processing in ImageJ software with the NeuronJ plugin, developed by Erik Meijering. Images from SEM (for cells without labelling on fibre mats), HCA (for cells with IF labelling), or bright field microscopes (for cells without labelling on glass or TCP) were converted their qualities to greyscale 8 bit before analysis. With the NeuronJ plugin, two points of a neurite were manually selected (i.e. the origin of the neurite at the cell body and the end of the neurite). After that, the distance of the neurite was traced and calculated automatically. Therefore, the neurite extension length was the distance that each neurite can

travel. The images were collected from at least five fields of a sample or a fibre mat (*i.e.* top left, top right, bottom left, bottom right, and centre of the sample) to avoid the bias of analysis.

The orientation of neurites was measured as a later step based on the displacement of neurites. As shown in Figure 5.2, both endpoints of each neurite were identified by ordered pairs of (x_1, y_1) and (x_2, y_2) . the angle (θ) in the unit of the degree was calculated following the equations below:

$$\tan \theta = \frac{(y_2 - y_1)}{(x_2 - x_1)}$$

$$\theta = \tan^{-1} \frac{(y_2 - y_1)}{(x_2 - x_1)}$$

where, the lower endpoint in the y-axis was commonly set at (x_1, y_1) . Therefore, θ will be represented the direction between $0^\circ - 180^\circ$ only.

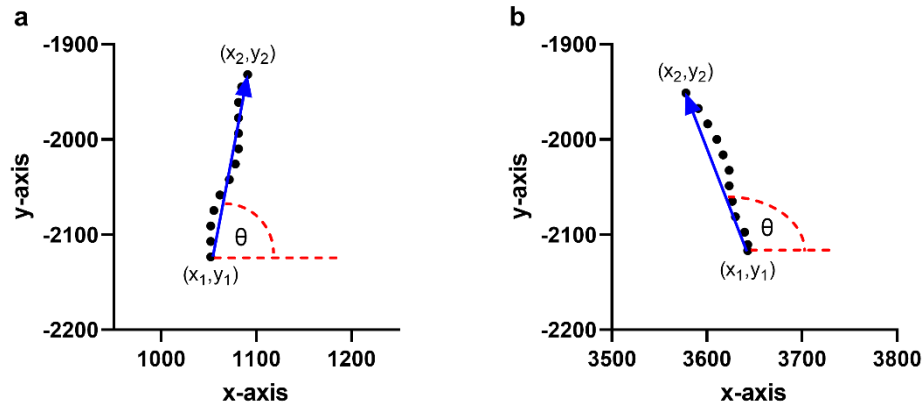


Figure 5.2 Examples of neurite orientation analysis, black dots-line and blue arrow represent the distance and displacement of neurite extension in coordinate x-y axis respectively: (a) showing θ in case of $X_2 > X_1$ and (b) showing θ in case of $X_2 < X_1$.

5.1.11. Statistical analysis

Data were analysed using GraphPad software (GraphPad Prism 9, version 9.2.0, USA) with the nonparametric test (Kruskal-Wallis test). p -values of less than 0.05 were considered statistically significant. Other definitions (*e.g.* asterisks, sample sizes, and statistical testing methods) were indicated in the figure captions.

For the measurement of cell metabolic activity and DNA concentration, the sample size (n) represented the number of fibre mats or wells of cells. The result of each sample is the average value from 3 replicates.

For the measurement of neurite extension length, n represented the number of neurites. Each condition may have a different sample size. However, the neurite length was measured from either SEM or HCA images; 3 – 5 images, representing 2 – 3 samples of fibre mats, were used for each condition (e.g. electrospun SF, IPN ($\alpha = 2.3$), and IPN 3.3 ($\alpha = 3.3$)). Images were collected from the same position every time (e.g. top left, top right, bottom left, bottom right, and centre of the sample) to avoid bias.

5.2. Results

5.2.1. NG108-15 grown on TCP substrates

Commonly, NG108-15 cultured in the growth medium can attach and grow individually on TCP substrates both with and without laminin coating. As shown in Figure 5.3, their morphologies were similar. Once the cell density is over-confluence, cells will be shrunk, become rounded shape, and detach from the substrate eventually. Additionally, the cell culture medium also turns yellow, indicating acid in the medium.

In differentiation media, NG108-15 were aggregated into clusters, which can then extend their neurites out. Cell clusters in the cAMP medium were likely to be larger and more clearly seen compared to those in the DMSO medium, as shown in Figure 5.4. The cell metabolic activity and DNA concentration of subconfluent NG108-15 in the different media, ascertained for 4 days, were shown in Figure 5.5.

On day 2, the cell confluence reached ~80 – 90% (Figure 5.3 (b and e)) in the growth medium, while it was ~50% in cAMP medium (Figure 5.4 (a and b)) and in DMSO medium (Figure 5.4 (e and f)). The metabolic activity and DNA concentration of each medium were significantly different. These results in descending order were in growth, cAMP, and DMSO media.

On day 4, cells were over-confluence in the growth medium (Figure 5.3 (c and f)). The metabolic activity and DNA concentration were decreased from day 2 due to cell detachment. In

contrast, cells were not over-confluent in the cAMP and the DMSO media since they were slightly increased compared to day 2 (Figure 5.4 (c, d, g, and h)). Interestingly, both metabolic activity and DNA concentration results of cells in the cAMP medium were higher than those in the DMSO medium.

The neurite extension length of NG108-15 was presented in Figure 5.6. In the growth medium, the neurites were short, with an average length of $40 \pm 10 \mu\text{m}$. The neurite length did not increase over time during culturing. Unfortunately, it was not possible to observe neurites in the over-confluent state (day 4). In differentiation media, the neurite lengths were increased over time. There was no difference in terms of neurite length between culturing in cAMP and DMSO media. After 2 days, the average neurite lengths in both differentiation media were $90 \pm 10 \mu\text{m}$; they were significantly longer than neurites in the growth medium. Moreover, they increased in length to $130 \pm 10 \mu\text{m}$ at day 3 and $220 \pm 30 \mu\text{m}$ at day 4.

The maximum neurite extension length, estimated by the percentile of 90, was $\sim 60 \mu\text{m}$ and $\sim 80 \mu\text{m}$ in the growth medium, $\sim 320 \mu\text{m}$ and $\sim 390 \mu\text{m}$ in cAMP medium, and $\sim 320 \mu\text{m}$ and $\sim 290 \mu\text{m}$ in DMSO medium on the substrate of TCP and TCP with laminin respectively. The direction of neurite outgrowth was random and likely to extend and connect from a cluster to another nearest one.

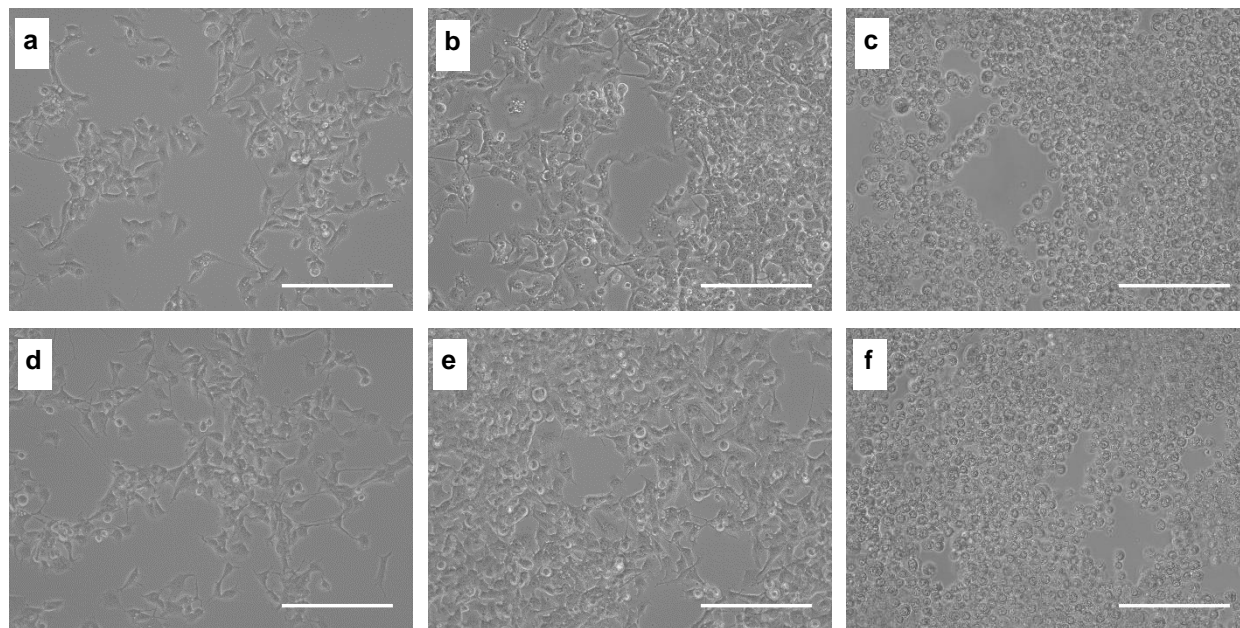


Figure 5.3 Cell morphology of NG108-15 culturing in growth medium on: (a – c) TPC and (d – f) laminin-coated TCP, the cell confluence of (a and d) ~50%, (b and e) ~80 – 90%, and (c and f) over-confluence. The scale bar represents 250 μm.

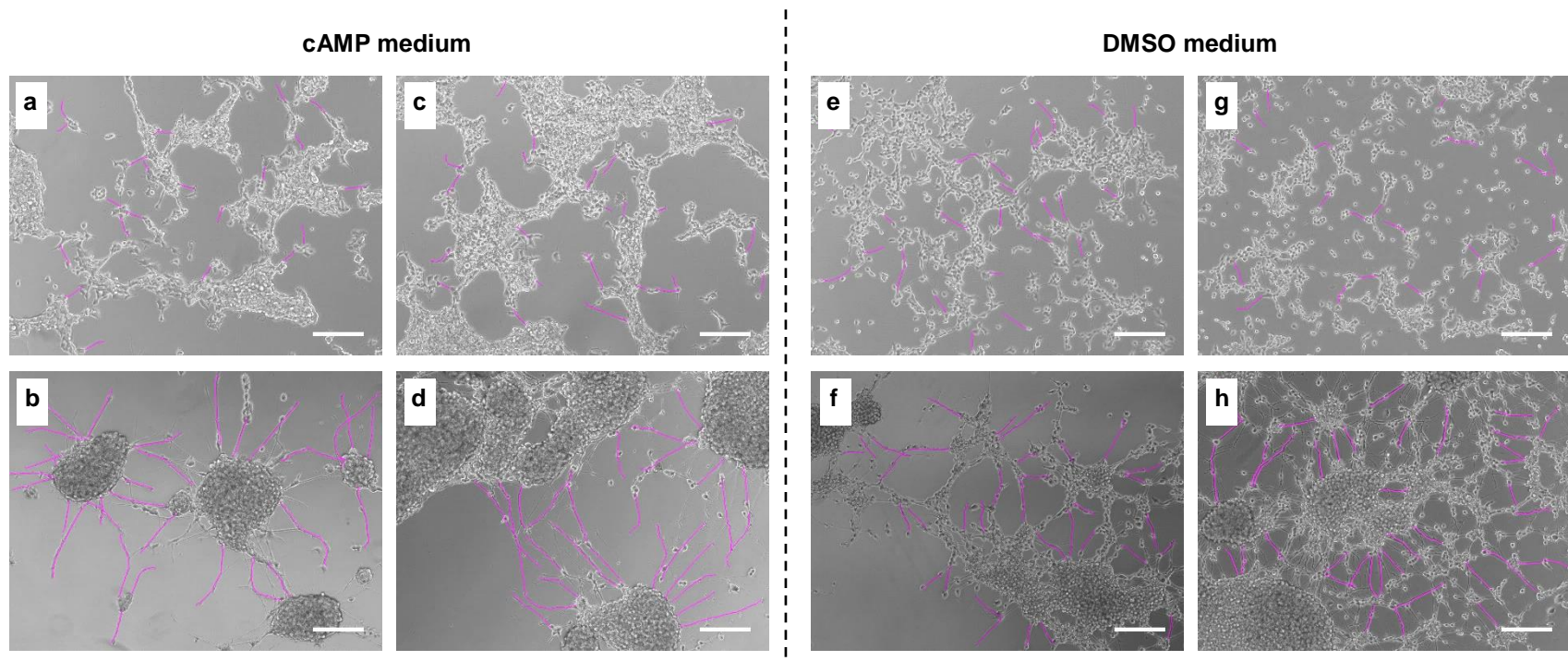


Figure 5.4 Cell morphology of NG108-15 culturing in (left) cAMP differentiation medium and (right) DMSO differentiation medium on different substrates and times: (a and e) TCP for 2 days, (b and f) TCP for 4 days, (c and g) laminin-coated TCP for 2 days, and (d and h) laminin-coated TCP for 4 days. Neurites are shown in magenta lines and the scale bar represents 250 μm.

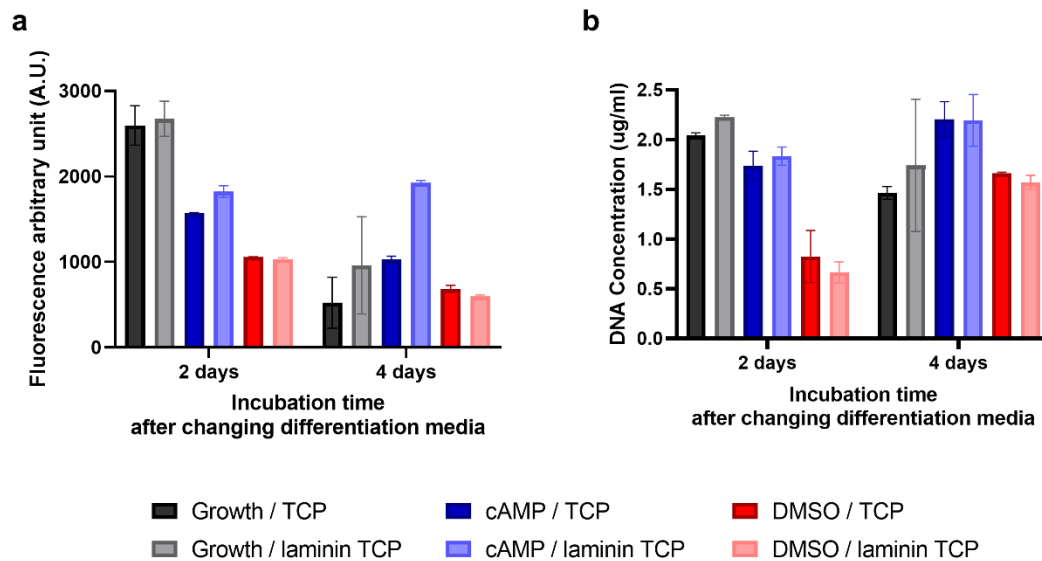


Figure 5.5 Cellular activities of NG108-15 cultured in different media: (a) cell metabolic activity and (b) DNA concentration of subconfluent NG108-15 in different cell culture media on TCP and laminin-coated TCP (n = 2 wells of cells).

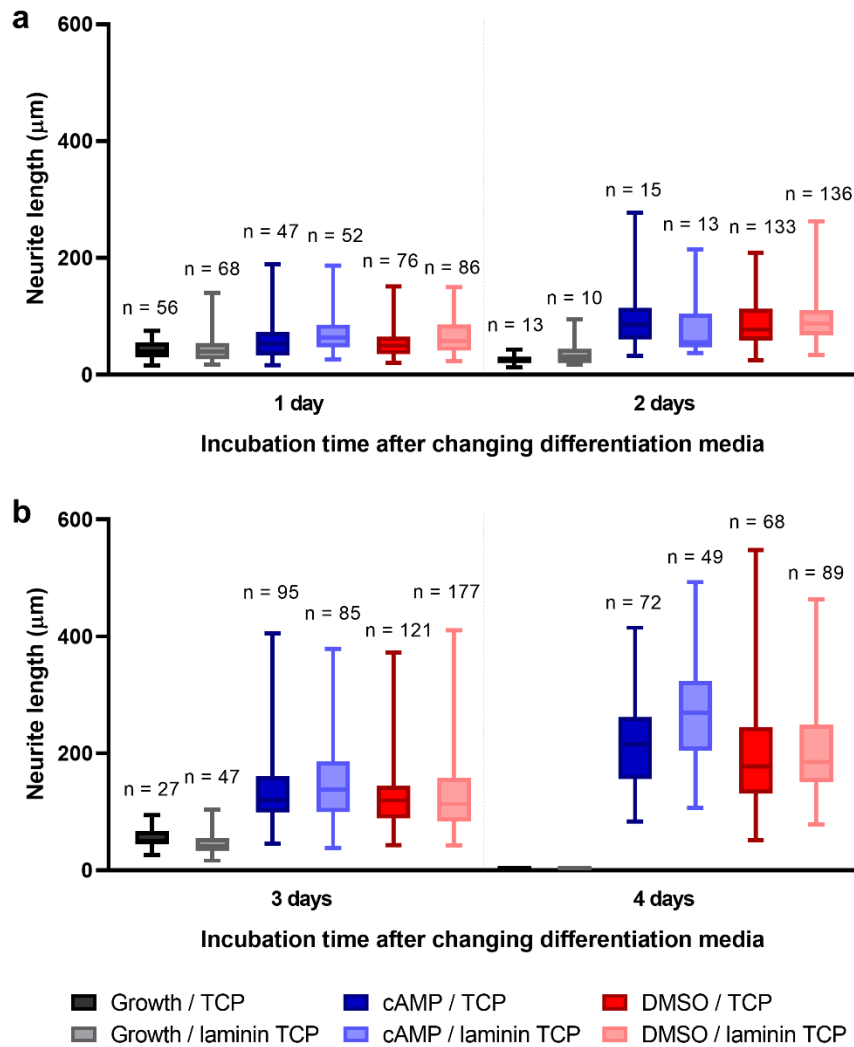


Figure 5.6 Neurite extension lengths of subconfluent NG108-15 in different cell culture media on TCP and laminin-coated TCP, box – whisker plots from min – max with the median at the middle line: (a) incubating time of 1 day and 2 days and (b) incubating time of 3 days and 4 days, n represents the number of neurites measured from 2 – 3 images (10x, bright field microscope) of 2 wells of cells.

5.2.2. NG108-15 grown on TCP substrates with conditioned media from electrospun SF and IPN mats

All the conditioned media used in this experiment were prepared at one time. The conditioned medium was then used for six parallel cell culture experiments (6 wells of cells). After changing the growth medium to conditioned media (pH = ~7.8), NG108-15 were still growing as normal on TCP substrate. However, the cell growth and proliferation in conditioned media were slightly different from the controls performed (culturing with the growth medium).

Live/dead staining illustrated the cell viability after incubating in conditioned media. As shown in Figure 5.7 and Figure 5.8, most of the cells were stained with green, representing live cells. However, the cell confluence in each conditioned medium was different, especially IPN ($\alpha = 1.8$). Its medium contained black particles as well as the conditioned medium of IPN ($\alpha = 1.3$), which were clearly seen under the bright field microscope, as shown in Figure 5.7 (g and h). Possibly these black particles are PEDOT:PSS that were washed out from the fibre mat during the conditioning process of medium with the test materials. Some particles were large and were able to be observed by eyes.

The metabolic activity and DNA concentration of NG108-15 cultured in the conditioned SF and IPN media were gradually increased by incubation time from 24 – 72 h. As shown in Figure 5.9, the metabolic activity in conditioned SF, IPN ($\alpha = 1.3$), and IPN ($\alpha = 1.8$) were significantly lower, while other conditions were similar to control (growth medium). On the other hand, the DNA concentrations in all conditioned media were significantly low compared to the control. Moreover, IPN ($\alpha = 1.3$) and IPN ($\alpha = 1.8$) were likely to support cell growth worse than IPN ($\alpha = 2.3$), IPN ($\alpha = 2.8$), and IPN ($\alpha = 3.3$).

Interestingly, conditioned media containing PEDOT:PSS particles showed low metabolic activity and DNA concentration results. This suggests that PEDOT:PSS particles in the conditioned medium somehow interfere with cell adhesion and cause cell detachment and should be filtered before experiments in the future.

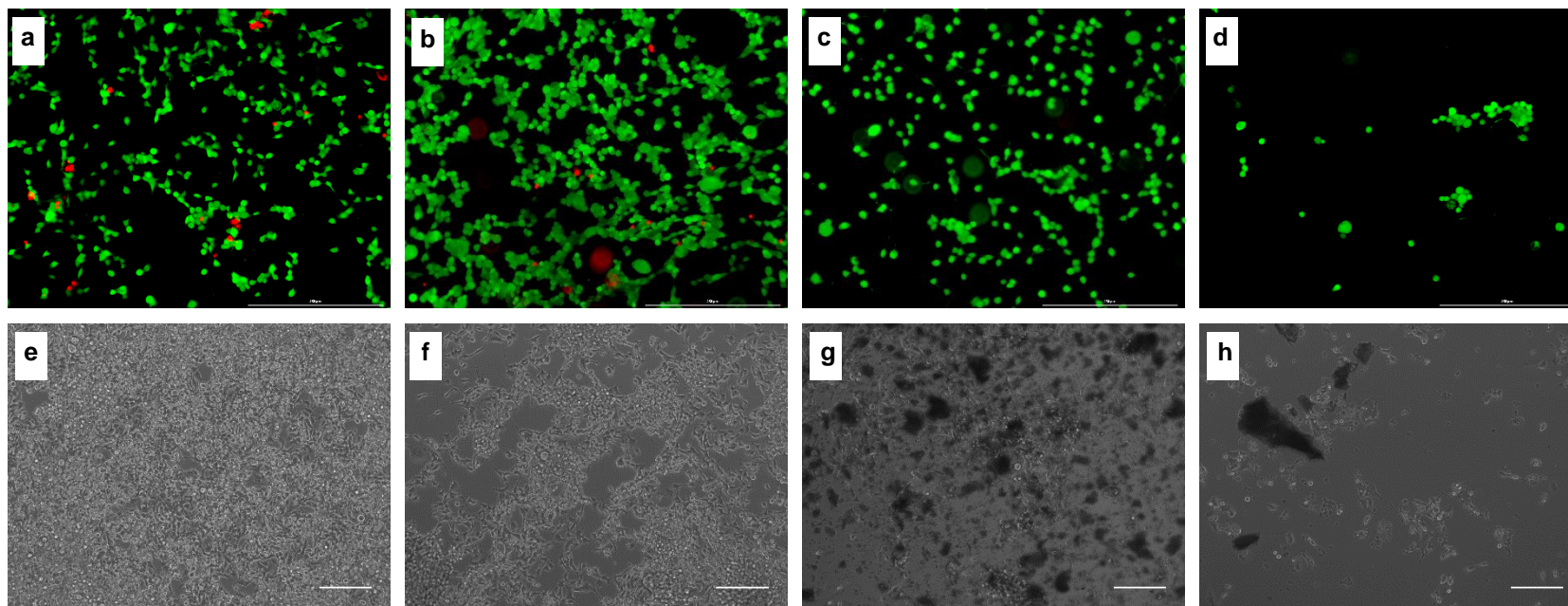


Figure 5.7 NG108-15 cultured in different conditioned media on TCP for 72 h: (a – d) live/dead staining and (e – h) bright field microscopy, (a and e) control growth medium, (b and f) conditioned SF medium, (c and g) conditioned IPN ($\alpha = 1.3$) medium, and (d and h) conditioned IPN ($\alpha = 1.8$) medium and the scale bar represented 250 μm .

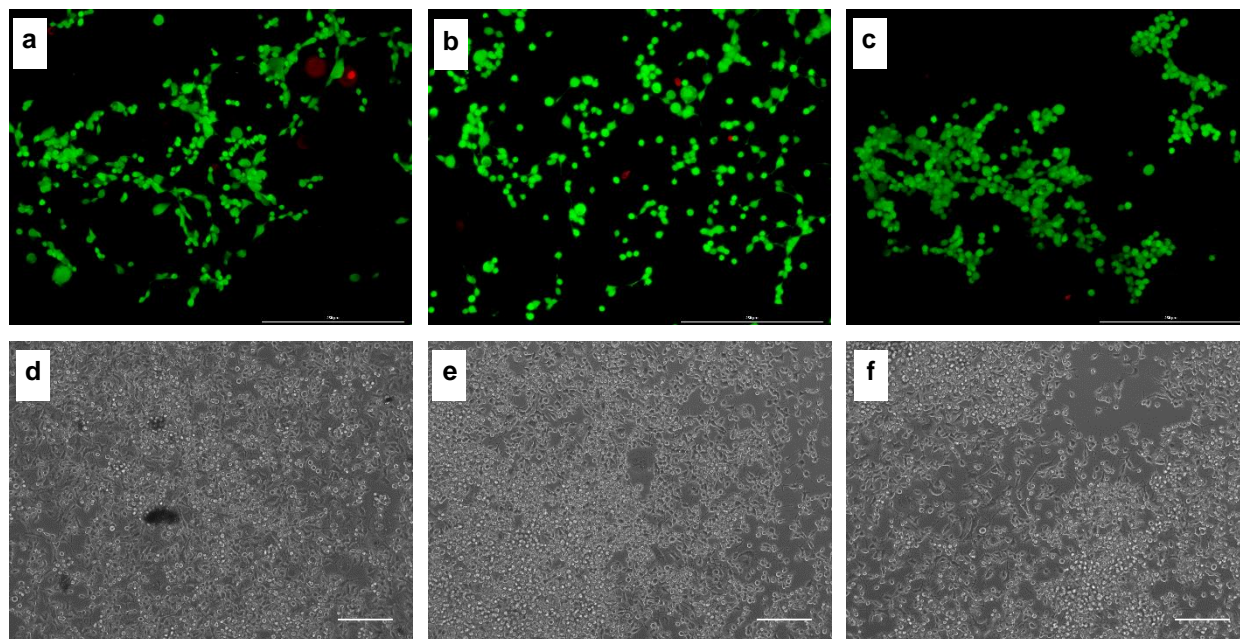


Figure 5.8 NG108-15 cultured in different conditioned media on TCP for 72 h: (a – c) live/dead staining and (d – f) bright field microscopy, (a and d) conditioned IPN ($\alpha = 2.3$) medium, (b and e) conditioned IPN ($\alpha = 2.8$) medium, and (c and f) conditioned IPN ($\alpha = 3.3$) medium and the scale bar represented 250 μm .

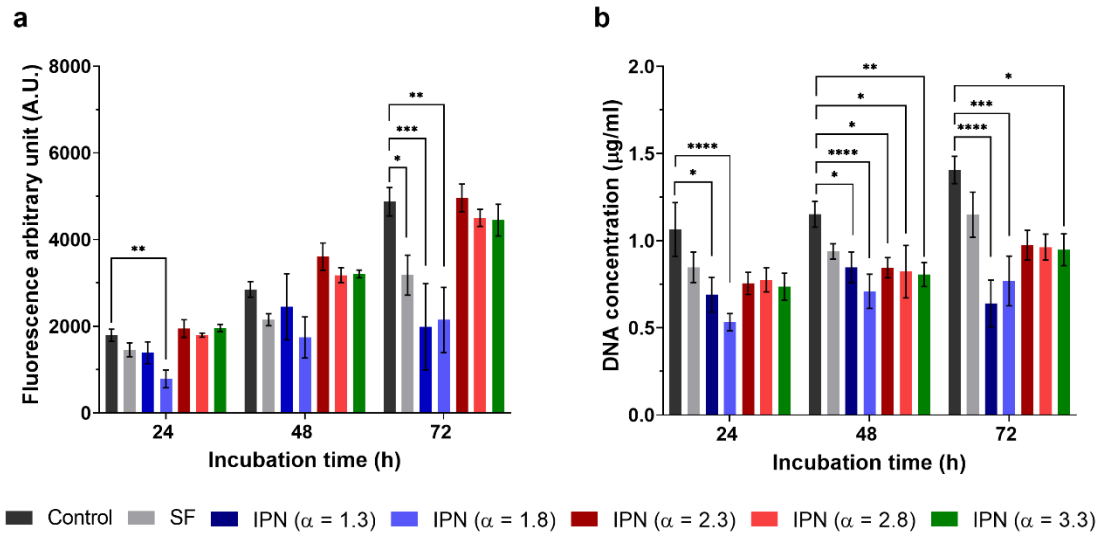


Figure 5.9 Characterisation of cell growth and proliferation of subconfluent NG108-15 in different conditioned media: (a) metabolic activity and (b) DNA concentration (n = 6 wells of cells in parallel experiments), the error bar represents SD, the statistical analysis with nonparametric (Kruskal-Wallis test), control is the growth medium, * represents $p < 0.05$, ** $p < 0.01$, *** $p < 0.001$, and **** $p < 0.0001$.

5.2.3. NG108-15 grown on electrospun SF and IPN mats without differentiation factors

Electrospun SF, IPN ($\alpha = 2.3$), and IPN ($\alpha = 3.3$) mats were tested with the direct contact assay to compare to the glass substrate as a control. Cells were ascertained for 4 time-points (day 1, 3, 5, and 7) with 3 parallel experiments/time-point; therefore, 12 samples of each fibre mat were prepared at one time for three parallel experiments of cell culture. The metabolic activity and DNA concentration of NG108-15 growing on substrates were presented in Figure 5.10.

Although metabolic activity and DNA concentration on fibre materials were not high as control, they were increased over time, suggesting electrospun SF and IPN mats can support cell adhesion and neuron growth. SF substrate showed higher metabolic activity and DNA concentration than other IPN mats at days 3 and 5, whether the mat was coated with laminin or not. However, these results between SF and both IPN mats were similar on day 7.

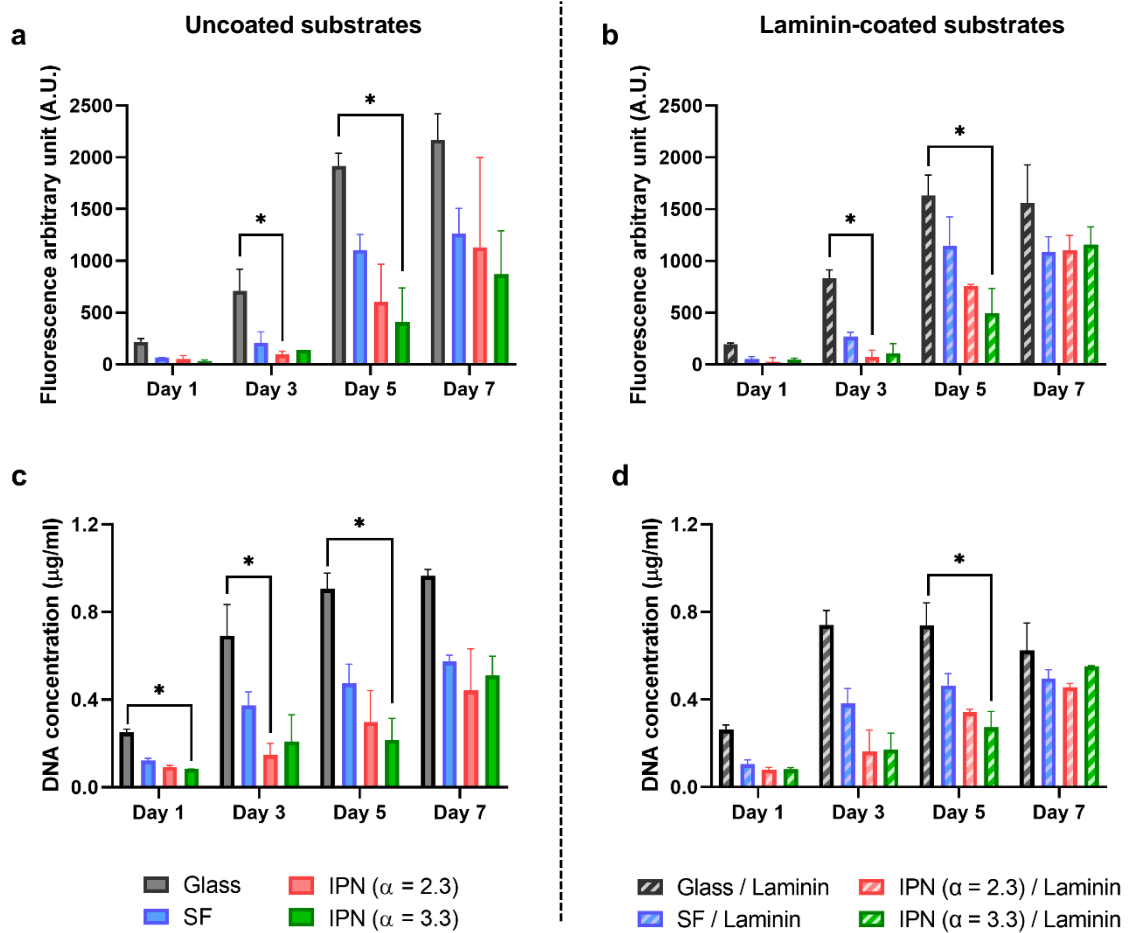


Figure 5.10 Characterisation of cell growth and proliferation of NG108-15 on electrospun SF and IPN mats: (a and b) metabolic activity and (c and d) DNA concentration ($n = 3$ samples of fibre mats in parallel experiments), the error bar represents SD, the statistical analysis with nonparametric (Kruskal-Wallis test), control is the growth medium, * represents $p < 0.05$

In the growth medium, the average neurite length of NG108-15 on electrospun SF and IPN mats were $\sim 30 \mu\text{m}$ in both with and without laminin coating. As shown in Figure 5.11, it appears that laminin-coated substrates promoted a longer length of neurites than uncoated substrates, particularly in the SF mat (day 7). The maximum length of neurites was $\sim 60 \mu\text{m}$ in SF, $\sim 100 \mu\text{m}$ in laminin-coated SF, and $\sim 100 \mu\text{m}$ in both IPN mats with and without laminin. The morphologies of cells grown on fibre mats with the growth medium were shown in Figure 5.12. The individual neurite length and its direction on fibre mats were presented in the polar scatter

and polar histogram as shown in Figure 5.13 and Figure 5.14 for uncoated fibres and laminin-coated fibres, respectively.

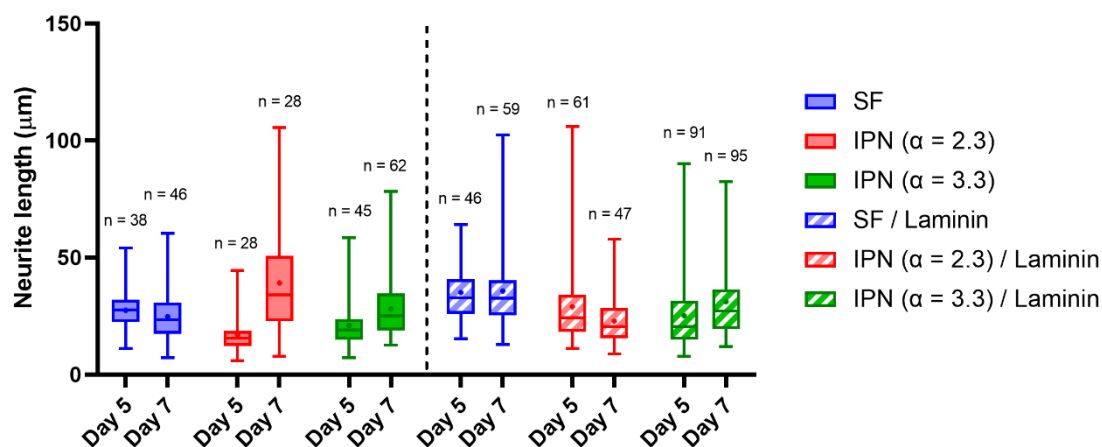


Figure 5.11 Neurite extension lengths of NG108-15 cultured in growth medium on different substrates, box – whisker plots from min – max with the median at the middle line, the mark (+) is mean, and n is the number of neurites on a fibre mat.

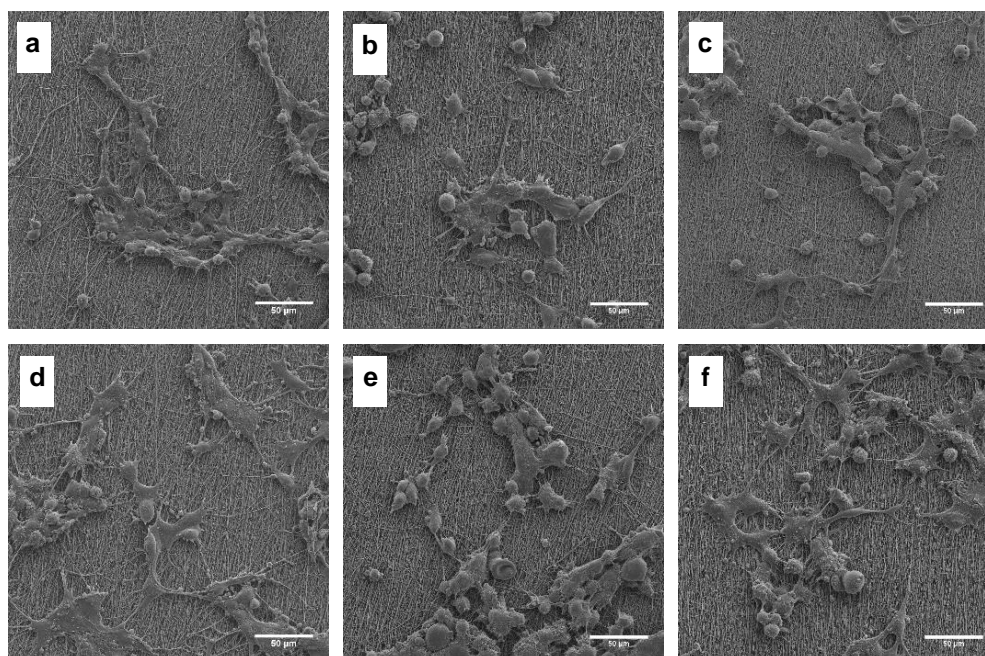


Figure 5.12 SEM images of NG108-15 cultured in growth medium on different electrospun mats for 7 days: (a) SF, (b) IPN ($\alpha = 2.3$), (c) IPN ($\alpha = 3.3$), (d) laminin-coated SF, (e) laminin-coated IPN ($\alpha = 2.3$), and (f) laminin-coated IPN ($\alpha = 3.3$), the scale bar of 50 μm .

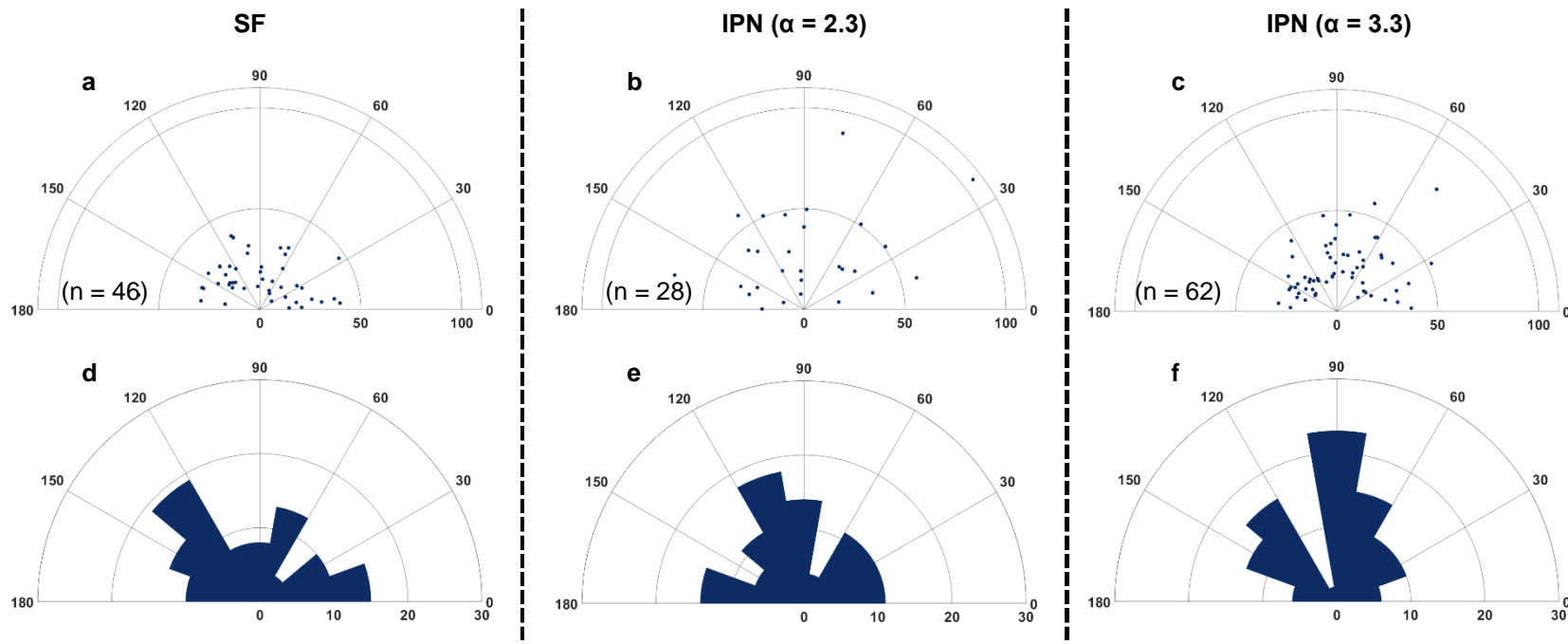


Figure 5.13 Example of neurite length and orientation of NG108-15 in growth phase cultured for 7 days on uncoated substrates: (a – c) polar scatter with the radius of 110 μm and (d – f) polar histogram with the radius of 30%, the position of 90° is the parallel direction to the fibre alignment, n is the number of neurites on a fibre mat. These graphs are replotted from the same data presented in Figure 5.11.

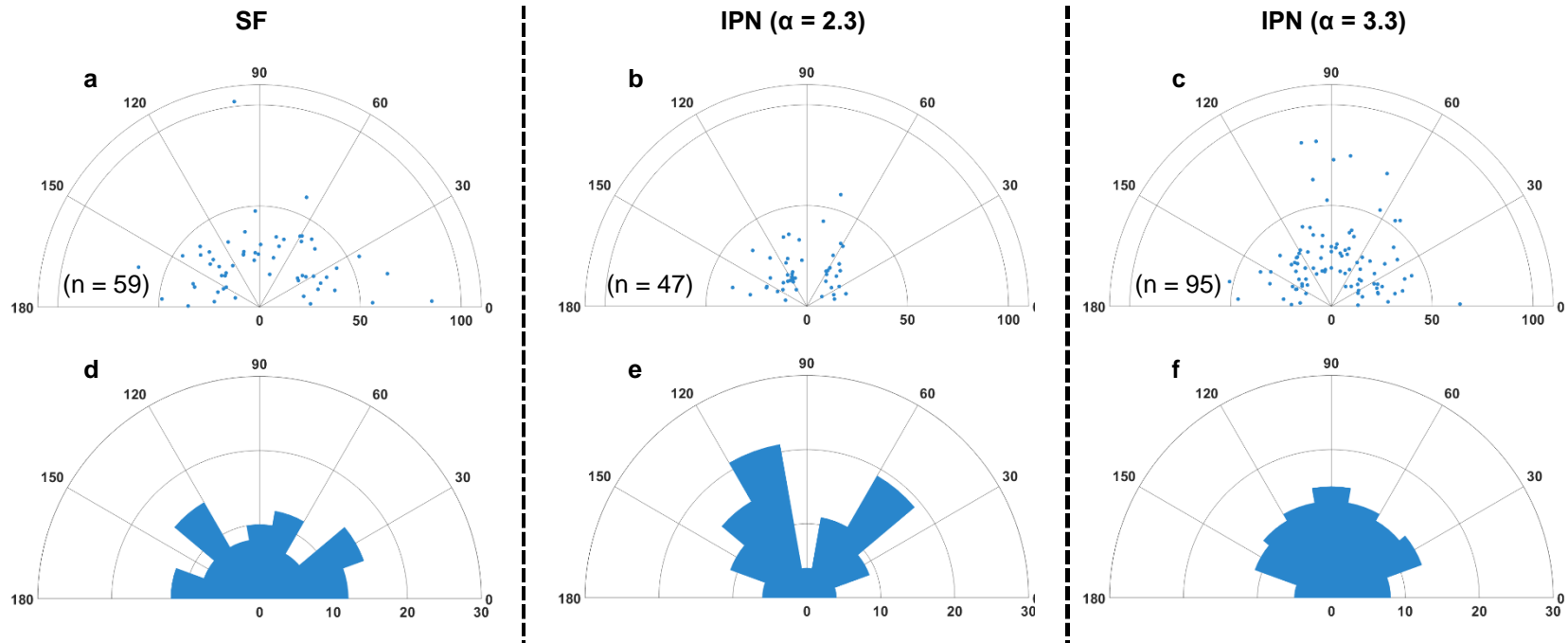


Figure 5.14 Example of neurite length and orientation of NG108-15 in growth phase cultured for 7 days on laminin-coated substrates: (a – c) polar scatter with the radian of $110\ \mu\text{m}$ and (d – f) polar histogram with the radian of 30%, the position of 90° is the parallel direction to the fibre alignment, n is the number of neurites on a fibre mat. These graphs are replotted from the same data presented in Figure 5.11.

5.2.4. NG108-15 grown on electrospun SF and IPN mats with differentiation factors

In the differentiation phase, NG108-15 on fibres were cultured in the cAMP medium and ascertained for 5 days. SEM and immunofluorescence staining revealed that NG108-15 cells aggregated into clusters and extended many more longer neurites in comparison to the growth phase cells.

In electrospun SF mat samples, laminin affected neurite outgrowth. As shown in Figure 5.15, the average neurite length was $\sim 60 - 80 \mu\text{m}$, and it was slightly higher up to $\sim 85 - 110 \mu\text{m}$ when coating with laminin. Also, the maximum length of neurites increased from $\sim 150 - 200 \mu\text{m}$ to $\sim 250 - 300 \mu\text{m}$. In contrast, neurite outgrowths on both IPN mats were similar between uncoated and laminin-coated groups. Their average neurite lengths were $\sim 75 - 85 \mu\text{m}$. However, the maximum length of neurites between IPN with and without laminin was different. It was $\sim 130 - 200 \mu\text{m}$ in IPN ($\alpha = 2.3$), $\sim 160 - 300 \mu\text{m}$ in IPN ($\alpha = 2.3$) with laminin, $\sim 160 - 250 \mu\text{m}$ in IPN ($\alpha = 3.3$), and $\sim 190 - 210 \mu\text{m}$ in IPN ($\alpha = 3.3$) with laminin, which was estimated by the percentile of 90 – 100. The SEM and immunofluorescence staining images of NG108-15 grown on fibre mats with differentiation media are shown in Figure 5.16.

Furthermore, many long neurites were orientated in the parallel direction of fibre alignment. From Figure 5.17 and Figure 5.18, the position of 90° of the polar scatters and polar histograms refer to the alignment direction of fibres. The longest neurite on every fibre substrate was always aligned in the position of $80^\circ - 100^\circ$. Approximately 60 – 80% of neurites was aligned in the position of $60^\circ - 120^\circ$. However, the small number of short neurites was placed in other positions (e.g. $0^\circ - 30^\circ$ and $150^\circ - 180^\circ$), which are likely to be perpendicular to fibre alignment.

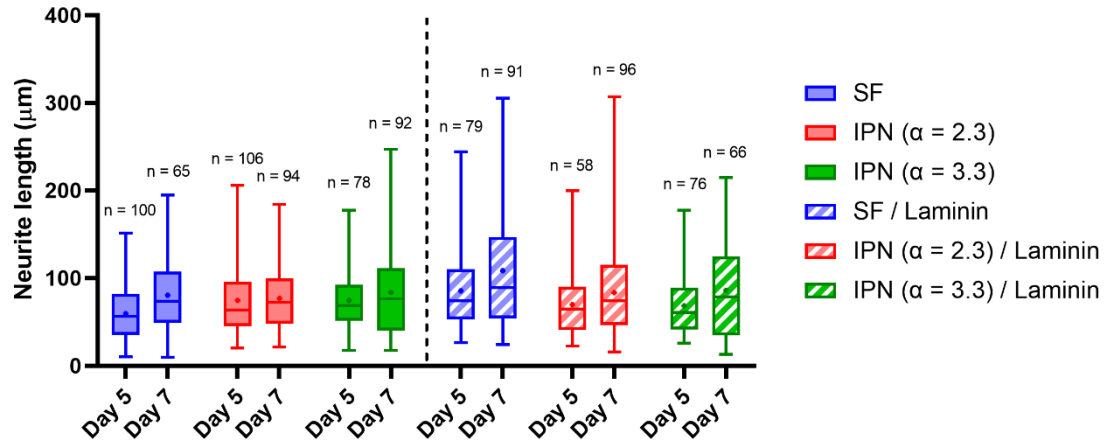


Figure 5.15 Neurite extension lengths of NG108-15 cultured in cAMP differentiation medium on different substrates, box – whisker plots from min – max with the median at the middle line, the mark (+) is mean, and n is the number of neurites on a fibre mat.

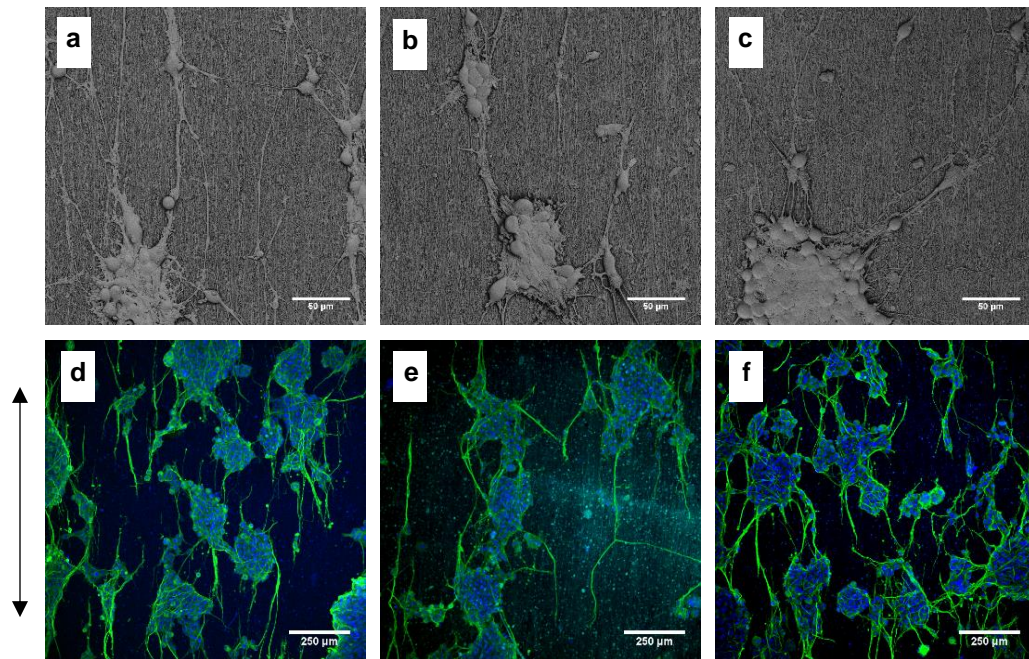


Figure 5.16 Differentiation phase of NG108-15 cultured in cAMP medium on laminin-coated substrates for 5 days: (a – c) SEM images of SF, IPN ($\alpha = 2.3$), and IPN ($\alpha = 3.3$) with the scale bar of 50 μm and (d – f) IF images of SF, IPN ($\alpha = 2.3$), and IPN ($\alpha = 3.3$) with the scale bar of 250 μm , β -III tubulin in neurites showed in green and nucleus showed in blue, the double-head arrow indicates the direction of aligned fibres.

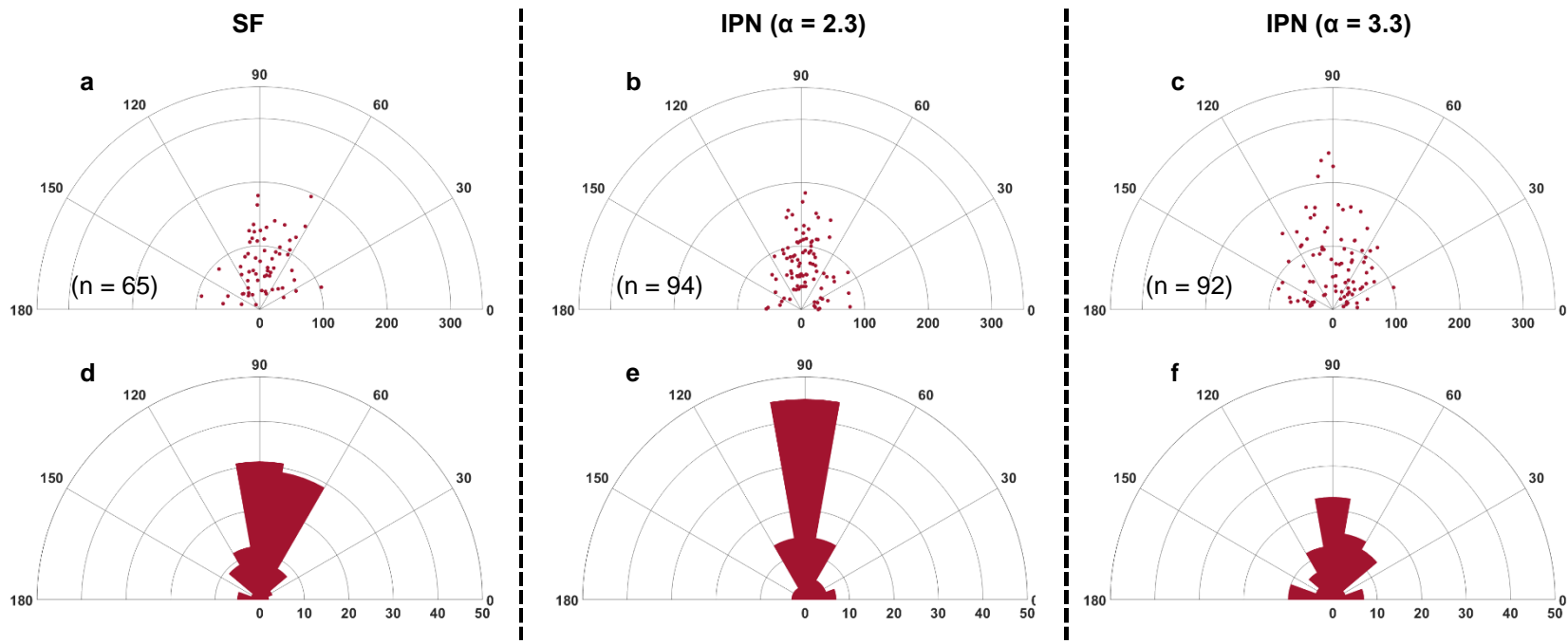


Figure 5.17 Example of neurite length and orientation of NG108-15 in differentiation phase cultured for 7 days on uncoated substrates: (a – c) polar scatter with the radius of 350 μm and (d – f) polar histogram with the radius of 50%, the position of 90° is the parallel direction to the fibre alignment, n is the number of neurites on a fibre mat. These graphs are replotted from the same data presented in Figure 5.15.

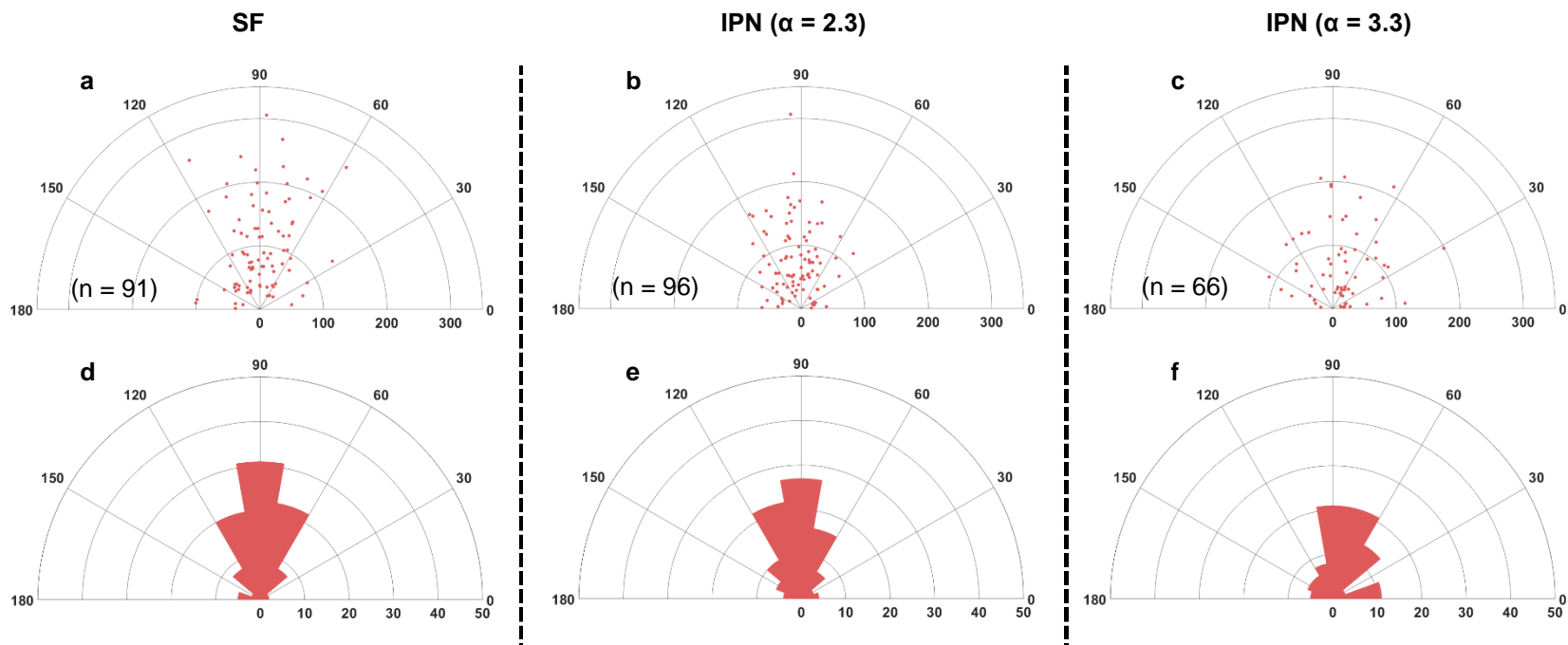


Figure 5.18 Example of neurite length and orientation of NG108-15 in differentiation phase cultured for 7 days on laminin-coated substrates: (a – c) polar scatter with the radius of 350 μm and (d – f) polar histogram with the radius of 50%, the position of 90° is the parallel direction to the fibre alignment, n is the number of neurites on a fibre mat. These graphs are replotted from the same data presented in Figure 5.15.

5.3. Discussion

5.3.1. Activation of cell differentiation

According to the results in this study, NG108-15 initially aggregated and extended longer neurites once culturing with cAMP and DMSO media. However, the cellular activity associated with increased cell number indicates that the cAMP medium supports cell growth better than the DMSO medium. This is maybe due to the higher percentage of FBS in the cAMP medium.

During the differentiation phase, the proliferation rate of NG108-15 cells was also likely to be decreased or inhibited compared to the growth phase, as mentioned in other studies [319-321]. These results confirm the differentiation of NG108-15 cells in both media. Morphology of differentiation cells and neurite length between two groups of media were similar. This is because cells are activated via the same pathway associating with angiotensin II (Ang II) and angiotensin receptors (AT), especially type 2 (AT₂) [321, 322].

Ang II is a peptide effector hormone in the body; it usually plays an important role in blood pressure and the cardiovascular system [323]. For instance, it causes vasoconstriction, stimulates the sympathetic nervous system, and increases the release of aldosterone. It also covers the role in inflammation, tissue injury, immunology, oxidative stress, and ageing [324]. As well as CNS, the NG108-15 cell line is a target tissue of Ang II and contains two subtypes of AT receptors: AT₁ and AT₂ [321].

Seidman K.J., *et al.*, 1996 reported that undifferentiated NG108-15 contains AT₁/AT₂ receptors in the ratio of 8:3, while DMSO medium can extremely increase the number of AT₂ and the AT₁/AT₂ ratio is reversed to 1:3 [322]. Moreover, Laflamme L., *et al.*, 1996 explained that Ang II induces neurite outgrowth of non-differentiated cells but it induces neurite involution of differentiated cells when culturing in the cAMP medium [321]. They also indicated that AT₂ acts on tubulin polymerisation and the level of microtubule-associated protein 2c (MAP2c) [321].

According to the above reviews [321, 322], they suggest that both cAMP and DMSO media might increase the level of AT₂ associated with the level of tubulin and microtubule, exposing neurite outgrowth eventually. Moreover, both media perhaps promote neuregulin mRNA

expression in NG108-15 [325], which is necessary for synapse formation and development of neuromuscular junction [326].

5.3.2. Toxicity of PEDOT:PSS and other chemical residues

In this study, the hazard from chemical residuals of material on neuronal cells may come from three processes: electrospinning, IPN of PEDOT:PSS, and sterilisation.

In the electrospinning solution preparation, FA can commonly evaporate in the normal atmosphere, and CaCl_2 residues can be dissolved and washed out by water. The risk from the electrospinning solution is then extremely low or no risk. In sterilisation, 70% EtOH was used as a disinfection solution. It can cause cell death if direct contact with cells. Since EtOH can evaporate and sterilised samples were always washed with PBS before use, it maybe that less and less EtOH is left. Provided any chemical residues from the mat are toxic to cells, it is maybe due to chemicals in the IPN process or PEDOT:PSS products.

The safety data sheets of each chemical in IPN protocol and PEDOT:PSS show that PSS and PEDOT:PSS products are non-hazardous according to Regulation (EC) No. 1272/2008. However, other chemicals used in the IPN process have hazards, for example, EDOT monomer as well as FeSO_4 is known to be a toxic irritant and $\text{Na}_2\text{S}_2\text{O}_8$ to be a toxic sensitiser. Other *in silico* toxicity screening studies also confirmed that PEDOT, PSS, and PEDOT:PSS products were non-sensitisers and non-mutagenic, while EDOT monomer was identified as a plausibly hepatotoxic and $\text{Na}_2\text{S}_2\text{O}_8$ as a plausible respiratory/skin sensitiser [257, 317, 318]. This emphasises the importance of effective washing prior to use in tissue engineering and biomedical applications.

The washing process after IPN in this study is effective and acceptable to get rid of all hazardous residues confirmed by results of cell viability *via* live/dead assay, as shown in Figure 5.7 and Figure 5.8. Although there were PEDOT:PSS particles in some conditioned media, most cells cultured in the conditioned medium of IPN ($\alpha = 2.3$), IPN ($\alpha = 2.8$), and IPN ($\alpha = 3.3$) were still alive with the same cell confluence as similar to control (growth medium). This result also reinforces the biocompatibility of PEDOT:PSS products. Live cells were stained with green in their bodies, while dead cells were seen as tiny red spots in their nuclei. Interestingly, dead cells were

often found in the middle area of the cell cluster. It indicates that cell death due to high cell confluence is a common behaviour of NG108-15 rather than due to the effect of chemical toxicity.

In the conditioned medium of IPN ($\alpha = 1.3$) and IPN ($\alpha = 1.8$), they contained a lot of PEDOT:PSS particles detaching from substrates. Their cell confluences were lower than control, also metabolic activities and DNA concentrations of cells were significantly low. Thus, large PEDOT:PSS particles interfere with cell adhesion and cell growth; this is maybe because floating particles in the medium can scrape cells from the substrate. On the other hand, dead cells would detach and be lost. However, the cause of cell detaching in the conditioned medium of IPN ($\alpha = 1.3$) and IPN ($\alpha = 1.8$) might be due to scraping rather than the chemical toxicity. Perhaps, the level of interference depends on the size and number of particles; this also suggests that the conditioned medium should be filtered before the test.

However, the above assumption that cells were damaged by the scraping of floating particles is based on the result of the indirect test with six parallel experiments of cell culture (6 wells of cells). In order to confirm this assumption, more numbers of independent experiments should be considered. Additionally, the conditioned medium should be filtered before use.

Interestingly, cell metabolic activity and DNA concentration, in the case of conditioned electrospun SF medium, were lower than control, as shown in Figure 5.9, suggesting that electrospun SF mats may release something affecting cell growth. Perhaps this is an effect of small basic pH of ~ 7.8 after soaking the material in the medium. The effects of pH of the cell culture medium on cell viability should be investigated in the future, even if the cell culture medium is likely buffering this effect anyway. However, metabolic activity and DNA concentration of cells cultured with all conditioned media were gradually increased every day. It is a good sign for using these developed materials as nerve tissue scaffolds.

On the other hand, FBS proteins and nutrients are possibly being trapped by the mats during the conditioning process of the medium. Hence, the conditioned medium is slightly nutrient-deprived, suggesting the investigation of the protein absorption in/on the fibre mat. Several methods are recommended for further studies, such as the NanoOrange® protein quantification

[121], an enzyme-linked immunosorbent assay (ELISA) [257], and serum protein adsorption assays and electrophoresis (Western blotting) [327].

5.3.3. Neuron growth and neurite extension on electrospun SF based materials

5.3.3.1. Effects of surface roughness and morphology of fibres

NG108-15 can grow and proliferate well on the smooth surface of the glass substrate, confirmed by cell metabolic activity and DNA concentration results, as shown in Figure 5.10. They can also grow on fibre substrate, but their results were not high as on the glass. Perhaps, NG108-15 prefer smooth glass substrate to electrospun SF based fibres. However, it is an over assumption to confirm that a smooth surface is better than fibre for cell adhesion and proliferation since they are different substrates.

The surface roughness and topography are important factors for cell adhesion, proliferation, and migration. In a 2D flat scaffold for nerve tissue engineering, neuronal cells easily attach to smooth surfaces compared to rough surfaces fabricated from the same substrate [328]. However, materials with the surface roughness of the nano-scale structure can highly support cell adhesion as well [329, 330]. Onesto V., *et al.*, 2017 explained an interesting idea of cell adhesion on nano-scale corrugated substrate. At the early phase of cell adhesion, cells have to move and deform their membranes to adapt to the surface profile. Then, substrate instability force dominates over cell-cell adhesion force resulting in cell clustering [330].

In this study, the metabolic activity and DNA concentration of cells on electrospun SF were lower than glass substrates; this is maybe due to cell adaptation for attaching to fibres rather than the chemical toxicity. Compared to the glass substrate, the period of cell adhesion on fibres may take a long time, possibly delaying cell growth and resulting in a lower number of cells. Nevertheless, these results were increased over time, indicating that fibre substrates can support cell proliferation.

In a fibre scaffold, nanofibres provides a high available surface area, which significantly affected cell adhesion, proliferation, and differentiation [331, 332]. Moreover, the nanofibre-based scaffold can mimic the architecture of native ECM and tissue structural properties [331, 333]. The

optimal condition of fibre diameter is depended on the application or the target tissue. In nerve regeneration, electrospinning fibres have been studied in a wide range from ~200 – 900 nm [227, 265, 334-336]. The fibre diameter was a control parameter without varying in this study; thus, it is still doubtful to confirm which diameter is the best condition for supporting neurite extension. However, the electrospun SF based material with a fibre diameter of ~200 nm shows impressive results for supporting neuron growth and neurite outgrowth.

Since the fibre diameter is much smaller than the size of the cell, which is ~30 μm in the rounded cell and ~60 μm in the expanded cell, it cannot align and control the direction of cell expansion and migration. However, the neurite outgrowth of cells during the differentiation phase is mostly extended along fibres, as clearly seen in Figure 5.16. Interestingly, the diameter of neurites is equal to that of fibres, as observed in this study. The unidirectional alignment of neurites on electrospun SF based materials is a good sign for fully functional peripheral nerve recovery. Combining electrospinning fibre with micropatterning scaffolds such as groove [310, 337, 338] and pillar [339-341] is an alternative suggestion for future study.

5.3.3.2. Effects of laminin coating on fibres

NG108-15 cells are sensitive not only to the acidic environment but also to mechanical forces. They are easily detached from the substrate when they are handled roughly. During cell culture, washing and changing medium must be performed softly and carefully. Coating substrates with laminin is a well-known protocol for enhancing NG108-15 cell adhesion; this maybe because neuronal cells have multiple cell-surface laminin receptors [342].

Laminin has an effect not only cell adhesion, but it can also promote neurite outgrowth. Kleinman H.K., *et al.*, 1998, explained that NG108-15 cells contains three membrane proteins of 67, 110, and 180 kDa specific to laminin binding. The membrane protein of 67 kDa supports cell attachment to laminin, while others involve in neurite formation [342].

In this study, laminin shows the ability to mainly support cell adhesion without effects on cell growth and proliferation in each material (*i.e.* TCP, glass, electrospun SF, and IPN mats). In contrast, laminin promotes neurite extension length on electrospun SF in both growth and

differentiation phases, as shown in Figure 5.11 and Figure 5.15. Possibly, this effect results from the level of laminin-immobilised SF fibres. By the physical coating method, laminin desorption or erosion is inevitable after a long period of soaking [343, 344]. Electrospun SF fibres have a high surface area to adsorb laminin; consequently, the level of laminin on the substrate should be high enough to retain throughout 7 days of the experiment.

In the case of IPN mats, laminin slightly promotes neurite outgrowth in IPN ($\alpha = 2.3$), but is ineffective in IPN ($\alpha = 3.3$), as shown in Figure 5.15. A previous study by Magaz A., *et al.*, 2020 showed that PEDOT:PSS on electrospun SF prepared by physical coating has a high level of protein adsorption compared to the pristine SF [120]. It was expected that laminin should be attached on IPN mats and also support neurite extension quite well. Therefore, the level of laminin on substrates and binding mechanism between laminin and PEDOT:PSS are interesting for further investigation. If the level of laminin on IPN mats are certainly high and stable throughout the period of the experiment, this may suggest that PEDOT:PSS can substantially promote neurite extension even if without laminin. On the other hand, the effect of laminin is maybe inhibited by PEDOT:PSS. Additionally, fibronectin and poly-L-lysine are interesting molecules for supporting cell adhesion, particularly in neurons cell culture (NG108-15) [345, 346]; the effect of different coating molecules on fibre mats is another suggestion for further study.

5.3.3.3. Effects of PEDOT:PSS on fibre

In comparison to electrospun SF, cell metabolic activity and DNA concentration of cells on IPN mats were significantly low, especially at day 3 and day 5, as shown in Figure 5.10. Interestingly, these results of cellular activities were equal at day 7 between electrospun SF and IPN mats.

In electrospun SF, cells strongly increase in number from day 1 to day 5. After that, they slightly increase from day 5 to day 7. In IPN mats, the cell growth behaviour in IPN ($\alpha = 2.3$) and IPN ($\alpha = 3.3$) are similar. The cellular activities on day 3 are slightly increased from day 1. After that, cells are highly increased from day 3 to day 7. It suggests that PEDOT:PSS on IPN mats somehow hinder the early period of cell adhesion.

However, this assumption that PEDOT:PSS hinders cell adhesion on fibres is different from other aspects. For example, Wang S., *et al.*, 2017 and 2018 reported that PEDOT and PEDOT:PSS. PEDOT-assembled gel scaffolds promote cell adhesion efficiency in the early state because of their nano-scale structures [347, 348]. Additionally, the electrostatic force between the positive charge of conductive polymers and the negative charge of the cell membrane due to proteoglycans, glycolipid, and glycoproteins probably induce cell-surface interaction [349]. Herein, the electrostatic induction is probably weak or ineffective because of the negative charges of PSS [158]. Moreover, the component of PSS is larger than PEDOT as explained in chapter 4 (Figure 4.8 (b)). It can be hypothesised that the net charges of the material may be negative causing the repulsive force to cells during the adhesion process, which should be investigated in the future.

On the other hand, PEDOT:PSS can promote neurogenic differentiation and the expression of β -III tubulin in neurites [160]. Since the proliferation rate of NG108-15 is reduced during differentiation as explained in section 5.3.1, it suggests that cells on IPN mats are lightly triggered to differentiate by PEDOT:PSS. Additionally, NG108-15 cells cultured in growth medium extend slightly longer neurites on the IPN mats compared to SF mat (Figure 5.11). From these results, perhaps, cell aggregation when culturing in the growth medium is another clue of cell differentiation on IPN mats. However, cell aggregation depends on surface properties (*i.e.* toughness, nano-structure, and protein adsorption). It is difficult to confirm that cell aggregation on IPN mats are due to differentiation. Therefore, the differentiation factor of NG108-15 cells cultured in growth medium on IPN mats is an interesting point for further study. The observation of AT₁, AT₂, MAP2c, and other genes related to β -III tubulin are recommended to confirm the ability to promote differentiation of PEDOT:PSS integrated SF fibres.

In the differentiation phase, the best conditions which can promote the longest neurite up to $\sim 300\ \mu\text{m}$ are SF with laminin and IPN ($\alpha = 2.3$) with laminin as shown in Figure 5.15 and Figure 5.18 (a and b). Even though the numbers of neurites with a length of over $200\ \mu\text{m}$ in SF with laminin are higher than in IPN ($\alpha = 2.3$) with laminin, it still shows that PEDOT:PSS does not inhibit neurite outgrowth if it is in the appropriate ratio. The IPN ($\alpha = 3.3$) contains a high level of PSS and has low mechanical properties (*i.e.* stress, strain, and toughness) compared to IPN ($\alpha =$

2.3). The mechanical properties are quite similar since fibre mats were mounted on glass before cell culture. Thus, the excess of PSS possibly interferes with the neurite outgrowth and laminin ability.

5.4. Conclusion

Electrospun SF and electrically conductive IPN material of PEDOT:PSS on electrospun SF are biocompatible materials and can effectively support neuron growth, proliferation, and especially neurite extension. The morphology of sub-micron aligned fibres with a diameter of $\sim 200\text{ }\mu\text{m}$ exhibits the trend of the uniform orientation of neurites following the direction of fibre alignment.

Chemical residues of IPN material may have toxicity; this highlights the importance of effective washing before using it as a scaffold for tissue engineering. Cell adhesion and proliferation on IPN mats are somehow lower than electrospun SF in the early period and they are equal in the late period of cell growth. This suggests that PEDOT:PSS interferes with cell-surface interaction. In terms of neurite outgrowth during differentiation, laminin improves neurite length on electrospun SF and IPN ($\alpha = 2.3$). However, the increase of neurite length is not clearly seen in IPN ($\alpha = 3.3$), indicating that the level of PSS in/on IPN material has a significant effect on neuron growth and neurite outgrowth.

The development of IPN of PEDOT:PSS in/on electrospun SF is a novel strategy. It is a new generation of biomedical materials. Unfortunately, the neurite length on IPN mats was not higher than that on the electrospun SF mat, as expected in the hypothesis of this chapter. However, the IPN ($\alpha = 2.3$) can support neuronal cell adhesion, proliferation, and neurite extension quite well rather than IPN ($\alpha = 3.3$). Therefore, the IPN ($\alpha = 2.3$) is a promising electrically conductive material, potentially enabling electrical stimulation of the cells and facilitating peripheral nerve regeneration.

CHAPTER 6

Effects of Electrical Regimes on Neuronal Cells

An application of an electrical regime is an alternative method for promoting neurite outgrowth of neurons, *in vitro*. Many research reports demonstrate that the neurite extension length under the influence of specific electrical regimes is longer than without and most neurites align in a parallel direction to the electric field. Particularly, direct stimulation through the cell culture medium either with direct current (DC) or pulse stimulation is an appropriate method for enhancing the length of neurite outgrowth. However, various electrical parameters (*e.g.* types of electrodes, voltage supplies, and frequencies) were mentioned as effective parameters in the literature, as shown in Table 2.2 and Table 2.3.

The first objective of this chapter is to figure out the suitable electrical parameters for enhancing neurite extension length of neuronal cells (NG108-15) grown on TCP with differentiation factors. Several parameters: types of electrodes (*e.g.* carbon and platinum), types of electrical currents (*e.g.* direct and pulse), and other parameters (*e.g.* voltage supplies, frequencies, pulse widths, and durations of the stimulation) were varied in experiments. In order to evaluate the optimal condition of electrical stimulation (Op-ES), the neurite extension length of NG108-15 cells was analysed using image analysis as per the similar protocol mentioned in chapter 5 (section 5.1.10). The condition, which can extend the longest neurite length, is the Op-ES and was then applied to the cells grown on the electrically conductive fibre mats in a later step.

By using the carbon electrode (8-well C-Dish™, IonOptix) with a monophasic pulse stimulation, the Op-ES is the voltage of 1 V, the pulse width of 2 ms, and the pulse cycle of 100 ms for 3 days continuously (24 h/day). The Op-ES was then applied to the system of NG108-15 cells grown on electrospun SF or IPN ($\alpha = 2.3$) mats with differentiation factors to study the neurite length and direction on the developed materials under the influence of electrical regimes as the specific aim of this chapter. It was expected that with the Op-ES, the neurite extension length on IPN ($\alpha = 2.3$) mat would be longer than cells cultured on the electrospun SF mat alone.

Prior to applying the Op-ES to the fibre mats (electrospun SF and IPN ($\alpha = 2.3$)), the finite element analysis was studied to roughly understand the electrical transport phenomena of the bioreactor, including the fibre mat and cell culture medium.

According to the result in chapter 4 (section 4.3.3), the electrical conductivity of the IPN ($\alpha = 2.3$) mat was 3×10^{-3} S/m. It is lower than the conductivity of the cell culture medium from the literature, which is 1.7017 S/m [350]. For this reason, perhaps the electric field (EF) and current density passed through the cell culture medium are higher than the fibre mats. The connection between the electrode and the fibre mats is maybe an important factor affecting the current through the mat. It was hypothesised that the electrical current through the fibre mat with and without contacting electrodes were different, resulting in the divergent cell growth and neurite extension of cells on the fibre mat. In order to prove this hypothesis, an experiment of electrical stimulation on fibre mats were then divided into two different systems: the half fibre (H-fibre) and the full fibre (F-fibre) representing the fibre mat without and with contacting electrodes, respectively.

The EF and current density in both systems (*i.e.* H-fibre and F-fibre) were simulated using COMSOL multiphysics® software with the computational model of the cell culture chamber (macroscale) prior to performing cell culture experiment. This model can briefly present the EF, current density, also electrical transport phenomena of the cell culture medium and fibre mats. Moreover, the microenvironment model of fibres was an optional model in this study to simulate the electrical current in fibres and on the surface of the fibre mat (material-medium interface). The effect of different rotations of the fibre mats to the EF, such as fibres parallel to EF and fibres perpendicular to EF, will be explained in this chapter.

The result of (1) the computational model, (2) electrical stimulation of NG108-15 cells on TCP (optimisation of electrical parameters), and (3) electrical stimulation of NG108-15 cells on fibre mats in both H-fibre and F-fibre are presented sequentially in this chapter. Finally, it was hoped that the preliminary result in this chapter would be an initial step for developing the use of an electrical regime and electrically conductive scaffold for peripheral nerve regeneration in the future.

6.1. Materials and Methods

6.1.1. Electrical stimulation apparatus

The carbon plate electrodes (8-well C-dish™, IonOptix) worked with either a DC generator or pulse generator to generate an electric field in the cell culture system. The C-dish™ was precisely fitted with the 8-well rectangular cell culture plate (Nalge Nunc International #167064). The cell culture medium or other electrolytes were added for 4 ml each well. In a pair of electrodes, one was a positive electrode (anode), and another was a negative (cathode) or ground electrode. The distance between electrodes was ~3 cm, and the size of an electrode was ~0.25 x 2.17 cm².

The C-dish™ was sprayed with 70% EtOH, followed by UV sterilisation for 20 min. It was then left in a sterile condition for at least overnight before use in cell culture. After use, the C-dish™ were immediately cleaned by rinsing with water. To get remove the protein adsorbed at the surface of electrodes, the C-dish™ was operated in the blank sample (PBS solution) by applying the reverse direction of electrical potentials (positive potential to ground and negative potential to the positive electrode) for 30 min.

6.1.2. Sample preparation for electrical stimulation

Electrospun SF and IPN ($\alpha = 2.3$) mats were prepared and mounted on glass coverslips for cell culture and electrical stimulation as per the same process described in section 5.1.1.2. The size of the glass coverslip was 2.2 x 3.2 cm², which was suitable to touch both electrodes of C-dish™. Herein, the effects of electrical stimulation were evaluated and compared between two different positions of materials, which were named half (H) and full (F) fibres, as shown in Figure 6.1.

In the half fibre (H-fibre), the final size of the fibre mat was ~2.0 x 3.2 cm² after mounting. It was placed in the middle of the glass coverslip. In the full fibre (F-fibre), the fibre mats covered all areas of the glass coverslip. Thus, the H and F conditions were represented the indirect and direct stimulation through materials, respectively. Moreover, the direction of fibre alignment was always parallel to the length of the glass coverslip.

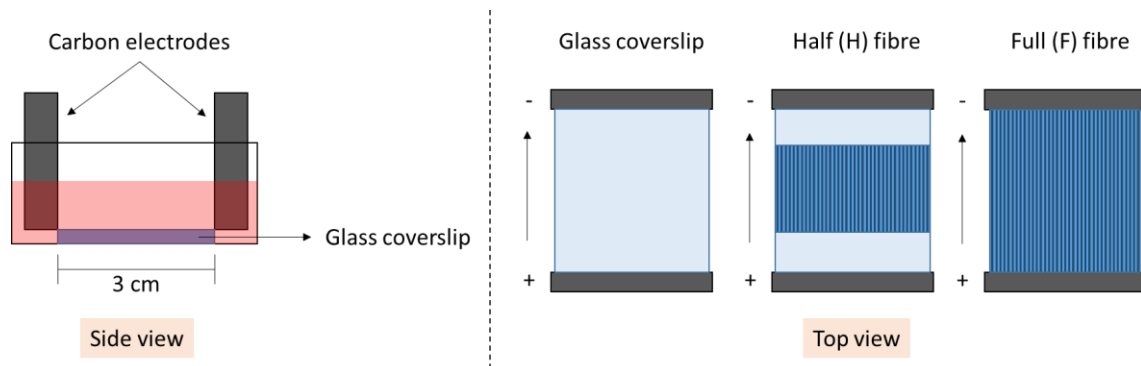


Figure 6.1 Schematic of fibre mat positions in the C-dish™ electrical stimulation system.

6.1.3. Finite element analysis by COMSOL Multiphysics®

The finite element analysis was used to briefly investigate the electric field (EF) and other related parameters during electrical stimulation in the cell culture system. Only the electrically conductive material system of IPN ($\alpha = 2.3$) in H-fibre and F-fibre conditions were focused on in this study. They were analysed by two different models: the macroscale of the whole cell culture chamber and the microenvironment of fibres.

6.1.3.1. Macroscale model of cell culture chamber

As shown in Figure 6.2, the macroscale study was modelled by the actual size of the bioreactor with four components: a rectangular cell culture well, a pair of carbon electrodes of C-dish™, a cell culture medium, and a fibre mat. The electrical properties (*i.e.* electrical conductivity and relative permittivity) of every component were automatically validated *via* the default value in the material library of COMSOL Multiphysics® software. Apart from the cell culture medium, the material of electrodes was identified as graphite, cell culture well plate as polystyrene (PS), and sample as PEDOT:PSS. The electrical properties of materials can be manually added following Table 6.1.

In the analysis, a study mode of time-dependent monophasic pulse stimulation with a 50% duty cycle was chosen. The amplitude voltage of 1, 2, and 3 V generated between electrodes, nominally representing the electric field of 33, 67, and 100 V/cm respectively, were varied in the

experiment. The results of EF and current density passed through both the medium and the electrically conductive mat were observed at the centre of the chamber.

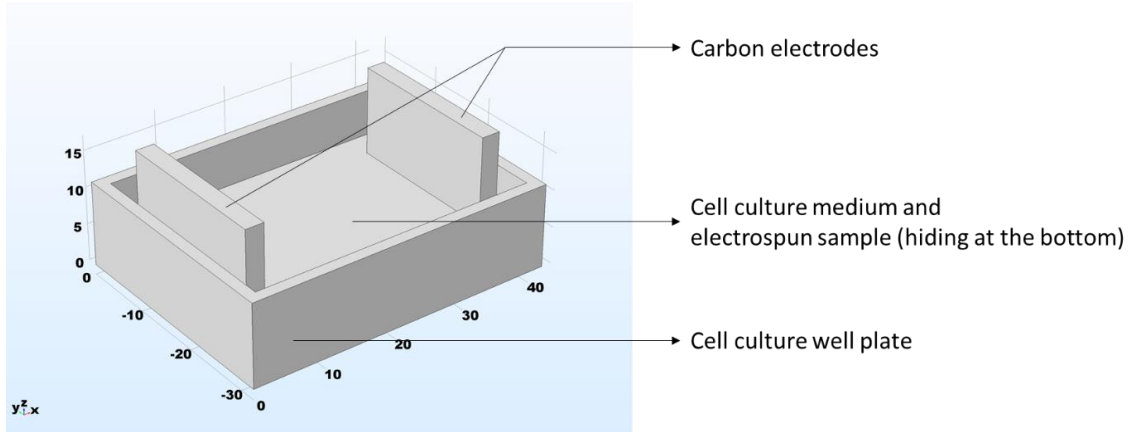


Figure 6.2 3D model of an electrical stimulation system with C-dish™ electrodes, the component of fibre mat is not shown in this figure.

Table 6.1 Materials properties used in electrical stimulation.

Materials	Electrical conductivity (S/m)	Relative permittivity
Graphite	3×10^3	1
Polystyrene (PS)	6.7×10^{-14}	2.6
Cell culture medium (ref. [350])	1.7017	80.1
PEDOT:PSS (ref. [350])	0.1	2.2
Silica glass	1×10^{-14}	2.09

6.1.3.2. Microenvironment model of fibres

The microenvironment model of fibres in COMSOL Multiphysics® software was developed by Miruna Verdes in Cartmell laboratory [350] and independently analysed by the author of this thesis. Actually, the model had five options of complexity for fibrous material. In this study, the rough conductive composite (RC) was used as a simple model to clarify the charge and current density in fibres and on the fibre-cell culture medium interface once the fibre mat is rotated at

different angles to the electric field (e.g. the aligned fibres parallel or perpendicular to the electric field). However, some simulation parameters were adjusted following the results found in this study. For example, the fibre diameter was 180 nm (explained in section 3.2.4), and the electrical conductivity of the IPN ($\alpha = 2.3$) mat was 3×10^{-3} S/m (explained in section 4.3.3). The relative permittivity of the IPN mat was assumed to be equal to that of silk fibroin of 7.81 [350].

In the analysis, the IPN fibre mat was arranged in two directions: parallel and perpendicular to EF. The results of space charge density (C/m^3) were observed at the surface of the material and in fibres.

6.1.4. NG108-15 Cell culture

The NG108-15 cell culture protocol and other related assays (*i.e.* laminin coating on samples, IF, measurement of neurite length, *etc.*) were similar to those mentioned in chapter 5. However, the cell seeding protocol on the substrate for electrical stimulation is described below.

6.1.4.1. Cell seeding on samples for electrical stimulation

The glass coverslips (control) and the samples of fibre mats were placed in 8-well rectangular cell culture plate. The total surface area of each rectangular well was 10.5 cm^2 . Thus, suspended NG108-15 cells were prepared at 52,500 cells in 4 ml of growth medium (cell seeding density of 5,000 cells/ cm^2). Then NG108-15 cells were seeded on prepared substrates and gently mixed until the cells were dispersed well in the cell culture medium. After seeding, cells were cultured in the growth medium for 3 days. The samples with subconfluent NG108-15 cells were transferred to a new 8-well rectangular cell culture plate. The DMSO differentiation medium was added to 4 ml each well and incubated for a day.

After that (on day 4), the sterilised C-dishTM was assembled on the cell culture plate and then an electrical regime was applied into the system. The lengths of neurite extension were ascertained for 3 days (on days 5, 6, and 7). In the meantime, the DMSO medium was refreshed on day 5. To avoid cell detachment, half the volume of the cell culture medium (2 ml) was taken out and refilled with the same volume.

It is to be noted that the cAMP medium was planned to use in the experiment as well; however, access to the laboratory was limited during the COVID-19 pandemic period. The experiment with the cAMP medium was not prioritised and therefore was not performed due to time limitations.

6.1.4.2. Cell fixation and measurement of neurite extension

In the sample with cells on the glass coverslip, the cells were observed and their images were collected using the bright field, inverted microscope (EVOS). In the sample of cells on the fibre mats, the cell dispersion after seeding was observed using the same technique mentioned in Chapter 5 (section 5.1.4). Cells were fixed with formalin solution followed by IF as mentioned in section 5.1.9. The measurement of neurite extension was explained in section 5.1.10.

6.1.5. Electrical stimulation of NG108-15 on electrospun SF and IPN mats

Prior to applying the electrical regime to the cells-material system, electrical parameters were optimised in growth medium and cells on glass coverslips. The purposes of this optimisation were to find the limitation of electrical stimulation period and voltage, which do not damage the cells or generate redox reactions of the medium. The details of electrical parameters in this study, adopted from Table 2.2 and Table 2.3, are presented in Table 6.2.

The finalised electrical parameters using C-dish™, were a pulse stimulation with an amplitude of 1 V, a pulse duration of 100 ms (*i.e.* frequency of 10 Hz), and a pulse width of 2 ms for 24 h/day. This electrical condition was applied to four cell-material systems: H-fibre, H-fibre with laminin, F-fibre, and F-fibre with laminin. Only the result of the neurite extension length was analysed daily in this 3 days study as mentioned above.

The measurement of neurite length was the same protocol mentioned in section 5.1.10. The *n* number represented the number of individual neurites collected from two parallel electrical stimulation experiments. The overall data were presented in box-whisker plots, and all data points (individual neurites) were illustrated in polar scatters. Owing to low numbers of repeats (2 parallel experiments), no statistical analysis (comparative analysis) was performed in this chapter.

Table 6.2 the electrical parameters for optimisation.

Electrical parameters	Details
Types of electrodes	Carbon plate electrodes (C-dish™) and L-shaped platinum wire electrodes (custom-made)
Types of electricity	Direct current stimulation (DC) and Pulse stimulation
Amplitudes of voltage	1, 2, and 3 v (representing ~33, ~67, and ~100 v/m respectively)
Pulse cycle period	5, 10, 100, and 1000 ms (representing 200, 100, 10, and 1 Hz respectively)
Pulse widths	2 ms
Times	1, 2, 4, 8, and 24 h/day

6.2. Results

6.2.1. Computational modelling

The computational model mainly presented the effects of EF (V/m) and current density (A/m²) in a whole system of the cell culture chamber. In this macroscale model, the PEDOT:PSS mat was simply designed as a smooth thin sheet without the morphology of fibres inside. The results were measured from only the middle position between electrodes. In addition, the results of the space charge density (C/m³) was illustrated in all areas of the microenvironment model of fibres.

6.2.1.1. EF and current density in cell culture chamber

The results of EF in the cell culture medium and PEDOT:PSS mat were similar; however, they were slightly lower than the input EF. These EF results of H-fibre were slightly higher than F-fibre. In contrast, the current density in the cell culture medium was approximately 2 folds higher than in PEDOT:PSS mat. However, the current density of H-fibre was slightly higher than F-fibre as well as EF results. All computational data is presented in Table 6.3 and Table 6.4.

Table 6.3 Computational results of electric field (EF) in cell culture chamber.

Input voltage	H-fibre		F-fibre	
	Medium	PEDOT:PSS mat	Medium	PEDOT:PSS mat
1 V (~33 V/m)	32 V/m	32 V/m	31 V/m	31 V/m
2 V (~67 V/m)	65 V/m	65 V/m	63 V/m	63 V/m
3 V (~100 V/m)	97 V/m	97 V/m	95 V/m	95 V/m

Table 6.4 Computational results of current density in cell culture chamber.

Input voltage	H-fibre		F-fibre	
	Medium	PEDOT:PSS mat	Medium	PEDOT:PSS mat
1 V (~33 V/m)	55 A/m ²	29 A/m ²	53 A/m ²	28 A/m ²
2 V (~67 V/m)	110 A/m ²	58 A/m ²	107 A/m ²	56 A/m ²
3 V (~100 V/m)	165 A/m ²	87 A/m ²	161 A/m ²	85 A/m ²

The distribution of current density in the cell culture chamber is illustrated in Figure 6.3. The highest points of current density were at the inner corners of electrodes, whilst the lowest density were at the corners of the cell culture chamber. By applying an input voltage of 3 V, the highest current density was ~240 A/m² in H-fibre and ~320 A/m² in F-fibre. From the inner corners and edges of electrodes to the middle point between electrodes, the current density gradually declined in H-fibre. In contrast, it largely decreased in F-fibre. In the PEDOT:PSS mat analysis, the current density at both edges of the mat, which were parallel to electrodes, was higher than other areas. In particular, the positions or the edges of the mat, touching the inner corners of electrodes, had the highest theoretical current density.

In a cycle of the pulse simulation model, the input voltage of 1, 2, or 3 V was generated for 0.5 s (ON), followed by the voltage of 0 V (OFF) for 0.5 s. The pulse duration was approximately 1.0 s in total. The simulation results showed that the EF and current density were steady, and their

directions were from positive to ground electrodes in the ON period. Both the EF and the current density were not immediately eliminated in the OFF period. They were however, drastically decreased, and a small amount of the EF and the current density was still observed in the system, as shown in Figure 6.4 and Figure 6.5. The level of retained EF and current density in the OFF period were in the range of nV/m and nA/m². Interestingly, the directions of retained EF and current density in the OFF period were dynamic and unsteady. The back and forth movements between both sides of electrodes and the middle point of the chamber were observed in the resting period, as shown in Figure 6.6 to Figure 6.9.

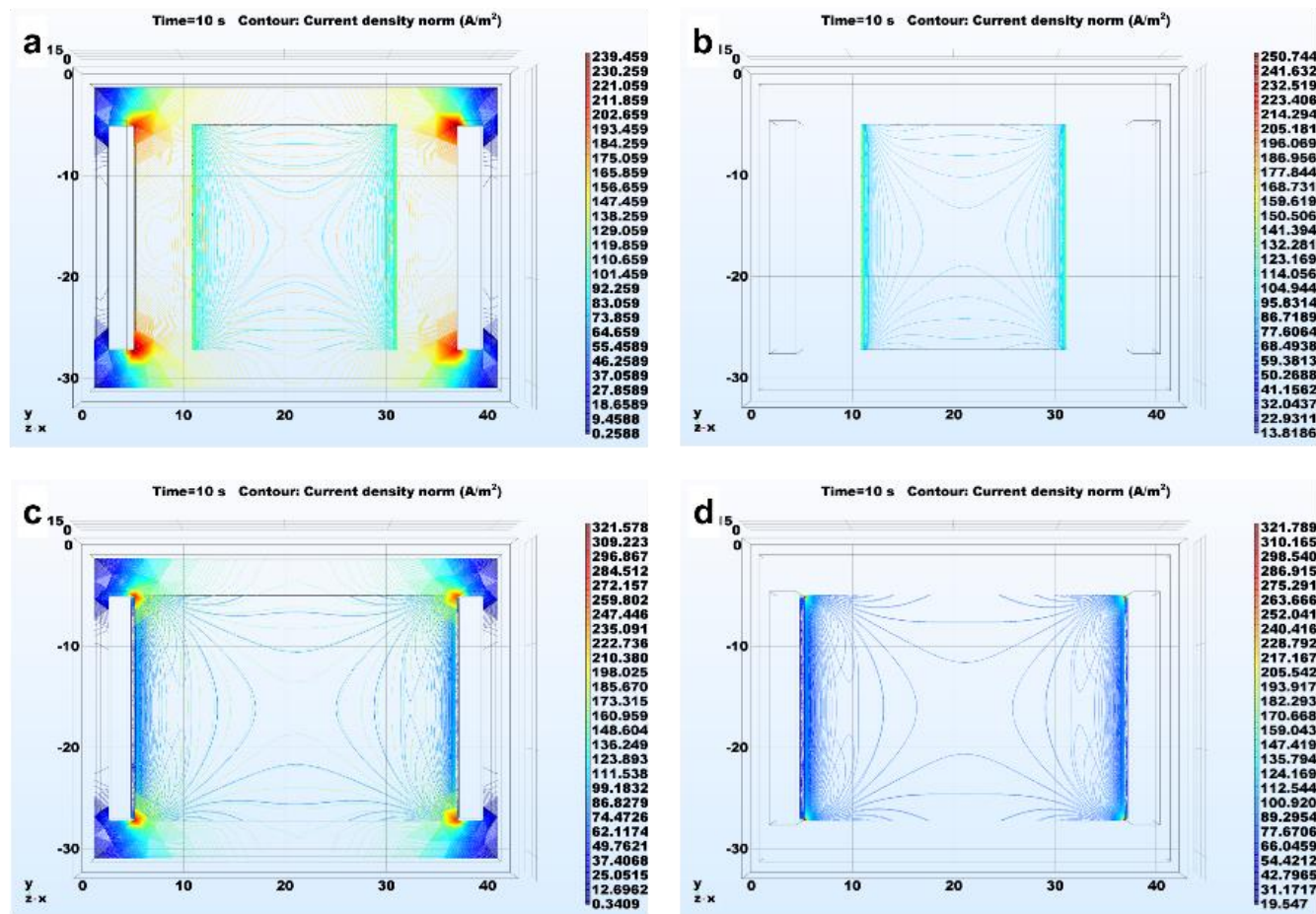


Figure 6.3 Distribution of current density in a cell culture chamber system with the applying voltage of 3 V: (a and c) distribution in the whole system, in (a) H-fibre, (c) F-fibre and (b and c) distribution in PEDOT:PSS mat, in (b) H-fibre, and (c) F-fibre.

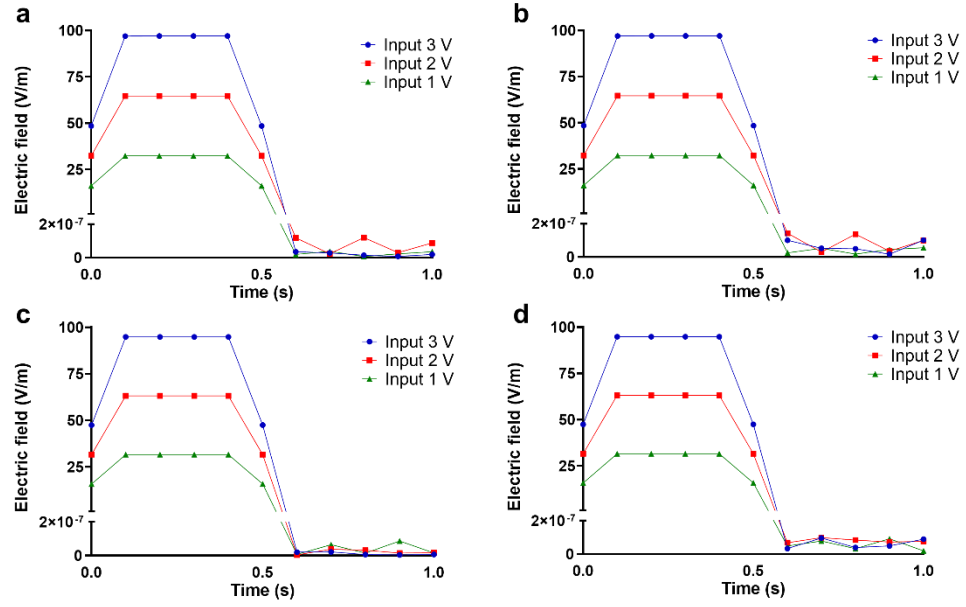


Figure 6.4 Electric field (EF) in the middle position of cell culture chamber system generated by the input of pulse stimulation: (a) medium of H-fibre, (b) PEDOT:PSS mat of H-fibre, (c) medium of F-fibre, and (d) PEDOT:PSS mat of F-fibre.

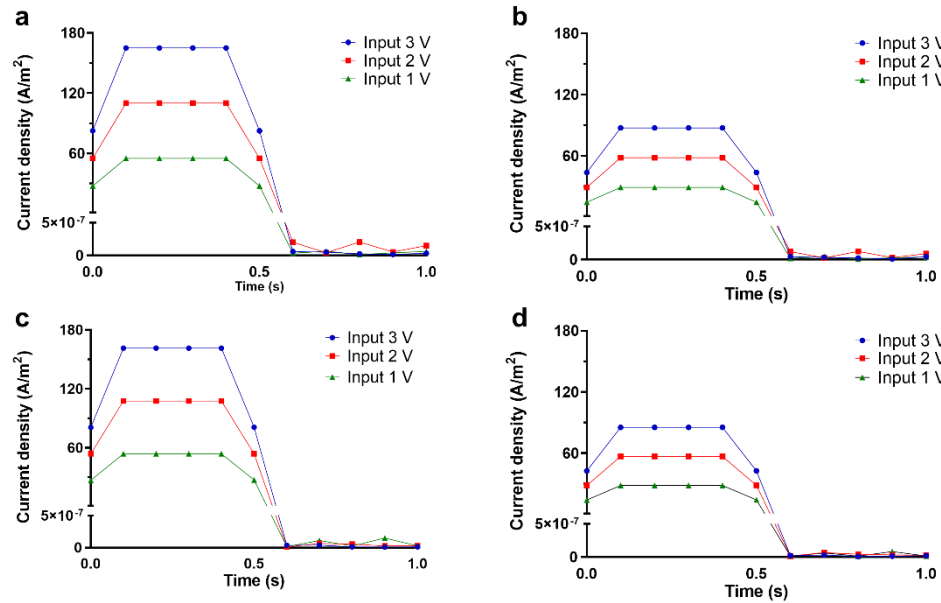


Figure 6.5 Current density in the middle position of cell culture chamber system generated by the input of pulse stimulation: (a) medium of H-fibre, (b) PEDOT:PSS mat of H-fibre, (c) medium of F-fibre, and (d) PEDOT:PSS mat of F-fibre.

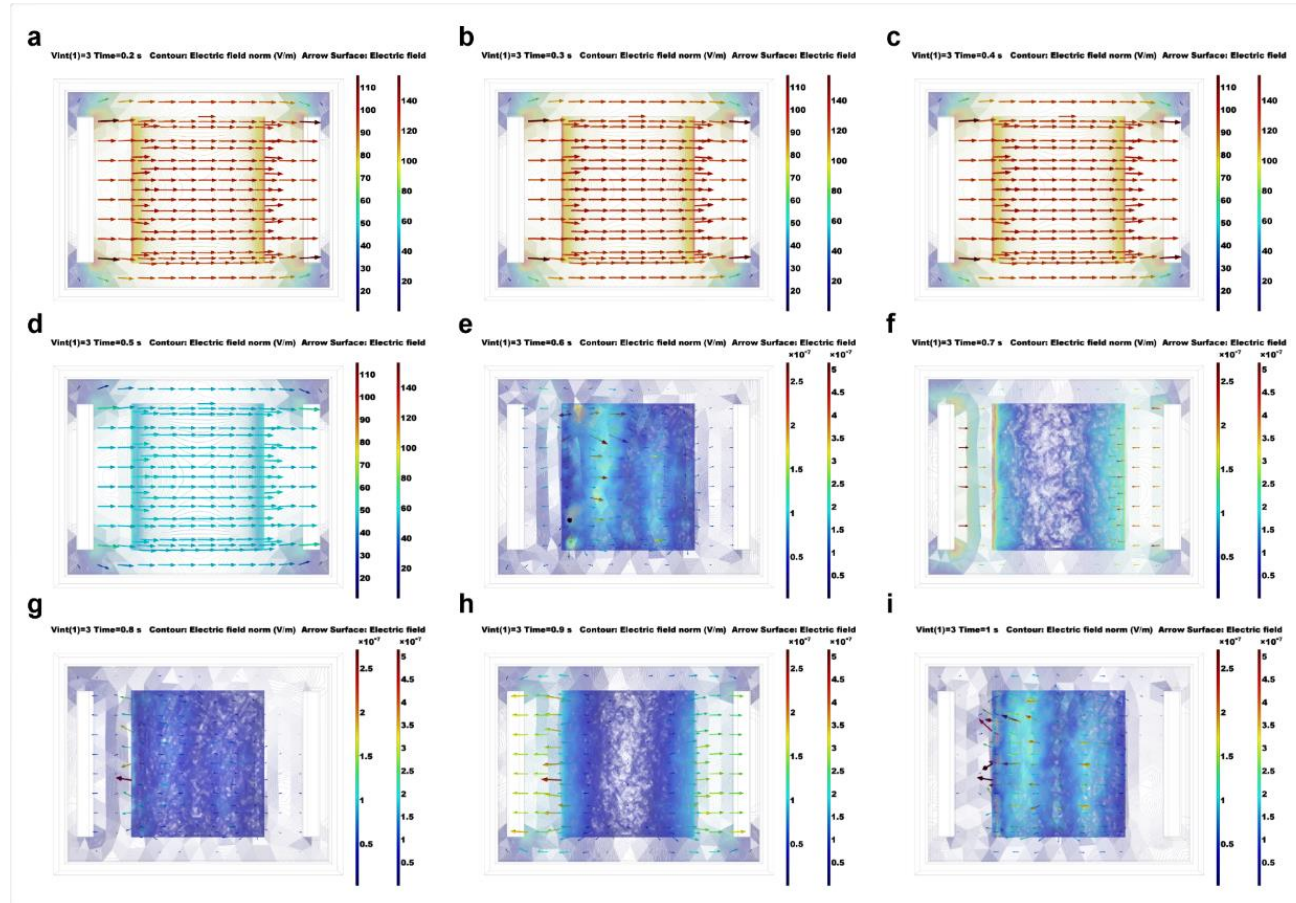


Figure 6.6 EF in H-fibre condition during a pulse stimulation with the input amplitude of 3 V: (a – c) ON period, $t = 0.2, 0.3$, and 0.4 s and (d – i) OFF period, $t = 0.5, 0.6, 0.7, 0.8, 0.9$, and 1.0 s respectively, the left scale is for arrow surface EF (V/m) and the right scale is for contour EF (V/m).

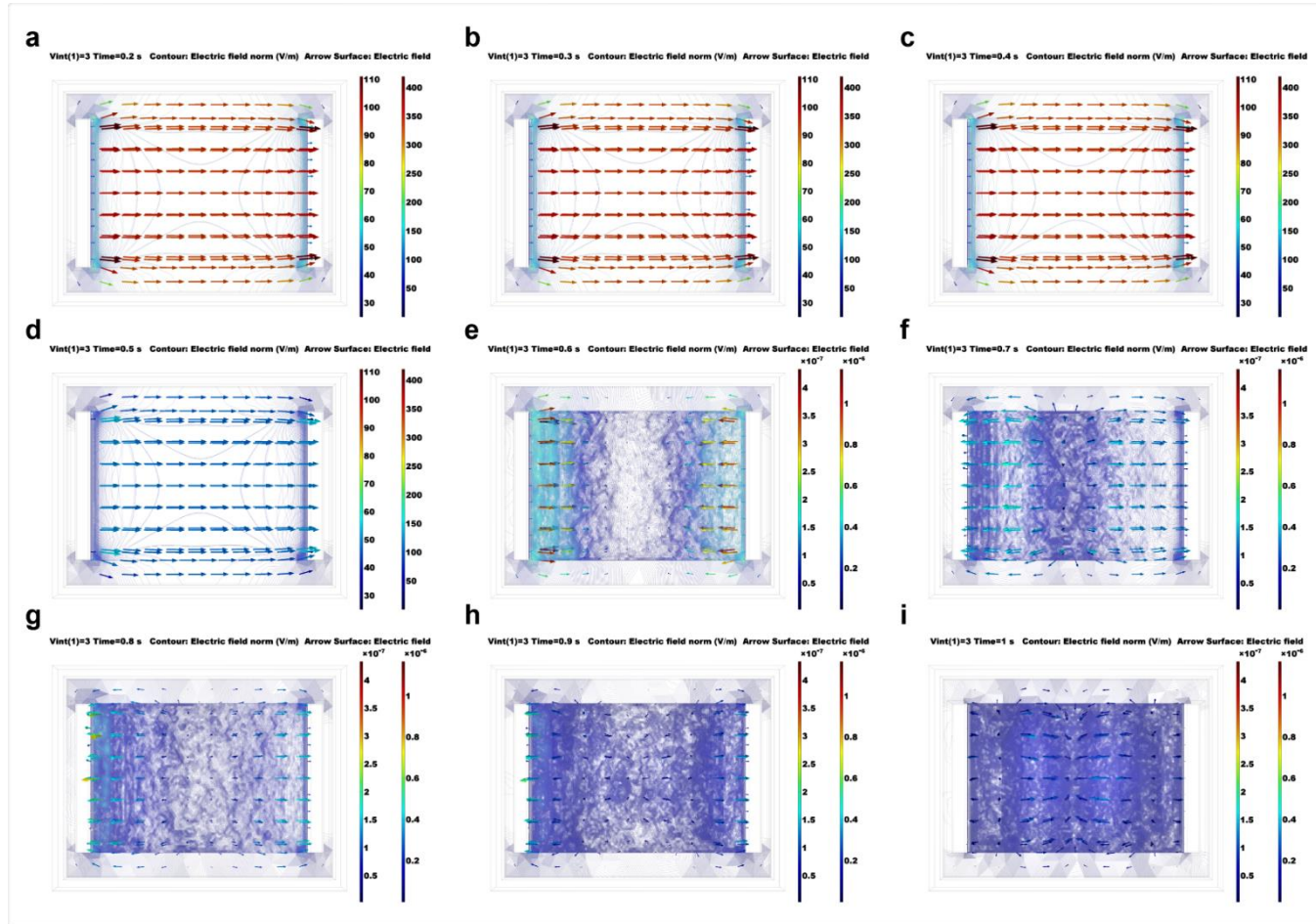


Figure 6.7 EF in F-fibre condition during a pulse stimulation with the input amplitude of 3 V: (a – c) ON period, $t = 0.2, 0.3$, and 0.4 s and (d – i) OFF period, $t = 0.5, 0.6, 0.7, 0.8, 0.9$, and 1.0 s respectively, the left scale is for arrow surface EF (V/m) and the right scale is for contour EF (V/m).

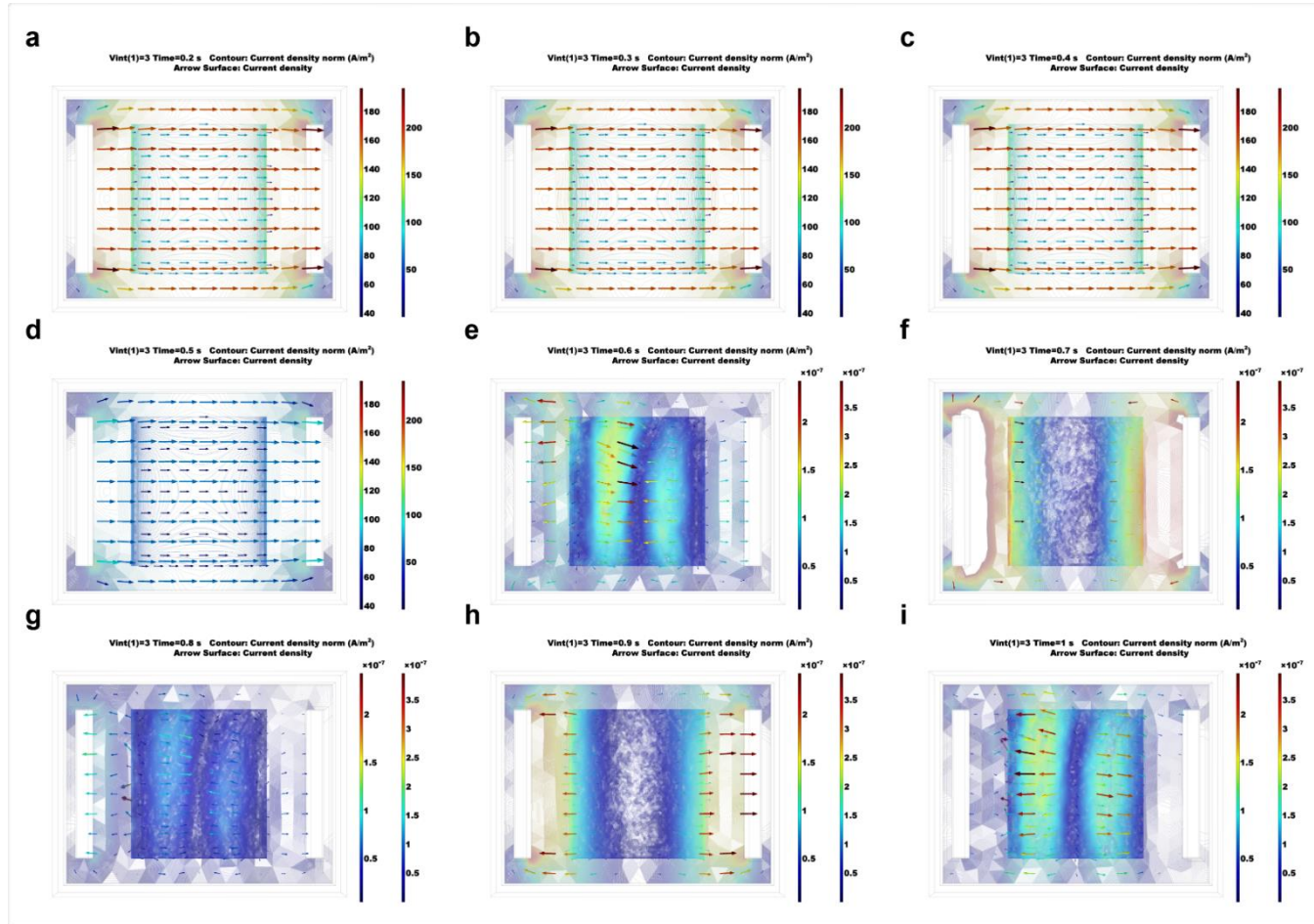


Figure 6.8 Current density in H-fibre condition during a pulse stimulation with the input amplitude of 3 V: (a – c) ON period, $t = 0.2, 0.3$, and 0.4 s and (d – i) OFF period, $t = 0.5, 0.6, 0.7, 0.8, 0.9$, and 1.0 s respectively, the left scale is for arrow surface current density (A/m^2) and the right scale is for contour current density (A/m^2).

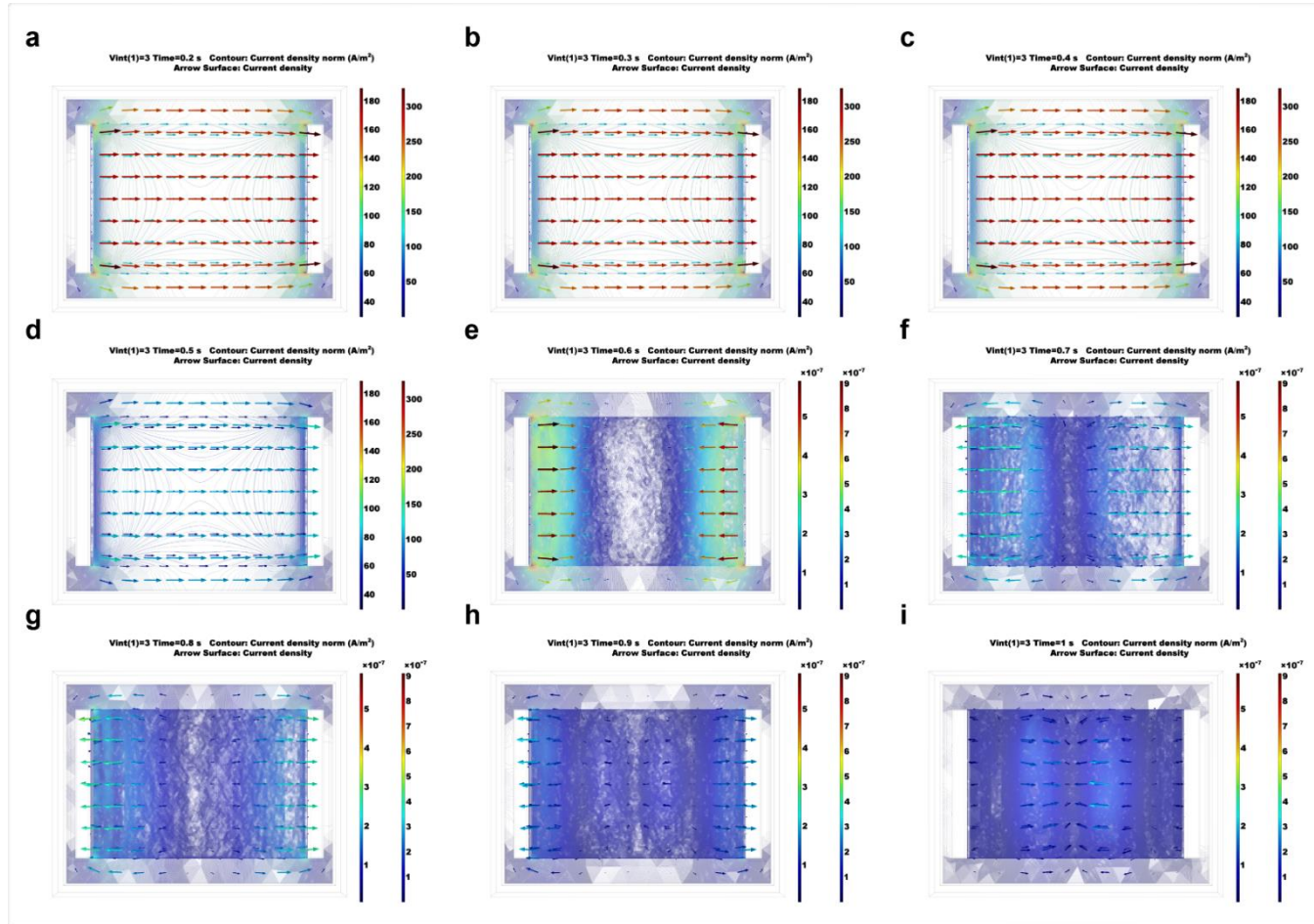


Figure 6.9 Current density in F-fibre condition during a pulse stimulation with the input amplitude of 3 V: (a – c) ON period, $t = 0.2, 0.3$, and 0.4 s and (d – i) OFF period, $t = 0.5, 0.6, 0.7, 0.8, 0.9$, and 1.0 s respectively, the left scale is for arrow surface current density (A/m^2) and the right scale is for contour current density (A/m^2).

6.2.1.2. Charge and current density in microenvironment of fibres

In electromagnetic theory, charge and current density are associated with a continuity equation. The space charge density ($\rho(\vec{r})$) demonstrates how particles occupy in space, and the current density ($\vec{J}(\vec{r})$) displays how particles pass through the boundary surface between neighbouring volumes. In each infinitesimal volume of the microenvironment model of fibres, $\rho(\vec{r})$ is estimated according to Gauss's law and $\vec{J}(\vec{r})$ according to Ohm's law as shown in the equations below:

$$\rho(\vec{r}) = \varepsilon_a \nabla \cdot \vec{E}(\vec{r})$$

$$\vec{J}(\vec{r}) = \sigma \vec{E}(\vec{r})$$

where, ε_a is the absolute permittivity of the medium, σ is the conductivity of the medium, ∇ is gradient operator, and $\vec{E}(\vec{r})$ is EF in each infinitesimal volume [350].

The rotation of the fibre mat affects both charge and current density in the microenvironment model. In the case of the mat parallel to EF, the charge density was likely to be neutral in almost all spaces (white). However, there were charges in both ends of the fibre mat, which may touch electrodes. The positive (red) and negative (blue) charges were highly accumulated in both ends, as shown in Figure 6.10 (a – c). The current density moved steadily in the same direction of EF along the fibre alignment (arrow lines).

In the case of the mat being perpendicular to EF, the model clearly illustrated the presence of charge density in all areas, as shown in Figure 6.10 (d – f). Even though the space of positive and negative charges was randomly generated, they were equally distributed in the whole mat as alternately coloured red – blue – red – blue. The direction of current passing through the medium was similar to the EF direction. Many directions of currents were observed in an individual fibre (Figure 6.10 (f)). The directions were opposite to the direction of EF and current in the medium. Moreover, the current was unable to pass from one fibre to another neighbouring fibre continuously. Every fibre of IPN mats had its character of current distribution, which might be unique and different from others.

In summary, the fibre mat parallel to EF had a low distribution of space charge density compared to the fibre mat perpendicular to EF. Its current density passing through medium and

fibres were in the same direction following EF. In addition, the current density passing through fibres, in the case of fibre mat perpendicular to EF, may flow in various directions, which were almost opposed to the EF.

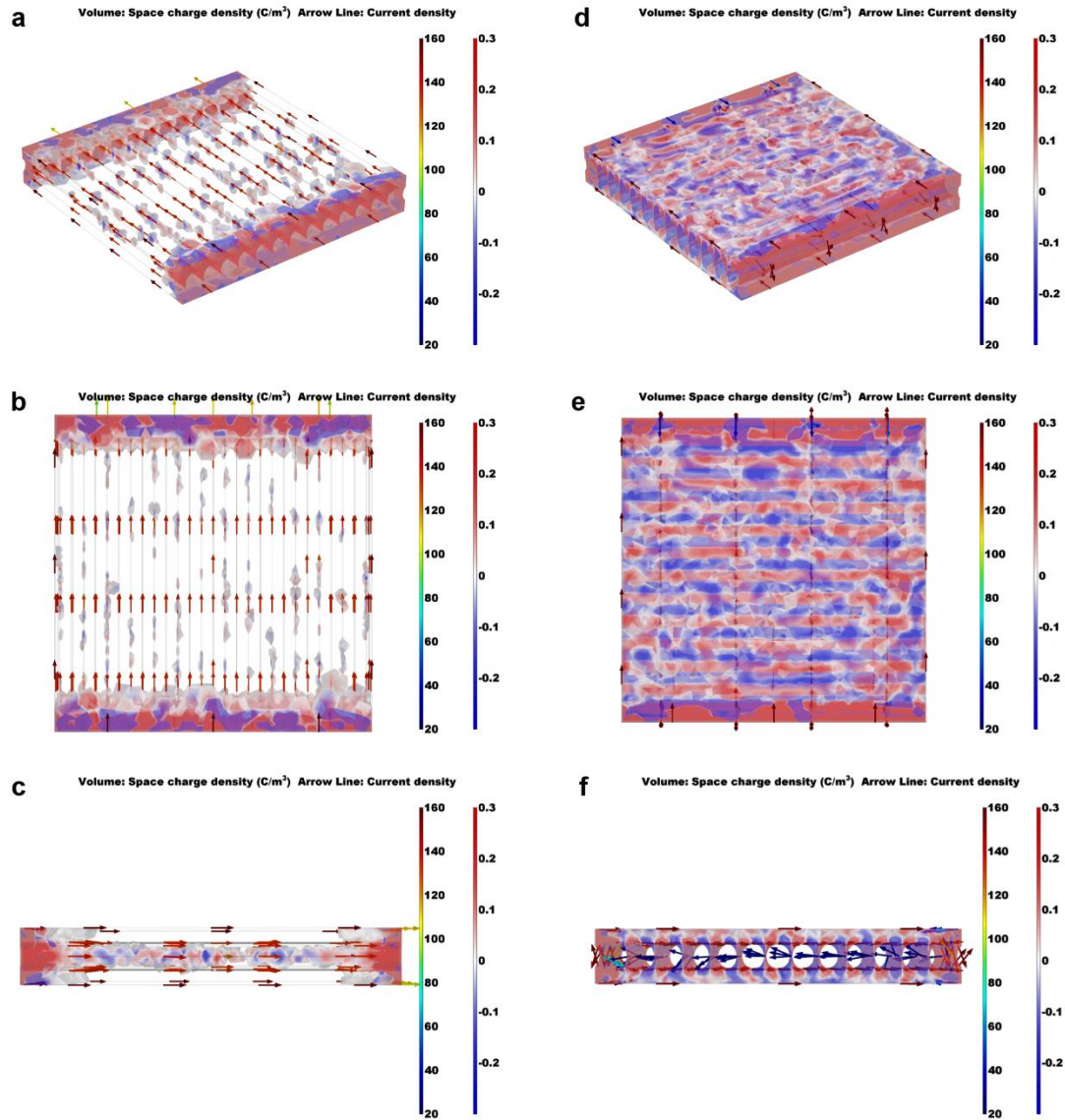


Figure 6.10 Space charge and current density at the microenvironment of fibres: (a – c) the input EF direction parallel to fibres and (d – e) the input EF direction perpendicular to the fibre alignment, the left scale is for arrow lines current density (A/m^2) and the right is for contour space charge density (C/m^3).

6.2.2. Optimisation of electrical parameters

6.2.2.1. Types of electrodes

An electrical regime using either carbon plate electrodes (C-dish™) or the L-shape platinum wire electrodes developed by Kasama Srirussami, Cartmell laboratory [351, 352] were optimised in cell culture medium by measuring the output voltage at electrodes during electrical stimulation with DC and pulse stimulation.

Typically, the output voltage was lower than the input. Both C-dish™ and L-shape platinum provide similar output in DC stimulation, while their output signals were in different shapes, as shown in Figure 6.11. The waveform of the L-shape platinum wire was distorted in pulse stimulation due to the electrode polarisation [179]. The output amplitude of the C-dish™ electrode and other related results were explained in Table 6.5. Since the C-dish™ is more suitable for pulse stimulation than the L-shape platinum, the C-dish™ was preferred in this study.

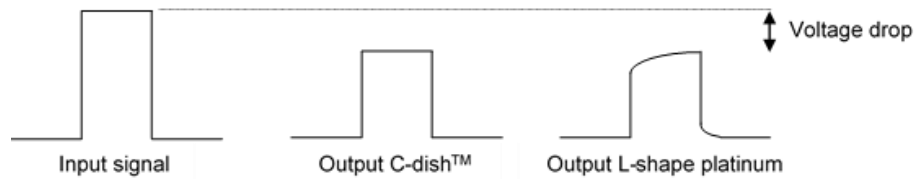


Figure 6.11 Schematic of the input and output signals of different types of electrodes measured in cell culture medium.

Table 6.5 Variation of electrical potential between C-dish™ electrodes in cell culture medium system

Input voltage (V)	Output voltage (V)	Estimated output EF (V/m)	Voltage drop (%)
0.5	0.36	6	28
1.0	0.76	25	24
1.5	1.24	41	17
2.0	1.60	53	20
2.5	2.00	67	20
3.0	2.40	80	20
3.5	2.80	93	20
4.0	3.24	108	19

6.2.2.2. DC stimulation of NG108-15 grown on TCP

After exposing culture medium to a DC stimulation with 3 V for 2 h, many bubbles were visually observed in the cell culture medium only at the surface area of the anode, suggesting the electrolysis of water, also known as a redox reaction. Subconfluent cells were detached from the substrate, and the suspended cells were rounded and aggregated into the cluster, as shown in Figure 6.12.

To confirm the cell viability after electrical stimulation, the stimulated cells were incubated for 24 h. They were still rounded, aggregated as clusters, and floated in cell culture medium without re-attaching TCP. Moreover, cells were likely to be shrunk compared to the early phase after electrical stimulation immediately. These morphologies (e.g. shrinkage) suggest cell death undoubtedly [353, 354] and there was no need to do the other assays such as trypan blue in this study. If the quantification of cell viability is needed in the future, the trypan blue assay would be recommended. Perhaps in this case, the DC stimulation was not suitable for the system of this study.

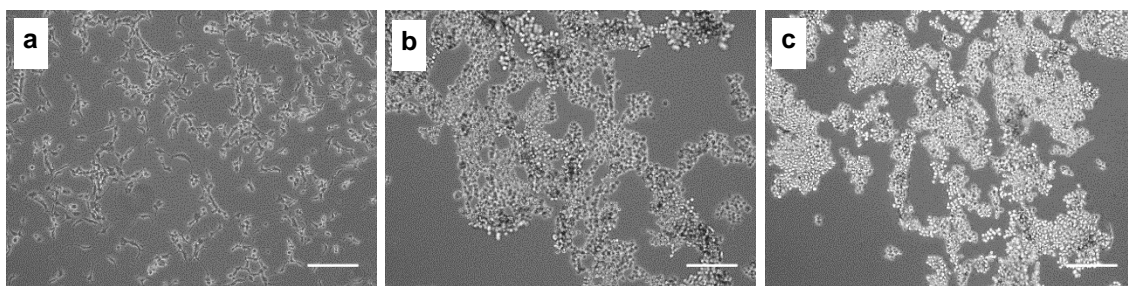


Figure 6.12 NG108-15 after electrical stimulation with DC of 3 V (~ 100 V/m) for 2 h: (a) before stimulation, (b) after stimulation, and (c) after stimulation and incubated for 24 h, the scale bar of 250 μm .

6.2.2.3. Pulse stimulation of NG108-15 grown on TCP

The monophasic pulse with the pulse width of 2 ms was a control parameter in experiments. The pulse amplitude and total periods of the pulse cycle were varied, as mentioned before (Table 6.2). The pulse stimulation was applied to the differentiated NG108-15 cells cultured in the DMSO medium. After stimulation, the results of cell detachment and neurite outgrowth were observed every day for 3 days.

The pulse stimulation with 3 V amplitude and 5 ms pulse cycle caused cell detachment after 2 h and cell death after 4 h of stimulation. In the case of 2 h stimulation, the detached cells were incubated again for 24 h. Unfortunately, the detached cells could not re-attach TCP, and many cell debris were also found. This suggests that the pulse stimulation with 3 V amplitude and 5 ms pulse cycle for 2 h maybe inducing programmed cell death or apoptosis, which should be considered in the future. Moreover, the colour of the cell culture medium around the anode had changed to light yellow after 2 h stimulation, indicating acidic products from electrolysis. The colour gradient from pink to yellow was seen from the ground electrode to the anode. However, the colour gradient was disappeared, and the medium colour was reversed to pink again after leaving at room temperature for 10 – 15 min without stimulation.

According to the previous studies, the C-dishTM was often used in a muscular system such as myoblast (C2C12 cell line) [355, 356] and cardiac muscle cells [357]. They explained that the pulse stimulation with a low frequency of ~ 1 Hz could stimulate cellular activity effectively.

Thus, the frequency of ~1 Hz was preferred in the following experiments. The period of the pulse cycle was then increased up to 1000 ms.

By the pulse stimulation with 1000 ms pulse cycle, 2 h/day for 5 days, cells were still alive in all conditions of amplitudes (1, 2, and 3 V). Cell morphology after electrical stimulation was similar to control in the condition of 1 V. However, a lot of cell detachment was observed at days 4 and 5 in the condition of 2 and 3 V, respectively. Interestingly, the stimulation with 1V amplitude, 1000 ms pulse cycle for 2 h/day and 24 h/day provided similar cell morphologies without cell detachment. No bubbles and colour changes in the medium were found in these conditions. It can be presumed that the monophasic pulse with 1 V amplitude is possible to stimulate NG108-15 cells continuously (24 h/day) without damaging them.

The optimal condition of electrical stimulation, which can promote neurite extension length, was investigated by varying the periods of pulse cycle at 10, 100, and 1000 ms representing the frequency of 100, 10, and 1 Hz, respectively based on the pulse of 1 V amplitude, 2 ms pulse width, and 24 h/day. The neurite extension length after stimulation is presented in Figure 6.13. The neurite length was increased by stimulation time on both uncoated TCP and laminin-coated TCP. The average neurite length was 110 – 150 μm for 1 day, 200 – 280 μm for 2 days, and 250 – 350 μm for 3 days stimulation.

The longest neurite length was ~600 μm after stimulation for 3 days in all periods of the pulse cycle. In particular, the pulse stimulation promoted longer neurite extension than control, which had the longest neurite of ~400 – 500 μm on uncoated TCP. On the other hand, the longest neurite after stimulation in all conditions was similar to control on the laminin-coated substrate. Although the average neurite length of stimulation with 1000 ms pulse cycle was significantly lower than that of other conditions and control, the longest neurite was still in the same length. Moreover, cells were formed like neural networks after pulse stimulation especially on laminin-coated TCP, as shown in Figure 6.14.

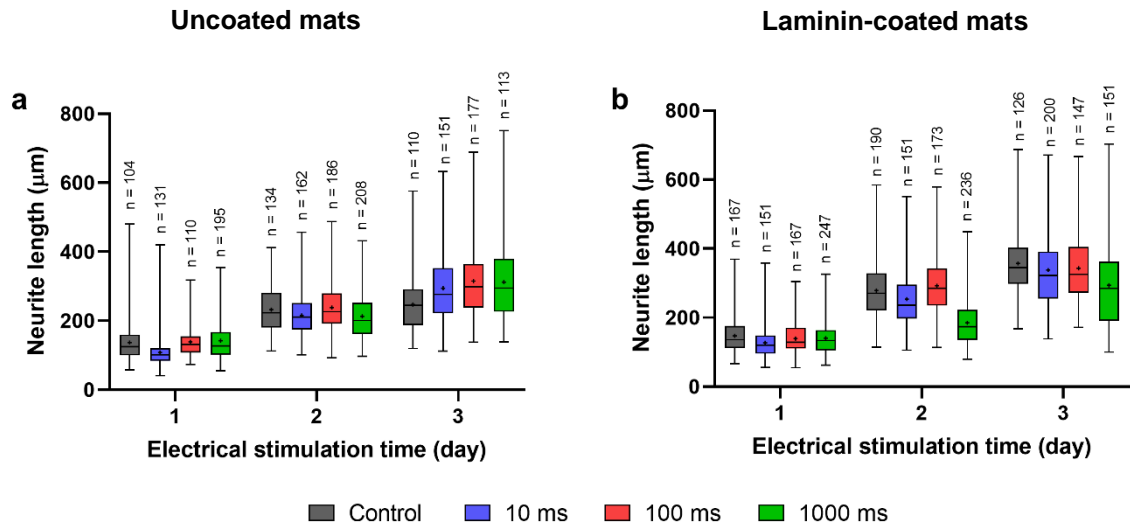


Figure 6.13 Neurite extension length after electrical stimulation with 1 V amplitude, 2 ms pulse cycle, 24 h/day, and various periods of pulse cycle (10, 100, and 1000 ms) on TCP, presented in a box – whisker plot from min – max with the median at the middle line and the mean at the mark (+): (a) uncoated TCP and (b) laminin-coated TCP, n represents the number of neurites measured from 2 wells of cells in parallel experiments of cell culture.

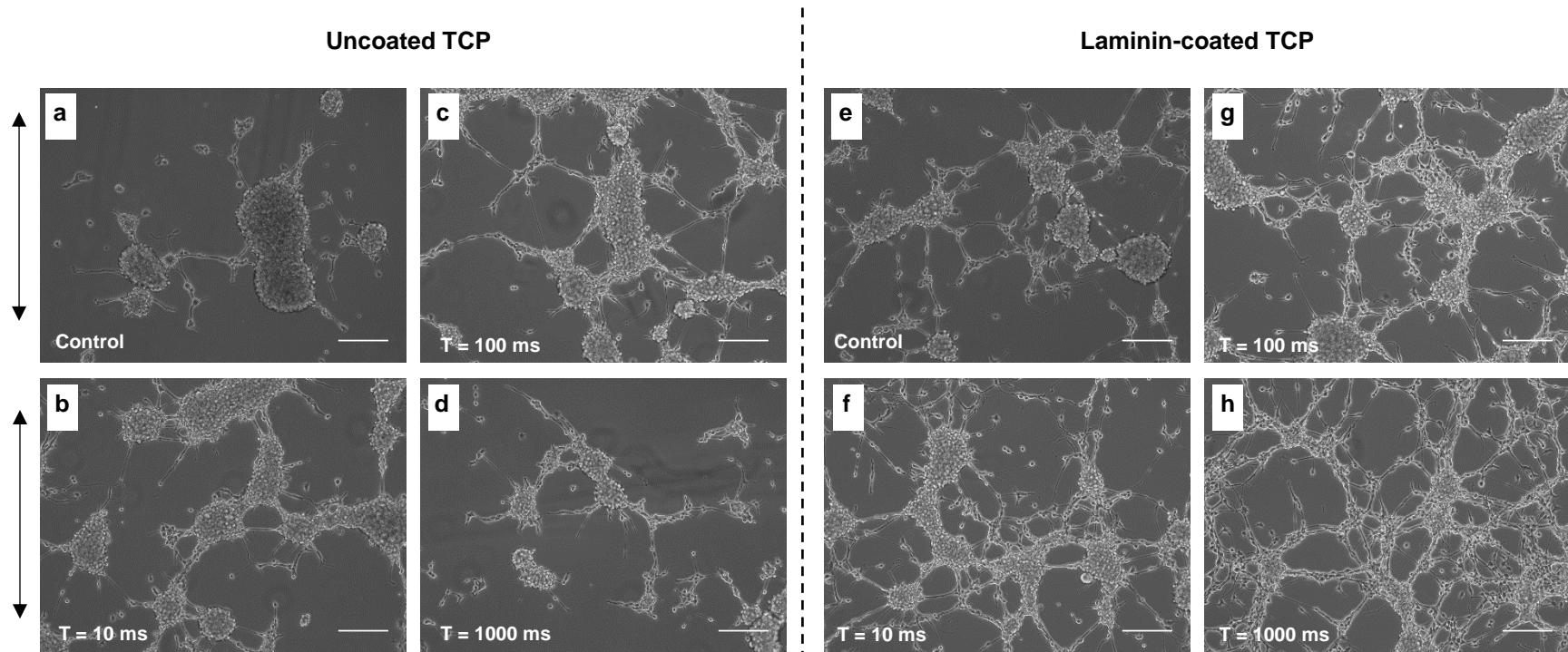


Figure 6.14 NG108-15 after electrical stimulation with 1 V pulse amplitude, 2 ms pulse width, and 24 h/day for 3 days, (left) uncoated TCP and (right) laminin-coated TCP, the stimulation with the variation of pulse cycle periods: (a and e) control without stimulation, (b and f) 10 ms, (c and g) 100 ms, and (d and h) 1000 ms, the scale bar of 250 μm . The arrow shows the direction of the EF.

6.2.3. Effect of electrical stimulation on neurite outgrowth for NG108-15 grown on electrospun SF and IPN ($\alpha = 2.3$) mats

According to the above results, the pulse stimulation with 1 V amplitude, 2 ms pulse width, 100 ms pulse cycle, and 24 h/day was evaluated as the optimal condition of electrical stimulation (Op-ES). The Op-ES was applied to two types of fibre mats: electrospun SF and IPN ($\alpha = 2.3$), which were prepared in four conditions: H-fibre, H-fibre with laminin, F-fibre, and F-fibre with laminin. Only the fibre alignment parallel to EF was focused on in this study.

6.2.3.1. Control (without ES)

In control (non-stimulation), the average neurite extension length of NG108-15 growing on IPN ($\alpha = 2.3$) were significantly higher than growing on electrospun SF in uncoated samples, as shown in Figure 6.15 (a). The longest neurite length was ~400 nm on IPN ($\alpha = 2.3$) and ~300 nm on electrospun SF.

In laminin-coated samples, the neurites on electrospun SF and IPN ($\alpha = 2.3$) were at a similar length at day 1, as shown in Figure 6.15 (b). In F-fibre, the average neurite length on IPN ($\alpha = 2.3$) was gradually increased by time, and it was higher than electrospun SF at days 2 and 3. In contrast, the average neurite length on IPN ($\alpha = 2.3$) was slightly lower than electrospun SF at day 3 in H-fibre. The maximum neurite length was ~300 – 400 nm in both uncoated and laminin-coated samples. The individual neurite length and its direction on fibre mats were plotted in polar scatter and polar histogram as shown in Figure 6.16 for the control of H-fibre and Figure 6.17 for the control of F-fibre.

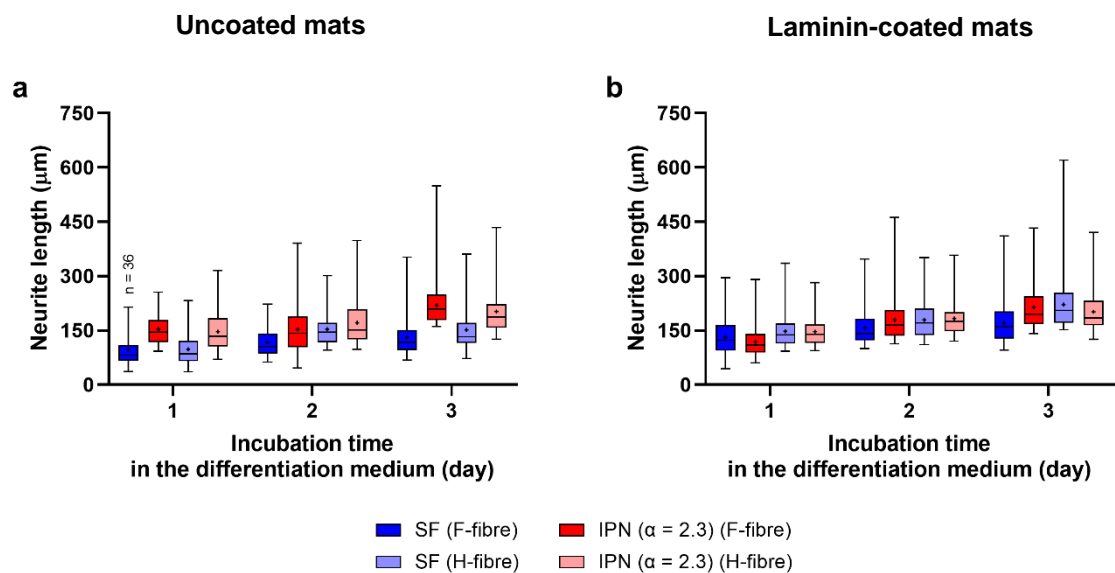


Figure 6.15 Neurite extension length on control materials (without ES) presented in a box – whisker plot from min – max with the median at the middle line and the mean at the mark (+): (a) uncoated mats and (b) laminin-coated mats ($n = 120$ neurites representing 2 samples of fibre mats in parallel experiments of cell culture) except the uncoated SF (F-fibre) at day 1 ($n = 36$).

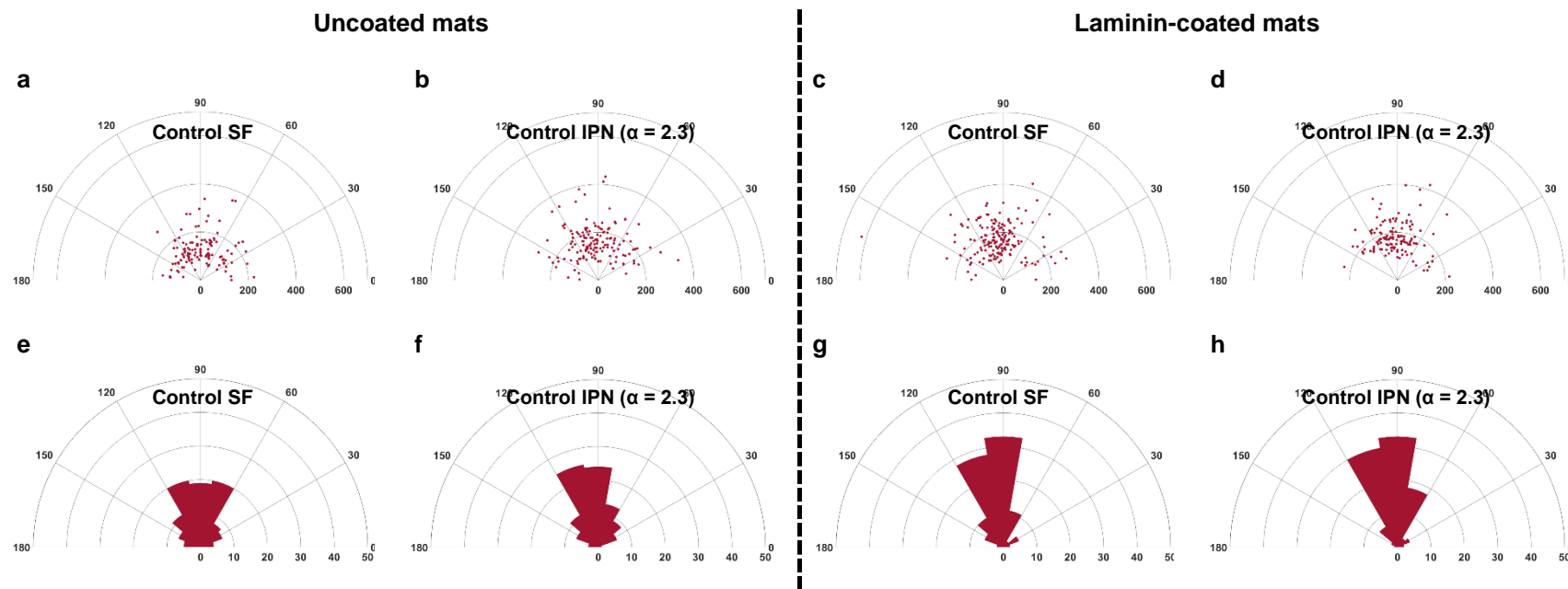


Figure 6.16 Example of neurite length and orientation of NG108-15 control (without the Op-ES) for 3 days on various materials of H-fibre condition: (left) uncoated mats, (right) laminin-coated mats, (a – d) polar scatter with the radian of 700 μm , and (e – h) polar histogram with the radian of 50%, the position of 90° is the parallel direction to the fibre alignment, ($n = 120$ neurites representing 2 samples of fibres in parallel experiments of cell culture). These graphs are replotted from the same data presented in Figure 6.15.

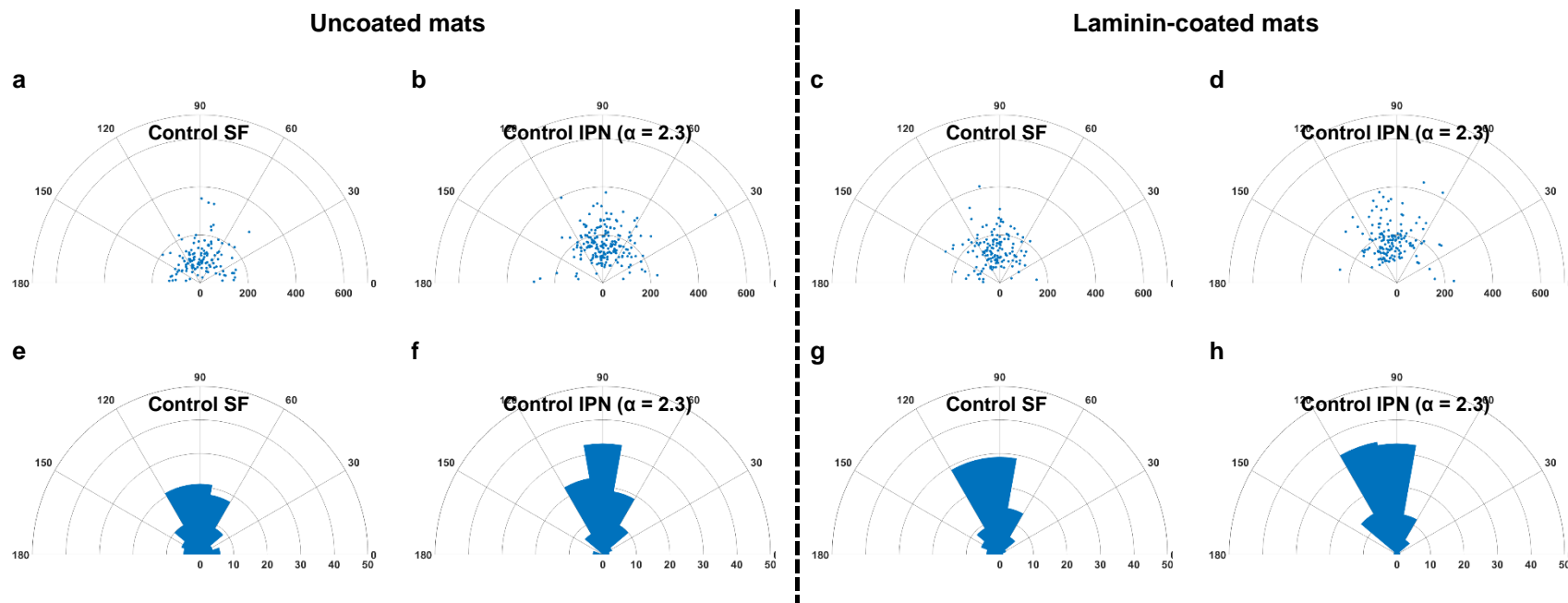


Figure 6.17 Example of neurite length and orientation of NG108-15 control (without the Op-ES) for 3 days on various materials of F-fibre condition: (left) uncoated mats, (right) laminin-coated mats, (a – d) polar scatter with the radian of 700 μm , and (e – h) polar histogram with the radian of 50%, the position of 90° is the parallel direction to the fibre alignment, ($n = 120$ neurites representing 2 samples of fibres in parallel experiments of cell culture). These graphs are replotted from the same data presented in Figure 6.15.

6.2.3.2. Electrical stimulation (ES) on fibre mats without contacting electrodes (H-fibre)

In Op-ES, the neurite outgrowth on fibre mats was analysed using IF images, as shown in Figure 6.18 as examples of staining. A cell cluster containing plenty of cells and nuclei were confirmed by the spots of DAPI staining (blue). The neurites were typically extended from the cell cluster, which was labelled with β -III tubulin staining (green). Most of the neurites were predominant to fibre alignment, which was in the vertical axis (Figure 6.18). The results of neurite extension length in the condition of H-fibre and F-fibre were plotted and shown in Figure 6.19.

Without laminin coating, the Op-ES was likely to inhibit the neurite extension length on both electrospun SF and IPN ($\alpha = 2.3$) mats compared to their controls without stimulation (Figure 6.19 (a)). However, the longest neurite of the IPN ($\alpha = 2.3$) with the Op-ES was ~ 500 nm, while that of the IPN without electrical stimulation was $\sim 300 - 400$ nm. Moreover, with Op-ES, the average neurite length on IPN ($\alpha = 2.3$) was significantly higher than on electrospun SF.

On the other hand, the Op-ES does not affect neurite extension on laminin-coated fibre mats (Figure 6.19 (b)). On day 1, the average neurite length on both fibre mats with Op-ES were lower than their controls, while they were similar to their controls on days 2 and 3 except for electrospun SF at day 3, which was little lower than its control.

In terms of neurite orientation, neurites were typically extended in many directions but most of them were in the same direction of fibre alignment, confirmed by the position of $80^\circ - 100^\circ$ in the polar plots as shown in Figure 6.20. In the case of uncoated samples, the Op-ES enhanced the neurite outgrowth following fibre alignment in both electrospun SF and IPN ($\alpha = 2.3$) mats. In electrospun SF, the percentage of neurites in the position of $80^\circ - 100^\circ$ was $\sim 20\%$ in control (without ES), while it was increased to $\sim 25\%$ after applying with the Op-ES (Figure 6.20 (e)). In IPN ($\alpha = 2.3$), it was $\sim 25\%$ in control (without ES), and it was increased to $\sim 30\%$ after Op-ES (Figure 6.20 (f)).

However, the Op-ES had no effect on neurite orientation on laminin-coated fibre mats. The percentage of neurites in the position of $80^{\circ} - 100^{\circ}$ was $\sim 30\%$ (Figure 6.20 (g and h)) as similar to the control (without ES).

6.2.3.3. Electrical stimulation (ES) on fibre mats with contacting electrodes (F-fibre)

The results of neurite extension length were presented in Figure 6.19 (c and d) and neurite orientation in Figure 6.21. Without laminin coating, the neurite extension length in Op-ES was lower than the control without stimulation in both fibre mats at days 1 and 3 (Figure 6.19 (c)). However, the Op-ES of IPN ($\alpha = 2.3$) provided the average neurite length longer than its control at day 2. With Op-ES, the average neurite length on IPN ($\alpha = 2.3$) was higher than on electrospun SF. The neurite length was gradually increased by time from day 1 – 2. After that, it was constant in both mats.

In laminin-coated fibre mats, the Op-ES inhibited neurite extension in both mats compared to their controls (Figure 6.19 (d)). However, the Op-ES on IPN ($\alpha = 2.3$) provided a longer neurite length than on electrospun SF. The neurite length was also increased by time throughout 3 days.

With Op-ES, more neurites were oriented predominantly to fibre alignment on uncoated electrospun SF. The percentage of neurites in the position of $80^{\circ} - 100^{\circ}$ was $\sim 30\%$ in Op-ES (Figure 6.21 (e)), while it was $\sim 20\%$ in control (without ES). However, it seems like the Op-ES had no effect on neurite orientation on electrospun SF with laminin and IPN ($\alpha = 2.3$) with and without laminin. Approximately 30% of neurites in these conditions were aligned in the position of $80^{\circ} - 100^{\circ}$, similar to their controls.

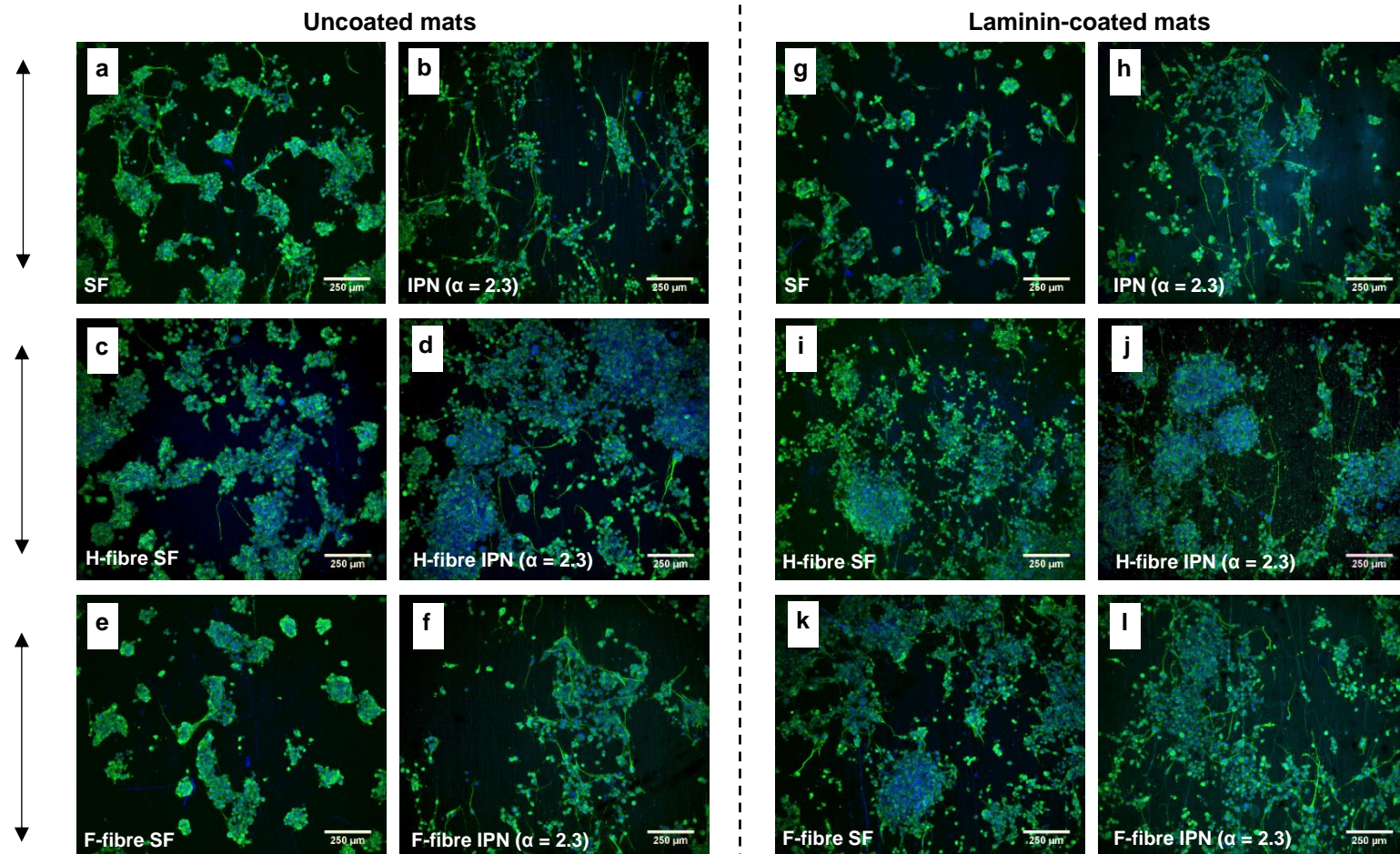


Figure 6.18 Immunofluorescence staining of NG108-15 after electrical stimulation with Op-ES for 3 days on various materials, (left) uncoated mats and (right) laminin-coated mats: (a, b, g, and h) control, (c, d, i, and j) stimulation on H-fibre, and (e, f, k, and l) stimulation on F-fibre, the double head arrow indicates the direction of aligned fibres.

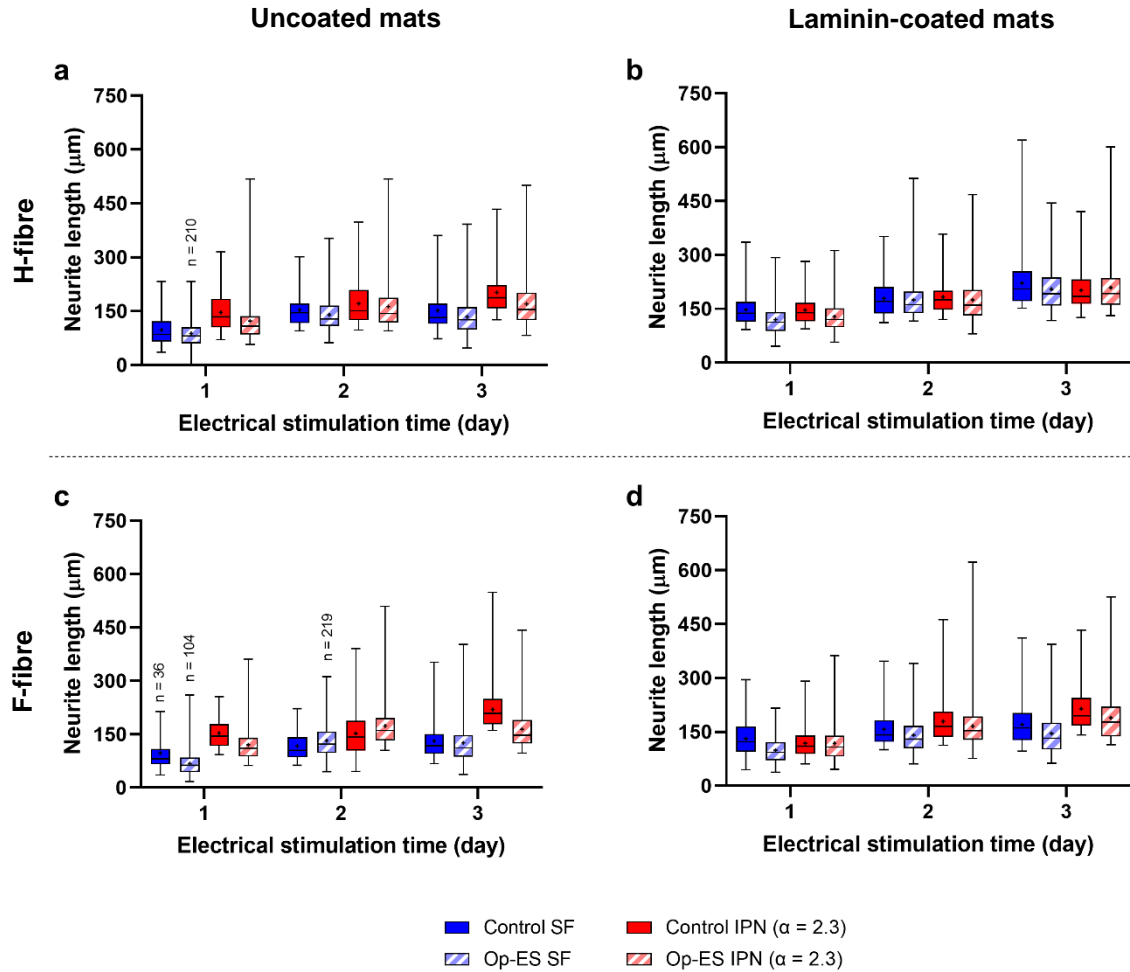


Figure 6.19 Neurite extension length on materials with the Op-ES presented in a box – whisker plot from min – max with the median at the middle line and the mean at the mark (+): (a) uncoated H-fibre, (b) laminin-coated H-fibre, (c) laminin-coated F-fibre, and (d) laminin-coated F-fibre, all of Op-ES groups ($n = 240$ neurites representing 2 samples of fibre mats in parallel experiments of electrical stimulation) and all of the control groups ($n = 120$) except some conditions n were shown in the figure.

It is to be noted that all of the control (without ES) in Figure 6.19 were replotted with the same data from Figure 6.15 in order to compare with the ES group with control.

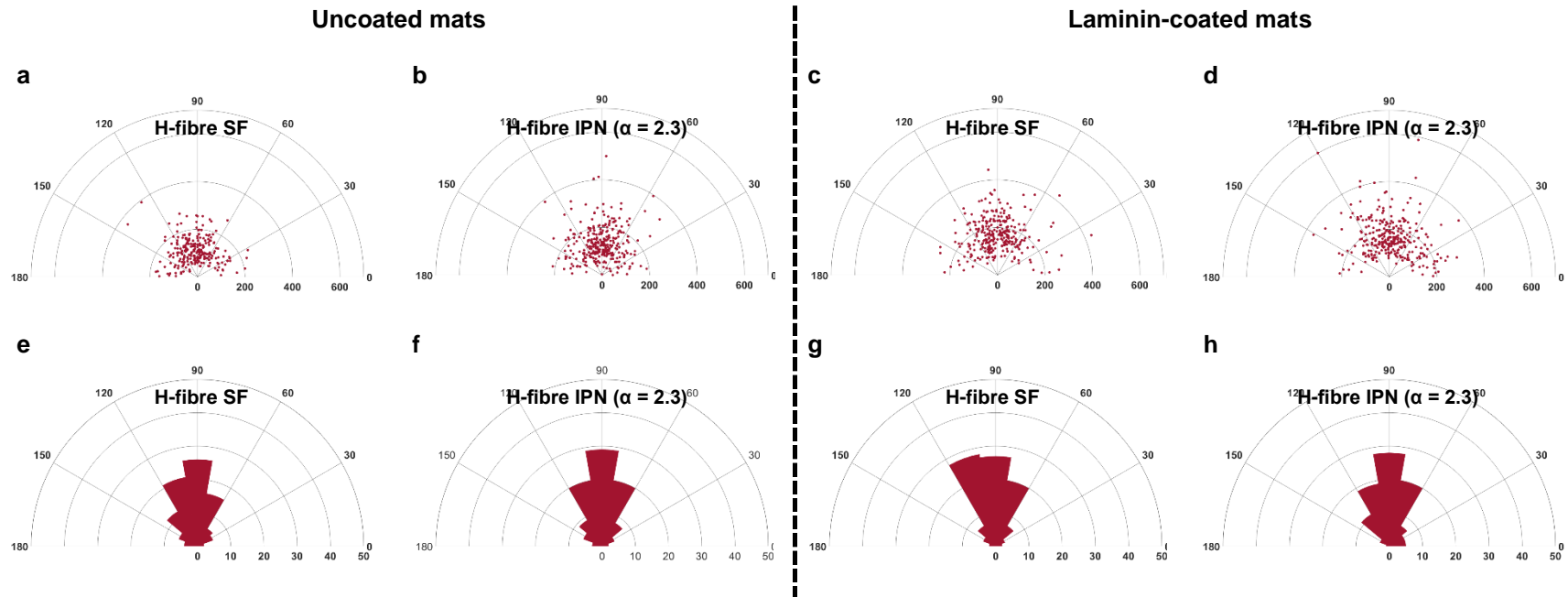


Figure 6.20 Example of neurite length and orientation of NG108-15 with the Op-ES for 3 days on various materials of H-fibre condition: (left) uncoated mats, (right) laminin-coated mats, (a – d) polar scatter with the radius of 700 μm , and (e – h) polar histogram with the radius of 50%, the position of 90° is the parallel direction to the fibre alignment, ($n = 240$ neurites representing 2 samples of fibres in parallel experiments of cell culture). These graphs are replotted from the same data presented in Figure 6.19.

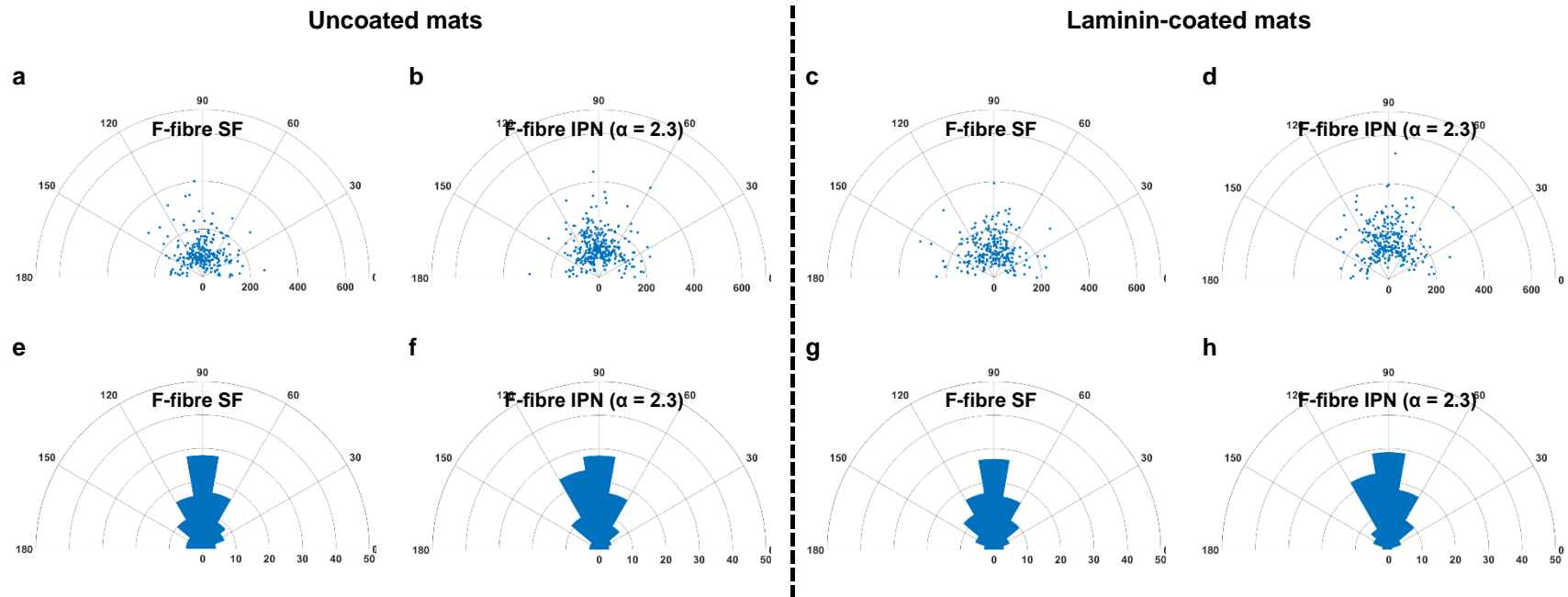


Figure 6.21 Example of neurite length and orientation of NG108-15 with the Op-ES for 3 days on various materials of F-fibre condition: (left) uncoated mats, (right) laminin-coated mats, (a – d) polar scatter with the radius of 700 μm , and (e – h) polar histogram with the radius of 50%, the position of 90° is the parallel direction to the fibre alignment, ($n = 240$ neurites representing 2 samples of fibres in parallel experiments of cell culture). These graphs are replotted from the same data presented in Figure 6.19.

6.3. Discussion

6.3.1. Effect of different types of electrode on electrical stimulation

In direct electrical stimulation, both *in vitro* and *in vivo*, several types of electrode materials have been studied before, such as platinum (Pt), gold (Au), Titanium (Ti), and Carbon (C) or graphite. Herein, the effect of using the custom-made L-shape Pt-electrode and C-electrode, C-dish™, were compared and evaluated. According to the result shown in Figure 6.11, the only different outcome between these two types of electrodes is the electrical waveform once applying a pulse stimulation.

Apart from excellent biocompatibility, the Pt-electrode has high electrical conductivity and high corrosion resistance. However, electrode polarisation is a disadvantage of using Pt-electrode as well as other metallic electrodes, which reduces the charge transfer efficiency [179, 181, 182]. It also influences the resistance and capacitance of the electrical double layer at the medium-electrode interface. Possibly, this effect leads to the electrical signal distortion found in this study.

Since cell culture medium is an electrolyte containing dissolved free ions, these ions move toward the electrode during electrical stimulation leading to the development of the ionic double layer at the medium-electrode interface [358]. The Randles equivalent circuit (Figure 4.2) can represent the RC model at this interface. This effect suggests that the voltage drop is a consequence of resistances at this interface. It typically occurs in both constant DC and pulse stimulation. On the other hand, the small curves distortion of output signals are the effects of charged and discharged voltages in the double-layer capacitor. It usually occurs in pulse stimulation since the capacitor is charged and discharged alternately.

The C-electrode has high charge transfer efficiency, conductivity, and corrosion resistance; however, it is brittle and may have high protein adsorption due to its porous surface [179, 181, 187, 189]. It highlights the importance of cleaning and washing after use. In this study, the voltage drop was found in C-electrode, indicating the formation of a double-layer during electrical stimulation. The C-electrode also provided the rectangular waveform as similar to input

without the character of charged and discharged voltage in the double layer capacitor. From the reasons above, the C-electrode is preferable to the Pt-electrode for use as a pulse stimulation electrode.

The C-dish™, IonOptix system, is widely used in the electrical stimulation for cells in culture, particularly in the study of the cardiac muscular system. Many studies used this system for stimulating the excitation-contraction coupling of myocytes associated with Ca²⁺ signalling [359, 360] and other related cellular mechanisms [361, 362]. A few studies used this system for nerve cells. For example, Yamada M., *et al.*, 2007 reported that mild electrical stimulation strongly influences embryonic stem cells to assume a neuronal fate [363]. Typically, electrical parameters applied in this IonOptix system are the pulse stimulation with a short pulse width, low frequency and high voltage such as pulse width of 2 and 5 ms, frequency of 0.5 and 1 Hz, and voltage of 10 – 40 V [355, 357]. Therefore, this is another suggestion that the C-dish™, IonOptix, may be suitable for pulse stimulation of cells in culture.

6.3.2. Distribution of EF and current density in cell culture system

According to the results of computational models, the EF in the cell culture medium was slightly reduced from the input EF (Table 6.3). It also shows the trend of decrease in voltage as similar to the experimental EF (Table 6.5). The current density distribution at the electrode-medium interface is higher than at the cell culture medium (the middle point of the cell culture chamber), as shown in Figure 6.3, suggesting the effect of the electrical double layer. Moreover, the PEDOT:PSS mat can alter the EF and current density in the cell culture medium.

In this study, the H-fibre and F-fibre represent the fibre mat without and with touching electrodes. The electrical signal directly transfers to the cell culture medium and secondarily to the fibre mat in the condition of H-fibre. Whilst, it transmits to both cell culture medium and fibre mat together in the case of F-fibre. Interestingly, the EF and current density in F-fibre were lower than in the H-fibre confirmed by the results of computational models in this study; perhaps, it is due to the resistance or impedance of fibres.

Even though PEDOT:PSS is an electrical conductive mat, its electrical conductivity is lower than the conductivity of the cell culture medium. Thus, the resistance of the IPN mat is high compared to that of the cell culture medium. The total impedance in the cell culture system is likely to be increased when the fibre mat touches electrodes; this is a possible reason why the voltage drop in the F-fibre is larger than the H-fibre. Interestingly the geometry of fibre (e.g. aligned and random fibres) the mat may affect the resistivity of fibre mat, resulting in the current passing through materials and cells. The length of fibre is directly proportional, while the cross-section area is inversely proportional to resistance. Therefore, the electrical current passing through the different geometries of fibres is another interesting point to investigate in further study, as shown in another previous study [350].

The electrical signal of the pulse stimulation is divided into two phases: pulsing (ON) and resting (OFF) periods. In the ON period, the EF and current density in the medium moved from the anode to ground electrodes steadily. They were expected to be stopped in the OFF period immediately. However, the computational model explains that the EF and current density were slightly retained in the system during the OFF period (Figure 6.4 and Figure 6.5). Their small fluctuations in the range of nanoscale are likely due to the ion movement following the ionic gradient.

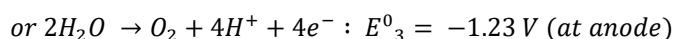
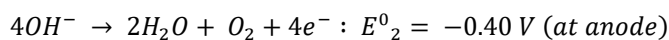
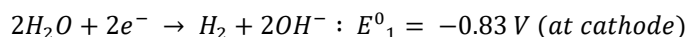
The region of the electrical double layer at the electrode-medium interface contains a high number of ions during the ON period of pulse stimulation. Once the pulse is OFF, ions will immediately move to the area containing a low number of ions, which is the middle of the chamber. It seems like they need to balance ions in the medium at equilibrium to minimise irreversible faradic processes [364]. The dynamic movement of EF and current density confirm that the balancing process occurs in the OFF period of pulse stimulation (Figure 6.6 to Figure 6.9).

Assuming PEDOT:PSS is dispersed in every single fibre homogeneously, the electrical conductivity of silk fibre is equal to PEDOT:PSS. The character of electrical current flow at the surface of the fibre mat depends on the direction of fibres in EF. Provided the fibre mat is parallel to EF, the electric currents in fibres and on the fibre surface will be occurred in the same direction (Figure 6.10 (c)). On the other hand, the fibre mat perpendicular to EF generated the complicated

distribution of space charge density at its surface leading to the reversed current in fibre (Figure 6.10 (e and f)). Therefore, this suggests that the fibre mat parallel to EF is more suitable than other rotations since many studies have shown the trend of neurite extension following the direction of EF [105, 116, 365-367].

6.3.3. Electrochemical reaction of cell culture medium during electrical stimulation

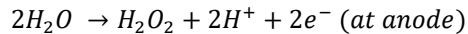
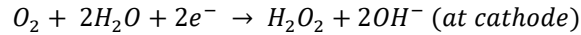
The constant DC stimulation with high voltage generates bubbles in the cell culture medium at the anode, indicating electrolysis. If the applied voltage is higher than the redox potential, the electrons in electrodes will transfer to ions in the cell culture medium resulting in the faradic by-products in the medium [182-184, 351, 368]. From the theory, the minimum potential for electrolysis of water is 1.23 V, which is calculated from half-reaction at cathode and anode as shown in the equations below [183, 368].



On the other hand, the overall reaction potential of electrolysis may be calculated by E^0_1 and E^0_3 . The electrolysis potential can also be 2.06 V. A few previous studies have then varied the voltage range of 1.23 – 2.06 V for electrolysis [369, 370].

Based on the results, the constant DC stimulation with 3 V amplitude is maybe too high and generates the electrolysis of the cell culture medium. Possibly, the bubbles at the anode are O_2 and the medium around that area contains H^+ as explained in equation E^0_3 . In pulse stimulation with 3 V amplitude and 40% duty cycle (2 ms pulse width and 5 ms pulse cycle) can induce redox reaction and electrolysis as well. Although the O_2 bubbles could not be seen at the anode, the cell culture medium around the anode was changed to yellow, indicating the acidic medium due to the increase of H^+ .

Apart from pH changing, hydrogen peroxide (H_2O_2) is another common by-product of DC stimulation and electrolysis. It can be generated by both reduction and oxidation at cathode and anode, respectively [182, 371], as shown in the equations below.



The by-product of H_2O_2 is also well-known as an oxidative reagent with cytotoxic effects on cells. In contrast, some previous studies revealed that H_2O_2 at the appropriate level promotes stem cell growth and differentiation to osteoblast [351, 352, 372] and regeneration of peripheral nerve cells [226, 373]. However, it should be better to avoid electrolysis and its by-products in the study due to the sensitivity of NG108-15 cells to the acidic environment. With either DC or pulse stimulation with a 40% duty cycle, NG108-15 cells were detached from the substrate (Figure 6.12). This maybe because of faradic by-products and/or the repulsive force from EF and current flow.

Therefore, the pulse stimulation with 1 V amplitude, which is certainly lower than the range of electrolysis potentials, is preferred in this study. According to the results, the pulses of 1 V with various duty cycles (0.2%, 2%, and 20%) do not damage cells, and they can support neurite extension on uncoated TCP. The 2% duty cycle (2 ms pulse width, 100 ms pulse cycle) shows the best trend of neurite extension compared to other duty cycles.

6.3.4. Effect of electrical stimulation on neurite outgrowth

According to the literature review (in section 2.10), electrical stimulation has been studied for peripheral nerve regeneration for a while. Many electrode systems of direct electrical stimulation were used before, such as three electrodes (anode, cathode, and quasi-reference) [374-376] and two electrodes (anode and cathode) [377-381]. The different bioreactors lead to the individuality of the electrical parameters in each study.

In general, many cellular mechanisms can be triggered by electrical stimulation, such as the activity of endogenous microenvironment, ion channels, membrane receptors, transport proteins, and competing signal pathways [382]. The cell signalling via voltage-gated Ca^{2+} channels is an important pathway relevant to neurite extension. The intracellular Ca^{2+} concentration rises

after electrical stimulation [383]. In addition, the Ca^{2+} influx leads to the upregulation of brain-derived neurotrophic factor (BDNF), resulting in neurite outgrowth [23, 384, 385]. On the other hand, electrical stimulation may induce apoptotic cells [386, 387]. In order to avoid cell damage, the parameters of electrical stimulation (e.g. voltage, frequency, and duration) should be deeply optimised before use.

In this study, only cell morphology after electrical stimulation is focused on, excluding the analysis of other cellular activities and signalling pathways. The effects of pulse stimulation with the condition of Op-ES (1 V amplitude, 2 ms pulse width, 100 ms pulse cycle, and 24 h/day) on neurite outgrowth will be discussed in three aspects: the neurite length, neurite orientation, and acceleration of neurite extension.

6.3.4.1. Cells on TCP substrates

Without the fibre mat, electrical stimulation can enhance neurite extension length on untreated TCP, while it has no significant difference compared to control in the case of laminin-coated TCP (Figure 6.13). This result suggests that the limitation of neurite outgrowth of NG108-15 is associated with laminin and cell density. The higher cell density, the lower space between cell clusters, resulting in short neurite length. However, the space between cell clusters is assumed to be equal in every sample since the cell seeding density is controlled at 5,000 cells/cm² every time. Therefore, laminin modulates neurite extension length chiefly, and it somehow hinders the effect of electrical stimulation. The conductivity of the laminin-coated fibre is strongly recommended to be inspected in the future.

In this study, the longest neurite (maximum length) of differentiated NG108-15 cells is ~600 μm . However, the average neurite length is ~150 – 250 μm as similar to other studies [120, 121, 208, 214, 388]. Without laminin, the neurites of cells are unable to reach the maximum length within 3 days after culturing in the differentiation medium (DMSO medium). However, laminin-coated TCP supports neurite extension well; the neurite attains the highest extension since day 2. Interestingly, the Op-ES in this study can slightly improve the longest neurite on uncoated TCP

compared to control (without ES), as shown in Figure 6.13 (a). In contrast, it does not affect laminin-coated TCP; the maximum and average neurite lengths are similar to control.

Direct electrical stimulation through the cell culture medium can promote neurite length only if cells are growing on uncoated TCP. Perhaps, the electrical stimulation parameters in this study (the Op-ES) are ineffective conditions to raise and accelerate neurite outgrowth.

In terms of neurite orientation, some previous studies revealed that neurites were aligned parallel to the EF direction [101, 366, 389, 390]. It is difficult to confirm the exact direction of neurite alignment in this study. Neurites can extend in many directions, as shown in the polar scatters (e.g. Figure 6.16 and Figure 6.17). Moreover, they are likely to form neural networks, possibly the regular morphology of NG108-15 cultured with the DMSO medium (Figure 6.14); the neurite is a bit difficult to trace and track. To confirm the alignment of neurites under the influence of EF, the cAMP medium, which may induce more visible neurites, is recommended for future study.

6.3.4.2. Cells on fibre mats

The neurite extension on H-fibre and F-fibre will not be compared in this study directly since they were independent experiments (cultured on different days with different cell passage numbers). Thus, the effects of the Op-ES in all four conditions of fibre mats: H-fibre, H-fibre with laminin, F-fibre, and F-fibre with laminin were compared to their controls (without ES). No comparison between fibre mat conditions has been performed due to a low number of experiments (2 parallel experiments per condition). If there are more numbers of experiments in the future, it is trustworthy to compare the data between groups.

In the case of control (without ES), the results explain that laminin is a crucial factor for neurite extension on fibre mats. Without laminin coating, IPN ($\alpha = 2.3$) can promote a longer neurite length than SF mat (Figure 6.15 (a)). It indicates that PEDOT:PSS integrating SF fibres support neurite extension quite well. With laminin coating, IPN and SF mats showed similar results of neurite extension (Figure 6.15 (b)). The results in this chapter also correspond to those in chapter

5. The binding mechanism of laminin on SF and PEDOT:PSS is suggested to be further investigated, as explained in chapter 5 (sections 5.3.3.2 and 5.3.3.3).

Without ES, other previous studies reported that NG108-15 cells grown on fibre mats with the DMSO medium extends the neurite outgrowth in a similar length found in this study, which is the average of ~100 – 250 μm [120, 121, 208]. Magaz A., *et al.*, 2020 and 2021 explained that the average length of NG108-15 cells on random fibres of rGO/SF and PEDOT:PSS/SF are ~100 – 150 μm [120, 121]. Soliman E., *et al.*, 2018 also revealed that gelatin/PCL aligned fibres promoted the neurite extension up to ~200 μm and aligned neurites following the fibre direction [208]. It highlights the importance of using aligned fibres to manipulate the neurite direction.

By applying the Op-ES to cells grown on fibre mats, the average neurite extension was lower than control in all four conditions: H-fibre, H-fibre with laminin, H-fibre, and F-fibre with laminin (Figure 6.19). These results on fibre mats are in contrast to those on TCP, particularly in uncoated TCP, in which the Op-ES promotes the neurite extension. Unfortunately, it was expected that the Op-ES should enhance neurite length, especially in both uncoated H-fibre and F-fibre. In contrast to other studies, the electrically conductive materials with ES promoted longer neurites than unstimulated conditions [98, 100-102, 104, 112]. Although the reasons why the Op-ES is likely to inhibit neurite extension on fibre mats are in doubt, it can be presumed that this is the effect of EF and electrical current flow through the fibre mats. Moreover, the further investigation of electrical stimulation parameter optimisation may provide more favourable results of neurite outgrowth.

Typically, the electrical conductivity of TCP is very low and is also known as non-conductive material. The electrical signal transfers to cells mainly *via* cell culture medium once culturing on TCP. Based on computational results, the EF and current flow definitely pass through the fibre mat whether it contacts electrodes or not. Thus, cells are triggered by the electrical signal passed through two electrically conductive media: the cell culture medium and the IPN fibre mat. Kotwal A., *et al.*, 2001 explained that electrical stimulation perhaps alters the protein adsorption on conductive material [24]. In comparison to the result in this study, it suggests that the Op-ES may affect protein adsorption of SF and IPN ($\alpha = 2.3$) mat and lead to poor cell adhesion and

neurite extension. Therefore, the protein adsorption of fibre mats during electrical stimulation should be further considered in order to confirm this presumption.

In both cases of H-fibre and F-fibre, uncoated IPN ($\alpha = 2.3$) with the Op-ES shows a possibility to enhance the longer neurite length than the uncoated electrospun SF mat with the Op-ES (Figure 6.19 (a, c)). This preliminary result is a promising trend of using electrically conductive materials with an external electrical regime for facilitating neurite outgrowth. However, more repeats of the experiment are still required in future to increase reproducibility and robust results. In terms of neurite orientation, the Op-ES on fibre mats does not manipulate the neurite direction, unfortunately. The Op-ES on fibre mats provides a similar result of neurite orientation to fibre mats without ES, as shown in polar histograms (e.g. Figure 6.16, Figure 6.17, Figure 6.20, and Figure 6.21). Nevertheless, in the case of IPN ($\alpha = 2.3$) with the Op-ES, the outstanding neurites with a length of more than 300 μm are aligned almost parallel to the fibre alignment.

Therefore, the neurite outgrowth is influenced by the morphology of fibre mats. The PEDOT:PSS on fibres enhance neurite length in the case of uncoated fibre mats. The Op-ES is maybe unable to control the neurite direction. On the other hand, the polar scatters show that the longest neurite is always alongside fibres. Possibly, it maybe concluded that the neurite direction is initiated and manipulated by the morphology of fibres, while the length of the neurite, where parallel to fibres, is promoted by the Op-ES.

6.3.5. Suggestions for the further analysis

Due to the limitation of access to the laboratory during the COVID-19 pandemic period, the results in this chapter are preliminary to determine the potential of using electrically conductive fibre mats with electrical stimulation for promoting neurite outgrowth. Several cellular activities of neurons (e.g. metabolic activity, DNA concentration, gene and protein expression, and the generation of ion flux) after stimulation should be investigated in the future.

Firstly, the electrical stimulation in another type of differentiation medium (*i.e.* cAMP medium) is preferred since it is maybe better to use with NG108-15 than DMSO medium confirmed by the result as in chapter 5 (Figure 5.4 to Figure 5.6). However, the components in both media

are different. The DMSO medium contains 9.5% DMSO with 0.5% FBS, while the cAMP medium contains 10% FBS. Hence, the conductivity of both cell culture media should be reconsidered before the experiment.

Apart from the common cellular analysis such as metabolic activity and DNA concentration representing cell viability and proliferation, the levels of Ca^{2+} and H_2O_2 generated during electrical stimulation should be investigated because they are associated with nerve regeneration [222, 223, 226].

The Ca^{2+} relates to axonal regeneration *via* many systems such as the growth-associated protein (*i.e.* GAP-43, B50, F1, or neuromodulin) [56] and the DLK-1 mitogen-activated kinase pathway (*i.e.* MAP Kinase or MAPK) [223]. In damaged nerves, the rise of intracellular Ca^{2+} activates GAP-43 to produce more numbers and longer neurites [56].

On the other hand, H_2O_2 is a common type of reactive oxygen species (ROS) that induces undesirable effects on cells (*e.g.* cell death). In contrast to the unpleasant results, H_2O_2 became a key signal for axon growth and recovery [226, 391]. Although there was no measurement of the H_2O_2 level in this study, it can be supposed that the H_2O_2 was generated indeed in the cell culture medium during electrical stimulation, confirmed by the electrolysis equation and the changing of medium colour.

The level of H_2O_2 *in vivo* is dynamic. It is increased during the early stages of regeneration (*e.g.* somitogenesis and organogenesis) and slightly decreased at the end of morphogenesis until exit in the adult [226]. Moreover, the H_2O_2 concentration gradient relates to nerve regeneration after amputation. It initially occurs and accumulates at the tip of the nerve stump, at the same time that Wallerian degradation happens at axons. The regrowth axons can directly extend to the end of the stump because they might follow the H_2O_2 gradient [392]. Interestingly, the H_2O_2 is a temporary product; it is undetectable when axons reach their initial areas, as shown in Figure 6.22.

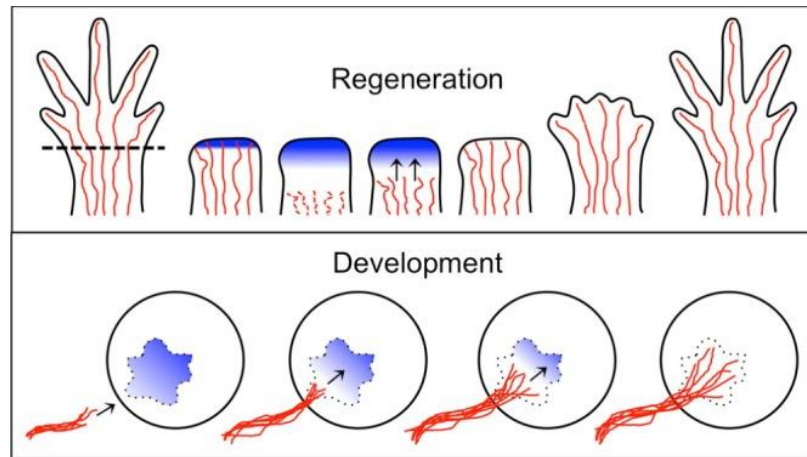


Figure 6.22 The interaction of nerves and H_2O_2 during the regeneration and development stages, blue areas and red lines represent the H_2O_2 gradients and axons, respectively [226].

According to the axonal growth following H_2O_2 gradients, it might be good if the level of H_2O_2 is produced in optimal concentration at the tip of the nerve stump. The large areas of H_2O_2 probably induce faster recovery. However, the strategy to provoke H_2O_2 in a specific target is quite complicated. Perhaps electrical stimulation is an alternative solution for generating H_2O_2 at the target tissue. Actually, electrical stimulation has been studied in wound healing and fracture organs for a while, and the production of H_2O_2 definitely occurs when applying the direct current [393, 394].

Finally, the relationship between electrical stimulation and H_2O_2 production is interesting to determine, especially in peripheral nerve regeneration. Even though the high level of H_2O_2 should be avoided because it could activate neurodegeneration diseases, the optimal gradient of H_2O_2 produced by the direct ES with the direct current is maybe an alternative approach that can attract axonal growth. The electrical stimulation and generation of H_2O_2 may lead to a novel strategy for fully functional nerve regeneration in the future.

6.4. Conclusion

Electrical stimulation is an alternative strategy for promoting neurite length and accelerating neurite outgrowth. With direct stimulation through the cell culture medium, the range of electrical potentials is imperative to optimise. Low voltage is maybe unable to trigger the cells, while high voltage may lead to cell death. Moreover, the faradic by-products generated by electrolysis during electrical stimulation should be avoided since they can create an extreme environment for NG108-15 cells, such as an acidic medium.

The monophasic pulse stimulation is preferable to use with the carbon plate electrodes, C-dish™. The optimal condition for electrical stimulation (Op-ES) is 1 V amplitude, 2 ms pulse width, 100 ms pulse cycle, and 24 h/day. This condition tends to increase neurite extension length of differentiated NG108-15 cultured on TCP without laminin. However, it has no effect on TCP with laminin.

The finite element analysis is a useful technique to describe and understand the electric field (EF) and current density in the cell culture system (*in vitro*) but may not be a promising model in the case of *in vivo*. The EF and current density primarily pass through the cell culture medium rather than the fibre mat since the electrical conductivity of the cell culture medium is higher than PEDOT:PSS. In pulse stimulation, the EF and current density are not stable all the time. They are high level and steadily move from anode to cathode in the stimulation period. However, they are still retained in the nano-level and dynamically move between electrodes in the resting period, where they are likely to balance their gradients. Interestingly, the rotating of the fibre mat in the chamber affects the direction of current through fibres. Providing the alignment of the fibre mat is in the parallel direction to EF, the current flow is stable without complicated space charge density at the fibre-medium interface.

Unfortunately, the Op-ES of differentiated NG108-15 cells grown on fibre mats both with and without touching to electrodes (F-fibre and H-fibre) were unable to promote neurite extension length and initiate the direction of neurite as expected in a hypothesis of this chapter. It implies that the electrical parameters have to be investigated and optimised again in the further step. However, the Op-ES on IPN ($\alpha = 2.3$) mat provides longer neurites than on the electrospun SF

mat; this shows a good sign for using electrically conductive material with an electrical regime to facilitate peripheral nerve regeneration in the future.

CHAPTER 7

Overall Conclusion

7.1. Summary

The electrically conductive scaffold of SF integrated PEDOT:PSS for peripheral nerve regeneration is an impressive achievement in this work. However, the combination of electrically conductive material and electrical stimulation requires further optimisation. The summary of each scope of the study will be described in the following topics.

7.1.1. Fabrication of non-woven mats (Chapter 3)

The double layer electrospinning is an effective method to fabricate a non-woven mat from SF with a fibre diameter of ~ 200 nm. The material thickness of ~ 100 μm is enough for handling with good processability. In this study, SF extracted from silk cocoons can be prepared as the electrospinning solution *via* a dialysis free protocol, which is far less time-consuming compared to a dialysis approach. The 10% wt/v of degummed SF in FA/CaCl₂ with the ratio of 98:2 ml/g is dissolved completely after incubating at 45° C overnight, and then the solution is available for electrospinning.

With the rotating mandrel collector, the alignment of fibres depends on the speed of the collector. The uniform alignment is directly proportional to the linear velocity of the rotating mandrel. The sub-micron electrospinning fibre is commonly in the random direction on the static collector, and it begins the aligned fibre when the linear speed of the rotating mandrel is $\sim 7.54 - 9.42$ m/s. In addition, the qualities of fibres are affected by the other electrospinning parameters such as high voltage supply, solution flow rate, working distance, relative humidity, and temperature.

The electrospun SF mat was partly re-dissolved in water due to the lack of β -sheet crystallisation in the structure. However, the β -sheet formation can be induced by the treatment of

80% EtOH for 20 min. Additionally, the EtOH treated electrospun SF should be preserved in water to avoid shrinkage as a consequence of evaporation.

7.1.2. Modification of electrical conductive property of the fibre mat (Chapter 4)

The IPN of PEDOT:PSS on electrospun SF is an effective technique to improve the electrical conductivity of fibre mat without the effect on fibre diameter. Obviously, the IPN mat had fully turned dark blue due to the presence of PEDOT:PSS in/on fibres.

The electrospun SF and IPN mats were relatively brittle in the dry state, while they were more flexible in the wet state due to water plasticiser. The number of β -sheet formations also affects the mechanical property of the electrospun SF mat. Moreover, the PEDOT and PSS contents influence the mechanical and electrical properties of the fibre mat. Although the electrical conductivity of IPN mats is uncertain in this study, the IPN mats show the character of electrically conductive material once measured with cyclic voltammetry.

7.1.3. *In vitro* biocompatibility (Chapter 5)

According to the safety data sheets, the chemicals used in the IPN process may have toxicity to cells. In order to reduce the risk of the chemical residues in fibre mat, effective washing is necessary prior to using the IPN mat as a scaffold.

As well as electrospun SF, the IPN ($\alpha = 2.3$) and IPN ($\alpha = 3.3$) mats can support cell adhesion and proliferation. However, somehow IPN mats hinder cell growth suggesting that PEDOT:PSS may interfere with cell-surface interaction. In the differentiation phase, NG108-15 cells are aggregated into clusters, and the neurites are extended from the clusters, probably in the parallel direction to fibre alignment. It indicates that a fibre diameter of $\sim 200\ \mu\text{m}$ is available to initiate the neurite direction. The neurite extension length on the IPN ($\alpha = 2.3$) is similar to that on the electrospun SF, while it is slightly higher than IPN ($\alpha = 3.3$). Therefore, the IPN ($\alpha = 2.3$) is the optimal condition of electrically conductive material, which has the potential to apply with electrical stimulation for facilitating peripheral nerve regeneration.

7.1.4. Electrical stimulation (Chapter 6)

The pulse ES is preferable in this study due to the low generation of faradic by-products, which could induce programmed cell death. Thus, the carbon plate electrode is chosen in this study since it generates the steady waveform of pulse signals. The direct ES with the monophasic pulse of 1 V amplitude, 2 ms pulse width, 100 ms pulse cycle (10 Hz frequency), 24 h/day is the optimal condition (Op-ES); it can promote neurite extension length on TCP without laminin coating slightly longer than control (without ES).

Unfortunately, the IPN ($\alpha = 2.3$) mat with the Op-ES is unable to enhance the neurite extension and orientation compared to control (without ES). However, it promotes longer neurites than the electrospun SF mat with ES. These results explain an initial step of the novel strategy for peripheral nerve regeneration using the combination of electrically conductive material and electrical stimulation.

7.2. General Discussion

According to the general objective, this study aims to fabricate an electrically conductive material based on SF for promoting peripheral nerve regeneration. The use of electrically conductive materials with electrical stimulation is an additional purpose.

It has been demonstrated in Chapter 3 that the optimisation of electrospinning protocol also SF preparation is accomplished. This optimised protocol is competent because it is reproducible with the same quality of fibres (*i.e.* fibre diameter and fibre alignment). The preparation of electrospinning SF solution *via* a dialysis free protocol is the strength of this study. It uses far less time for preparing compared to the well-known protocol with dialysis [20]. The results in Chapter 4 have also shown that the IPN is a promising technique for incorporating the network of PEDOT:PSS in/on electrospun SF mats. Even though the conductivity of IPN mats is imprecisely clarified, the IPN mats are electrically conductive material confirmed by the cyclic voltammetry. The results in Chapter 5 are a key to determining whether the electrically conductive IPN mat is possible to use as a peripheral nerve scaffold or not. It exhibits that the electrospun SF and IPN mats are biocompatible and can support the proliferation of NG108-15 cells. Although

IPN mats somehow hinder cell growth compared to the electrospun SF mat, NG108-15 cells grown on the IPN ($\alpha = 2.3$) mat with the differentiation medium can extend their neurites similarly to those on the electrospun SF mat. Neurites are mostly aligned parallel to the alignment of fibres.

The results throughout Chapters 3, 4, and 5 suggest remarkable achievement of electrically conductive fibre for peripheral nerve scaffold as the goal of this study. The electrically conductive material based on SF fibres can support and guide the direction of neurite outgrowth, also possible to use as a peripheral nerve scaffold. Nevertheless, some results are different from the literature suggesting further investigation in the future study. For example, PEFOT:PSS incorporated materials should enhance cell proliferation compared to the pristine material without PEDOT:PSS [120, 347, 348].

The results presented in Chapter 6 are the preliminary study of using the IPN mat with electrical stimulation for facilitating effective regeneration of the peripheral nerve. Most of the results are negative; the IPN mat with ES is unable to promote neurite extension length compared to control (without ES). Further optimisation of electrical parameters may give more favourable results on neurite outgrowth.

7.3. Limitations of Study

7.3.1. Electrospinning tools

In this study, the speed of the rotating mandrel collector is controlled manually by the rotary knob without the monitoring system to show the exact rotating speed. Although using a digital tachometer can estimate the collector speed roughly, the consistency of the speed is difficult to maintain each time. Moreover, a rotating mandrel has a belt system that connects the collecting drum and the rotating motor. Sometimes, the speed of the collector was unintentionally changed during a long period of electrospinning due to the elasticity of the rubber belt unless the rotating knob is in a fixed position.

Therefore, the morphology of fibres each time is a little different, in particular the alignment of fibre. However, the fibres are mostly aligned in the same direction when using the high speed of mandrel, and the overall property of the electrospun SF mat is still the same.

7.3.2. Cell culture

Typically, NG108-15 cells are easily detached from the substrates during washing and changing medium. Although the detached cells are able to re-attach on the substrate, this interferes with cell growth behaviours. Therefore, the time-dependent cellular activities of NG108-15 (*e.g.* metabolic activity and DNA concentration) are not able to assess from a similar sample throughout the period of the experiment. For example, at least 9 samples were prepared for 3 days of observation (*i.e.* 3 samples/day). Live cell staining dyes [395-398] and imaging systems that allow continuous monitoring throughout the period of experiments (*e.g.* CQ1 benchtop HCA system) [399] is recommended in the further studies. Fluo-4 AM is a promising reagent for live cells NG108-15 staining [398].

7.4. Future Work

7.4.1. Electrically conductive material fabrication

The electrical conductivity of the IPN mat is in doubt even though it is definitely electrically conductive confirmed by cyclic voltammetry. To understand the relationship between PEDOT:PSS contents and electrical conductivity, the electrical conductivity should be investigated in the future. However, the EIS measurement *via* a potentiostat has many control parameters that affect the conductivity result, such as electrode system, working distance, sample-solution interface, and type of electrolyte. The different setups of EIS may lead to low precision measurement.

The measurement *via* advanced tools such as scanning electrochemical microscopy (SECM) and scanning ion conductance microscopy (SICM) [316] is suggested as the alternative for further study.

7.4.2. Electrical stimulation *via* electrically conductive material

The cellular activities, indicating cell viability and proliferation, and the neurite extension length were focused on in this study. Other cellular mechanisms of cells on electrically conductive IPN mat after ES are out of scope. Molecular effects of cells and cell signalling associated with neurite

extension have to be considered in the future to fulfil the knowledge of using ES as an alternative for peripheral nerve treatment.

If cells are actually fine and robust under the influence of the electrical regime, several cellular mechanisms are recommended to assess: the activity of Ca^{2+} flux and the voltage-gated calcium channels [56, 400-402], intracellular H_2O_2 [393, 394], and the expression of GAP43 [56, 403]. On the other hand, the electrophysiological property of neuronal cells during ES is another curiosity since NG108-15 is an electrically excitable cell line, which can generate an action potential. The measurement of action potential of NG108-15 will explain not only the nerve recovery but also the nerve functionality.

Moreover, other types of ES methods: direct ES with three electrodes, direct ES with salt bridge, conductive ES, and inductive ES should be considered as well as the pattern/design of a bioreactor in order to figure out the optimal condition for neurite outgrowth.

7.4.3. Potential applications

The electrically conductive material, IPN material of PEDOT:PSS on electrospun SF, shows the possibility to support neurite outgrowth following the fibre alignment *in vitro*. Furthermore, this developed material could be potentially utilised in other biomedical applications such as scaffold for other tissue and invasive biomedical electrodes.

In peripheral nerve applications, the developed materials (electrospun SF and PEDOT:PSS/electrospun SF mats) in this study are biocompatible with a suitable fibre diameter to manipulate the unidirectional alignment of most neurites. However, the SF-based material should be tested with other cell types (e.g. SCs, DRGs, and also MSCs) in the future to indicate the possibility to use with the complex peripheral nerve system [404-406]. For example, the purpose of testing with SCs is for using the material as a cells-based scaffold or supporting neurite outgrowth, DRGs for supporting nerve tissue including neurons and SCs, and MSCs for supporting neurogenic differentiation. The electrophysiology (*i.e.* action potential) of nerve cells on the SF-based material should be ascertained in the future to confirm the function of regenerated neurons and axons [407].

This material may be flexible and able to fold or roll as the hollow tube of nerve conduit. However, the suitable thickness of the material, which can be processed to be the nerve conduit and the stability in the wet state after processing should be investigated in the future. On the other hand, this material could possibly be used as the inner wall or intraluminal of other nerve conduits instead of rolling it as the nerve conduit alone.

In the case of other applications of tissue regenerations, the electrically conductive aligned fibres are also fit the requirement of muscle tissue, particularly the cardiac muscular system [115, 408]. The morphology of cardiac muscles is generally aligned, and they are electrically excitable, resulting in excitation-contraction coupling. The use of electrically conductive aligned fibres could increase the possibility of regeneration. Importantly, the use of pulse ES through material could enhance muscle movement like the exercise program for muscle cells.

Finally, the electrically conductive SF-based material can use as the invasive electrode due to its biocompatibility and flexibility [91, 409]. However, the biomedical electrodes for either measuring body signals or stimulating tissue functions require high conductivity properties to transfer electrical signals accurately. Currently, the conductivity of the developed material may not be high enough. If it is improved, it may increase the opportunity to use as an electrode in the future. Alternatively, this scaffold can be used as a simple creation of a 3D *in vitro* peripheral nerve for pharmaceutical and mechanical testing.

REFERENCES

1. Meadows, R.M., D.R. Sengelaub, and K.J. Jones, *Chapter 29 - Cellular Aspects of Nerve Injury and Regeneration A2 - Tubbs, R. Shane*, in *Nerves and Nerve Injuries*, E. Rizk, et al., Editors. 2015, Academic Press: San Diego. p. 433-449.
2. Ichihara, S., Y. Inada, and T. Nakamura, *Artificial nerve tubes and their application for repair of peripheral nerve injury: an update of current concepts*. *Injury-International Journal of the Care of the Injured*, 2008. **39**: p. S29-S39.
3. Panagopoulos, G.N., P.D. Megaloikonomos, and A.F. Mavrogenis, *The Present and Future for Peripheral Nerve Regeneration*. *Orthopedics*, 2017. **40**(1): p. E141-E156.
4. Schilling, B.K., et al., *Intramuscular injection of skeletal muscle derived extracellular matrix mitigates denervation atrophy after sciatic nerve transection*. *J Tissue Eng*, 2021. **12**: p. 20417314211032491.
5. Bergmeister, K.D., et al., *Acute and long-term costs of 268 peripheral nerve injuries in the upper extremity*. *PLoS One*, 2020. **15**(4): p. e0229530.
6. Neal, S., *Chapter 33 - Peripheral Nerve Injury of the Upper Extremity A2 - Tubbs, R. Shane*, in *Nerves and Nerve Injuries*, E. Rizk, et al., Editors. 2015, Academic Press: San Diego. p. 505-524.
7. Faroni, A., et al., *Peripheral nerve regeneration: experimental strategies and future perspectives*. *Adv Drug Deliv Rev*, 2015. **82-83**: p. 160-7.
8. Noble, J., et al., *Analysis of upper and lower extremity peripheral nerve injuries in a population of patients with multiple injuries*. *Journal of Trauma-Injury Infection and Critical Care*, 1998. **45**(1): p. 116-122.
9. Taylor, C.A., et al., *The incidence of peripheral nerve injury in extremity trauma*. *American Journal of Physical Medicine & Rehabilitation*, 2008. **87**(5): p. 381-385.
10. Kouyoumdjian, J.A., *Peripheral nerve injuries: A retrospective survey of 456 cases*. *Muscle & Nerve*, 2006. **34**(6): p. 785-788.
11. Hirasawa, Y., et al., *Statistical study on peripheral nerve injury*. Vol. 45. 1976. 213-21.
12. Daly, W., et al., *A biomaterials approach to peripheral nerve regeneration: bridging the peripheral nerve gap and enhancing functional recovery*. *Journal of The Royal Society Interface*, 2012. **9**(67): p. 202-221.
13. Ali, S.A., et al., *Effect of Motor versus Sensory Nerve Autografts on Regeneration and Functional Outcomes of Rat Facial Nerve Reconstruction*. *Sci Rep*, 2019. **9**(1): p. 8353.
14. Chrzaszcz, P., et al., *Application of peripheral nerve conduits in clinical practice: A literature review*. *Neurol Neurochir Pol*, 2018. **52**(4): p. 427-435.
15. Nectow, A.R., K.G. Marra, and D.L. Kaplan, *Biomaterials for the Development of Peripheral Nerve Guidance Conduits*. *Tissue Engineering Part B-Reviews*, 2012. **18**(1): p. 40-50.
16. Meek, M.F. and J.H. Coert, *US Food and Drug Administration/Conformit Europe-Approved Absorbable Nerve Conduits for Clinical Repair of Peripheral and Cranial Nerves*. *Annals of Plastic Surgery*, 2008. **60**(1).
17. *Clinical efficacy and safety: nervous system*. [cited 2022 January 21]; Available from: <https://www.ema.europa.eu/en/human-regulatory/research-development/scientific-guidelines/clinical-efficacy-safety/clinical-efficacy-safety-nervous-system>.
18. *Pmda - Pharmaceuticals and Medical Devices Agency*. [cited 2022 January 21]; Available from: <https://www.pmda.go.jp/english/>.
19. Das, S., et al., *Electrospun silk-polyaniline conduits for functional nerve regeneration in rat sciatic nerve injury model*. *Biomedical Materials*, 2017. **12**(4).
20. Rockwood, D.N., et al., *Materials fabrication from Bombyx mori silk fibroin*. *Nature Protocols*, 2011. **6**(10): p. 1612-1631.
21. Hardy, J.G., J.Y. Lee, and C.E. Schmidt, *Biomimetic conducting polymer-based tissue scaffolds*. *Current Opinion in Biotechnology*, 2013. **24**(5): p. 847-854.
22. Balint, R., N.J. Cassidy, and S.H. Cartmell, *Conductive polymers: Towards a smart biomaterial for tissue engineering*. *Acta Biomaterialia*, 2014. **10**(6): p. 2341-2353.

23. Haastert-Talini, K. and C. Grothe, *Chapter Five - Electrical Stimulation for Promoting Peripheral Nerve Regeneration*, in *International Review of Neurobiology*, S. Geuna, et al., Editors. 2013, Academic Press. p. 111-124.
24. Kotwal, A. and C.E. Schmidt, *Electrical stimulation alters protein adsorption and nerve cell interactions with electrically conducting biomaterials*. *Biomaterials*, 2001. **22**(10): p. 1055-64.
25. Purves, D., *Neuroscience*. 1997, Sunderland, Mass.: Sunderland, Mass. : Sinauer Associates.
26. Hormuzdi, S.G., et al., *Electrical synapses: a dynamic signaling system that shapes the activity of neuronal networks*. *Biochimica Et Biophysica Acta-Biomembranes*, 2004. **1662**(1-2): p. 113-137.
27. Pereda, A.E., *Electrical synapses and their functional interactions with chemical synapses*. *Nature Reviews Neuroscience*, 2014. **15**(4): p. 250-263.
28. Dharani, K., *Chapter 2 - Physiology of the Neuron*, in *The Biology of Thought*, K. Dharani, Editor. 2015, Academic Press: San Diego. p. 31-52.
29. Marieb, E.N., *Essentials of Human Anatomy & Physiology, Global Edition*. 2015: Pearson Education Limited.
30. Dharani, K., *Chapter 6 - Dendrites and Primary Thoughts*, in *The Biology of Thought*, K. Dharani, Editor. 2015, Academic Press: San Diego. p. 109-122.
31. Harty, B.L. and K.R. Monk, *Unwrapping the unappreciated: recent progress in Remak Schwann cell biology*. *Current Opinion in Neurobiology*, 2017. **47**: p. 131-137.
32. Arcilla, C.K. and P. Tadi, *Neuroanatomy, Unmyelinated Nerve Fibers*, in *StatPearls*. 2021: Treasure Island (FL).
33. Jessen, K.R. and R. Mirsky, *The Success and Failure of the Schwann Cell Response to Nerve Injury*. *Frontiers in Cellular Neuroscience*, 2019. **13**(33).
34. Jessen, K.R., R. Mirsky, and A.C. Lloyd, *Schwann Cells: Development and Role in Nerve Repair*. *Cold Spring Harb Perspect Biol*, 2015. **7**(7): p. a020487.
35. Rubin, D.I. and R.C. Hermann, *CHAPTER 105 - PERIPHERAL NERVE INJURY A2 - Schapira, Anthony H. V*, in *Neurology and Clinical Neuroscience*, A. Editors, et al., Editors. 2007, Mosby: Philadelphia. p. 1409-1422.
36. Sunderland, S., *The Anatomy and Physiology of Nerve Injury*. *Muscle & Nerve*, 1990. **13**(9): p. 771-784.
37. Martini, F.H., J.L. Nath, and E.F. Bartholomew, *Fundamentals of Anatomy & Physiology, Global Edition*. 2015: Pearson Education Limited.
38. Fry, C.H. and R.I. Jabr, *The action potential and nervous conduction*. *Surgery - Oxford International Edition*. **28**(2): p. 49-54.
39. Schwartz, J.H., *Neurotransmitters*, in *Encyclopedia of the Human Brain*, V.S. Ramachandran, Editor. 2002, Academic Press: New York. p. 601-611.
40. Cooper, J.R., *Neurotransmitters*, in *International Encyclopedia of the Social & Behavioral Sciences*, N.J. Smelser and P.B. Baltes, Editors. 2001, Pergamon: Oxford. p. 10612-10619.
41. Zucker, R.S., D.M. Kullmann, and P.S. Kaeser, *Chapter 15 - Release of Neurotransmitters*, in *From Molecules to Networks (Third Edition)*, J.H. Byrne, R. Heidelberger, and M.N. Waxham, Editors. 2014, Academic Press: Boston. p. 443-488.
42. Moini, J. and P. Piran, *Chapter 1 - Histophysiology*, in *Functional and Clinical Neuroanatomy*, J. Moini and P. Piran, Editors. 2020, Academic Press. p. 1-49.
43. Seddon, H.J., *A classification of nerve injuries*. *British Medical Journal*, 1942. **1942**: p. 237-239.
44. Sunderland, S., *A classification of peripheral nerve injuries producing loss of function*. *Brain*, 1951. **74**(4): p. 491-516.
45. Mavrogenis, A.F., et al., *Current treatment concepts for neuromas-in-continuity*. *Injury*, 2008. **39 Suppl 3**: p. S43-8.
46. Wang, M.L., et al., *Peripheral nerve injury, scarring, and recovery*. *Connect Tissue Res*, 2019. **60**(1): p. 3-9.

47. Parvizi, J. and G.K. Kim, *Chapter 154 - Nerve Injuries Related to Orthopaedics*, in *High Yield Orthopaedics*, J. Parvizi and G.K. Kim, Editors. 2010, W.B. Saunders: Philadelphia. p. 317-319.
48. Ditty, B.J., N.B. Omar, and C.J. Rozzelle, *Chapter 24 - Surgery for Peripheral Nerve Trauma A2 - Tubbs, R. Shane*, in *Nerves and Nerve Injuries*, E. Rizk, et al., Editors. 2015, Academic Press: San Diego. p. 373-381.
49. Uzman, B.G., D.S. Snyder, and G.M. Villegas, *Status of Peripheral Nerve Regeneration*, in *Neural Regeneration and Transplantation*, F.J. Seil, Editor. 1989, Alan R. Liss, Inc.: New York, the United State of America.
50. Reid, A.J., et al., *N-Acetylcysteine alters apoptotic gene expression in axotomised primary sensory afferent subpopulations*. *Neuroscience Research*, 2009. **65**(2): p. 148-155.
51. Nagtegaal, I.D., E.A. Lakke, and E. Marani, *Trophic and tropic factors in the development of the central nervous system*. *Arch Physiol Biochem*, 1998. **106**(3): p. 161-202.
52. Bazan, J.F. and C. Wiesmann, *Chapter 41 - The Mechanism of NGF Signaling Suggested by the p75 and TrkA Receptor Complexes A2 - Bradshaw, Ralph A*, in *Handbook of Cell Signaling (Second Edition)*, E.A. Dennis, Editor. 2010, Academic Press: San Diego. p. 277-285.
53. Petruska, J.C. and L.M. Mendell, *Nerve Growth Factor A2 - Squire, Larry R*, in *Encyclopedia of Neuroscience*. 2009, Academic Press: Oxford. p. 71-78.
54. Wang, S.P., et al., *Chitosan/gelatin porous scaffolds assembled with conductive poly(3,4-ethylenedioxythiophene) nanoparticles for neural tissue engineering*. *Journal of Materials Chemistry B*, 2017. **5**(24): p. 4774-4788.
55. Wang, S.P., et al., *Fabrication and characterization of conductive poly (3,4-ethylenedioxythiophene) doped with hyaluronic acid/poly (L-lactic acid) composite film for biomedical application*. *Journal of Bioscience and Bioengineering*, 2017. **123**(1): p. 116-125.
56. Holahan, M.R., *GAP-43 in synaptic plasticity: molecular perspectives*. *Research and Reports in Biochemistry*, 2015. **5**: p. 137-146.
57. Freeman, R.S., et al., *NGF deprivation-induced gene expression: after ten years, where do we stand?*, in *Progress in Brain Research*. 2004, Elsevier. p. 111-126.
58. Wehner, D., et al., *Wnt signaling controls pro-regenerative Collagen XII in functional spinal cord regeneration in zebrafish*. *Nature Communications*, 2017. **8**.
59. Bettinger, C.J., et al., *Biocompatibility of biodegradable semiconducting melanin films for nerve tissue engineering*. *Biomaterials*, 2009. **30**(17): p. 3050-3057.
60. Ray, W.Z. and S.E. Mackinnon, *Management of nerve gaps: autografts, allografts, nerve transfers, and end-to-side neurorrhaphy*. *Exp Neurol*, 2010. **223**(1): p. 77-85.
61. Gao, Y., et al., *Nerve autografts and tissue-engineered materials for the repair of peripheral nerve injuries: a 5-year bibliometric analysis*. *Neural Regen Res*, 2015. **10**(6): p. 1003-8.
62. Arslantunali, D., et al., *Peripheral nerve conduits: technology update*. *Med Devices (Auckl)*, 2014. **7**: p. 405-24.
63. Kehoe, S., X.F. Zhang, and D. Boyd, *FDA approved guidance conduits and wraps for peripheral nerve injury: a review of materials and efficacy*. *Injury*, 2012. **43**(5): p. 553-72.
64. Gu, X., F. Ding, and D.F. Williams, *Neural tissue engineering options for peripheral nerve regeneration*. *Biomaterials*, 2014. **35**(24): p. 6143-6156.
65. Vijayavenkataraman, S., *Nerve guide conduits for peripheral nerve injury repair: A review on design, materials and fabrication methods*. *Acta Biomaterialia*, 2020. **106**: p. 54-69.
66. Sarker, M.D., et al., *Regeneration of peripheral nerves by nerve guidance conduits: Influence of design, biopolymers, cells, growth factors, and physical stimuli*. *Progress in Neurobiology*, 2018. **171**: p. 125-150.
67. Park, S.C., et al., *Ultrasound-stimulated peripheral nerve regeneration within asymmetrically porous PLGA/Pluronic F127 nerve guide conduit*. *J Biomed Mater Res B Appl Biomater*, 2010. **94**(2): p. 359-66.
68. Zhang, P.X., et al., *Tissue engineering for the repair of peripheral nerve injury*. *Neural Regen Res*, 2019. **14**(1): p. 51-58.

69. Mohammadi, R., et al., *Pulsed electromagnetic fields accelerate functional recovery of transected sciatic nerve bridged by chitosan conduit: an animal model study*. Int J Surg, 2014. **12**(12): p. 1278-85.
70. Huang, J.H., et al., *Electrical Stimulation Accelerates Motor Functional Recovery in the Rat Model of 15-mm Sciatic Nerve Gap Bridged by Scaffolds With Longitudinally Oriented Microchannels*. Neurorehabilitation and Neural Repair, 2010. **24**(8): p. 736-745.
71. DeSantana, J.M., et al., *Effectiveness of transcutaneous electrical nerve stimulation for treatment of hyperalgesia and pain*. Curr Rheumatol Rep, 2008. **10**(6): p. 492-9.
72. Chen, Y.S., et al., *Effects of percutaneous electrical stimulation on peripheral nerve regeneration using silicone rubber chambers*. J Biomed Mater Res, 2001. **57**(4): p. 541-9.
73. Yao, C.H., et al., *Electrical stimulation improves peripheral nerve regeneration in streptozotocin-induced diabetic rats*. Journal of Trauma and Acute Care Surgery, 2012. **72**(1): p. 199-205.
74. Cheng, W.L. and C.C.K. Lin, *The effects of different electrical stimulation protocols on nerve regeneration through silicone conduits*. Journal of Trauma-Injury Infection and Critical Care, 2004. **56**(6): p. 1241-1246.
75. Huang, J.H., et al., *Electrical Stimulation Accelerates Motor Functional Recovery in Autograft-Repaired 10 mm Femoral Nerve Gap in Rats*. Journal of Neurotrauma, 2009. **26**(10): p. 1805-1813.
76. Haastert-Talini, K., et al., *Electrical Stimulation Accelerates Axonal and Functional Peripheral Nerve Regeneration across Long Gaps*. Journal of Neurotrauma, 2011. **28**(4): p. 661-674.
77. Gordon, T., O.A. Sulaiman, and A. Ladak, *Chapter 24: Electrical stimulation for improving nerve regeneration: where do we stand?* Int Rev Neurobiol, 2009. **87**: p. 433-44.
78. Aebischer, P., et al., *Piezoelectric guidance channels enhance regeneration in the mouse sciatic nerve after axotomy*. Brain Res, 1987. **436**(1): p. 165-8.
79. Roman, G.C., et al., *Stimulation of Sciatic-Nerve Regeneration in the Adult-Rat by Low-Intensity Electric-Current*. Experimental Neurology, 1987. **98**(2): p. 222-232.
80. Bannaga, A., et al., *Magnetic stimulation accelerating rehabilitation of peripheral nerve injury*. J Huazhong Univ Sci Technolog Med Sci, 2002. **22**(2): p. 135-9.
81. Rochkind, S., S. Geuna, and A. Shainberg, *Chapter 25 Phototherapy in Peripheral Nerve Injury: Effects on Muscle Preservation and Nerve Regeneration*, in *International Review of Neurobiology*. 2009, Academic Press. p. 445-464.
82. Rochkind, S., et al., *Laser phototherapy (780 nm), a new modality in treatment of long-term incomplete peripheral nerve injury: a randomized double-blind placebo-controlled study*. Photomed Laser Surg, 2007. **25**(5): p. 436-42.
83. Rochkind, S., et al., *Efficacy of 780-nm laser phototherapy on peripheral nerve regeneration after neurotube reconstruction procedure (double-blind randomized study)*. Photomed Laser Surg, 2007. **25**(3): p. 137-43.
84. Gigo-Benato, D., et al., *Low-power laser biostimulation enhances nerve repair after end-to-side neurorrhaphy: a double-blind randomized study in the rat median nerve model*. Lasers Med Sci, 2004. **19**(1): p. 57-65.
85. Camara, C.N., et al., *Histological analysis of low-intensity laser therapy effects in peripheral nerve regeneration in Wistar rats*. Acta Cir Bras, 2011. **26**(1): p. 12-8.
86. Corey, J.M., et al., *Aligned electrospun nanofibers specify the direction of dorsal root ganglia neurite growth*. J Biomed Mater Res A, 2007. **83**(3): p. 636-45.
87. Wang, H.B., et al., *Varying the diameter of aligned electrospun fibers alters neurite outgrowth and Schwann cell migration*. Acta Biomater, 2010. **6**(8): p. 2970-8.
88. Kim, J.I., et al., *A Controlled Design of Aligned and Random Nanofibers for 3D Bi-functionalized Nerve Conduits Fabricated via a Novel Electrospinning Set-up*. Sci Rep, 2016. **6**: p. 23761.
89. Zhang, J.G., et al., *The aligned core-sheath nanofibers with electrical conductivity for neural tissue engineering*. Journal of Materials Chemistry B, 2014. **2**(45): p. 7945-7954.

90. Zhou, Z.F., et al., *Electrospinning of PELA/PPY Fibrous Conduits: Promoting Peripheral Nerve Regeneration in Rats by Self-Originated Electrical Stimulation*. *Acs Biomaterials Science & Engineering*, 2016. **2**(9): p. 1572-1581.
91. Cui, Y., et al., *A Stretchable and Transparent Electrode Based on PEGylated Silk Fibroin for In Vivo Dual-Modal Neural-Vascular Activity Probing*. *Advanced Materials*, 2021. **33**(34): p. 2100221.
92. Teshima, T., et al., *Mobile Silk Fibroin Electrode for Manipulation and Electrical Stimulation of Adherent Cells*. *Advanced Functional Materials*, 2016. **26**(45): p. 8185-8193.
93. Yin, H., et al., *A novel hydrogen peroxide biosensor based on horseradish peroxidase immobilized on gold nanoparticles–silk fibroin modified glassy carbon electrode and direct electrochemistry of horseradish peroxidase*. *Sensors and Actuators B: Chemical*, 2009. **137**(2): p. 747-753.
94. Yin, H., et al., *Amperometric biosensor based on immobilized acetylcholinesterase on gold nanoparticles and silk fibroin modified platinum electrode for detection of methyl paraoxon, carbofuran and phoxim*. *Journal of Electroanalytical Chemistry*, 2009. **637**(1): p. 21-27.
95. Chiang, C.K., et al., *Electrical Conductivity in Doped Polyacetylene*. *Physical Review Letters*, 1977. **39**(17): p. 1098-1101.
96. Shirakawa, H., T. Ito, and S. Ikeda, *Electrical properties of polyacetylene with various cis-trans compositions*. *Die Makromolekulare Chemie*, 1978. **179**(6): p. 1565-1573.
97. Anderson, M., et al., *Peripheral Nerve Regeneration Strategies: Electrically Stimulating Polymer Based Nerve Growth Conduits*. *Crit Rev Biomed Eng*, 2015. **43**(2-3): p. 131-59.
98. Lee, J.Y., et al., *Polypyrrole-coated electrospun PLGA nanofibers for neural tissue applications*. *Biomaterials*, 2009. **30**(26): p. 4325-35.
99. Prabhakaran, M.P., et al., *Electrospun conducting polymer nanofibers and electrical stimulation of nerve stem cells*. *J Biosci Bioeng*, 2011. **112**(5): p. 501-7.
100. Moroder, P., et al., *Material properties and electrical stimulation regimens of polycaprolactone fumarate-polypyrrole scaffolds as potential conductive nerve conduits*. *Acta Biomater*, 2011. **7**(3): p. 944-53.
101. Nguyen, H.T., et al., *Electric field stimulation through a biodegradable polypyrrole-co-polycaprolactone substrate enhances neural cell growth*. *J Biomed Mater Res A*, 2014. **102**(8): p. 2554-64.
102. Meng, S., *Nerve cell differentiation using constant and programmed electrical stimulation through conductive non-functional graphene nanosheets film*. *Tissue Engineering and Regenerative Medicine*, 2014. **11**(4): p. 274-283.
103. Song, J., et al., *Polymerizing Pyrrole Coated Poly (l-lactic acid-co-ε-caprolactone) (PLCL) Conductive Nanofibrous Conduit Combined with Electric Stimulation for Long-Range Peripheral Nerve Regeneration*. *Front Mol Neurosci*, 2016. **9**: p. 117.
104. Koppes, A.N., et al., *Robust neurite extension following exogenous electrical stimulation within single walled carbon nanotube-composite hydrogels*. *Acta Biomater*, 2016. **39**: p. 34-43.
105. Zhou, X., et al., *Enhancement of neurite adhesion, alignment and elongation on conductive polypyrrole-poly(lactide acid) fibers with cell-derived extracellular matrix*. *Colloids Surf B Biointerfaces*, 2017. **149**: p. 217-225.
106. Zhou, Z., et al., *Effective nerve cell modulation by electrical stimulation of carbon nanotube embedded conductive polymeric scaffolds*. *Biomater Sci*, 2018. **6**(9): p. 2375-2385.
107. Liu, R., et al., *Electrical stimulation mediated the neurite outgrowth of PC-12 cells on the conductive polylactic acid/reduced graphene oxide/polypyrrole composite nanofibers*. *Applied Surface Science*, 2021. **560**: p. 149965.
108. Aznar-Cervantes, S., et al., *Fabrication of conductive electrospun silk fibroin scaffolds by coating with polypyrrole for biomedical applications*. *Bioelectrochemistry*, 2012. **85**: p. 36-43.

109. Hardy, J.G., et al., *Instructive Conductive 3D Silk Foam-Based Bone Tissue Scaffolds Enable Electrical Stimulation of Stem Cells for Enhanced Osteogenic Differentiation*. *Macromol Biosci*, 2015. **15**(11): p. 1490-6.
110. Aznar-Cervantes, S., et al., *Fabrication of electrospun silk fibroin scaffolds coated with graphene oxide and reduced graphene for applications in biomedicine*. *Bioelectrochemistry*, 2016. **108**: p. 36-45.
111. Sun, B.B., et al., *Polypyrrole-coated poly(L-lactic acid-co-epsilon-caprolactone)/silk fibroin nanofibrous membranes promoting neural cell proliferation and differentiation with electrical stimulation*. *Journal of Materials Chemistry B*, 2016. **4**(41): p. 6670-6679.
112. Aznar-Cervantes, S., et al., *Electrospun silk fibroin scaffolds coated with reduced graphene promote neurite outgrowth of PC-12 cells under electrical stimulation*. *Materials Science & Engineering C-Materials for Biological Applications*, 2017. **79**: p. 315-325.
113. Dodel, M., et al., *Electrical stimulation of somatic human stem cells mediated by composite containing conductive nanofibers for ligament regeneration*. *Biologicals*, 2017. **46**: p. 99-107.
114. Niu, Y., et al., *Enhancing neural differentiation of induced pluripotent stem cells by conductive graphene/silk fibroin films*. *J Biomed Mater Res A*, 2018. **106**(11): p. 2973-2983.
115. Zhao, G., et al., *Reduced graphene oxide functionalized nanofibrous silk fibroin matrices for engineering excitable tissues*. *NPG Asia Materials*, 2018. **10**(10): p. 982-994.
116. Zhao, Y.H., et al., *Novel conductive polypyrrole/silk fibroin scaffold for neural tissue repair*. *Neural Regen Res*, 2018. **13**(8): p. 1455-1464.
117. Nune, M., et al., *Melanin incorporated electroactive and antioxidant silk fibroin nanofibrous scaffolds for nerve tissue engineering*. *Mater Sci Eng C Mater Biol Appl*, 2019. **94**: p. 17-25.
118. Zhao, Y., et al., *Application of conductive PPy/SF composite scaffold and electrical stimulation for neural tissue engineering*. *Biomaterials*, 2020. **255**: p. 120164.
119. Liang, Y., et al., *Conductive polypyrrole-encapsulated silk fibroin fibers for cardiac tissue engineering*. *Biomaterials*, 2021. **276**: p. 121008.
120. Magaz, A., et al., *Modulation of Neuronal Cell Affinity on PEDOT-PSS Nonwoven Silk Scaffolds for Neural Tissue Engineering*. *ACS Biomater Sci Eng*, 2020. **6**(12): p. 6906-6916.
121. Magaz, A., et al., *Graphene oxide and electroactive reduced graphene oxide-based composite fibrous scaffolds for engineering excitable nerve tissue*. *Mater Sci Eng C Mater Biol Appl*, 2021. **119**: p. 111632.
122. Kundu, B., et al., *Silk fibroin biomaterials for tissue regenerations*. *Adv Drug Deliv Rev*, 2013. **65**(4): p. 457-70.
123. Altman, G.H., et al., *Silk-based biomaterials*. *Biomaterials*, 2003. **24**(3): p. 401-16.
124. Wang, Y., et al., *Controlling silk fibroin conformation for dynamic, responsive, multifunctional, micropatterned surfaces*. *Proc Natl Acad Sci U S A*, 2019. **116**(43): p. 21361-21368.
125. Cuniff, P.M., et al., *Mechanical and thermal properties of dragline silk from the spider *Nephila clavipes**. *Polymers for Advanced Technologies*, 1994. **5**(8): p. 401-410.
126. Chen, S., et al., *Mechanical properties of Bombyx mori silkworm silk fibre and its corresponding silk fibroin filament: A comparative study*. *Materials & Design*, 2019. **181**: p. 108077.
127. Koh, L.-D., et al., *Structures, mechanical properties and applications of silk fibroin materials*. *Progress in Polymer Science*, 2015. **46**: p. 86-110.
128. Pins, G.D., et al., *Self-assembly of collagen fibers. Influence of fibrillar alignment and decorin on mechanical properties*. *Biophysical Journal*, 1997. **73**(4): p. 2164-2172.
129. Yang, L., et al., *Mechanical Properties of Native and Cross-linked Type I Collagen Fibrils*. *Biophysical Journal*, 2008. **94**(6): p. 2204-2211.
130. Engelberg, I. and J. Kohn, *Physico-mechanical properties of degradable polymers used in medical applications: A comparative study*. *Biomaterials*, 1991. **12**(3): p. 292-304.
131. Gosline, J.M., et al., *The mechanical design of spider silks: from fibroin sequence to mechanical function*. *Journal of Experimental Biology*, 1999. **202**(23): p. 3295-3303.

132. Lifson, S. and C. Sander, *Antiparallel and parallel beta-strands differ in amino acid residue preferences*. Nature, 1979. **282**(5734): p. 109-11.
133. Maréchal, Y., 2 - *Geometrical Properties of H-Bonds and H-Bonded Organized Supramolecular Structures*, in *The Hydrogen Bond and the Water Molecule*, Y. Maréchal, Editor. 2007, Elsevier: Amsterdam. p. 25-47.
134. Ye, S., et al., *Chapter Seven - Structure and Orientation of Interfacial Proteins Determined by Sum Frequency Generation Vibrational Spectroscopy: Method and Application*, in *Advances in Protein Chemistry and Structural Biology*, C.Z. Christov, Editor. 2013, Academic Press. p. 213-255.
135. Zhang, X. and Z. Pan, *Microstructure Transitions and Dry-Wet Spinnability of Silk Fibroin Protein from Waste Silk Quilt*. Polymers (Basel), 2019. **11**(10).
136. Qi, Y., et al., *A Review of Structure Construction of Silk Fibroin Biomaterials from Single Structures to Multi-Level Structures*. International Journal of Molecular Sciences, 2017. **18**(3).
137. Kamalha, E., et al., *FTIR and WAXD Study of Regenerated Silk Fibroin*. Advanced Materials Research, 2013. **677**: p. 211-215.
138. Puerta, M., et al., *Influence of ethanol post-treatments on the properties of silk protein materials*. SN Applied Sciences, 2019. **1**(11): p. 1443.
139. Yanagisawa, S., et al., *Improving cell-adhesive properties of recombinant Bombyx mori silk by incorporation of collagen or fibronectin derived peptides produced by transgenic silkworms*. Biomacromolecules, 2007. **8**(11): p. 3487-92.
140. Yang, M., et al., *Silklike materials constructed from sequences of Bombyx mori silk fibroin, fibronectin, and elastin*. J Biomed Mater Res A, 2008. **84**(2): p. 353-63.
141. Zhou, J., et al., *In vitro and in vivo degradation behavior of aqueous-derived electrospun silk fibroin scaffolds*. Polymer Degradation and Stability, 2010. **95**(9): p. 1679-1685.
142. Luo, Z., et al., *Effect of Pore Size on the Biodegradation Rate of Silk Fibroin Scaffolds*. Advances in Materials Science and Engineering, 2015. **2015**: p. 315397.
143. Horan, R.L., et al., *In vitro degradation of silk fibroin*. Biomaterials, 2005. **26**(17): p. 3385-93.
144. Li, M., M. Ogiso, and N. Minoura, *Enzymatic degradation behavior of porous silk fibroin sheets*. Biomaterials, 2003. **24**(2): p. 357-65.
145. Kojthung, A., et al., *Effects of gamma radiation on biodegradation of Bombyx mori silk fibroin*. International Biodeterioration & Biodegradation, 2008. **62**(4): p. 487-490.
146. Meinel, A.J., et al., *Optimization strategies for electrospun silk fibroin tissue engineering scaffolds*. Biomaterials, 2009. **30**(17): p. 3058-67.
147. Singh, B.N., N.N. Panda, and K. Pramanik, *A novel electrospinning approach to fabricate high strength aqueous silk fibroin nanofibers*. Int J Biol Macromol, 2016. **87**: p. 201-7.
148. Kishimoto, Y., et al., *Electrospinning of silk fibroin from all aqueous solution at low concentration*. Mater Sci Eng C Mater Biol Appl, 2017. **73**: p. 498-506.
149. Zhang, K.H., Q.Z. Yu, and X.M. Mo, *Fabrication and Intermolecular Interactions of Silk Fibroin/Hydroxybutyl Chitosan Blended Nanofibers*. International Journal of Molecular Sciences, 2011. **12**(4): p. 2187-2199.
150. Liu, Z., et al., *Preparation of Electrospun Silk Fibroin Nanofibers from Solutions Containing Native Silk Fibrils*. Journal of Applied Polymer Science, 2015. **132**(1).
151. Zhang, F., et al., *Mechanisms and Control of Silk-Based Electrospinning*. Biomacromolecules, 2012. **13**(3): p. 798-804.
152. Sukigara, S., et al., *Regeneration of Bombyx mori silk by electrospinning - part 1: processing parameters and geometric properties*. Polymer, 2003. **44**(19): p. 5721-5727.
153. Kim, S.H., et al., *Silk fibroin nanofiber. Electrospinning, properties, and structure*. Polymer Journal, 2003. **35**(2): p. 185-190.
154. Min, B.M., et al., *Electrospinning of silk fibroin nanofibers and its effect on the adhesion and spreading of normal human keratinocytes and fibroblasts in vitro*. Biomaterials, 2004. **25**(7-8): p. 1289-1297.
155. Minoura, N., M. Tsukada, and M. Nagura, *Physico-chemical properties of silk fibroin membrane as a biomaterial*. Biomaterials, 1990. **11**(6): p. 430-4.

156. Forciniti, L., et al., *Schwann cell response on polypyrrole substrates upon electrical stimulation*. Acta Biomaterialia, 2014. **10**(6): p. 2423-2433.
157. Park, H.S., et al., *Redox-active charge carriers of conducting polymers as a tuner of conductivity and its potential window*. Sci Rep, 2013. **3**: p. 2454.
158. Nuramdhani, I., et al., *Electrochemical Impedance Analysis of a PEDOT:PSS-Based Textile Energy Storage Device*. Materials (Basel), 2017. **11**(1).
159. Volkov, A.V., et al., *Understanding the Capacitance of PEDOT:PSS*. Advanced Functional Materials, 2017. **27**(28): p. 1700329.
160. Sirivisoot, S., R. Pareta, and B.S. Harrison, *Protocol and cell responses in three-dimensional conductive collagen gel scaffolds with conductive polymer nanofibres for tissue regeneration*. Interface Focus, 2014. **4**(1): p. 20130050.
161. Hardy, J.G., et al., *Conducting polymer-based multilayer films for instructive biomaterial coatings*. Future Sci OA, 2015. **1**(4): p. FSO79.
162. Persano, L., et al., *Industrial Upscaling of Electrospinning and Applications of Polymer Nanofibers: A Review*. Macromolecular Materials and Engineering, 2013. **298**(5): p. 504-520.
163. Jose Varghese, R., et al., *Chapter 3 - Introduction to nanomaterials: synthesis and applications*, in *Nanomaterials for Solar Cell Applications*, S. Thomas, et al., Editors. 2019, Elsevier. p. 75-95.
164. Yan, G., H. Niu, and T. Lin, *Chapter 7 - Needle-less Electrospinning*, in *Electrospinning: Nanofabrication and Applications*, B. Ding, X. Wang, and J. Yu, Editors. 2019, William Andrew Publishing. p. 219-247.
165. Sabantina, L., *Chapter 11 - Nanocarbons-based textiles for flexible energy storage*, in *Nanosensors and Nanodevices for Smart Multifunctional Textiles*, A. Ehrmann, T.A. Nguyen, and P. Nguyen Tri, Editors. 2021, Elsevier. p. 163-188.
166. Mailley, D., A. Hébraud, and G. Schlatter, *A Review on the Impact of Humidity during Electrospinning: From the Nanofiber Structure Engineering to the Applications*. Macromolecular Materials and Engineering, 2021. **306**(7): p. 2100115.
167. Taylor, G.I., *Disintegration of water drops in an electric field*. Proceedings of the Royal Society of London. Series A. Mathematical and Physical Sciences, 1964. **280**(1382): p. 383-397.
168. Wunner, F.M., et al., *5.13 Electrospinning With Polymer Melts – State of the Art and Future Perspectives*, in *Comprehensive Biomaterials II*, P. Ducheyne, Editor. 2017, Elsevier: Oxford. p. 217-235.
169. Bhattacharjee, P.K. and G.C. Rutledge, *5.12 Electrospinning and Polymer Nanofibers: Process Fundamentals*, in *Comprehensive Biomaterials II*, P. Ducheyne, Editor. 2017, Elsevier: Oxford. p. 200-216.
170. Hohman, M.M., et al., *Electrospinning and electrically forced jets. II. Applications*. Physics of Fluids, 2001. **13**(8): p. 2221-2236.
171. Reneker, D.H., et al., *Bending instability of electrically charged liquid jets of polymer solutions in electrospinning*. Journal of Applied Physics, 2000. **87**(9): p. 4531-4547.
172. McEachin, Z. and K. Lozano, *Production and characterization of polycaprolactone nanofibers via forcespinning™ technology*. Journal of Applied Polymer Science, 2012. **126**(2): p. 473-479.
173. Brown, T.D., et al., *Melt electrospinning of poly(epsilon-caprolactone) scaffolds: phenomenological observations associated with collection and direct writing*. Mater Sci Eng C Mater Biol Appl, 2014. **45**: p. 698-708.
174. Qin, C.C., et al., *Melt electrospinning of poly(lactic acid) and polycaprolactone microfibers by using a hand-operated Wimshurst generator*. Nanoscale, 2015. **7**(40): p. 16611-5.
175. Chen, Q., et al., *Direct write micro/nano optical fibers by near-field melt electrospinning*. Opt Lett, 2017. **42**(24): p. 5106-5109.
176. Suresh, S., A. Becker, and B. Glasmacher, *Impact of Apparatus Orientation and Gravity in Electrospinning-A Review of Empirical Evidence*. Polymers (Basel), 2020. **12**(11).
177. Karak, N., *1 - Fundamentals of polymers*, in *Vegetable Oil-Based Polymers*, N. Karak, Editor. 2012, Woodhead Publishing. p. 1-30.

178. Maity, S., A. Chatterjee, and J. Ganguly, *18 - Stimuli-responsive sugar-derived hydrogels: A modern approach in cancer biology*, in *Green Approaches in Medicinal Chemistry for Sustainable Drug Design*, B.K. Banik, Editor. 2020, Elsevier. p. 617-649.
179. Sriussamee, K., *Direct Electrical Stimulation Approaches for Bone Repair and Regeneration*, in *Department of Materials*. 2019, University of Manchester. p. 196.
180. Balint, R., N.J. Cassidy, and S.H. Cartmell, *Electrical stimulation: a novel tool for tissue engineering*. *Tissue Eng Part B Rev*, 2013. **19**(1): p. 48-57.
181. Thirivikraman, G., S.K. Boda, and B. Basu, *Unraveling the mechanistic effects of electric field stimulation towards directing stem cell fate and function: A tissue engineering perspective*. *Biomaterials*, 2018. **150**: p. 60-86.
182. Merrill, D.R., M. Bikson, and J.G. Jefferys, *Electrical stimulation of excitable tissue: design of efficacious and safe protocols*. *J Neurosci Methods*, 2005. **141**(2): p. 171-98.
183. Grimnes, S. and Ø.G. Martinsen, *Chapter 2 - Electrolytics*, in *Bioimpedance and Bioelectricity Basics (Third Edition)*, S. Grimnes and Ø.G. Martinsen, Editors. 2015, Academic Press: Oxford. p. 9-36.
184. Grimnes, S. and Ø.G. Martinsen, *Chapter 7 - Electrodes*, in *Bioimpedance and Bioelectricity Basics (Third Edition)*, S. Grimnes and Ø.G. Martinsen, Editors. 2015, Academic Press: Oxford. p. 179-254.
185. Meng, S., M. Rouabhia, and Z. Zhang, *Electrical Stimulation in Tissue Regeneration*, in *Applied Biomedical Engineering*. 2011.
186. Dunwell, M., Y. Yan, and B. Xu, *Understanding the influence of the electrochemical double-layer on heterogeneous electrochemical reactions*. *Current Opinion in Chemical Engineering*, 2018. **20**: p. 151-158.
187. Tandon, N., et al., *Characterization of electrical stimulation electrodes for cardiac tissue engineering*. *Conf Proc IEEE Eng Med Biol Soc*, 2006. **2006**: p. 845-8.
188. Serena, E., et al., *Electrical stimulation of human embryonic stem cells: cardiac differentiation and the generation of reactive oxygen species*. *Exp Cell Res*, 2009. **315**(20): p. 3611-9.
189. Tandon, N., et al., *Optimization of electrical stimulation parameters for cardiac tissue engineering*. *J Tissue Eng Regen Med*, 2011. **5**(6): p. e115-25.
190. Toshev, Y., et al., *Protective coating of zinc and zinc alloys for industrial applications*, in *4M 2006 - Second International Conference on Multi-Material Micro Manufacture*, W. Menz, S. Dimov, and B. Fillon, Editors. 2006, Elsevier: Oxford. p. 323-326.
191. Sean Brossia, C., *11 - The use of probes for detecting corrosion in underground pipelines*, in *Underground Pipeline Corrosion*, M.E. Orazem, Editor. 2014, Woodhead Publishing. p. 286-303.
192. Gupta, A. and P. Pal, *Flexible Sensors for Biomedical Application*, in *Environmental, Chemical and Medical Sensors*, S. Bhattacharya, et al., Editors. 2018, Springer Singapore: Singapore. p. 287-314.
193. Bibi, F., et al., *A Review: Origins of the Dielectric Properties of Proteins and Potential Development as Bio-Sensors*. *Sensors (Basel)*, 2016. **16**(8).
194. Pethig, R. and D.B. Kell, *The passive electrical properties of biological systems: their significance in physiology, biophysics and biotechnology*. *Phys Med Biol*, 1987. **32**(8): p. 933-70.
195. Atrons, A., et al., *Understanding the Corrosion of Mg and Mg Alloys*, in *Encyclopedia of Interfacial Chemistry*, K. Wandelt, Editor. 2018, Elsevier: Oxford. p. 515-534.
196. Ellis, C.L.C., et al., *Chapter 6 - Ion Migration in Hybrid Perovskites: Evolving Understanding of a Dynamic Phenomenon*, in *Perovskite Photovoltaics*, S. Thomas and A. Thankappan, Editors. 2018, Academic Press. p. 163-196.
197. Papavinasam, S., *Chapter 11 - Monitoring – External Corrosion*, in *Corrosion Control in the Oil and Gas Industry*, S. Papavinasam, Editor. 2014, Gulf Professional Publishing: Boston. p. 715-750.
198. Telegdi, J., A. Shaban, and G. Vastag, *Biocorrosion—Steel*, in *Encyclopedia of Interfacial Chemistry*, K. Wandelt, Editor. 2018, Elsevier: Oxford. p. 28-42.

199. INSTRUMENTS, G. *Basics of Electrochemical Impedance Spectroscopy*. [cited 2022 January 24]; Available from: <https://www.gamry.com/application-notes/EIS/basics-of-electrochemical-impedance-spectroscopy/>.
200. Mei, B.-A., et al., *Physical Interpretations of Nyquist Plots for EDLC Electrodes and Devices*. The Journal of Physical Chemistry C, 2018. **122**(1): p. 194-206.
201. Armstrong, P.F., C.T. Brighton, and A.M. Star, *Capacitively coupled electrical stimulation of bovine growth plate chondrocytes grown in pellet form*. J Orthop Res, 1988. **6**(2): p. 265-71.
202. Hartig, M., U. Joos, and H.P. Wiesmann, *Capacitively coupled electric fields accelerate proliferation of osteoblast-like primary cells and increase bone extracellular matrix formation in vitro*. Eur Biophys J, 2000. **29**(7): p. 499-506.
203. Vaca-Gonzalez, J.J., et al., *Capacitively coupled electrical stimulation of rat chondroepiphysis explants: A histomorphometric analysis*. Bioelectrochemistry, 2019. **126**: p. 1-11.
204. Khalifeh, J.M., et al., *Electrical Stimulation and Bone Healing: A Review of Current Technology and Clinical Applications*. IEEE Rev Biomed Eng, 2018. **11**: p. 217-232.
205. Seo, N., et al., *Low-frequency pulsed electromagnetic field pretreated bone marrow-derived mesenchymal stem cells promote the regeneration of crush-injured rat mental nerve*. Neural Regen Res, 2018. **13**(1): p. 145-153.
206. Ivkov, R., et al., *Application of high amplitude alternating magnetic fields for heat induction of nanoparticles localized in cancer*. Clin Cancer Res, 2005. **11**(19 Pt 2): p. 7093s-7103s.
207. Pateman, C.J., et al., *Nerve guides manufactured from photocurable polymers to aid peripheral nerve repair*. Biomaterials, 2015. **49**: p. 77-89.
208. Soliman, E., et al., *Aligned electrospun fibers for neural patterning*. Biotechnol Lett, 2018. **40**(3): p. 601-607.
209. Sun, M., et al., *In vitro and in vivo testing of novel ultrathin PCL and PCL/PLA blend films as peripheral nerve conduit*. J Biomed Mater Res A, 2010. **93**(4): p. 1470-81.
210. Fukazawa, T., et al., *Electrical stimulation accelerates neuromuscular junction formation through ADAM19/neuregulin/ErbB signaling in vitro*. Neurosci Lett, 2013. **545**: p. 29-34.
211. Doeblner, J.A., *Effects of neutral ionophores on membrane electrical characteristics of NG108-15 cells*. Toxicol Lett, 2000. **114**(1-3): p. 27-38.
212. Doeblner, J.A., *Effects of protonophores on membrane electrical characteristics in NG108-15 cells*. Neurochem Res, 2000. **25**(2): p. 263-8.
213. Kingham, P.J., et al., *Adipose-derived stem cells differentiate into a Schwann cell phenotype and promote neurite outgrowth in vitro*. Exp Neurol, 2007. **207**(2): p. 267-74.
214. Kraus, D., et al., *The Neuro-spheroid—A novel 3D in vitro model for peripheral nerve regeneration*. Journal of Neuroscience Methods, 2015. **246**: p. 97-105.
215. Acosta-García, M.C., et al., *Simultaneous recording of electrical activity and the underlying ionic currents in NG108-15 cells cultured on gold substrate*. Heliyon, 2018. **4**(2): p. e00550.
216. Gheith, M.K., et al., *Stimulation of Neural Cells by Lateral Currents in Conductive Layer-by-Layer Films of Single-Walled Carbon Nanotubes*. Advanced Materials, 2006. **18**(22): p. 2975-2979.
217. Pawar, K., et al., *Recombinant Spider Silk and Collagen-Based Nerve Guidance Conduits Support Neuronal Cell Differentiation and Functionality in Vitro*. ACS Applied Bio Materials, 2019. **2**(11): p. 4872-4880.
218. Nakae, H., *Morphological differentiation of rat pheochromocytoma cells (PC12 cells) by electric stimulation*. Brain Res, 1991. **558**(2): p. 348-52.
219. Geremia, N.M., et al., *Electrical stimulation promotes sensory neuron regeneration and growth-associated gene expression*. Exp Neurol, 2007. **205**(2): p. 347-59.
220. Huang, J., et al., *Electrical stimulation to conductive scaffold promotes axonal regeneration and remyelination in a rat model of large nerve defect*. PLoS One, 2012. **7**(6): p. e39526.
221. Zhu, R., et al., *Electrical stimulation affects neural stem cell fate and function in vitro*. Exp Neurol, 2019. **319**: p. 112963.

222. Kamber, D., H. Erez, and M.E. Spira, *Local calcium-dependent mechanisms determine whether a cut axonal end assembles a retarded endbulb or competent growth cone*. Exp Neurol, 2009. **219**(1): p. 112-25.
223. Ghosh-Roy, A., et al., *Calcium and cyclic AMP promote axonal regeneration in Caenorhabditis elegans and require DLK-1 kinase*. J Neurosci, 2010. **30**(9): p. 3175-83.
224. Kulbatski, I., D.J. Cook, and C.H. Tator, *Calcium Entry through L-Type Calcium Channels Is Essential for Neurite Regeneration in Cultured Sympathetic Neurons*. Journal of Neurotrauma, 2004. **21**(3): p. 357-374.
225. Kimura, K., et al., *Electrically induced neurite outgrowth of PC12 cells on the electrode surface*. Med Biol Eng Comput, 1998. **36**(4): p. 493-8.
226. Meda, F., A. Joliot, and S. Vríz, *Nerves and hydrogen peroxide: how old enemies become new friends*. Neural Regen Res, 2017. **12**(4): p. 568-569.
227. Xie, J., et al., *Nerve guidance conduits based on double-layered scaffolds of electrospun nanofibers for repairing the peripheral nervous system*. ACS Appl Mater Interfaces, 2014. **6**(12): p. 9472-80.
228. Shang, S., et al., *The effect of electrospun fibre alignment on the behaviour of rat periodontal ligament cells*. Eur Cell Mater, 2010. **19**: p. 180-92.
229. Ayres, C.E., et al., *Measuring fiber alignment in electrospun scaffolds: a user's guide to the 2D fast Fourier transform approach*. Journal of Biomaterials Science-Polymer Edition, 2008. **19**(5): p. 603-621.
230. Barth, A., *Infrared spectroscopy of proteins*. Biochim Biophys Acta, 2007. **1767**(9): p. 1073-101.
231. Krimm, S. and J. Bandekar, *Vibrational Spectroscopy and Conformation of Peptides, Polypeptides, and Proteins*, in *Advances in Protein Chemistry*, C.B. Anfinsen, J.T. Edsall, and F.M. Richards, Editors. 1986, Academic Press. p. 181-364.
232. Byler, D.M. and H. Susi, *Examination of the Secondary Structure of Proteins by Deconvolved Ftir Spectra*. Biopolymers, 1986. **25**(3): p. 469-487.
233. Litvinov, R.I., et al., *The alpha-Helix to beta-Sheet Transition in Stretched and Compressed Hydrated Fibrin Clots*. Biophysical Journal, 2012. **103**(5): p. 1020-1027.
234. Wilson, D., R. Valluzzi, and D. Kaplan, *Conformational transitions in model silk peptides*. Biophysical Journal, 2000. **78**(5): p. 2690-2701.
235. Allardyce, B.J., et al., *The impact of degumming conditions on the properties of silk films for biomedical applications*. Textile Research Journal, 2015. **86**(3): p. 275-287.
236. Ohgo, K., et al., *Preparation of non-woven nanofibers of Bombyx mori silk, Samia cynthia ricini silk and recombinant hybrid silk with electrospinning method*. Polymer, 2003. **44**(3): p. 841-846.
237. Ajisawa, A., *Dissolution of silk fibroin with calciumchloride/ethanol aqueous solution*. The Journal of Sericultural Science of Japan, 1998. **67**(2): p. 91-94.
238. Matsumoto, A., et al., *Mechanisms of silk fibroin sol-gel transitions*. J Phys Chem B, 2006. **110**(43): p. 21630-8.
239. Nogueira, G.M., et al., *Hydrogels from silk fibroin metastable solution: Formation and characterization from a biomaterial perspective*. Materials Science and Engineering: C, 2011. **31**(5): p. 997-1001.
240. Chen, J.P., S.H. Chen, and G.J. Lai, *Preparation and characterization of biomimetic silk fibroin/chitosan composite nanofibers by electrospinning for osteoblasts culture*. Nanoscale Research Letters, 2012. **7**: p. 1-11.
241. Liu, Q., et al., *Exploring the Structural Transformation Mechanism of Chinese and Thailand Silk Fibroin Fibers and Formic-Acid Fabricated Silk Films*. International journal of molecular sciences, 2018. **19**(11): p. 3309.
242. Yazawa, K., et al., *Influence of Water Content on the beta-Sheet Formation, Thermal Stability, Water Removal, and Mechanical Properties of Silk Materials*. Biomacromolecules, 2016. **17**(3): p. 1057-66.
243. Hu, X., et al., *Regulation of silk material structure by temperature-controlled water vapor annealing*. Biomacromolecules, 2011. **12**(5): p. 1686-96.
244. Guan, J., D. Porter, and F. Vollrath, *Thermally induced changes in dynamic mechanical properties of native silks*. Biomacromolecules, 2013. **14**(3): p. 930-7.

245. Lewis, G.N. and M. Calvin, *The Color of Organic Substances*. Chemical Reviews, 1939. **25**(2): p. 273-328.
246. Park, B.K. and I.C. Um, *Effect of Relative Humidity on the Electrospinning Performance of Regenerated Silk Solution*. Polymers (Basel), 2021. **13**(15).
247. Kopp, A., et al., *Effect of process parameters on additive-free electrospinning of regenerated silk fibroin nonwovens*. Bioact Mater, 2020. **5**(2): p. 241-252.
248. Jin, H.J. and D.L. Kaplan, *Mechanism of silk processing in insects and spiders*. Nature, 2003. **424**(6952): p. 1057-61.
249. Yuan, H., Q. Zhou, and Y. Zhang, 6 - *Improving fiber alignment during electrospinning*, in *Electrospun Nanofibers*, M. Afshari, Editor. 2017, Woodhead Publishing. p. 125-147.
250. Huang, Z.-M., et al., *A review on polymer nanofibers by electrospinning and their applications in nanocomposites*. Composites Science and Technology, 2003. **63**(15): p. 2223-2253.
251. Teo, W.E., R. Inai, and S. Ramakrishna, *Technological advances in electrospinning of nanofibers*. Sci Technol Adv Mater, 2011. **12**(1): p. 013002.
252. Li, D., Y. Wang, and Y. Xia, *Electrospinning Nanofibers as Uniaxially Aligned Arrays and Layer-by-Layer Stacked Films*. Advanced Materials, 2004. **16**(4): p. 361-366.
253. Li, D., Y. Wang, and Y. Xia, *Electrospinning of Polymeric and Ceramic Nanofibers as Uniaxially Aligned Arrays*. Nano Letters, 2003. **3**(8): p. 1167-1171.
254. Katta, P., et al., *Continuous Electrospinning of Aligned Polymer Nanofibers onto a Wire Drum Collector*. Nano Letters, 2004. **4**(11): p. 2215-2218.
255. Yang, D., et al., *Fabrication of Aligned Fibrous Arrays by Magnetic Electrospinning*. Advanced Materials, 2007. **19**(21): p. 3702-3706.
256. Liu, Y., et al., *Magnetic-Field-Assisted Electrospinning of Aligned Straight and Wavy Polymeric Nanofibers*. Advanced Materials, 2010. **22**(22): p. 2454-2457.
257. Magaz, A., et al., *Electroresponsive Silk-Based Biohybrid Composites for Electrochemically Controlled Growth Factor Delivery*. Pharmaceutics, 2020. **12**(8).
258. Kaewpirom, S. and S. Boonsang, *Influence of alcohol treatments on properties of silk-fibroin-based films for highly optically transparent coating applications*. RSC Advances, 2020. **10**(27): p. 15913-15923.
259. Um, I.C., et al., *The role of formic acid in solution stability and crystallization of silk protein polymer*. Int J Biol Macromol, 2003. **33**(4-5): p. 203-13.
260. Hu, X., D. Kaplan, and P. Cebe, *Dynamic Protein–Water Relationships during β -Sheet Formation*. Macromolecules, 2008. **41**(11): p. 3939-3948.
261. Puerta, M., M.S. Peresin, and A. Restrepo-Osorio, *Effects of Chemical Post-treatments on Structural and Physicochemical Properties of Silk Fibroin Films Obtained From Silk Fibrous Waste*. Front Bioeng Biotechnol, 2020. **8**: p. 523949.
262. Terada, D., et al., *The outermost surface properties of silk fibroin films reflect ethanol-treatment conditions used in biomaterial preparation*. Mater Sci Eng C Mater Biol Appl, 2016. **58**: p. 119-26.
263. Agarwal, N., D.A. Hoagland, and R.J. Farris, *Effect of moisture absorption on the thermal properties of Bombyx mori silk fibroin films*. Journal of Applied Polymer Science, 1997. **63**(3): p. 401-410.
264. Jin, H.J., et al., *Water-Stable Silk Films with Reduced β -Sheet Content*. Advanced Functional Materials, 2005. **15**(8): p. 1241-1247.
265. Xie, J., et al., *Conductive Core–Sheath Nanofibers and Their Potential Application in Neural Tissue Engineering*. Advanced Functional Materials, 2009. **19**(14): p. 2312-2318.
266. Cordin, M., T. Bechtold, and T. Pham, *Effect of fibre orientation on the mechanical properties of polypropylene–lyocell composites*. Cellulose, 2018. **25**(12): p. 7197-7210.
267. *Composites Fibres 2*. [cited 2022 January 24]; Available from: <https://textbooks.elsevier.com/manualsprotectedtextbooks/9780750663809/static/composites/composites2b.htm>.
268. Ye, L., et al., *The fabrication of double layer tubular vascular tissue engineering scaffold via coaxial electrospinning and its 3D cell coculture*. Journal of Biomedical Materials Research Part A, 2015. **103**(12): p. 3863-3871.

269. Mouro, C., R. Fangueiro, and I.C. Gouveia, *Preparation and Characterization of Electrospun Double-layered Nanocomposites Membranes as a Carrier for Centella asiatica (L.)*. Polymers, 2020. **12**(11): p. 2653.
270. Horii, T., et al., *Synthesis of highly conductive PEDOT:PSS and correlation with hierarchical structure*. Polymer, 2018. **140**: p. 33-38.
271. Zhao, Q., et al., *The structure and properties of PEDOT synthesized by template-free solution method*. Nanoscale Res Lett, 2014. **9**(1): p. 557.
272. Susanti, E., P. Wulandari, and Herman, *Effect of localized surface plasmon resonance from incorporated gold nanoparticles in PEDOT:PSS hole transport layer for hybrid solar cell applications*. Journal of Physics: Conference Series, 2018. **1080**: p. 012010.
273. Yang, J., et al., *Electrochemically Active, Compressible and Conducting Silk Fibroin Hydrogels*. Industrial & Engineering Chemistry Research, 2020. **XXXX**.
274. Woicik, J.C., *Hard X-ray Photoelectron Spectroscopy (HAXPES) Preface*. Hard X-Ray Photoelectron Spectroscopy (Haxpes), 2016. **59**: p. V-Vi.
275. Panaccione, G. and K. Kobayashi, *Hard X-ray photoemission spectroscopy: Variable depth analysis of bulk, surface and interface electronic properties*. Surface Science, 2012. **606**(3-4): p. 125-129.
276. Regoutz, A., et al., *A novel laboratory-based hard X-ray photoelectron spectroscopy system*. Review of Scientific Instruments, 2018. **89**(7).
277. Spencer, B.F., et al., *Hard X-rays and inelastic background modelling extend photoelectron spectroscopy below the surface for the detection of buried layers*. Applied Surface Science, 2020.
278. Trzhaskovskaya, M.B. and V.G. Yarzhemsky, *Dirac-Fock photoionization parameters for HAXPES applications*. Atomic Data and Nuclear Data Tables, 2018. **119**: p. 99-174.
279. Trzhaskovskaya, M.B. and G. Yarzhemsky, *Dirac-Fock photoionization parameters for HAXPES applications, Part II: Inner atomic shells*. Atomic Data and Nuclear Data Tables, 2019. **129**.
280. Seah, M.P., *A Quantitative Framework for the Analysis of Surfaces by Aes and Xps*. Analisis, 1981. **9**(5): p. 171-180.
281. Tanuma, S., C.J. Powell, and D.R. Penn, *Calculations of Electron Inelastic Mean Free Paths .5. Data for 14 Organic-Compounds over the 50-2000 Ev Range*. Surface and Interface Analysis, 1994. **21**(3): p. 165-176.
282. Fairley, N., CasaXPS. <http://www.casaxps.com>, 2019.
283. Gilbert, J.L., *1.2 Electrochemical Behavior of Metals in the Biological Milieu*, in *Comprehensive Biomaterials II*, P. Ducheyne, Editor. 2017, Elsevier: Oxford. p. 19-49.
284. Bhattacharjee, P. and M. Ahearne, *Fabrication and Biocompatibility of Electroconductive Silk Fibroin/PEDOT: PSS Composites for Corneal Epithelial Regeneration*. Polymers (Basel), 2020. **12**(12).
285. Alhummiyany, H., S. Rafique, and K. Sulaiman, *XPS Analysis of the Improved Operational Stability of Organic Solar Cells Using a V2O5 and PEDOT:PSS Composite Layer: Effect of Varied Atmospheric Conditions*. Journal of Physical Chemistry C, 2017. **121**(14): p. 7649-7658.
286. Yan, H. and H. Okuzaki, *Effect of solvent on PEDOT/PSS nanometer-scaled thin films: XPS and STEM/AFM studies*. Synthetic Metals, 2009. **159**(21-22): p. 2225-2228.
287. Xing, K.Z., et al., *The electronic structure of poly(3,4-ethylene-dioxythiophene): studied by XPS and UPS*. Synthetic Metals, 1997. **89**(3): p. 161-165.
288. Shah, S.A.A., et al., *Electrochemically Enhanced Drug Delivery Using Polypyrrole Films*. Materials (Basel), 2018. **11**(7).
289. FluorTools.com. *Red-shift or blue-shift spectra*. [cited 2022 March 19]; Available from: <http://www.fluortools.com/software/ae/documentation/edit-spectra/shift>.
290. Xia, Y. and L. Yun, *Fabrication and properties of conductive conjugated polymers/silk fibroin composite fibers*. Composites Science and Technology, 2008. **68**(6): p. 1471-1479.
291. Mousavi, S.T., et al., *Electroactive Silk Fibroin Films for Electrochemically Enhanced Delivery of Drugs*. Macromolecular Materials and Engineering, 2020. **305**(6): p. 2000130.

292. Hardy, J.G., et al., *Into the groove: instructive silk-polypyrrole films with topographical guidance cues direct DRG neurite outgrowth*. Journal of Biomaterials Science-Polymer Edition, 2015. **26**(17): p. 1327-1342.
293. Zhu, M., et al., *Fabrication and Osteoblastic Adhesion Behavior of Regenerated Silk Fibroin/PLLA Nanofibrous Scaffold by Double Syringe Electrospinning*. Fibers and Polymers, 2019. **20**(9): p. 1850-1856.
294. Chan, A.H.P., et al., *Altered processing enhances the efficacy of small-diameter silk fibroin vascular grafts*. Scientific Reports, 2019. **9**(1): p. 17461.
295. Zhou, J., C. Cao, and X. Ma, *A novel three-dimensional tubular scaffold prepared from silk fibroin by electrospinning*. Int J Biol Macromol, 2009. **45**(5): p. 504-10.
296. Jin, H.J., et al., *Human bone marrow stromal cell responses on electrospun silk fibroin mats*. Biomaterials, 2004. **25**(6): p. 1039-47.
297. Amiraliyan, N., M. Nouri, and M. Haghighat Kish, *Structural characterization and mechanical properties of electrospun silk fibroin nanofiber mats*. Polymer Science Series A, 2010. **52**(4): p. 407-412.
298. Cebe, P., et al., *Silk I and Silk II studied by fast scanning calorimetry*. Acta Biomater, 2017. **55**: p. 323-332.
299. Boulet-Audet, M., F. Vollrath, and C. Holland, *Identification and classification of silks using infrared spectroscopy*. The Journal of experimental biology, 2015. **218**(Pt 19): p. 3138-3149.
300. Xiao, S., et al., *Mechanical response of silk crystalline units from force-distribution analysis*. Biophys J, 2009. **96**(10): p. 3997-4005.
301. Mo, C., et al., *The effect of water on the conformation transition of Bombyx mori silk fibroin*. Vibrational Spectroscopy, 2009. **51**(1): p. 105-109.
302. Tobias, D.J., S.F. Sneddon, and C.L. Brooks, 3rd, *Stability of a model beta-sheet in water*. J Mol Biol, 1992. **227**(4): p. 1244-52.
303. Andiappan, M., et al., *Electrospun eri silk fibroin scaffold coated with hydroxyapatite for bone tissue engineering applications*. Prog Biomater, 2013. **2**(1): p. 6.
304. Mohammadzadehmoghadam, S. and Y. Dong, *Fabrication and Characterization of Electrospun Silk Fibroin/Gelatin Scaffolds Crosslinked With Glutaraldehyde Vapor*. Frontiers in Materials, 2019. **6**(91).
305. He, H. and J. Ouyang, *Enhancements in the Mechanical Stretchability and Thermoelectric Properties of PEDOT:PSS for Flexible Electronics Applications*. Accounts of Materials Research, 2020. **1**(2): p. 146-157.
306. Li, P., et al., *Stretchable and conductive polymer films for high-performance electromagnetic interference shielding*. Journal of Materials Chemistry C, 2016. **4**(27): p. 6525-6532.
307. Taroni, P.J., et al., *Toward Stretchable Self-Powered Sensors Based on the Thermoelectric Response of PEDOT:PSS/Polyurethane Blends*. Advanced Functional Materials, 2018. **28**(15): p. 1704285.
308. Tsukada, S., H. Nakashima, and K. Torimitsu, *Conductive polymer combined silk fiber bundle for bioelectrical signal recording*. PLoS One, 2012. **7**(4): p. e33689.
309. He, M., et al., *Fabrication and characterization of electrospun feather keratin/poly(vinyl alcohol) composite nanofibers*. RSC Advances, 2017. **7**(16): p. 9854-9861.
310. Mobasser, A., et al., *Polymer scaffolds with preferential parallel grooves enhance nerve regeneration*. Tissue Eng Part A, 2015. **21**(5-6): p. 1152-62.
311. Reina, M.A., et al., *Chapter 7 - Microscopic Morphology and Ultrastructure of Human Peripheral Nerves*, in *Nerves and Nerve Injuries*, R.S. Tubbs, et al., Editors. 2015, Academic Press: San Diego. p. 91-106.
312. Islam, M.S., et al., *Extracting structural features of rat sciatic nerve using polarization-sensitive spectral domain optical coherence tomography*. J Biomed Opt, 2012. **17**(5): p. 056012.
313. Rydevik, B.L., et al., *An in vitro mechanical and histological study of acute stretching on rabbit tibial nerve*. Journal of Orthopaedic Research, 1990. **8**(5): p. 694-701.

314. Benoudjit, A., M.M. Bader, and W.W.A. Wan Salim, *Study of electropolymerized PEDOT:PSS transducers for application as electrochemical sensors in aqueous media*. Sensing and Bio-Sensing Research, 2018. **17**: p. 18-24.
315. Stöcker, T., A. Köhler, and R. Moos, *Why does the electrical conductivity in PEDOT:PSS decrease with PSS content? A study combining thermoelectric measurements with impedance spectroscopy*. Journal of Polymer Science Part B: Polymer Physics, 2012. **50**(14): p. 976-983.
316. Shkirskiy, V., et al., *Electrochemical Impedance Measurements in Scanning Ion Conductance Microscopy*. Anal Chem, 2020. **92**(18): p. 12509-12517.
317. Ashton, M.D., et al., *Wirelessly triggered bioactive molecule delivery from degradable electroactive polymer films*. Polymer International, 2021. **70**(4): p. 467-474.
318. Distler, T., et al., *Electrically Conductive and 3D-Printable Oxidized Alginate-Gelatin Polypyrrole:PSS Hydrogels for Tissue Engineering*. Adv Healthc Mater, 2021. **10**(9): p. e2001876.
319. Krystosek, A., *Neurite formation by neuroblastoma-glioma hybrid cells (NG108-15) in defined medium: stochastic initiation with persistence of differentiated functions*. J Cell Physiol, 1985. **125**(2): p. 319-29.
320. Gendron, L., et al., *Signals from the AT2 (angiotensin type 2) receptor of angiotensin II inhibit p21ras and activate MAPK (mitogen-activated protein kinase) to induce morphological neuronal differentiation in NG108-15 cells*. Mol Endocrinol, 1999. **13**(9): p. 1615-26.
321. Laflamme, L., et al., *Angiotensin II induction of neurite outgrowth by AT2 receptors in NG108-15 cells. Effect counteracted by the AT1 receptors*. J Biol Chem, 1996. **271**(37): p. 22729-35.
322. Seidman, K.J., et al., *Differentiation of NG108-15 neuroblastoma cells by serum starvation or dimethyl sulfoxide results in marked differences in angiotensin II receptor subtype expression*. J Neurochem, 1996. **66**(3): p. 1011-8.
323. Fyhrquist, F., K. Metsarinne, and I. Tikkanen, *Role of angiotensin II in blood pressure regulation and in the pathophysiology of cardiovascular disorders*. J Hum Hypertens, 1995. **9 Suppl 5**: p. S19-24.
324. Benigni, A., P. Cassis, and G. Remuzzi, *Angiotensin II revisited: new roles in inflammation, immunology and aging*. EMBO Mol Med, 2010. **2**(7): p. 247-57.
325. Pun, S., et al., *NG108-15 cells express neuregulin that induces AChR alpha-subunit synthesis in cultured myotubes*. FEBS Lett, 1997. **418**(3): p. 275-81.
326. Kataria, H., A. Alizadeh, and S. Karimi-Abdolrezaee, *Neuregulin-1/ErbB network: An emerging modulator of nervous system injury and repair*. Prog Neurobiol, 2019. **180**: p. 101643.
327. Motta, A., et al., *Serum Protein Absorption on Silk Fibroin Fibers and Films: Surface Opsonization and Binding Strength*. Journal of Bioactive and Compatible Polymers, 2002. **17**(1): p. 23-35.
328. Brunetti, V., et al., *Neurons sense nanoscale roughness with nanometer sensitivity*. Proc Natl Acad Sci U S A, 2010. **107**(14): p. 6264-9.
329. Khan, S.P., G.G. Auner, and G.M. Newaz, *Influence of nanoscale surface roughness on neural cell attachment on silicon*. Nanomedicine, 2005. **1**(2): p. 125-9.
330. Onesto, V., et al., *Nano-topography Enhances Communication in Neural Cells Networks*. Sci Rep, 2017. **7**(1): p. 9841.
331. Vasita, R. and D.S. Katti, *Nanofibers and their applications in tissue engineering*. International journal of nanomedicine, 2006. **1**(1): p. 15-30.
332. Zamani, F., et al., *The influence of surface nanoroughness of electrospun PLGA nanofibrous scaffold on nerve cell adhesion and proliferation*. J Mater Sci Mater Med, 2013. **24**(6): p. 1551-60.
333. Kai, D., et al., *Electrospun synthetic and natural nanofibers for regenerative medicine and stem cells*. Biotechnol J, 2013. **8**(1): p. 59-72.
334. Xie, J., et al., *The differentiation of embryonic stem cells seeded on electrospun nanofibers into neural lineages*. Biomaterials, 2009. **30**(3): p. 354-362.

335. Schaub, N.J., et al., *Electrospun Fibers for Spinal Cord Injury Research and Regeneration*. J Neurotrauma, 2016. **33**(15): p. 1405-15.
336. Swindle-Reilly, K.E., C.S. Paranjape, and C.A. Miller, *Electrospun poly(caprolactone)-elastin scaffolds for peripheral nerve regeneration*. Prog Biomater, 2014. **3**(1): p. 20.
337. Sun, M., et al., *Novel thin-walled nerve conduit with microgrooved surface patterns for enhanced peripheral nerve repair*. J Mater Sci Mater Med, 2010. **21**(10): p. 2765-74.
338. Hsu, S.H., C.H. Su, and I.M. Chiu, *A novel approach to align adult neural stem cells on micropatterned conduits for peripheral nerve regeneration: a feasibility study*. Artif Organs, 2009. **33**(1): p. 26-35.
339. Park, J., et al., *Directed migration of cancer cells guided by the graded texture of the underlying matrix*. Nat Mater, 2016. **15**(7): p. 792-801.
340. Park, M., et al., *Control over Neurite Directionality and Neurite Elongation on Anisotropic Micropillar Arrays*. Small, 2016. **12**(9): p. 1148-52.
341. Gautam, V., et al., *Engineering Highly Interconnected Neuronal Networks on Nanowire Scaffolds*. Nano Lett, 2017. **17**(6): p. 3369-3375.
342. Kleinman, H.K., et al., *Laminin receptors for neurite formation*. Proc Natl Acad Sci U S A, 1988. **85**(4): p. 1282-6.
343. Li, X., et al., *Biofunctionalized silk fibroin nanofibers for directional and long neurite outgrowth*. Biointerphases, 2019. **14**(6): p. 061001.
344. Chen, W.S., et al., *The Effect of Laminin Surface Modification of Electrospun Silica Nanofiber Substrate on Neuronal Tissue Engineering*. Nanomaterials (Basel), 2018. **8**(3).
345. Taylor, C.S., et al., *Cost effective optimised synthetic surface modification strategies for enhanced control of neuronal cell differentiation and supporting neuronal and Schwann cell viability*. Journal of Biomedical Materials Research Part B: Applied Biomaterials, 2021. **109**(11): p. 1713-1723.
346. Hopper, A.P., et al., *Amine functionalized nanodiamond promotes cellular adhesion, proliferation and neurite outgrowth*. Biomedical Materials, 2014. **9**(4): p. 045009.
347. Wang, S., et al., *Chitosan/gelatin porous scaffolds assembled with conductive poly(3,4-ethylenedioxythiophene) nanoparticles for neural tissue engineering*. J Mater Chem B, 2017. **5**(24): p. 4774-4788.
348. Wang, S., et al., *3D culture of neural stem cells within conductive PEDOT layer-assembled chitosan/gelatin scaffolds for neural tissue engineering*. Mater Sci Eng C Mater Biol Appl, 2018. **93**: p. 890-901.
349. Blau, A., *Cell adhesion promotion strategies for signal transduction enhancement in microelectrode array in vitro electrophysiology: An introductory overview and critical discussion*. Current Opinion in Colloid & Interface Science, 2013. **18**(5): p. 481-492.
350. Verdes, M., et al., *Finite Element Modelling of a Cellular Electric Microenvironment*. JoVE, 2021(171): p. e61928.
351. Srirussamee, K., et al., *Direct electrical stimulation enhances osteogenesis by inducing Bmp2 and Spp1 expressions from macrophages and preosteoblasts*. Biotechnol Bioeng, 2019. **116**(12): p. 3421-3432.
352. Srirussamee, K., et al., *Changes in the extracellular microenvironment and osteogenic responses of mesenchymal stem/stromal cells induced by in vitro direct electrical stimulation*. J Tissue Eng, 2021. **12**: p. 2041731420974147.
353. Ziegler, U. and P. Groscurth, *Morphological Features of Cell Death*. Physiology, 2004. **19**(3): p. 124-128.
354. Balvan, J., et al., *Multimodal Holographic Microscopy: Distinction between Apoptosis and Oncosis*. PLOS ONE, 2015. **10**(3): p. e0121674.
355. Nedachi, T., H. Fujita, and M. Kanzaki, *Contractile C2C12 myotube model for studying exercise-inducible responses in skeletal muscle*. Am J Physiol Endocrinol Metab, 2008. **295**(5): p. E1191-204.
356. Fujita, H., T. Nedachi, and M. Kanzaki, *Accelerated de novo sarcomere assembly by electric pulse stimulation in C2C12 myotubes*. Exp Cell Res, 2007. **313**(9): p. 1853-65.
357. Genovese, J.A., et al., *Electrostimulation induces cardiomyocyte predifferentiation of fibroblasts*. Biochem Biophys Res Commun, 2008. **370**(3): p. 450-5.

358. Ben Ishai, P., et al., *An assessment of comparative methods for approaching electrode polarization in dielectric permittivity measurements*. Rev Sci Instrum, 2012. **83**(8): p. 083118.
359. Mills, G.D., et al., *Phosphorylation of phospholamban at threonine-17 reduces cardiac adrenergic contractile responsiveness in chronic pressure overload-induced hypertrophy*. Am J Physiol Heart Circ Physiol, 2006. **291**(1): p. H61-70.
360. Ahlers, B.A., et al., *Effects of sarcoplasmic reticulum Ca²⁺-ATPase overexpression in postinfarction rat myocytes*. J Appl Physiol (1985), 2005. **98**(6): p. 2169-76.
361. Luiken, J.J., et al., *Electrostimulation enhances FAT/CD36-mediated long-chain fatty acid uptake by isolated rat cardiac myocytes*. Am J Physiol Endocrinol Metab, 2001. **281**(4): p. E704-12.
362. Qi, X.Y., et al., *Cellular signaling underlying atrial tachycardia remodeling of L-type calcium current*. Circ Res, 2008. **103**(8): p. 845-54.
363. Yamada, M., et al., *Electrical stimulation modulates fate determination of differentiating embryonic stem cells*. Stem Cells, 2007. **25**(3): p. 562-70.
364. Woods, V.M., I.F. Triantis, and C. Toumazou, *Offset prediction for charge-balanced stimulus waveforms*. Journal of Neural Engineering, 2011. **8**(4): p. 046032.
365. Patel, N. and M.M. Poo, *Orientation of neurite growth by extracellular electric fields*. J Neurosci, 1982. **2**(4): p. 483-96.
366. Rajnicek, A.M., K.R. Robinson, and C.D. McCaig, *The direction of neurite growth in a weak DC electric field depends on the substratum: contributions of adhesivity and net surface charge*. Dev Biol, 1998. **203**(2): p. 412-23.
367. Lynch, K.J., O. Skalli, and F. Sabri, *Growing Neural PC-12 Cell on Crosslinked Silica Aerogels Increases Neurite Extension in the Presence of an Electric Field*. J Funct Biomater, 2018. **9**(2).
368. Senftle, F.E., J.R. Grant, and F.P. Senftle, *Low-voltage DC/AC electrolysis of water using porous graphite electrodes*. Electrochimica Acta, 2010. **55**(18): p. 5148-5153.
369. Ergin Şahin, M., *A photovoltaic powered electrolysis converter system with maximum power point tracking control*. International Journal of Hydrogen Energy, 2020. **45**(16): p. 9293-9304.
370. Zou, H., et al., *A dual-electrolyte based air-breathing regenerative microfluidic fuel cell with 1.76V open-circuit-voltage and 0.74V water-splitting voltage*. Nano Energy, 2016. **27**: p. 619-626.
371. Brummer, S.B., J. McHardy, and M.J. Turner, *Electrical stimulation with Pt electrodes: Trace analysis for dissolved platinum and other dissolved electrochemical products*. Brain Behav Evol, 1977. **14**(1-2): p. 10-22.
372. Khaw, J.S., et al., *Electrical stimulation of titanium to promote stem cell orientation, elongation and osteogenesis*. Acta Biomater, 2021.
373. Rieger, S. and A. Sagasti, *Hydrogen peroxide promotes injury-induced peripheral sensory axon regeneration in the zebrafish skin*. PLoS Biol, 2011. **9**(5): p. e1000621.
374. Schmidt, C.E., et al., *Stimulation of neurite outgrowth using an electrically conducting polymer*. Proceedings of the National Academy of Sciences, 1997. **94**(17): p. 8948-8953.
375. Park, J.S., et al., *Electrical pulsed stimulation of surfaces homogeneously coated with gold nanoparticles to induce neurite outgrowth of PC12 cells*. Langmuir, 2009. **25**(1): p. 451-7.
376. Gomez, N. and C.E. Schmidt, *Nerve growth factor-immobilized polypyrrole: bioactive electrically conducting polymer for enhanced neurite extension*. J Biomed Mater Res A, 2007. **81**(1): p. 135-49.
377. Huang, Y.J., et al., *Carbon nanotube rope with electrical stimulation promotes the differentiation and maturity of neural stem cells*. Small, 2012. **8**(18): p. 2869-77.
378. Koppes, A.N., et al., *Electrical stimulation of schwann cells promotes sustained increases in neurite outgrowth*. Tissue Eng Part A, 2014. **20**(3-4): p. 494-506.
379. Durgam, H., et al., *Novel degradable co-polymers of polypyrrole support cell proliferation and enhance neurite out-growth with electrical stimulation*. J Biomater Sci Polym Ed, 2010. **21**(10): p. 1265-82.

380. Rodriguez Sala, M., et al., *Enhanced neurite outgrowth on electrically conductive carbon aerogel substrates in the presence of an external electric field*. Soft Matter, 2021. **17**(17): p. 4489-4495.
381. Imaninezhad, M., et al., *Directed and enhanced neurite outgrowth following exogenous electrical stimulation on carbon nanotube-hydrogel composites*. J Neural Eng, 2018. **15**(5): p. 056034.
382. Chen, C., et al., *Electrical stimulation as a novel tool for regulating cell behavior in tissue engineering*. Biomaterials Research, 2019. **23**(1): p. 25.
383. Adams, R.D., B. Gupta, and A.B. Harkins, *Validation of electrical stimulation models: intracellular calcium measurement in three-dimensional scaffolds*. J Neurophysiol, 2017. **118**(2): p. 1415-1424.
384. Gordon, T., *The role of neurotrophic factors in nerve regeneration*. Neurosurg Focus, 2009. **26**(2): p. E3.
385. Wenjin, W., et al., *Electrical stimulation promotes BDNF expression in spinal cord neurons through Ca(2+)- and Erk-dependent signaling pathways*. Cell Mol Neurobiol, 2011. **31**(3): p. 459-67.
386. Hu, M., et al., *Electrical stimulation enhances neuronal cell activity mediated by Schwann cell derived exosomes*. Sci Rep, 2019. **9**(1): p. 4206.
387. Love, M.R., et al., *Effects of electrical stimulation on cell proliferation and apoptosis*. J Cell Physiol, 2018. **233**(3): p. 1860-1876.
388. Iseki, K., et al., *Gliosis-specific transcription factor OASIS coincides with proteoglycan core protein genes in the glial scar and inhibits neurite outgrowth*. Biomedical Research, 2012. **33**(6): p. 345-353.
389. Alexander, J.K., B. Fuss, and R.J. Colello, *Electric field-induced astrocyte alignment directs neurite outgrowth*. Neuron Glia Biol, 2006. **2**(2): p. 93-103.
390. Gokoffski, K.K., et al., *Physiologic Electrical Fields Direct Retinal Ganglion Cell Axon Growth In Vitro*. Invest Ophthalmol Vis Sci, 2019. **60**(10): p. 3659-3668.
391. Bórquez, D.A., et al., *Dissecting the role of redox signaling in neuronal development*. Journal of Neurochemistry, 2016. **137**(4): p. 506-517.
392. Meda, F., et al., *Nerves Control Redox Levels in Mature Tissues Through Schwann Cells and Hedgehog Signaling*. Antioxidants & redox signaling, 2016. **24**(6): p. 299-311.
393. Kuzyk, P.R. and E.H. Schemitsch, *The science of electrical stimulation therapy for fracture healing*. Indian J Orthop, 2009. **43**(2): p. 127-31.
394. Bodamyali, T., et al., *Effect of faradic products on direct current-stimulated calvarial organ culture calcium levels*. Biochem Biophys Res Commun, 1999. **264**(3): p. 657-61.
395. Abcam. *Live cell staining dyes*. [cited 2022 March 13]; Available from: <https://www.abcam.com/kits/cytopainter-kits-and-reagents>.
396. Scientific, T.F. *5 Steps to Live-Cell Imaging*. [cited 2022 March 13]; Available from: <https://www.thermofisher.com/th/en/home/life-science/cell-analysis/cellular-imaging/fluorescence-microscopy-and-immunofluorescence-if/microscopy-reagents-and-media/live-cell-imaging-reagents.html>.
397. Merck. *Live Cell Imaging Reagents*. [cited 2022 March 13]; Available from: <https://www.sigmaaldrich.com/GB/en/products/cell-culture-and-analysis/cell-analysis/live-cell-imaging-reagents>.
398. Yasuda, R., et al., *Imaging calcium concentration dynamics in small neuronal compartments*. Sci STKE, 2004. **2004**(219): p. pl5.
399. Healthcare, B. *CQ1 Benchtop High-Content Analysis System*. [cited 2022 March 13]; Available from: <https://www.biotronhealthcare.com/cq1-benchtop-high-content-analysis-system/>.
400. Kimura, Y. and H. Higashida, *Dissection of bradykinin-evoked responses by buffering intracellular Ca²⁺ in neuroblastoma x glioma hybrid NG108-15 cells*. Neuroscience Research, 1992. **15**(3): p. 213-220.
401. Goshima, Y., S. Ohsako, and T. Yamauchi, *Overexpression of Ca²⁺/calmodulin-dependent protein kinase II in Neuro2a and NG108-15 neuroblastoma cell lines promotes neurite outgrowth and growth cone motility*. The Journal of Neuroscience, 1993. **13**(2): p. 559.

402. Peng, K., X.-D. Chen, and S.-P. Liang, *The effect of Huwentoxin-I on Ca²⁺ channels in differentiated NG108-15 cells, a patch-clamp study*. Toxicon, 2001. **39**(4): p. 491-498.
403. Ching, R.C., M. Wiberg, and P.J. Kingham, *Schwann cell-like differentiated adipose stem cells promote neurite outgrowth via secreted exosomes and RNA transfer*. Stem Cell Research & Therapy, 2018. **9**(1): p. 266.
404. Hu, A., et al., *Electrospun silk fibroin nanofibers promote Schwann cell adhesion, growth and proliferation*. Neural regeneration research, 2012. **7**(15): p. 1171-1178.
405. Xu, S., et al., *In vitro biocompatibility of electrospun silk fibroin mats with Schwann cells*. Journal of Applied Polymer Science, 2011. **119**(6): p. 3490-3494.
406. Li, G., et al., *Laminin-Coated Electrospun Regenerated Silk Fibroin Mats Promote Neural Progenitor Cell Proliferation, Differentiation, and Survival in vitro*. Frontiers in Bioengineering and Biotechnology, 2019. **7**(190).
407. Benfenati, V., et al., *Biofunctional Silk/Neuron Interfaces*. Advanced Functional Materials, 2012. **22**(9): p. 1871-1884.
408. Tsui, J.H., et al., *Conductive silk-polypyrrole composite scaffolds with bioinspired nanotopographic cues for cardiac tissue engineering*. Journal of Materials Chemistry B, 2018. **6**(44): p. 7185-7196.
409. Yong, J., et al., *A Silk Fibroin Bio-Transient Solution Processable Memristor*. Scientific Reports, 2017. **7**(1): p. 14731.